ANALYZING IN-CYLINDER FLOW VARIATIONS IN A MOTORED SPARK IGNITION ENGINE USING PROPER ORTHOGONAL DECOMPOSITION

by

Preeti Suzanne Abraham

A dissertation submitted in partial fulfillment
of the requirements for the degree of
Doctor of Philosophy
(Mechanical Engineering)
in the University of Michigan
2013

Doctoral Committee:

Professor Volker Sick, Chair
Associate Professor Luis P. Bernal
Professor Steven L. Ceccio
David L. Reuss

For Appa and Amma

ACKNOWLEDGMENTS

I would like to thank my advisor, Dr. Volker Sick, for his guidance and support throughout my years as a graduate student. I would also like to thank Dr. Dave Reuss for building my engine, answering my many questions, and allowing me to learn from his vast experience. The conversations Volker, Dave, and I have had while trying to interpret my data are some of the most exhilarating memories of my graduate career.

Thank you also to Dr. Steve Ceccio and Dr. Luis Bernal for agreeing to serve on my committee. I am most honored. Your thoughts and comments on my dissertation proposal have been invaluable guides.

I have had the privilege of being a member of the Large-Eddy Simulation Working Group for the past several years. This collaborative group has been the source of many edifying discussions on the synergy between experimental and computational engine research. I would particularly like to thank Dr. Xiaofeng Yang and Dr. Tang-Wei Kuo from General Motors Research and Development and Dr. Kai Liu, presently at Cummins Combustion Research, and Dr. Daniel Haworth of Pennsylvania State University for allowing me to use their large-eddy simulation data in my dissertation.

My research has been made possible through the generous financial sponsorship of General Motors through the Engine Systems Research Laboratory of the General Motors/University of Michigan Institute of Automotive Research and Education.

I would also like to thank my current and former labmates at the Quantitative Laser Diagnostics Laboratory for their help and support through the years: Dr. Claudia Fajardo, Dr. Ali Alharbi, Dr. Brian Peterson, Dr. Michael Cundy, Dr. Kevin Peterson, Dr. Michael Mosburger, Omar Almagri, Hao Chen, Philipp Schiffmann, Mark Greene, Yu-Hung Chang, Louise Lu, and Peter Lillo. Thank you for helping me run my engine, process data, troubleshoot in the lab, and better understand scientific concepts. Work done by Dave, Philipp, and Mark on verifying encoder and valve timings and pressure transducer errors has also been integral to this dissertation.

My family, particularly my grandmother, my parents, my (many!) aunts, and my brother, has been a constant source of love and encouragement through my time as a graduate student. Thank you also to my best friend, Kristel, for the emails and the visits, for being there for me always. I am also immeasurably grateful to my husband, Justin, for taking care of me and loving me and being my strength on days when I had none.

TABLE OF CONTENTS

LIST OF FIGURES

LIST OF TABLES

ABSTRACT

The development of clean and efficient internal combustion engine technologies is inhibited by the current limitations in understanding cycle-to-cycle combustion variations. Cycle-to-cycle in-cylinder flow variations are thought to be one of the leading causes of cycle-to-cycle combustion variations. In this study, high-speed particle image velocimetry (PIV) data was acquired in an optical research engine with varying spatial resolution and dynamically varying time separations between PIV images for optimal velocity dynamic range throughout the engine cycle. Proper orthogonal decomposition (POD) was then used to quantitatively examine the cycle-to-cycle flow variations and intra-cycle flow evolution in these data sets. One of the causes of in-cylinder flow variations was found to be the oscillatory motion of the intake valve during its opening and closing. The scaling of in-cylinder flow with engine speed was also studied by measuring in-cylinder velocities at three different engine speeds. Further, the use of POD as a tool for differentiating between flow patterns in different data sets was demonstrated by comparing experimental data with two different large-eddy simulation data sets.

It was found that the level of cycle-to-cycle variability in intake valve oscillations influences in-cylinder flow patterns during the intake stroke. Changes in intake valve oscillations may be triggered by engine speed transients, but may also occur between different engine runs. POD was used to show that the direction and magnitude of the flow patterns during intake scale, on average, with the horizontal position of the intake valve. However, it was not possible to establish a one-on-one connection between intake valve motion and intake flow for individual

cycles. Neither was a clear link found between variations in intake flow pattern and flow close to top dead center compression using two-component velocity data from the central tumble plane of the optical engine. POD was also shown to be an effective and quantitative tool for the comparison of large experimental data sets at three different engine speeds, and large combined experimental and computational data sets at 800 rpm, accurately reflecting differences in in-cylinder flow evolution and variation between the data sets.

CHAPTER 1

INTRODUCTION

This chapter outlines the motivation for studying in-cylinder flow variations and the objectives of this dissertation. Background information and a survey of relevant literature on cycle-to-cycle flow variations, turbulence, proper orthogonal decomposition, intake flows, particle image velocimetry, and large-eddy simulation are also presented. This chapter concludes with an outline of the rest of the dissertation.

1.1 Motivation and Objectives

Since their invention, internal combustion engines have transformed modern civilization by providing a means of fast, safe and inexpensive personal transportation to millions of people. However, as the world population rises and more nations industrialize, the demand for automobiles increases as the reserves of fossil fuels that they run on dwindle. A part of the solution to this problem is designing internal combustion engines that utilize currently available fossil fuels more efficiently.

In order to design better internal combustion engines, it is important to gain a more complete understanding of flow phenomena such as turbulence and cycle-to-cycle flow variation. Cycle-to-cycle flow variations are fluctuations in the bulk flow in unsteady, periodic flow, such as in-cylinder flow in an engine. Traditional velocity decompositions consider all fluctuations about an ensemble average in-cylinder flow to be turbulence. However, cycle-to-cycle variations

in the bulk flow caused by varying initial and boundary conditions can lead to an overestimation of turbulence in such a decomposition. An accurate estimate of small-scale turbulence is essential for the development of turbulent combustion models. Further, cycle-to-cycle variations in in-cylinder flow form an important contribution to cycle-to-cycle combustion variations, which limit the use of exhaust gas recirculation, lean air-fuel mixtures, and lower idle speeds, among other technologies that increase engine efficiency. In particular, the development of gasoline direct injection technology, which uses air-fuel mixture stratification to create combustible mixtures that are lean overall, is hampered by the extreme resultant cycle-to-cycle combustion variations that lead to higher emissions, engine noise, and poor drivability.

This study analyzes high-speed digital particle image velocimetry (PIV) data using proper orthogonal decomposition (POD) to characterize cycle-to-cycle flow variations in engines. Two-component velocity data was acquired from the central tumble plane of an optical engine using high-speed PIV with varying spatial resolutions and time separations between images to optimize the PIV velocity dynamic range for the entire cycle. An error analysis was done to quantify the benefits of using two different spatial resolutions. Further, the errors associated with constant and variable PIV time separations are compared.

Variations in valve flow and pressure fluctuations in the intake system are potential sources of cycle-to-cycle flow variations. High-speed pressure transducers in the intake and exhaust systems were used to acquire pressure data every half crank angle degree in synch with the in-cylinder velocity data. This pressure data was examined to ensure test repeatability and to detect cycle-to-cycle variations. The valve in the optical engine used in these experiments displayed a horizontal oscillation during opening and closing. The correlation between these oscillations and in-cylinder flow structure was also determined using POD.

In this work, POD has also been used to compare experimental velocity data acquired at three different engine speeds to determine the scaling of in-cylinder flow structures and flow evolution with engine speed. As a comparative tool, POD was applied to a combined data set with both experimental PIV data and the results of large-eddy simulation (LES) engine models developed by collaborators at General Motors and Pennsylvania State University. LES can capture the cycle-to-cycle flow variations seen in experimental engine data. Thus, the validation and improvement of LES engine models is essential for the development of new engine technologies.

1.2 Cycle-to-Cycle Flow Variations and Turbulence in Engines

Turbulence has traditionally been defined using the Reynolds Average Navier-Stokes (RANS) decomposition, as shown in Equation (1.1):

$$u = \langle u \rangle + u' \tag{1.1}$$

RANS decomposition considers, u', which is the fluctuation about the mean velocity, to be associated with turbulence alone. However, this is an inappropriate approach to analyzing the periodic, unsteady flow in an engine. Varying initial conditions at the start of different cycles and periodically varying boundary conditions throughout a cycle result in cycle-to-cycle variations in in-cylinder bulk flow. Thus, a RANS decomposition of in-cylinder flow would lead to an over-prediction of small-scale turbulence intensity, which accounts for turbulent kinetic energy dissipation and is input into combustion models for engines.

Turbulence is a stochastic fluctuation about the bulk flow that is a consequence of the inherent instability of flows at high Reynolds numbers. Any perturbations, however small, in initial or boundary conditions are magnified in turbulent flow to create chaotic velocity distributions. According to Kolmogorov's theory of energy cascade, large-scale turbulent

structures break down to small-scale turbulent structures. At small scales, turbulence is held to be universal in nature; that is, small-scale turbulence in various types of flows share common characteristics [1]. The turbulent flame speed is proportionate to the magnitude of this small-scale turbulence. Thus, in order to gain an accurate understanding of combustion in engines using universal turbulent combustion models, an accurate estimate of the small-scale turbulence intensity is essential.

The nature of mean flow in an engine also needs to be taken into account when performing decompositions of in-cylinder flow. While consistent flow structures at various crank angles may be discernible in an engine with highly directed flow, undirected flow in an engine may lead to instantaneous velocity distributions at various crank angles that vary vastly from cycle-to-cycle. Thus, the mean flow in engines with undirected flow may have little relevance to the instantaneous velocity distributions. This is well illustrated in a study conducted by Reuss on an earlier configuration of the two-valve pancake-chamber transparent combustion chamber (TCC) engine presented in this dissertation, as shown in Figure 1.1.

Instantaneous Flow Fields – Directed Flow

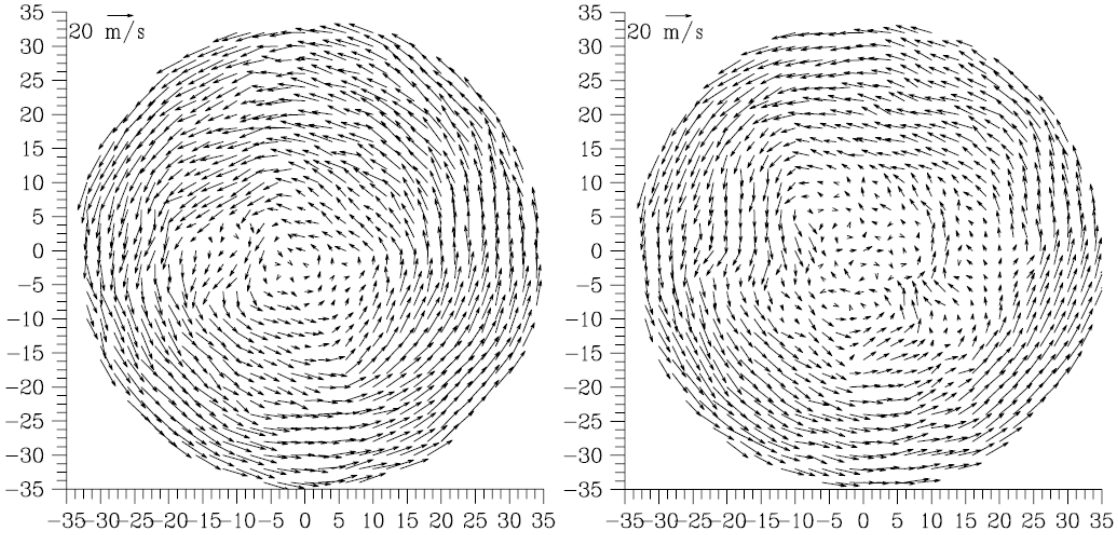

(a) *(b)*

Instantaneous Flow Fields – Undirected Flow

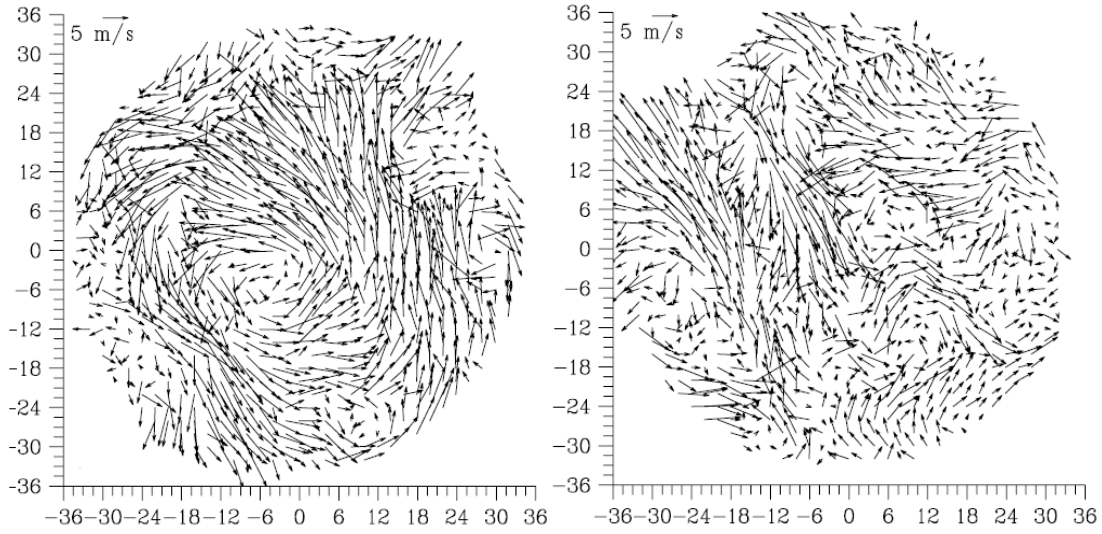

(c) *(d)*

Ensemble-Averaged Flow Fields

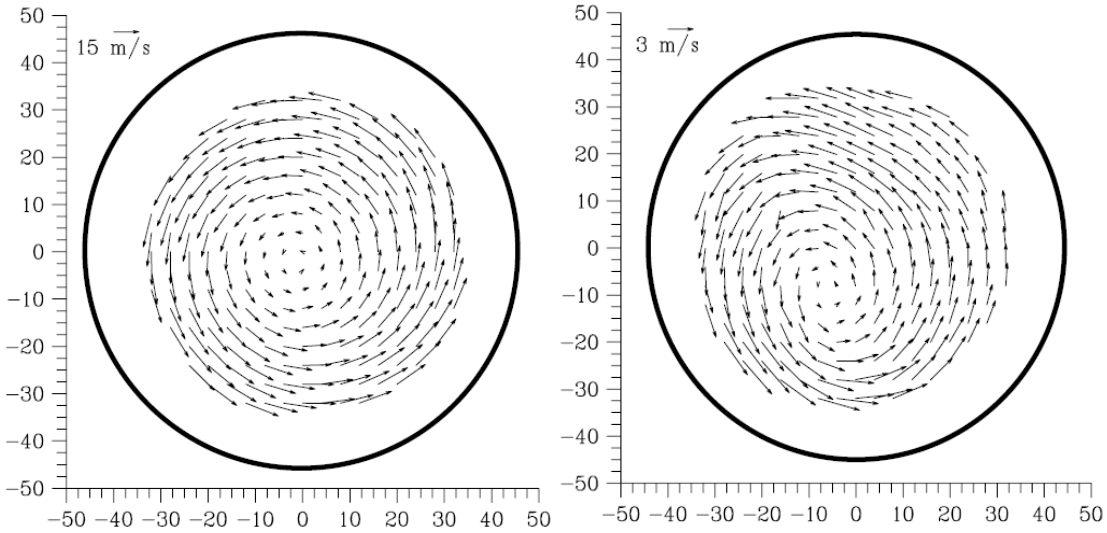

(e) *(f)*

Figure 1.1: *Instantaneous velocity distributions and ensemble means (calculated from 200 realizations; every eighth vector shown) for directed (a, b, and e) and undirected (c, d, and f) flows at TDC, mid-plane, of an earlier configuration of the TCC engine [2]*

Thus, in engines with undirected flow, examining fluctuations about the large-scale bulk flow may be more relevant. Also, misfires and partial burns, which are rare events that exhibit extreme cycle-to-cycle combustion and flow variation, may unduly influence mean flow calculations and lead to the underestimation of cycle-to-cycle variations.

Research into an appropriate velocity decomposition to describe in-cylinder flow in engines is ongoing. Many studies have used decompositions of the type shown in Equation (1.2) [2-5].

$$u = \langle u \rangle + u'_{lp} + u'_{hp} \tag{1.2}$$

In Equation (1.2), a cut-off frequency separates fluctuations about the mean velocity into a low-pass component, u'_{lp}, which is considered to be cycle-to-cycle variations, and a high-pass component, u'_{hp}, which is considered to be turbulence.

The cut-off frequency can be defined in several different ways. The idea of using the autocorrelation function or the integral time or length scale to determine the cut-off frequency is derived from classical turbulence theory [5]. The temporal autocorrelation function, $\rho(\tau)$, for a time difference τ, is generally defined as shown in Equation (1.3)[1].

$$\rho(\tau) = \frac{\overline{u'_{turb}(t)u'_{turb}(t+\tau)}}{\overline{u'^2_{turb}}} \tag{1.3}$$

The spatial autocorrelation function, $(\vec{r})$, is defined in a similar fashion. The integral time scale is an approximate measure of how long the turbulence remains correlated with itself. It is defined as shown in Equation (1.4).

$$\Lambda_t = \int_0^{+\infty} \rho(\tau) d\tau \tag{1.4}$$

The integral length scale, $\Lambda_{\vec{r}}$, is defined similarly.

The autocorrelation and integral scales of turbulence are functions of the turbulent velocity fluctuations. Thus, using these measures to determine the turbulence requires an

estimate of the turbulence, which is provided by u' from a RANS decomposition [5]. Amelio, et al. [5] used a temporal autocorrelation function to determine the cut-off frequency. The coherence time was determined in a somewhat arbitrary manner by finding the intercept with zero of the interpolation of the linear decaying zone following the maximum of the autocorrelation function. It was found to vary with crank angle, engine speed, and LDV measurement location. It is unclear how this fact is taken into account while computing cut-off frequencies. The cut-off frequency was found to increase as the engine speed increases, and as the LDV measuring point moved from a region of more directed flow (near the intake valves) to a region of more undirected flow (at the center of the cylinder, or near the exhaust valves).

A related method of determining the cut-off frequency is finding the knee-frequency at the beginning of the region with an f-5/3 slope in the turbulence power spectral density, or normalized turbulent kinetic energy spectral density [5]. The turbulent kinetic energy spectral density is computed as the Fourier transform of the autocorrelation function. The region with an f-5/3 slope characterizes stationary, isotropic turbulence [1]. Stationary turbulence has statistical properties that are independent of time and spatial location, which is not necessarily the case in in-cylinder flow. However, small-scale in-cylinder turbulence is expected to be isotropic in nature. Amelio, et al. [5] found that the knee in the power spectral densities examined was not very clear and thus could not be used to find the cut-off frequency. Li, et al. [4] used the power spectral density calculated from the spatial autocorrelation function to determine cut-off frequency. This is also found to vary with crank angle. This study used an engine running at a single speed of 1200 rpm, so the effect of varying speed on cut-off frequency could not be confirmed. The cut-off frequency is found to be 0.075 mm^{-1} in both coordinates in the horizontal PIV measurement plane, and 0.05 mm^{-1} in the x coordinate and 0.125 mm^{-1} in the y coordinate in

the vertical measurement planes [4]. It is unclear how the effect of varying crank angles on the cut-off frequency was accounted for.

Another method for calculating the cut-off frequency is to compute the fast Fourier transform of the ensemble-averaged velocity and choose the cut-off frequency as the frequency above which the magnitude of the transform approaches zero. This is a reasonable criterion as very little small-scale turbulent fluctuation is expected to remain in the ensemble mean calculated from a sufficiently large data set. Figure 1.2 shows the dependence of cut-off frequencies obtained using this method on engine speed and LDV measurement location.

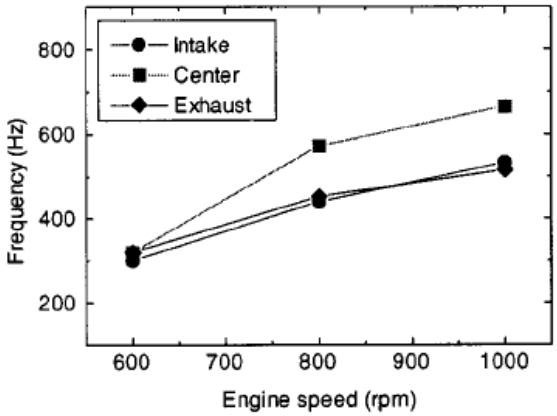

Figure 1.2: *Cut-off frequency obtained from the fast Fourier transform of the ensemble-averaged velocity [5]*

St. Hill, et al. [3] used this method to select a cut-off frequency of 250 Hz for LDA data obtained from an engine running at 500 rpm. This appears to be consistent with the values shown in Figure 1.2. It is unclear what effect varying crank angles have on the cut-off frequency calculated using this method. Liu et al. [6] chose cut-off frequencies using the fast Fourier transform of the total fluctuating velocity component.

Although some level of arbitrariness is present in the methods listed above that are used to determine the cut-off frequency, variations of up to ± 100 Hz in the cut-off frequency result in

negligible changes in the turbulence intensity calculated [3, 5]. However, a study by Enotiadis et al. argues against the use of somewhat arbitrarily selected cut-off frequencies, stating that the deterministic nature of flow structures in the fluctuating velocity component must be used to separate random turbulence from cycle-to-cycle flow variations [7].

The arguments against the relevance of ensemble averaging to in-cylinder flows led to velocity decompositions, such as the one defined in Equations (1.5) and (1.6), that do not include the concept of a mean flow [8].

$$u = u_{CYCM} + u'_{hp} \tag{1.5}$$

$$u_{CCVCM} = \langle u_{CYCM} \rangle - u_{CYCM} \tag{1.6}$$

Equation (1.5) separates the instantaneous velocity into a low-pass filtered cycle average velocity and a high-pass filtered turbulent velocity. The cut-off frequency used is 300 Hz. This is based on the calculated motion of the flow structures. The variation of cut-off frequency with crank angle is not discussed. The engine was run at 1500 rpm, and PIV data was gathered in the primary tumble plane (plane parallel to the cylinder axis). Equation (1.6) defines the cycle-to-cycle variation of a particular cycle as the difference between the mean cycle average velocity and the cycle average velocity of that cycle [8].

Attempts have also been made to analyze cycle-to-cycle flow variability using tumble or swirl ratios [6, 9, 10]. Tumble or swirl ratios are measures of the dominance of the large-scale tumble or swirl vortex in the in-cylinder flow. Highly directed flows will have large tumble or swirl ratios. Thus, examining the mean and variance of tumble or swirl ratios in a highly directed flow provides an estimate of the cycle-to-cycle flow variation of the largest length scale of the bulk flow velocity. However, spatially resolved information, and information about the other length scales in the bulk flow is not provided.

1.3 Proper Orthogonal Decomposition

Proper orthogonal decomposition (POD) has also been used to differentiate between bulk flow, cycle-to-cycle flow variations, and turbulence. POD of a set $V_{i=1\ to\ N}$ produces a set of orthonormal basis functions $\varphi_{i=1\ to\ N}$, as shown in Equation (1.7).

$$V_i = \sum_{j=1}^{N} c_{ij}\varphi_j \tag{1.7}$$

These basis functions, or modes, are determined by minimizing the expression $\sum_{i=1}^{N}\left\|V_i - \sum_{j=1}^{N} c_{ij}\varphi_j\right\|$ while imposing orthogonality. In this expression, ||.|| denotes the l^2-norm. Each coefficient c_{ij} is determined by projecting V_i onto φ_j [11]. When applying POD to 2-D PIV velocity vector fields, both $V_{i=1\ to\ N}$ and $\varphi_{i=1\ to\ N}$ are functions of two spatial coordinates and time. For phase-dependent POD, $V_{i=1\ to\ N}$ is a set of velocity vector fields (snapshots) obtained at a single crank angle from multiple cycles. For phase-invariant POD, snapshots sampled at multiple crank angles and from multiple cycles are analyzed [12].

POD requires that all input velocity fields have vectors at the same spatial locations. Thus, for phase-invariant POD, it is necessary to account for the different size fields-of-view in particle image velocimetry data at each crank angle as the piston sweeps the cylinder. For this purpose, the vector field grids were linearly transformed to a common grid to match that at midstroke. Then, the velocity vectors were interpolated from the original to the common grid. Thus, all vector fields would have an equal number of vectors. In addition, velocity magnitudes at each velocity field from each crank angle were normalized by the square root of the energy in that vector field. This transformation is needed because POD is an energy-weighted decomposition and would otherwise have been biased by the varying kinetic energy levels in vector fields from various parts of the engine cycle [13].

POD basis functions are normalized and then ordered by their energy fraction, defined in Equation (1.8).

$$E_j = \frac{\sum_{i=1}^{N} \frac{1}{2} c_{ij}^2}{\sum_{j=1}^{N} \sum_{i=1}^{N} \frac{1}{2} c_{ij}^2} \tag{1.8}$$

The energy fraction associated with a particular mode is the average mass-specific kinetic energy fraction that it contributes to elements in the set $V_{i=1 \text{ to } N}$. $0.5*c_{ij}^2$ is the mass-specific kinetic energy contributed by mode φ_j to V_i. While Equation (1.8) applies directly for phase dependent POD, it can be simplified for phase-invariant analysis due to the energy normalization, as shown in Equation (1.9).

$$E_{j,Phase-Invariant\ POD} = \frac{\sum_{i=1}^{N} \frac{1}{2} c_{ij}^2}{\sum_{j=1}^{N} \sum_{i=1}^{N} \frac{1}{2} c_{ij}^2} = \frac{\sum_{i=1}^{N} \frac{1}{2} c_{ij}^2}{\sum_{i=1}^{N} 1} = \frac{1}{N} \sum_{i=1}^{N} \frac{1}{2} c_{ij}^2 \tag{1.9}$$

Thus for phase-dependent POD, E_j is the fraction of the energy summed over all cycles at the single crank angle. For phase-invariant POD E_j is the fraction of transformed and normalized total energy summed over all crank angles and all cycles. The first few modes, ordered by their energy fraction, contain velocity structures that occur in many velocity vector fields, or dominate a few velocity vector fields. Any velocity vector field may be approximated well using just the first few modes, as energy fractions usually decay sharply with increasing mode order.

The relevance index, $RI_{U,V}$, is the metric chosen to quantify the equivalence of structures present in two different velocity vector fields U and V. It may be used to compare POD modes to ensemble average velocity fields or velocity fields reconstructed using a limited number of lower order modes to the original velocity fields. It is computed by projecting one velocity field onto another and is defined as shown in Equation (1.10).

$$RI_{U,V} = \frac{(U,V)}{\|U\|.\|V\|} \tag{1.10}$$

In Equation (1.10), the numerator is the inner product of two velocity fields over the whole domain. If U and V are identical, $RI_{U,V}$ will be equal to 1. If $RI_{U,V}$ is equal to -1, U and V are exactly opposite. U and V are orthogonal if $RI_{U,V}$ is equal to 0 [12].

POD has previously been used to differentiate between cyclic flow variations and turbulence. Baby et al.[14] used the first mode to represent the mean in-cylinder velocity. The engine used in this study has a highly directed tumble motion; thus, it was expected that the bulk flow velocity would be expressed in the first few modes, and that it would be very close to the ensemble mean velocity. Modes 2-4 were reconstructed to represent the cyclic variability, and the rest of the modes represented the turbulence. Mode 4 was chosen somewhat arbitrarily as the last mode in the truncation by varying the last mode and looking for asymptotic behavior.

Cosadia et al.[15] found that determining a cut-off mode was not possible, as the cumulative energy fractions of the POD of the instantaneous velocity fields converged very slowly despite the presence of a strong in-cylinder swirl motion. Enaux et al. [16] used the ratio between the energy fractions of the first and second modes as a measure of cyclic flow variations. Chen et al. [17, 18] proposed that, if the first mode is a good estimate of the mean flow, the POD coefficients of the first mode may be used to estimate the mass-specific kinetic energy contribution of the mean flow to any velocity field used in the decomposition, thus estimating how closely a particular velocity field compares to the mean flow. Similarly, the mass-specific kinetic energy contribution of all higher modes estimates the RANS turbulence in a specific velocity field. Thus, the cyclic variability of the mean flow and of the turbulence may be quantified. Vu et al. [19] also used the relevance index to determine that the first two modes from POD analyses at 90°, 180°, and 270° ATDCE described the mean flow at these crank angles. This study further divided the rest of the modes into two parts describing the cycle-to-

cycle flow variations and small-scale homogenous isotropic turbulence using a cutoff mode. This cutoff mode was determined by evaluating the skewness and flatness of the turbulent flow reconstructed using various ranges of POD modes. These studies performed the POD analysis on velocity fields at single crank angles from several cycles (phase-dependent POD).

Additionally, phase-invariant POD has been used to analyze cyclic variability, where the coefficients are used to quantify cyclic flow variability [12, 13, 20, 21]. In this case POD is applied to intra-cycle velocity fields from contiguous crank angles and cycles. However, the first mode need not necessarily be the dominant mode at a specific crank angle. Thus, the first mode from a phase-invariant POD analysis cannot be understood as an estimate of the ensemble average flow at all crank angles. Phase-invariant POD has also been used to analyze in-cylinder flow evolution [12, 21]. One of its initial applications was the analysis of separate particle image velocimetry (PIV) and computational fluid dynamics (CFD) data sets obtained during the intake and compression strokes of various simplified piston and single valve or intake channel configurations [12]. The results showed the evolution of the tumble vortex formed and its breakdown into small-scale turbulence.

A similar phase-invariant POD analysis was used to study the tumble vortex breakdown in the crank angle range of 270° to 360° ATDCE (After Top Dead Center Exhaust) in a more realistic optical engine with a pent roof head and four valves [21]. It was found that the first mode of the phase-invariant POD contained aspects of a large-scale tumble vortex. The coefficients of the first mode then provided an estimate of the dominance of the tumble vortex at various crank angles. As the phase-invariant POD coefficients provide information about both the evolution of flow structures in a cycle and cyclic flow variability, they can provide insight

into intra-cycle flow correlations and may be used to find the cause and effect of unusual flow patterns.

Liu, et al.[13] used both phase-dependent and phase-invariant POD to study cycle-to-cycle flow variability in LES simulations of swirling and non-swirling flow in a piston-cylinder assembly with a single axisymmetric valve at a constant lift, motored at 200 rpm. It was found that the degree of flow directedness varied over the course of the engine cycle. The amount of energy present in the first mode in phase-dependent POD decreased at TDC and BDC and the spread in the phase-invariant POD coefficients over the cycles analyzed was greatest at TDC and BDC, showing that cycle-to-cycle flow variability was highest at TDC and BDC. Although the trends are similar for swirling and non-swirling flow, it was found that cycle-to-cycle flow variations at TDC are greater in non-swirling flow than in swirling flow. It was also found that phase-invariant POD modes and energy distributions showed no significant difference when computed using as few as 30 vector fields per engine cycle or as many as 360. This convergence may be exploited to interpolate between measured data to improve time resolution [22, 23].

1.4 Intake Flows

Cycle-to-cycle in-cylinder flow variations towards TDCC (Top Dead Center Combustion) may be influenced by cycle-to-cycle variations flow variations earlier in the cycle. In order to determine if cycle-to-cycle variations in intake valve flows have an influence on combustion events, the persistence of large-scale intake flow structures towards TDCC and the relationship between intake flow variations and turbulent kinetic energy intensities at TDCC must be verified. Cycle-to-cycle variations in intake flow are caused by phenomena such as ‘jet flapping’ and intake valve oscillations. ‘Jet flapping’ is characterized by periodic flow detachment from and reattachment to the valve or the valve seat. Thus, the intake jet ‘flaps’

between the valve and the valve seat. Intake valve oscillations, also referred to as 'valve ringing' may occur during valve actuation in older production engines due to an increase in valve assembly clearances over time. This phenomenon may also be observed in the engine studied in this dissertation.

Intake flows have traditionally been studied using steady flow experimental setups or computations where air is forced through an engine head with an intake valve open to a constant lift into a cylinder with an attached exhaust system instead of a piston [24-27]. A further simplification of this setup involves the replacement of the engine head with a single port/valve assembly [28, 29]. A more realistic version of this experimental setup includes a moving piston, although the valve still remains stationary [30]. Another study used a modified steady flow experimental setup with moving valves [31].

Steady flow intake valve experiments are far simpler to conduct than those that examine intake valve flow under regular operating conditions. They are justified by the quasi-steady assumption which states that the instantaneous velocity profile of intake valve flow depends only upon the valve lift and the instantaneous mass flow through the valve. Intake valve flow is thought to be unaffected by interactions with in-cylinder flow and the piston as intake valve flows are associated with a much smaller time scale than velocities associated with an engine [24].

However, a study by Mattarelli, et al. [32] demonstrates that steady flow tests and standard engine operation are nonequivalent. A 3D CFD simulation (using commercial software) of the intake stroke, including intake valve opening and closing, of a conventional four stroke turbocharged diesel engine was compared to both experimental and numerical steady flow test data. Intake valve strategies that were found to increase the swirl ratio using steady flow testing

were found to offer no added advantage when tested using the intake stroke simulation. Further, the in-cylinder flow field at BDC during the intake stroke simulation was found to contain both swirl and tumble vortices of comparable strength. As expected, piston and intake valve motion influence in-cylinder flow development during standard engine operation.

Intake valve and in-cylinder flows have been studied in running engines with moving valves [33-39]. The effects of valve seat angle, maximum valve lift, and induction swirl on in-cylinder flow was studied using a pancake chamber engine with a compression ratio of 3.5, motored at 200 rpm. It was found in all cases that the flow structures generated at intake in the axial plane nearly disappear by IVC. However, in the tangential plane (15 mm below the head), the swirling flow generated during intake persists towards TDCC in all cases. The relevance of these results to engine operating at higher speeds requires verification [34].

The in-cylinder flow generated by five different intake valve configurations in a production four-valve spark ignition engine with a pent-roof chamber, Siamese intake port, and a shallow piston dish was studied by Khaligi, et al. [36] using a RANS model with k-ε turbulence modeling and transient water analog flow visualization. With both intake valves activated and unshrouded, no coherent large-scale flow structures are generated during induction. When one intake valve is deactivated, a coherent large-scale swirl structure is detected at the end of the intake stroke and persists into the compression stroke. The flow visualization data shows cycle-to-cycle variations in the swirl structure. When only one intake valve with a 90° shroud is activated, both tumble and swirl flow structures are seen at the end of the intake stroke and persist until TDCC. When both intake valves are activated and have a 180° shroud, a purely tumbling flow structure is generated during intake and persists until TDCC.

In a study by Arcoumanis, et al. [33], several other engine configurations with only single intake valves were run at 200 rpm. It was found that an off-centre intake valve without swirl-enhancing port vanes produces a double vortex flow structure in the swirl plane during induction that does not persist through compression. However, the addition of port vanes transforms the flow during induction into a strong swirling motion at TDCC. The swirl center location in this case displays cycle-to-cycle variability. The fluctuations along the cylinder axis about the cycle mean swirl velocity are less than the cycle-to-cycle variations in the large-scale flow.

Most of the studies mentioned above use LDA, which only provides instantaneous flow velocities at a point, or qualitative flow visualization techniques. However, Kim, et al. [37] study the effect of intake valve angle (the angle between the valve stem and the cylinder axis) on in-cylinder flow using PIV. The engines used were run at 1800 rpm. Flow velocities in four swirl planes and three tumble planes were obtained at 60°, 120°, 180°, 210°, 240°, 270°, 300°, and 320° ATDCE. It was found that the engine with the narrow intake valve angle had a stronger tumble flow than the engine with the normal intake valve angle. In both cases, the overall tumble flow structure is preserved until the end of compression. However, this study does not present data with high time resolution, nor does it discuss cycle-to-cycle flow variations and turbulence.

PIV was also used to examine the relationship between flow structures in the intake runner and the cylinder in a motored spark ignition engine with a pent-roof four-valve cylinder head and an intake runner providing optical access. The engine was motored at 1500 rpm, and PIV data was taken in the intake runner in the central vertical plane at 149° ATDCE (IPL) and in-cylinder in the primary tumble plane at 149°, 240°, and 300° ATDCE. Ensemble mean velocity vectors show that the tumble motion generated by the intake flow does not persist through the compression stroke, confirming the conclusions arrived at by Khaligi, et al. [36].

Instantaneous velocity fields show cycle-to-cycle variations during induction and the early part of the compression stroke, but these variations become negligible during the later stages of compression [35].

Another PIV study by Wilson et al. [40] found that valve overlap influences the in-cylinder flow patterns observed. Positive valve overlap created a large-scale tumble vortex that persevered during the compression stroke. However, negative valve overlap resulted in unstructured piston-driven upward flow during the compression stroke. This also led to an approximately 50% increase in flow fluctuations.

A study by Khaligi, et al. [30] discusses a multidimensional finite-volume based RANS simulation of the intake runner, valve, and in-cylinder flow in a previous configuration of the TCC engine presented in this dissertation. The differences between the engine configurations include a smaller compression ratio (8:1) and a lower intake pressure (46 kPaA) in [30]. Turbulent kinetic energies were calculated using a standard k-ε model. The simulation results were verified using qualitative flow visualization performed during induction in a transient water analog. During the experiments the intake valve lift was held constant at 8 mm while the piston moved. Configurations with both shrouded and unshrouded valves were modeled. The unshrouded intake valve configuration was found to generate a large-scale tumble motion in the plane bisecting the valve and the spark plug at BDC at the end of the intake stroke. This tumble motion is created when the intake valve jet attaches itself to the cylinder wall and is redirected by the piston. However, this structure becomes weaker during compression and dissipates by TDCC, creating more turbulent kinetic energy. The turbulent kinetic energy field is non-homogeneous during the compression stroke and at TDCC.

The present TCC engine configuration utilizes unshrouded valves. Although the simulations presented in [30] do not account for the positive valve overlap of the experimental engine configuration or cycle-to-cycle flow variations, they provide an estimate of the velocity fields that will be seen in the present TCC engine configuration. The intake valve configuration with the 120° shroud placed approximately parallel to the line bisecting the valve and the spark plug produces strong swirling and tumbling flow structures by BDC at the end of the intake stroke. The large-scale swirl motion is preserved up to TDCC. Thus, the swirl motion does not contribute significantly to turbulent kinetic energy generation during compression.

Most of the studies mentioned in this section discuss intake valve flows that generate coherent large-scale in-cylinder flows that persist during the compression stroke. Thus, cycle-to-cycle variations in intake valve flows are expected to result in cycle-to-cycle variations in in-cylinder flows at the time of crucial combustion events. If the coherent large-scale structures created by the intake valve flow dissipate before TDCC, cycle-to-cycle variations in the intake valve flow would likely result in cycle-to-cycle variations in turbulence intensity distributions during combustion events. Thus, cycle-to-cycle variations in intake valve flows in engines with directed in-cylinder flow are expected to affect engine performance.

1.5 Particle Image Velocimetry

Particle Image Velocimetry (PIV) calculates fluid velocity as the displacement of a fluid element divided by the time interval in which the displacement takes place. The displacement of a fluid element is determined by following particles added to the flow. The location of the seeding particles in a particular plane at different times is found by illuminating the flow with short laser light sheet pulses and photographing the Mie-scattered light from the particles. Initial PIV images from engines were captured on film, but most PIV experiments nowadays are

conducted using digital photographic techniques. Although film offers significantly better spatial resolution, high-speed digital cameras provide superior time resolution. The processing of digital PIV images is also much faster. While film-based PIV often used single-frame double-exposure recording, digital PIV uses frame-straddling techniques that result in only one exposure per frame. Thus, there are no directional ambiguities that need to be resolved during image processing. PIV velocity vectors are found using autocorrelation on single-frame double-exposure images, or cross-correlation on frame-straddled images.

Seeding particles used in PIV must be sufficiently small to accurately follow the fluid motion, but they also need to be large enough to scatter an adequate amount of light to enable detection. When the seeding particle density is much greater than the density of the fluid studied, Equation (1.11) describes how well the unsteady motion of the seeding particle describes the unsteady fluid flow [41].

$$\frac{\overline{u'^2_p}}{\overline{u'^2_f}} = \left[1 + \frac{\omega_c \rho_p d_p^2}{18\mu}\right]^{-1} \tag{1.11}$$

If values of ω_c, which is the angular turbulent frequency, are known from the temporal turbulence power spectral density, seeding particle response at a particular particle diameter can be determined. A seeding particle response of $\frac{\overline{u'^2_p}}{\overline{u'^2_f}} = 0.95$ is considered acceptable. The scattering cross-section, which is the measure of the light scattering capability of a particle, is defined as the ratio of the total scattered power to the incident laser intensity. Figure 1.3 illustrates the dependence of the scattering cross-section on particle diameter.

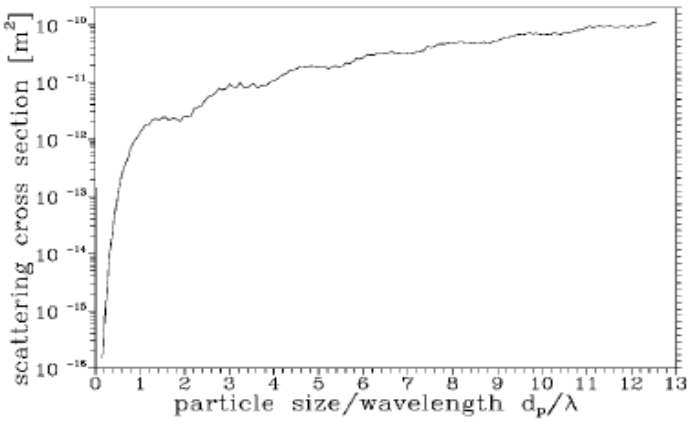

Figure 1.3: *Scattering cross-section as a function of particle size and incident wavelength in a medium of refractive index 1.6 [41]*

Once the seeding particle size is determined from Equation (1.10), Figure 1.3 can be used to ensure an acceptable signal-to-noise ratio.

PIV experiments are characterized by the dynamic spatial range (DSR) and dynamic velocity range (DVR) of the experimental setup. DSR is defined as the dimensions of the field-of-view (l_x X l_y) divided by the smallest resolvable displacement. Since the smallest resolvable displacement is less than the displacement associated with the maximum velocity (Δx_{pmax}), the minimum value of the DSR is defined as shown in Equation (1.12) [42].

$$DSR = \frac{l_x}{\Delta x_{pmax}} \tag{1.12}$$

DVR is defined as the maximum velocity measurable (u_{max}) divided by the minimum resolvable velocity. The minimum resolvable velocity is defined as the RMS error in velocity measurement (σ_u), which depends on the RMS error in displacement as shown in Equation (1.13) [42].

$$\sigma_u = \frac{\sigma_{\Delta X}}{M\Delta t} = \frac{c_\tau d_\tau}{M\Delta t} \tag{1.13}$$

Equation (1.13) indicates that it is more difficult to precisely locate the center of a larger image than a smaller one. The diameter of the recorded seeding particle image is determined as shown in Equation (1.14) [42].

$$d_\tau^2 = d_e^2 + d_r^2 = M^2\left(1.5dz\lambda + d_p^2\right) + d_r^2 \tag{1.14}$$

Thus, the DVR may be determined as shown in Equation (1.15) [42].

$$DVR = \frac{M\Delta x_{pmax}}{c_\tau d_\tau} \tag{1.15}$$

In order to achieve high values of both DVR and DSR, as is necessary for PIV measurements in turbulent flows, DVR*DSR, which is a characteristic of the PIV measurement system should be maximized.

PIV experimental parameters also depend on certain other criteria. 32 X 32 pixel interrogation windows are recommended for digital PIV experiments. Although a smaller interrogation window size would increase the spatial resolution of the velocity vector field produced, it also increases the uncertainty of the velocity vectors produced. This is believed to be due to the greater probability of particle images being truncated at the edge of the smaller interrogation window [43]. A seeding particle image diameter of 4 pixels is recommended to avoid undersampling so that the location of the particle center can be determined with better precision. Maximum in-plane and out-of-plane particle image displacement should be one-quarter of the interrogation window size, and the velocity gradient over the interrogation window should at the most be 5% of the mean velocity to minimize particle images moving in or out of the interrogation window. The number of seeding particle images per interrogation window should be between 10 and 20 to achieve a good signal-to-noise ratio [44]. The thickness of the light sheet should be at least 32 pixels to minimize the loss of particle images due to out-of-plane motion.

An additional concern when conducting PIV experiments in engines is the effect of the cylinder wall thickness and curvature on the PIV images of tumble planes. The cylinder wall causes nonlinear changes to the coordinate system in the image plane and asymmetric distortions

of seeding particle images. Using thin-walled cylinders and calculating PIV velocity vectors only in the central portion of the plane imaged, where the angle between the particles and the optical axis is small, will minimize these errors [45]. Using a calibration plate may also allow the PIV processing software to correct some of these errors.

1.6 Large-Eddy Simulations

Large-Eddy Simulation (LES) engine models explicitly address the issue of the cycle to cycle variability in flow and combustion. While RANS models compute a mean engine cycle by a process of convergence, LES models compute several engine cycles by directly resolving flow quantities at the larger scales and modeling them only at the smaller sub-grid scales. Since the small-scale turbulence is expected to be universal in nature, LES turbulence models are more general than RANS models. RANS velocity decompositions count all fluctuations about the mean as turbulence, so RANS engine models must also account for cycle-to-cycle variability, and are more engine geometry specific. Another important distinction between RANS and LES modeling is that improving the grid resolution improves only the numerical accuracy of a RANS model, while a finer mesh increases the dynamic range of the resolved scales in an LES computation. At the limit, LES computations converge to direct numerical simulation (DNS), where all turbulence scales are resolved. Compared to RANS, LES is particularly suitable for internal combustion engines because LES is expected to capture more flow structures on the same computational grid and provide better predictive capability with less empirical input required [46, 47].

Over the last twenty years, significant progress has been made in LES for IC engines. Early reviews of LES applications to IC engines include Celik et al. [48] and Haworth [46]. Early LES attempts on IC engines were limited to simple engine configurations; these works

include LES for a simplified motored engine configuration by Haworth et al. [49], a study of turbulence statistics for a motored engine configuration by Celik et al.[50, 51], turbulent premixed-flame propagation in IC engines on relatively coarse grids by Naitoh et al. [52], and LES of diesel fuel injection and combustion by Smirnov et al. and Smith et al. [53, 54].

For more realistic configurations, Vermorel et al. [55] and Richard et al. [56] applied LES with a flame-surface-density-based combustion model (coherent flame model) to a single-cylinder, spark-ignited four-valve engine. Vermorel et al. [57] also studied the same engine using LES with a more advanced combustion model (extended coherent flame model). Laget et al. [58] performed LES for a four-cylinder engine based on the work of Vermorel et al. [55-57]. The main focus of these works was to estimate cycle-to-cycle variations and to study the root causes for cycle-to-cycle variations in IC engines using a high fidelity LES code. Although only a small number (approximately ten) of engine cycles were simulated in these works, the results showed encouraging qualitative and quantitative agreement with experiments.

LES computations for engines have been found to agree well with experimental results [16, 46, 56, 59]. Haworth computed in-cylinder flows in an earlier unshrouded-valve configuration of the TCC engine presented in this document, and found that the LES flows had velocity magnitudes comparable to the measured flow velocities [46]. Naitoh, et al. [59] use the ability of LES to simulate cycle-to-cycle variations to find locations on the grid where cycle-to-cycle flow variations are minimum. Moving the spark plug in a gasoline direct injection engine to such a location would minimize the effect of cycle-to-cycle flow variations on engine performance. Of course, an area with low cycle-to-cycle flow variations may not exist for a given engine, or placing a spark plug in this area might lead to consistent but poor combustion

due to other effects like wall quenching. A recent review of LES applications in internal combustion engines by Rutland [60] summarizes the status of this field.

1.7 Document Outline

Chapter 1 has outlined the motivation and objectives of this work, along with a brief literature survey of cycle-to-cycle flow variations and in-cylinder turbulence, POD, intake flows, PIV and LES in engines. Chapter 2 contains details of the optical engine and PIV equipment used in the experiments presented in this dissertation, as well as the PIV experimental settings and post-processing routines used. Chapter 3 is an assessment of the quality of PIV data acquired using variable time separations between PIV images and varying spatial resolution. Chapter 4 compares experimental data acquired at different engine speeds using tools such as proper orthogonal decomposition and ensemble averaging. Chapter 5 examines three different experimental data sets acquired at 800 rpm to assess differences in intake valve motion as a source of in-cylinder intake flow variations. Chapter 6 compares experimental data acquired at 800 rpm with two different sets of LES computations. Chapter 7 summarizes this dissertation and its conclusions, as well as plans for future work.

CHAPTER 2

EXPERIMENTAL DATA ACQUISITION

This chapter includes a description of the optical engine and the equipment used in the particle image velocimetry experiments presented in this dissertation. Also presented are details of the PIV experimental settings and the post-processing methods used to obtain velocity vector fields from the raw PIV images.

2.1 Optical Engine

The transparent combustion chamber (TCC) engine used in the PIV experiments described in this dissertation is a two-valve single-cylinder pancake-chamber engine with a simple geometry that was designed for both high optical accessibility and to be rendered easily in a computational fluid dynamics mesh. The time-resolved velocity and pressure data gathered from this engine are also being used to verify LES engine models developed by collaborators at the University of Wisconsin, Pennsylvania State University, General Motors and Sandia National Laboratories. These data are available upon request. A previous installation of this engine with a quartz ring in the cylinder allowing optical access to only the combustion chamber has been studied [2, 61, 62]. Figure 2.1 describes the current engine geometry.

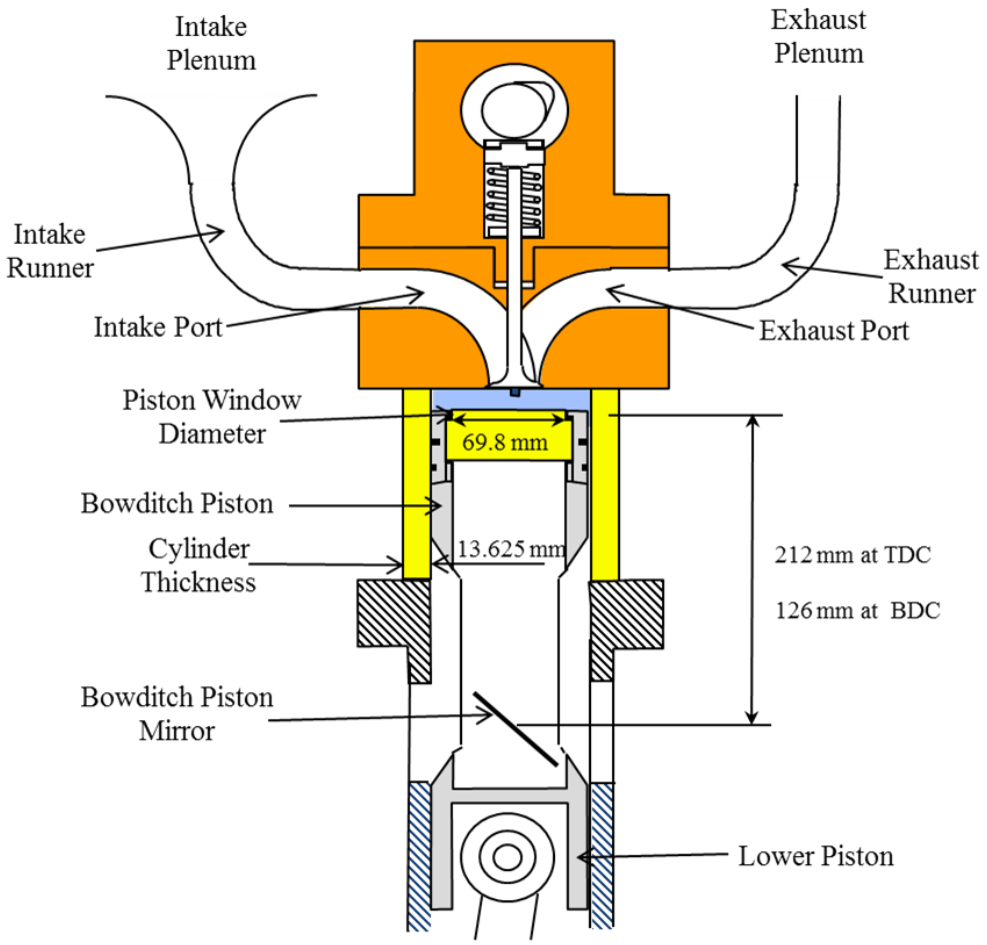

Figure 2.1: *Transparent combustion chamber engine [2]*

Although the present installation of the TCC engine has only been run motored, a spark plug was included in the build so that the in-cylinder flow in its vicinity would be more realistic. The ground strap of the spark plug points towards the intake valve and is in the plane that bisects the valves. The piston in this engine consists of two halves: the lower piston, which is attached to the crankshaft via the connecting rod, and the upper Bowditch piston [63], which is a hollow cylinder with slots that allow access to the inside and a quartz piston window of thickness 6 mm at the top. The Bowditch piston has three sets of rings: a lower two-piece Rulon compression ring, a felt oiler ring in the middle, and an upper single-piece carbon-impregnated Teflon compression ring. The felt oiler ring is dampened using silicone oil, which lubricates the piston.

Carbon from the Teflon compression ring also acts as a lubricant. The Bowditch piston accommodates an elliptical 45° mirror that reflects light in the region of 532 nm and 355 nm. This mirror remains stationary during engine operation and can be used to turn a laser light sheet up into the cylinder along a vertical (tumble) plane, or to view a horizontal (swirl) plane illuminated by a light sheet. The engine specifications are given in Table 2.1.

Bore	92 mm
Stroke	86 mm
Connecting Rod Length	231 mm
Crank Radius	43 mm
Geometric Compression Ratio	10:1
Displacement	0.57 L
Clearance Volume	0.064 L
Intake Valve Opening	712° ATDCE
Intake Valve Peak Lift	114° ATDCE
Intake Valve Closing	240° ATDCE
Exhaust Valve Opening	484° ATDCE
Exhaust Valve Peak Lift	606° ATDCE
Exhaust Valve Closing	12° ATDCE

Table 2.1: *TCC Engine Geometry and Valve Timings*

The TCC engine intake and exhaust systems consist of plenums attached to the ports in the engine head via runners. A bell mouth is used to transition between the intake plenum and runner in order to avoid detached flow around sharp corners. The intake plenum and intake and exhaust runner surfaces are heated to the desired intake air temperature (45 °C in all the experimental data presented in this thesis) and are insulated to minimize heat loss from the intake air. The intake air is metered using a critical orifice system with an upstream pressure of about 720 kPaA. A mass flow meter was added to check the intake air mass flow rate expected from the critical flow orifice calibrations. Air is allowed to run through the intake system before running the engine so it can reach an equilibrium temperature. In order to avoid over-pressuring the intake plenum during warm-up, an engine bypass is opened to allow the air to bypass the engine and be

routed directly to the exhaust. The intake plenum is also equipped with an emergency pressure release valve that opens when the intake plenum pressure reaches approximately 650 kPaA. The pressure in the exhaust plenum is controlled using a variable flow valve at the plenum exit. Part of the intake air is directed to the air seeder. A mass flow meter is used to monitor the air flow to the seeder. The intake air flow was seeded with silicone oil droplets with a nominal diameter of 1 μm. The air seeder used is a six-jet atomizer. The seeded air is added back to the intake air just past the intake air heater.

The TCC engine has been extensively instrumented. Especially noteworthy are the high-speed (maximum measured frequency of 40 kHz) absolute pressure transducers (Kistler, 4007BA5F) that were installed at the intake plenum inlet and exhaust plenum outlet, and in the runner blocks between the runners and the ports in the engine head. These have a pressure range of 0 – 500 kPaA, may be overpressured to 1500 kPaA, and have a natural frequency of over 100 kHz. They have been used to capture highly time-resolved details of the pressure waves in the intake and exhaust systems. These high-speed pressure transducers were calibrated each day before running the engine by opening the intake and exhaust systems and adjusting the offsets to accurately read the air pressure inside the test cell. It was later found that the pressure transducer in the intake port runner block drifted enough during a day of testing that this daily calibration was insufficient to maintain accuracy. The extent of this drift was determined by comparing the ambient pressure measured by the intake port pressure transducer to the ambient pressure measured by the ambient pressure transducer after an engine test. The offset thus determined was added during post-processing to the intake port pressures measured during the engine test. The corrected average intake port pressure obtained was then used to find an offset to correct all of the experimental intake port pressures presented in this dissertation. This method for correcting

the high-speed intake port pressures was developed by Philipp Schiffmann, Mark Greene, and Dr. David Reuss.

The high speed pressure transducer signals, including the cylinder pressure signal, have been displayed and recorded using a high-speed digital data acquisition device with a 15 bit 12 channel 2 MHz digitizer module (A & D Technology, Phoenix). The cylinder pressure transducer has a nominal sensitivity of 68 pC/bar and a natural frequency of 50 kHz. The cylinder pressure signal is pegged at 495° ATDCE off of the 10° average of the high-speed pressure signal at the intake plenum inlet about 500° ATDCE. For the data presented in this thesis, these high-speed measurements were used to closely control the pressure boundary conditions to ensure test repeatability.

Other pressure and temperature signals are displayed and recorded using a low-speed digital data acquisition device with a 50 Hz acquisition speed (National Instruments, CompactDAQ). Engine speed and crank angle data are acquired using an incremental rotary encoder attached to the crank shaft that outputs one pulse per revolution and two pulses per crank angle. A Hall effect sensor paired with a gear within the crankcase outputs one pulse per cycle. These signals are preprocessed and then used to time the high-speed data acquisition device and the high speed controller for the laser and camera. The timing of the high-speed data acquisition system and the PIV high speed controller were verified by examining the engine piston position and corrected as necessary during post-processing. The engine valve timings were also verified optically. The crank angles at which the valves reached peak lift were found to be within 1° of the design timings presented in Table 2.1. This encoder and valve timing verification was conducted by Philipp Schiffmann, Mark Greene, and Dr. David Reuss.

2.2 Laser

The laser used in the PIV experiment described in this chapter is a frequency-doubled Q-switched dual-cavity diode-pumped Nd:YLF (Neodymium-doped Yttrium Lithium Fluoride) laser (Quantronix, Darwin-Duo). It outputs green light at 527 nm, and is capable of repetition rates between 0.1 kHz and 10 kHz. The polarization of the output beam is circular. Both laser cavities can be triggered independently using an external trigger. At the time of the PIV experiments presented in this thesis, the laser divergence was rather large, with the beam diameter doubling after approximately 1 m travel. The beam quality factor given in the manual is approximately 35.

The laser sheet created for the PIV experiments presented in this thesis had a thickness of 2 mm and was placed in the tumble plane bisecting the valves and containing the spark plug ground strap. Previous studies of this engine in which PIV data was acquired in the horizontal cutting plane have shown that the out-of-plane velocity component in this experiment would be comparable in magnitude to the in-plane velocity components [2, 61, 62]. Thus, a laser sheet thickness of 2 mm, which is in between the interrogation spot sizes of the high and low spatial resolution cameras, was chosen to reduce out-of-plane seeding particle loss between PIV frames.

2.3 Cameras and Lenses

Two high-speed cameras with complementary metal oxide semiconductor (CMOS) sensors were used for simultaneous high and low spatial resolution PIV measurements. The Phantom v7.3 (from Vision Research; used for the high spatial resolution PIV data acquisition) has a dynamic range of 14 bits, a pixel size of 22 μm, and a full sensor resolution of 800 X 600 pixels. The Phantom v1610 (from Vision Research; used for the low spatial resolution PIV data acquisition) has a dynamic range of 12 bits, a pixel size of 28 μm, and a full sensor resolution of

1280 X 800 pixels. 210 mm focal length camera lenses (Nikon Micro-Nikkor 210 mm ED) were used to minimize parallax errors. Lenses with a longer focal length and a subsequently smaller imaging solid angle result in smaller parallax errors.

Figure 2.2 shows the experimental setup for simultaneous high and low spatial resolution PIV measurements.

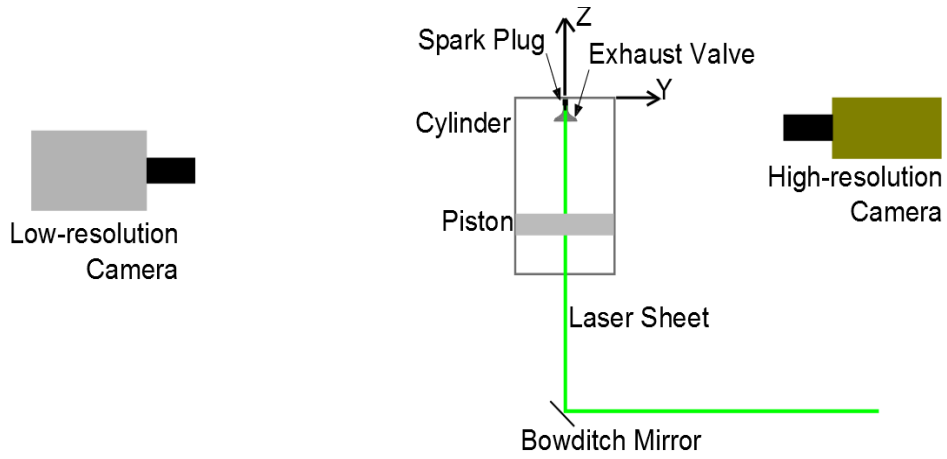

Figure 2.2: *Experimental setup for data sets S_2012_06_21_01, S_2012_06_25_01, and S_2012_06_27_02*

The field-of-view of the low spatial resolution camera included the entire illuminated tumble plane from the piston at bottom dead center (BDC) to the engine head. The magnification was 0.306. The camera lens aperture was set to f/4 to ensure that sufficient light reached the camera sensor while maintaining adequate depth-of-focus. The field-of-view of the high spatial resolution camera included the area around the spark plug and the valve jets. The magnification was 0.443. The camera lens aperture was set to f/5.6 to maintain adequate depth-of-focus. Figure 2.3 shows the images acquired by both cameras.

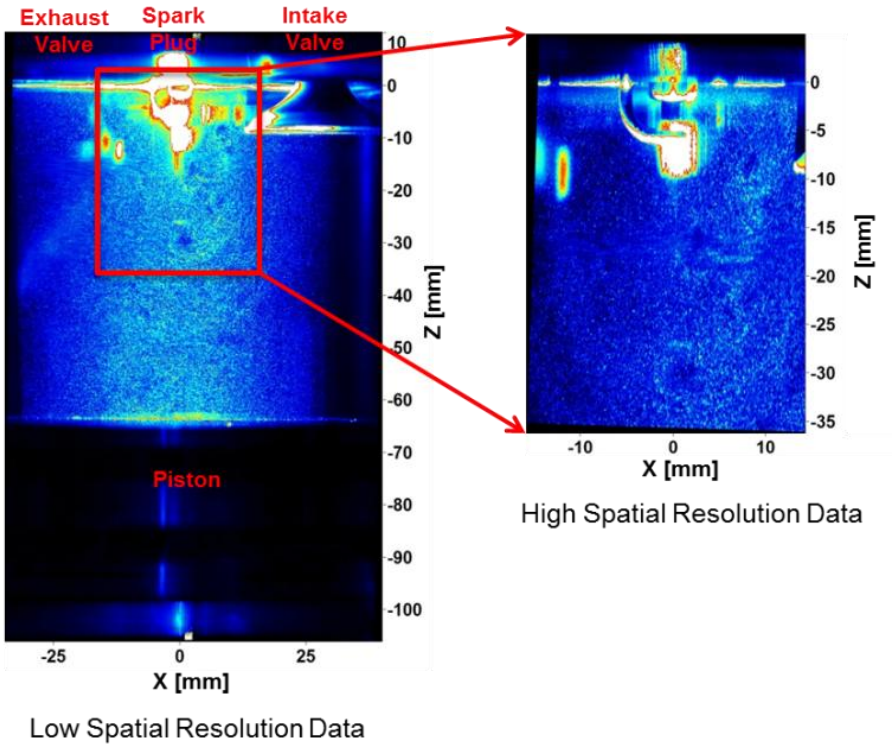

Figure 2.3: *PIV images acquired simultaneously at high and low spatial resolution*

In the data sets S_2011_05_24_03 and S_2011_11_21_02, only one camera was used to acquire low spatial resolution PIV data. In S_2011_11_21_02, the Phantom v7.3 was used with the 210 mm focal length camera lenses described above. In S_2011_05_24_03, the Phantom v7.1 high-speed camera (Vision Research) was used with the 210 mm lenses. The Phantom v7.1 has a dynamic range of 12 bits, a pixel size of 22 μm, and a full sensor resolution of 800 X 600 pixels.

2.4 PIV Settings

S_2011_05_24_03 contains 2901 PIV image pairs acquired during consecutive cycles at 100° ATDCE and 800 rpm engine speed. The time difference (dt) between the PIV image pairs was 20 μs, which was later found to be too long for adequate resolution of the large intake jet velocities. The field-of-view of the PIV images acquired was from the cylinder head to the piston. The magnification was 0.180 along the X axis and 0.171 along the Z axis. The nominal

pressure of the portion of the intake air diverted through the seeder was 115 kPaA, with 4 atomizer jets open.

S_2011_11_21_02 contains PIV image pairs acquired during 66 consecutive cycles from 0° through 360° ATDCE, every 2°, at 800 rpm. The dt was 10 μs to better resolve large intake jet velocities. The field-of-view of the PIV images acquired was from the cylinder head to the piston. The magnification was 0.163. The nominal pressure of the intake air through the seeder was 115 kPaA, with 2 atomizer jets open. The seeding density for S_2011_11_21_02 was reduced when compared to S_2011_05_24_03 to minimize overseeding towards TDC compression.

S_2012_06_25_01, S_2012_06_21_01, and S_2012_06_27_02 contain high and low spatial resolution PIV image pairs acquired during 70 consecutive cycles from 0° through 715° ATDCE, every 5°, at 400, 800, and 1600 rpm, respectively. The dt was varied as a function of crank angle to obtain cycle-resolved PIV data with optimal velocity resolution ranges during different parts of each engine cycle. Tables 2.2 through 2.4 list the different dts used in each of the three data sets. The smallest dt that could be set using the PIV data acquisition system was 6 μs. The magnification was 0.443 for the high spatial resolution measurements and 0.306 for the low spatial resolution measurements. The nominal pressure of the intake air through the seeder was 115 kPaA, 122 kPaA, and 128 kPaA, for S_2012_06_25_01, S_2012_06_21_01, and S_2012_06_27_02, respectively, with 3 atomizer jets open. These pressures were scaled up with engine speed to increase the mass flow rate of the air through the seeder.

Crank Angle Range (° ATDCE)		dt (μs)
0	140	9.5
145	180	18.5
185	220	42.5
225	330	72.5
335	360	82.5
365	490	162.5
495	530	6.0
535	715	22.5

Table 2.2: *Variable PIV time separation (dt) settings for S_2012_06_25_01*

Crank Angle Range (° ATDCE)		dt (μs)
0	140	6.0
145	180	9.5
185	220	17.5
225	240	32.5
245	360	42.5
365	490	83.5
495	530	6.0
535	715	13.5

Table 2.3: *Variable PIV time separation (dt) settings for S_2012_06_21_01*

Crank Angle Range (° ATDCE)		dt (μs)
0	140	6.0
145	180	7
185	220	11
225	240	18.5
245	360	23.5
365	490	43.5
495	530	6.0
535	715	8.5

Table 2.4: *Variable PIV time separation (dt) settings for S_2012_06_27_02*

2.5 PIV Processing

The raw PIV images were acquired and processed using a commercial software package (LaVision, DaVis Versions 7 and 8). This software package, along with the associated high-speed laser and camera controller (LaVision, High Speed Controller), allowed for user-input dynamically varying dts throughout the engine cycle for the data sets S_2012_06_25_01, S_2012_06_21_01, and S_2012_06_27_02. First, the raw images were dewarped and scaled using images of a calibration target set in the plane of the laser sheet. This process corrects for the errors caused by imaging through a curved quartz cylinder. The calibration target for S_2012_06_25_01, S_2012_06_21_01, and S_2012_06_27_02 consisted of 1 mm diameter dots spaced 5 mm apart printed on a transparency such that it could be imaged by both PIV cameras without having to be moved. Thus, the calibration process was also used to create a common coordinate system for both the high and low spatial resolution images, ensuring that they could be overlaid exactly. For S_2011_05_24_03, a rectangular plate 50.8 mm by 21.7 mm was used as a calibration target to scale the raw PIV images. A three dimensional calibration plate (LaVision, Type # 11) with 2 mm deep grooves and 2.2 mm diameter dots spaced 10 mm apart at each depth was used to scale the images in S_2011_11_21_02.

Next, a sliding background subtraction was carried out to improve the signal-to-noise ratio of the PIV images from all data sets. The background subtraction removed intensity fluctuations in the image that had a length scale larger than 10 pixels. Thus, intensity fluctuations due to a non-uniform light sheet or reflections were removed while the Mie scattering off the PIV seeding particles was retained. Then, velocity vectors in all data sets were calculated using a multi-pass PIV algorithm employing interrogation where windows of decreasing size (128 X 128 pixels to 32 X 32 pixels) were used with a 50% overlap. Predictor vectors obtained using larger interrogation windows are used to determine window shifts to obtain better correlations during

the next pass with smaller windows. This results in a spatial resolution of 2.93 mm with a separation between velocity vectors of 1.46 mm for the low-resolution data, and a spatial resolution of 1.59 mm with a separation between velocity vectors of 0.80 mm for the high-resolution data for the data sets S_2012_06_25_01, S_2012_06_21_01, and S_2012_06_27_02, for example.

Some vector post-processing was performed for all data sets. Vectors with a correlation peak ratio (Q) less than 1.4 were deleted. Q is defined in Equation (2.1).

$$Q = \frac{P_1 - m}{P_2 - m} \tag{2.1}$$

In Equation (2.1), P_1 and P_2 are the heights of first and second highest peaks in the PIV correlation plane and m is the lowest value in the correlation plane. Higher values of Q indicate more confidence in the associated vector. A four-pass bad vector removal process was also implemented. During the first pass, the median velocity of the eight immediate neighbors of each vector and the RMS of these neighboring vectors with respect to the median velocity were determined. The vector was removed if the difference between its magnitude and the median velocity was greater than 2 times the RMS of the neighboring vectors. During the second pass, vectors with less than 3 neighboring vectors were marked and then removed at the end of the pass. The third pass attempted to fill in good vectors. If there were at least 3 neighboring vectors, the median velocity and RMS were calculated again and each vector removed earlier was reinserted if the difference between its magnitude and the median velocity was less than 3 times the RMS of the neighboring vectors. Vectors corresponding to the four highest correlation peaks were considered. As all the vectors remaining after the second pass were considered to be good vectors, the calculated RMS values were much lower than those calculated during the first pass. This reduced the possibility of reinserting a bad vector during the third pass. The third pass was

repeated until no more vectors could be reinserted. The fourth pass removed groups of less than 5 vectors. Finally, interpolation was used to fill in vectors by averaging all non-zero neighboring vectors. At least 2 out of a possible 8 neighboring vectors needed to be non-zero in order to calculate an interpolation [64].

2.6 Summary

This chapter describes the transparent combustion chamber (TCC) engine and high-speed particle image velocimetry (PIV) equipment used in the experiments presented in this work. The TCC engine has a simple geometry that allows for relatively easy mesh generation for computational fluid dynamics. It is also equipped with high-speed pressure transducers in the intake and exhaust systems that provide data every 0.5° to ensure repeatable boundary conditions for comparisons with computational data. This chapter also includes details of the PIV experimental settings and the post-processing methods used to obtain velocity vector fields. Some of the experiments presented in this dissertation used two cameras using different magnifications to improve spatial resolution, and varying time separations between PIV images to optimize the velocity ranges measured. An assessment of the variable time separation settings is presented in the next chapter.

CHAPTER 3

QUALITY OF VARIABLE TIME SEPARATION PIV DATA

The quality of the in-cylinder PIV data acquired using variable time separations between PIV images and varying spatial resolutions is assessed in four ways. First, the perspective errors caused by out-of-plane particle displacements are estimated. Second, first-choice vectors (vectors not changed by the PIV post-processing routines) are quantified. Third, the number of vectors outside the PIV interrogation constraints is determined. Finally, the contribution of the noise to the measured flow kinetic energy is quantified between variable and constant dts. The variable dt data set acquired at a nominal engine speed of 800 rpm is also compared with single-camera, single dt data at the same engine speed.

3.1 Perspective Errors

The out-of-plane displacement of PIV seeding particles may be interpreted as an in-plane displacement by a non-stereoscopic imaging system when the seeding particles are off the optical axis. The resulting perspective errors in the measured velocity components (e_x and e_z) may be calculated according to Equations (3.1) and (3.2) [65].

$$e_x = \frac{\Delta y}{\Delta x}\frac{x_p}{d_O} \tag{3.1}$$

$$e_z = \frac{\Delta y}{\Delta z}\frac{z_p}{d_O} \tag{3.2}$$

In Equations (3.1) and (3.2), Δx and Δz are in-plane displacements and Δy is the out-of-plane displacement. x_p and z_p are the distance between the point at which the optical axis and the object

plane intersect and the seeding particles projected onto the x and z axes, respectively. d_O is the perpendicular distance between the object plane and the camera lens plane and may be calculated using Equation (3.3).

$$d_O = \frac{(1+M)f}{M}, \tag{3.3}$$

where M is the magnification and f is the focal length.

Given the magnification, focal length, and estimates of in-plane and out-of-plane displacements, the maximum perspective errors for each of the measured velocity components may be determined by finding the maximum x_p and z_p for each camera. For the high spatial resolution camera, the maximum values of e_x and e_z are estimated to be 2% and 3%, respectively. For the low spatial resolution camera, the maximum values of e_x and e_z are estimated to be 4% and 5%, respectively.

3.2 Number of First-Choice Vectors

The number of first-choice vectors is an indication of the quality of the PIV images acquired and the suitability of the PIV parameter settings. These counts are best understood in the context of all vectors in the PIV fields-of-view. Of course, the total number of vectors in the field-of-view changes throughout the cycle with piston and valve motion as shown graphically in Figure 3.1.

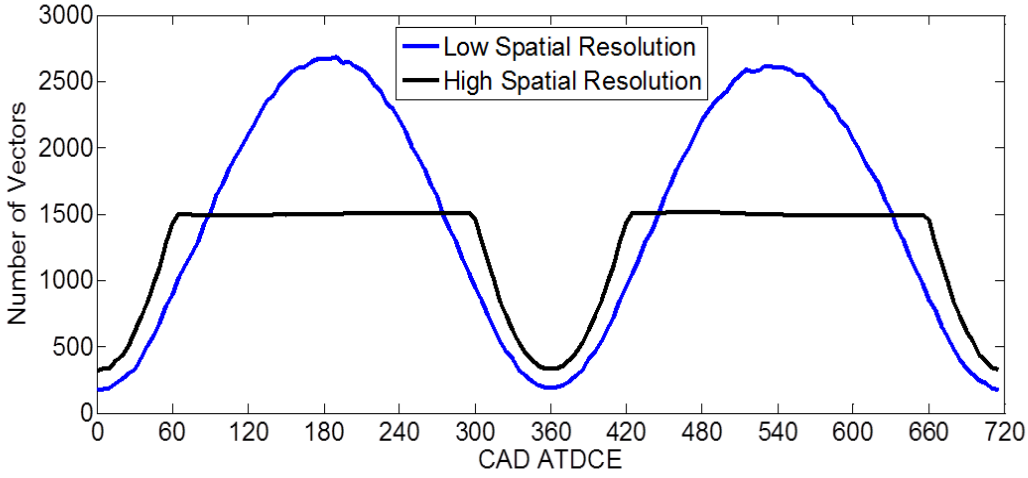

Figure 3.1: *Number of velocity vectors contained in low spatial resolution (blue) and high spatial resolution (black) velocity fields in S_2012_06_21_01*

Once the piston moves out of the high spatial resolution camera's field-of-view, the number of vectors present in the high spatial resolution velocity fields remains constant except when the laser sheet is blocked by open valves. Although Figure 3.1 shows only the number of velocity vectors as a function of crank angle contained in the data set S_2012_06_21_01, this is very similar to the number of velocity vectors in S_2012_06_25_01 and S_2012_06_27_02.

Figure 3.2 shows the ensemble average percentage of first-choice vectors and the ensemble average number of non-first-choice vectors throughout the cycle for the high spatial resolution data in the variable dt data sets acquired at 400, 800 and 1600 rpm.

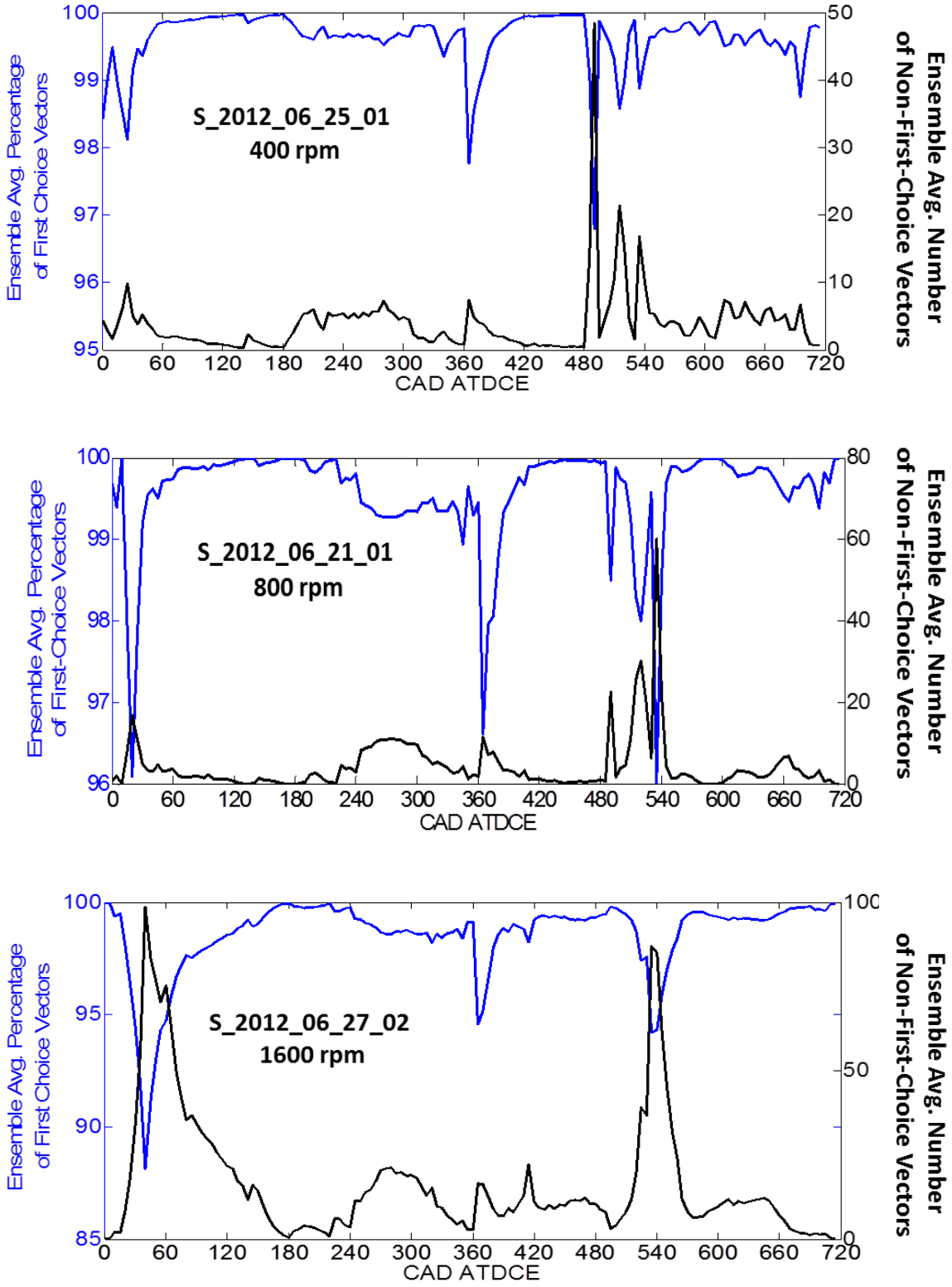

Figure 3.2: *Ensemble average percentage of first-choice and ensemble average number of non-first-choice vectors in the* ***high*** *spatial resolution data*

Figure 3.2 indicates that, on average for the three variable dt data sets, the percentage of first-choice vectors in the high spatial resolution data remains above 98% except for three crank angle ranges: during the early part of the intake valve opening, about top dead center (TDC) compression, and during the early part of the exhaust valve opening. The lower percentage of first-choice vectors about TDC compression is understood by referring to Figure 3.1, which shows that the total number of vectors in the velocity field is at a minimum at TDC compression. Thus, even though the number of non-first-choice vectors around TDC compression is similar to that observed earlier in the compression stroke, the percentage of first-choice vectors is lower than 98%. During the early part of intake and exhaust valve opening, the high velocities and velocity gradients may not have been accurately captured with the minimum possible dt of 6 μs used for all three variable dt data sets in that crank angle range, resulting in more non-first-choice vectors.

A comparison of the three graphs in Figure 3.2 show that the ensemble average percentage of first-choice vectors during the early part of the intake valve opening, about TDC compression, and during the early part of the exhaust valve opening decrease with increasing engine speed for the high spatial resolution data. The variable dts chosen for the early intake and exhaust valve opening were the minimum possible dt of 6 μs, with an exception of a 9.5 μs dt for the early part of intake valve opening at 400 rpm. Even with a decrease in dt from the 400 rpm data set to the 800 rpm data set during the early part of intake valve opening, the increase in valve jet velocities with increasing speed result in increasing particle displacements between image pairs in the early parts of intake and exhaust valve opening. These larger particle displacements lead to poorer PIV correlations, as reflected by the decrease in percentage of first-choice vectors with increasing engine speed in these crank angle ranges. The decreasing

percentage of first-choice vectors about TDC compression with increasing engine speed reflect the increasing number of non-first choice vectors in the crank angle range of about 240° to 420° ATDCE. Although the quartz engine cylinder was cleaned between runs, the quartz acquires an oil film during engine runs whose thickness increases with engine speed. This oil film, combined with non-optimally increasing seeding densities during the compression stroke, lead to PIV correlations in this crank angle range that are increasingly poorer with increasing engine speed.

Figure 3.3 shows the ensemble average percentage of first-choice vectors and the ensemble average number of non-first-choice vectors throughout the cycle for the low spatial resolution data in the variable dt data sets acquired at 400, 800 and 1600 rpm.

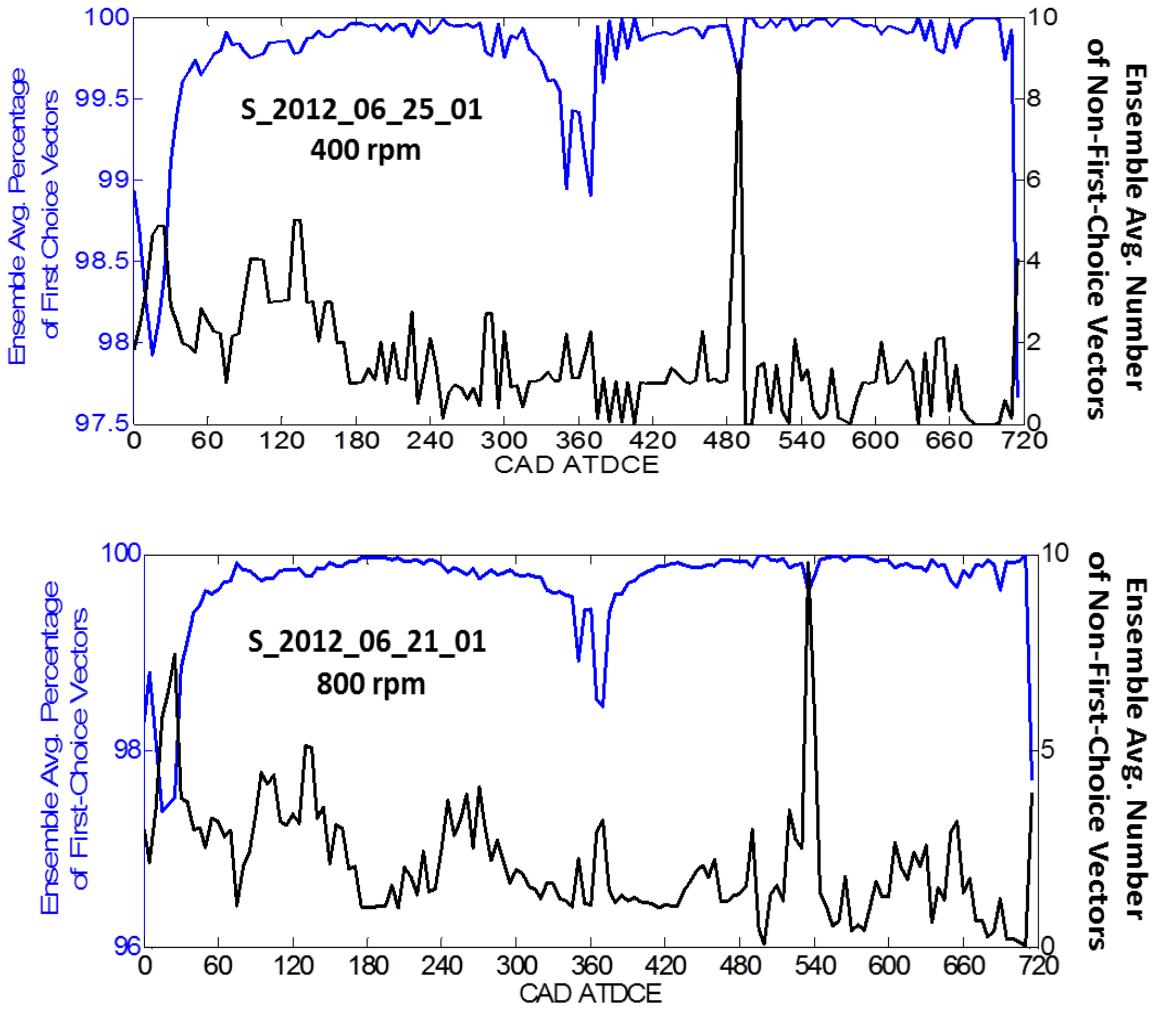

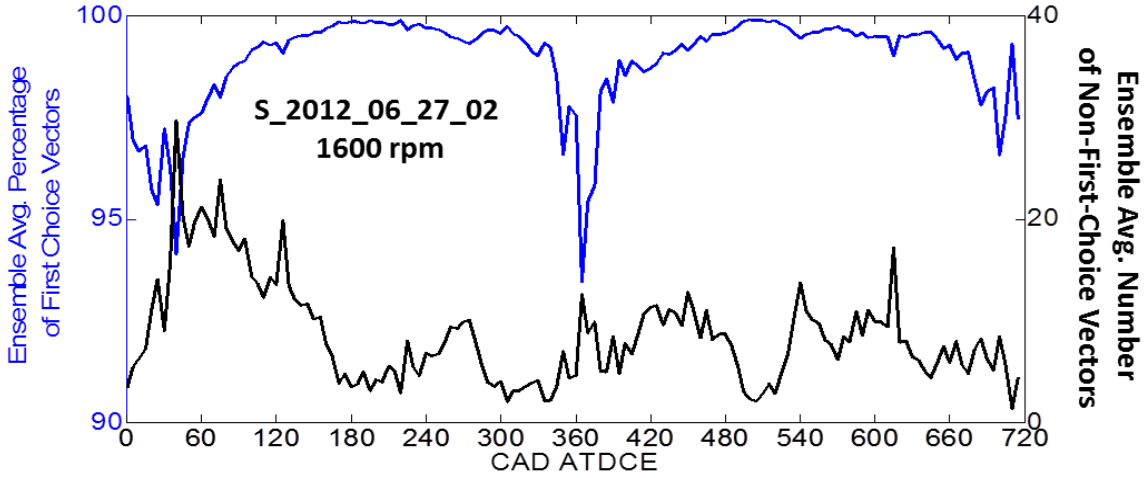

Figure 3.3: *Ensemble average percentage of first-choice and ensemble average number of non-first-choice vectors in the* ***low*** *spatial resolution data*

Figure 3.3 shows that the percentage of first-choice vectors in the low spatial resolution data is also high on average, remaining above 99% except for crank angle ranges during the early part of intake valve opening and near TDC. Thus, the PIV images acquired are of good quality and the PIV parameter settings are acceptable through most of the engine cycle for both the high and low spatial resolution data.

3.3 Velocity Dynamic Range and Noise

Figure 3.4 shows the range of velocities observed during three randomly chosen cycles compared to the dynamic range of the PIV measurements, for both the high and low spatial resolution PIV measurements, at 400, 800, and 1600 rpm. The velocity magnitude associated with a particular pixel displacement is calculated according to Equation 3.4.

$$Velocity\ Magnitude = \frac{(Pixel\ Displacement)(Pixel\ Size)}{(Magnification)(dt)} \tag{3.4}$$

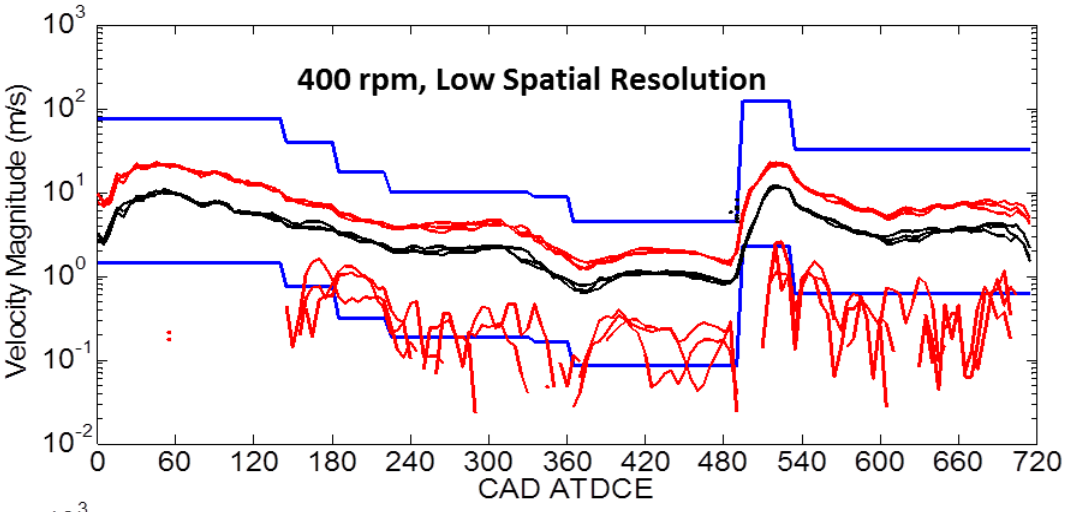
400 rpm, Low Spatial Resolution
Velocity Magnitude (m/s)
CAD ATDCE

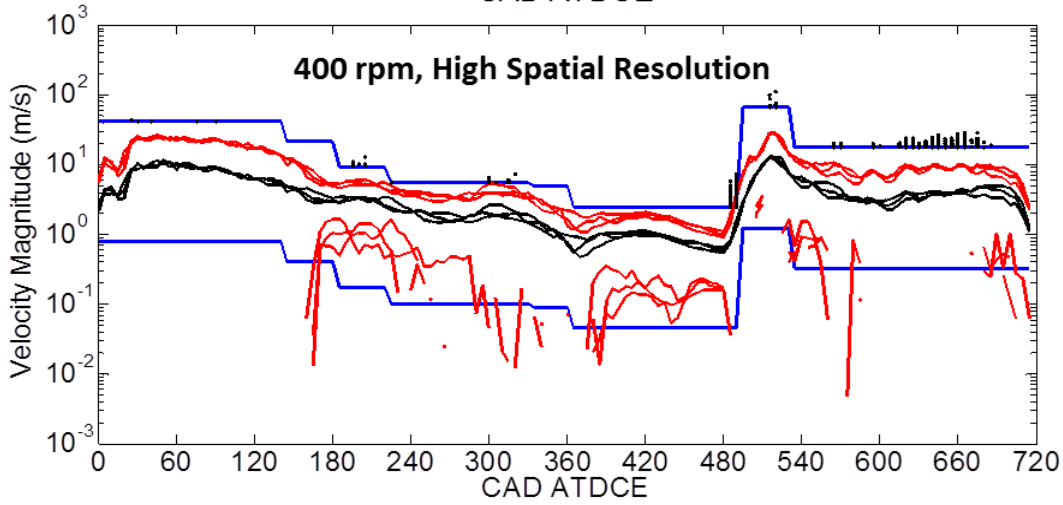
400 rpm, High Spatial Resolution
Velocity Magnitude (m/s)
CAD ATDCE

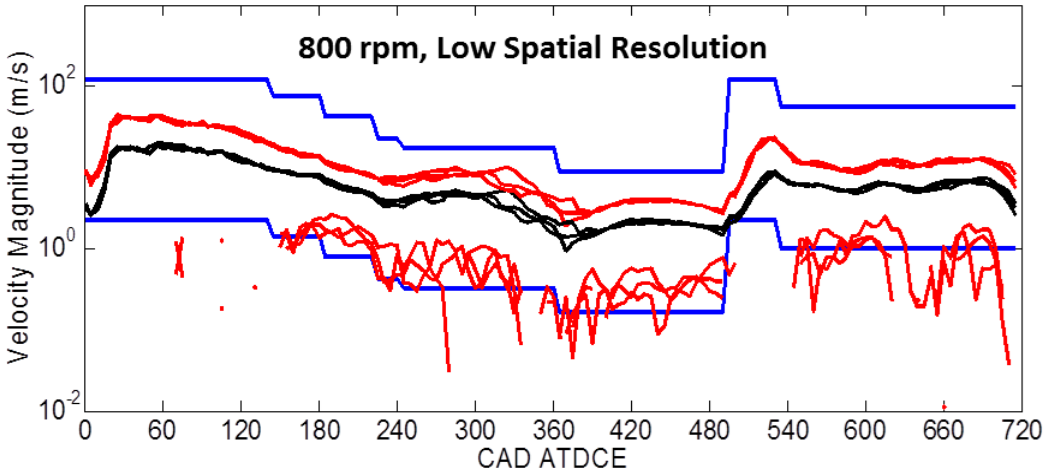
800 rpm, Low Spatial Resolution
Velocity Magnitude (m/s)
CAD ATDCE

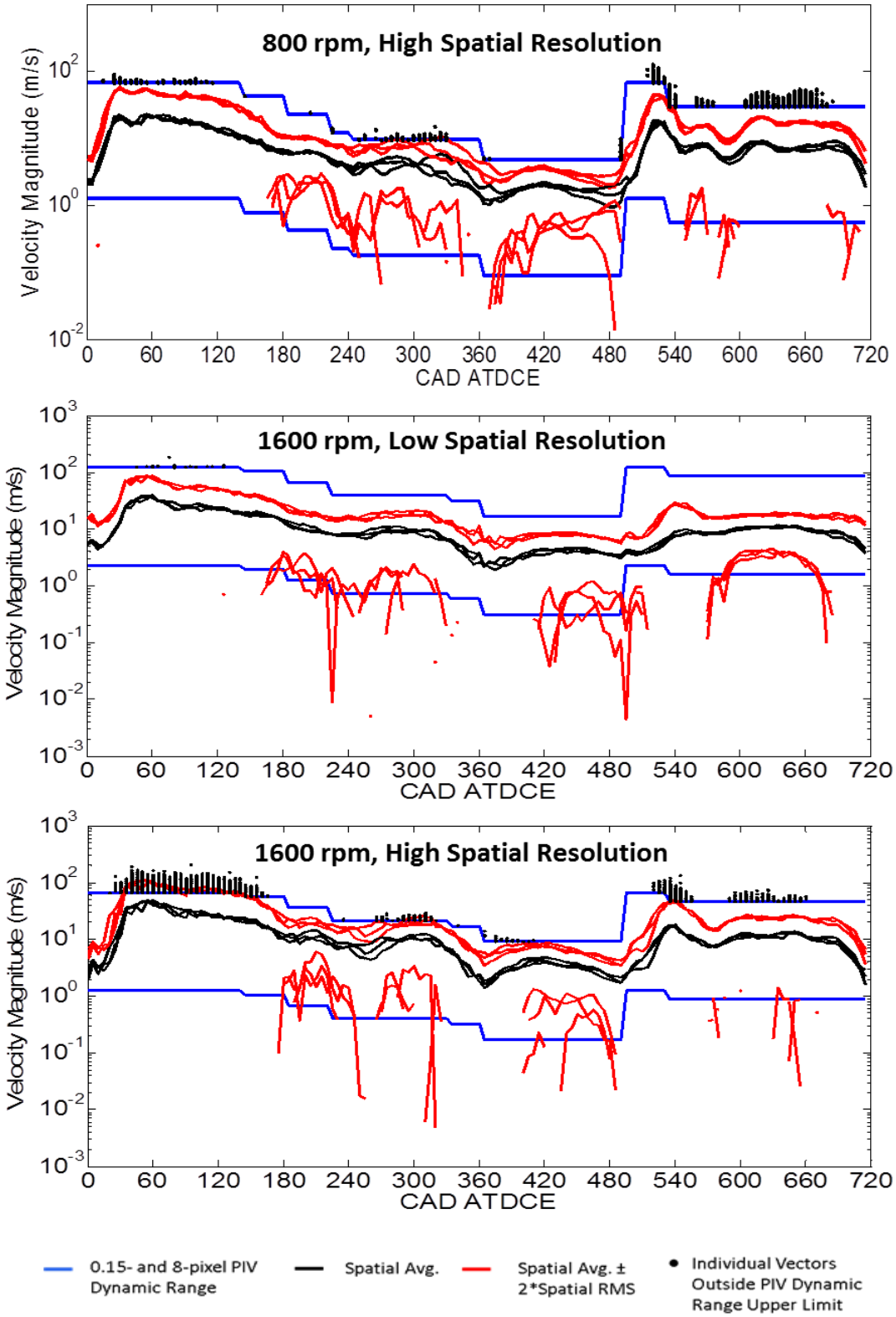

Figure 3.4: *Velocity ranges of three randomly chosen cycles compared to PIV dynamic ranges at three engine speeds (zero and negative values not plotted)*

The low velocity limit of the dynamic range is based on the 0.15 pixel noise and the high velocity limit from the 8-pixel maximum displacement. Of course, the measured RMS of 0.15 pixel displacement is a combination of velocity and interrogation noise, and thus is a conservative estimate. The limits change during the cycle due to changing dts. The dts were chosen based on initial survey measurements, such that most of the pixel displacements fall within these limits.

As shown by the black dots above the high limit in Figure 3.4, the smallest available dt (6 μs) was not small enough to capture the very high velocities during the early intake and exhaust valve opening (0°-120° and 600°-700° ATDCE). The dts used during the compression stroke (240°-360° ATDCE) were a compromise; here measurements are seen to exceed both the low and high limits. Since the variable dts were set to optimize the dynamic range of the high spatial resolution measurements, the maximum particle displacements are mostly less than 8 pixels throughout the cycle for the low spatial resolution measurements.

The number of vectors outside the upper limit in the high spatial resolution data is quantified in Figure 3.5. The largest percentage of vectors above the 8-pixel limit is seen in the 1600 rpm data at about 60° ATDCE, during the early part of intake valve opening. This is unlike the corresponding graphs for the 400 and 800 rpm data, which show the largest percentage of vectors above the 8-pixel limit during the early part of exhaust valve opening. This suggests that the high velocities during the early part of exhaust valve opening (485°-510° ATDCE) were too large to be captured for the 1600 rpm data. Even when using a multi-pass PIV algorithm, PIV correlations may not capture particle displacements that are much greater than a quarter of the final interrogation window size.

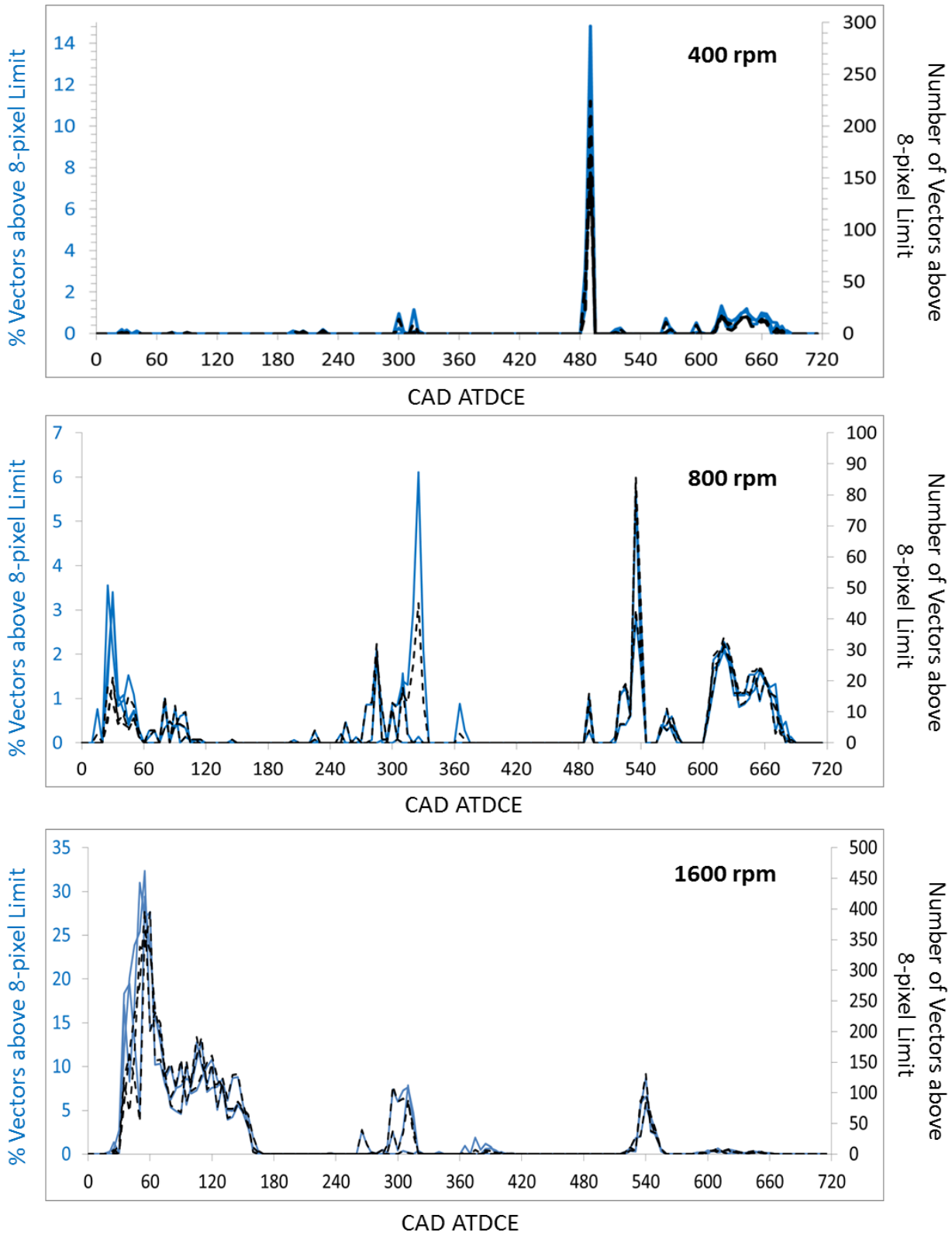

Figure 3.5: *Vectors from three randomly chosen cycles above upper limit of high spatial resolution PIV dynamic range at three engine speeds in Figure 3.4*

Figure 3.6 shows the fraction and absolute number of noise vectors (vectors below the 0.15 pixel displacement limit) throughout three randomly chosen cycles at 400, 800, and 1600 rpm. The number of noise vectors is largest during the early part of intake and exhaust valve opening because the dt was set to capture the high velocity valve jets, which occupy only a small portion of the field-of-view. The displacements in the other regions are very small. The percentage of noise vectors is also large towards TDC when the total number of vectors in the velocity fields is lowest. The low spatial resolution measurements have greater percentages of noise vectors than the high spatial resolution measurements. These noise vectors, assumed to be random, introduce errors in the derived kinetic energy.

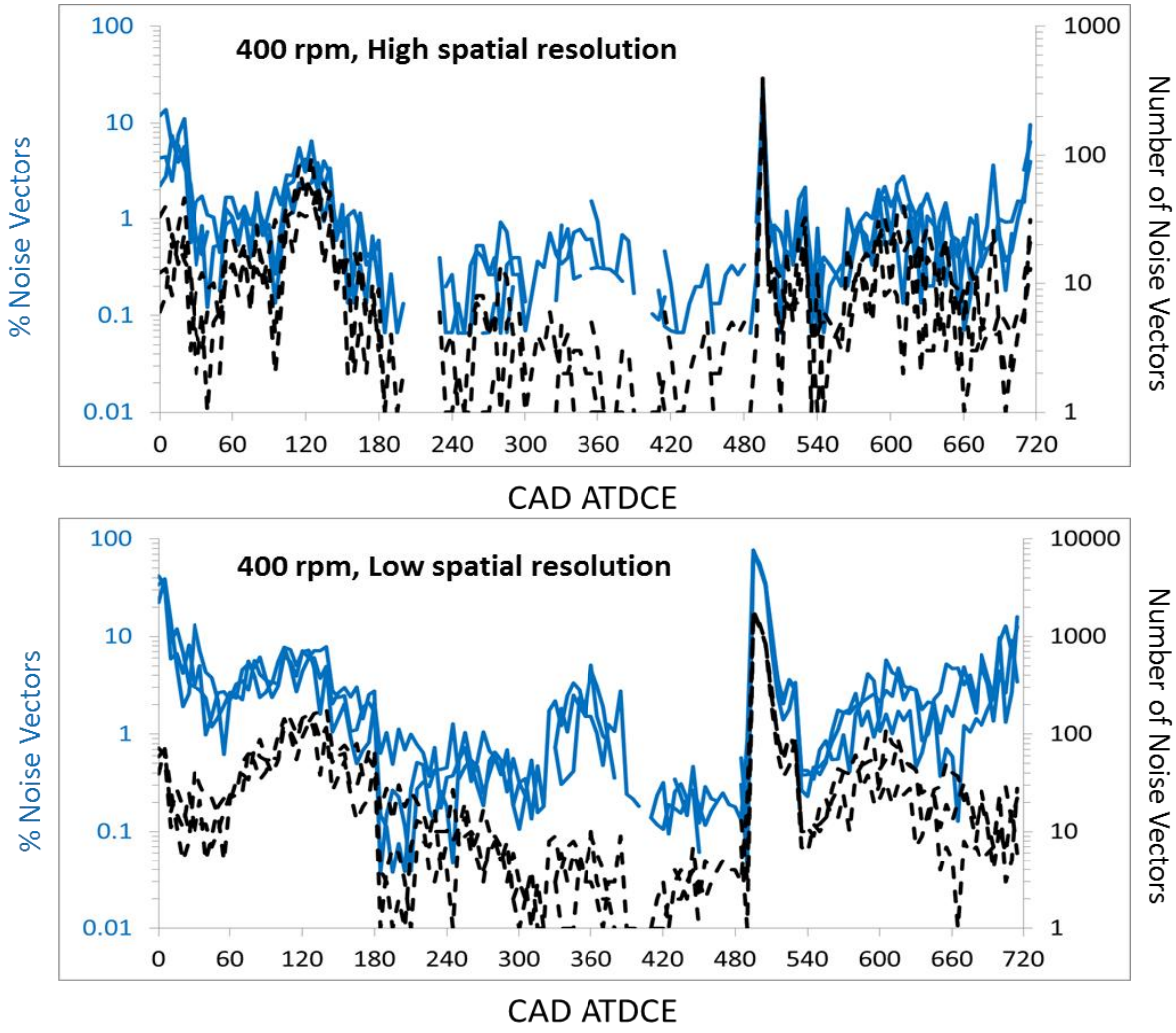

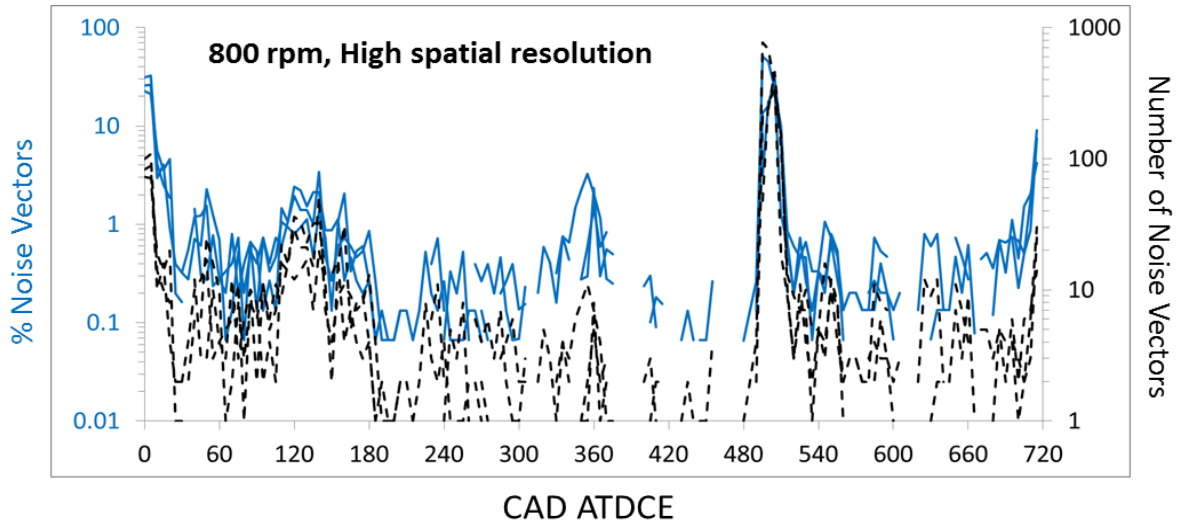
800 rpm, High spatial resolution
% Noise Vectors
Number of Noise Vectors
100
10
1
0.1
0.01
1000
100
10
1
0
60
120
180
240
300
360
420
480
540
600
660
720
CAD ATDCE

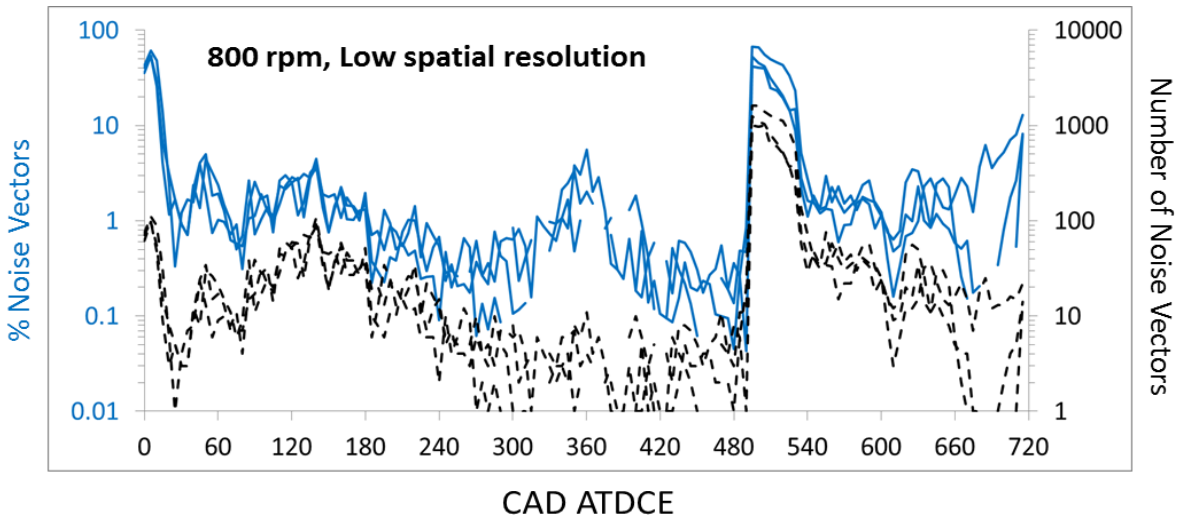
800 rpm, Low spatial resolution
% Noise Vectors
Number of Noise Vectors
100
10
1
0.1
0.01
10000
1000
100
10
1
0
60
120
180
240
300
360
420
480
540
600
660
720
CAD ATDCE

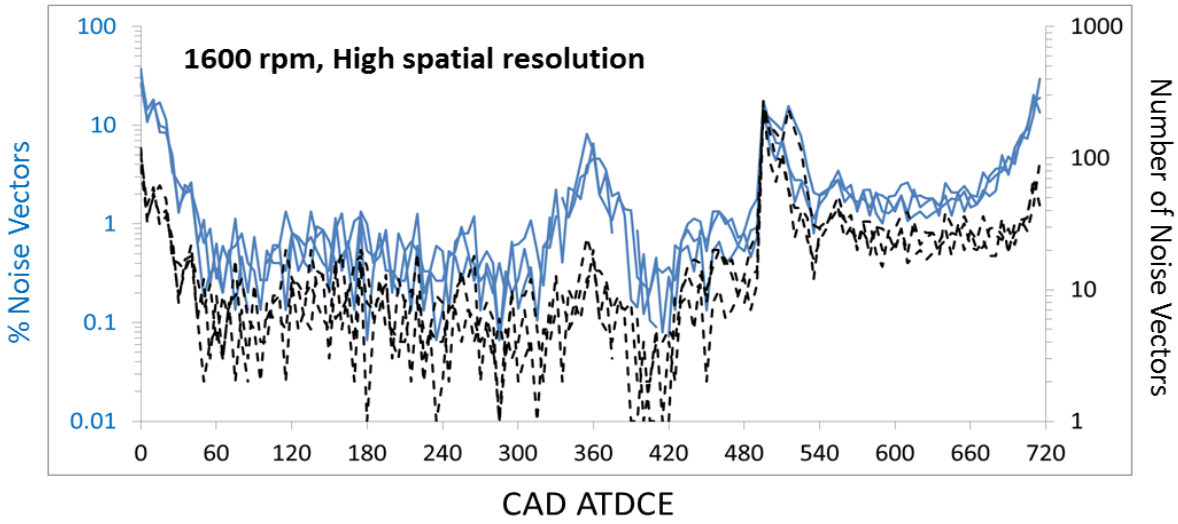
1600 rpm, High spatial resolution
% Noise Vectors
Number of Noise Vectors
100
10
1
0.1
0.01
1000
100
10
1
0
60
120
180
240
300
360
420
480
540
600
660
720
CAD ATDCE

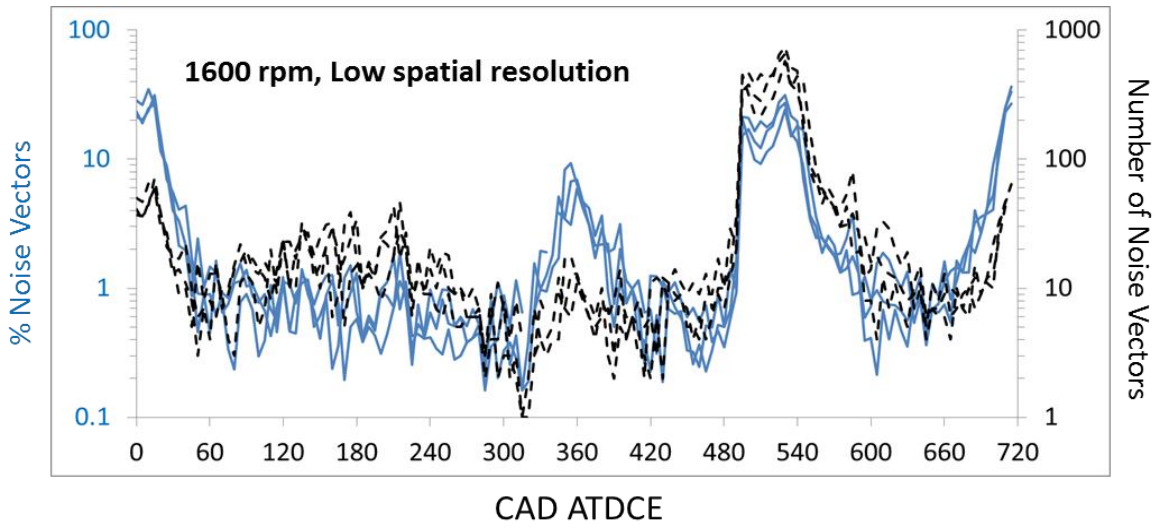

Figure 3.6: *Vectors from three randomly chosen cycles below lower limit of the PIV dynamic range at three engine speeds in Figure 3.4 (zero values not plotted)*

Figure 3.7 examines the contribution of noise vectors to the total mass-specific kinetic energies in instantaneous velocity fields throughout three randomly chosen cycles at 400, 800, and 1600 rpm. The results lead to the conclusion that kinetic energy is not significantly influenced by noise vectors in the high spatial resolution measurements in crank angle ranges outside of early intake and exhaust valve opening. However, the contribution of the noise vectors to kinetic energy is larger in the low spatial resolution data.

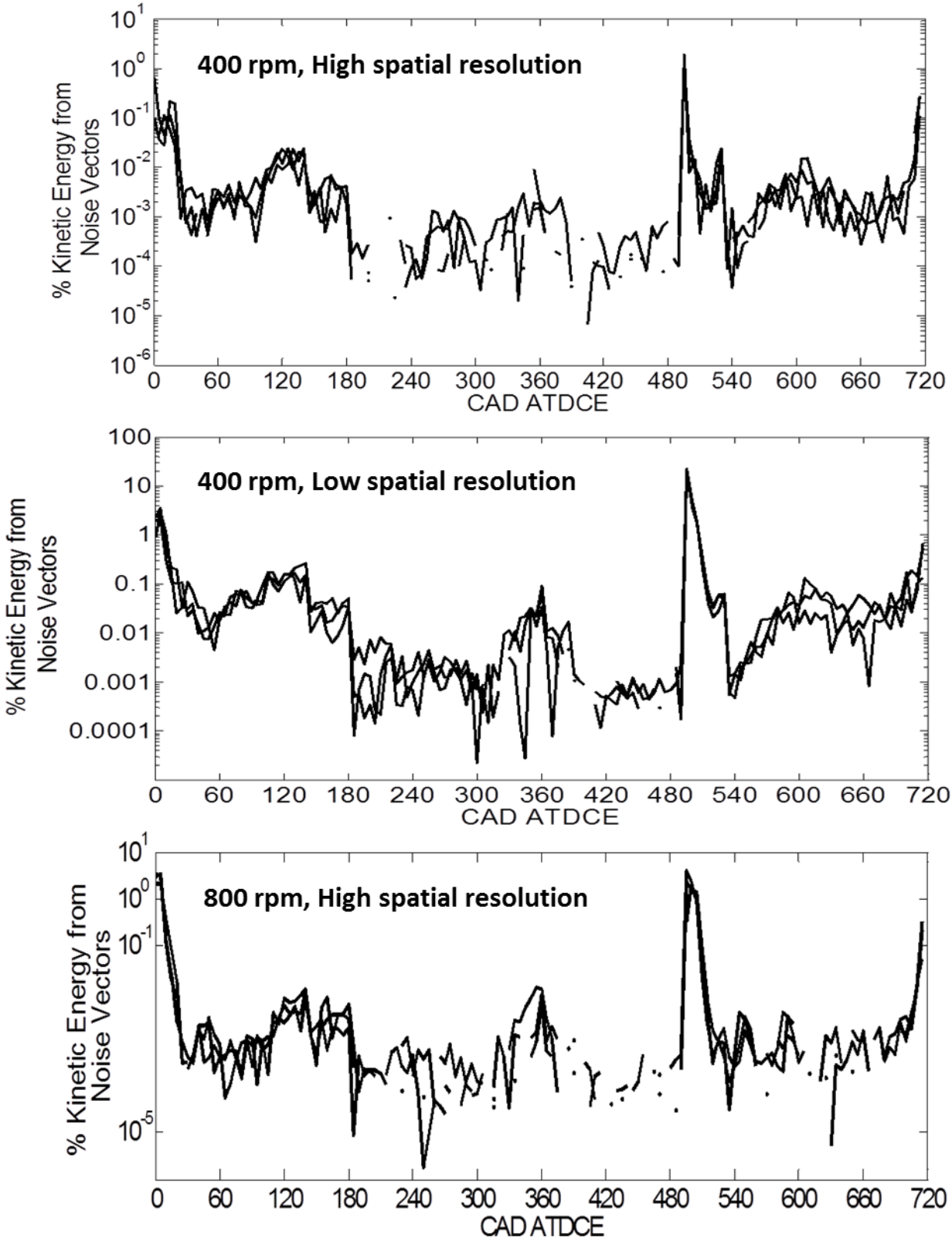
400 rpm, High spatial resolution
% Kinetic Energy from Noise Vectors
CAD ATDCE
400 rpm, Low spatial resolution
% Kinetic Energy from Noise Vectors
CAD ATDCE
800 rpm, High spatial resolution
% Kinetic Energy from Noise Vectors
CAD ATDCE

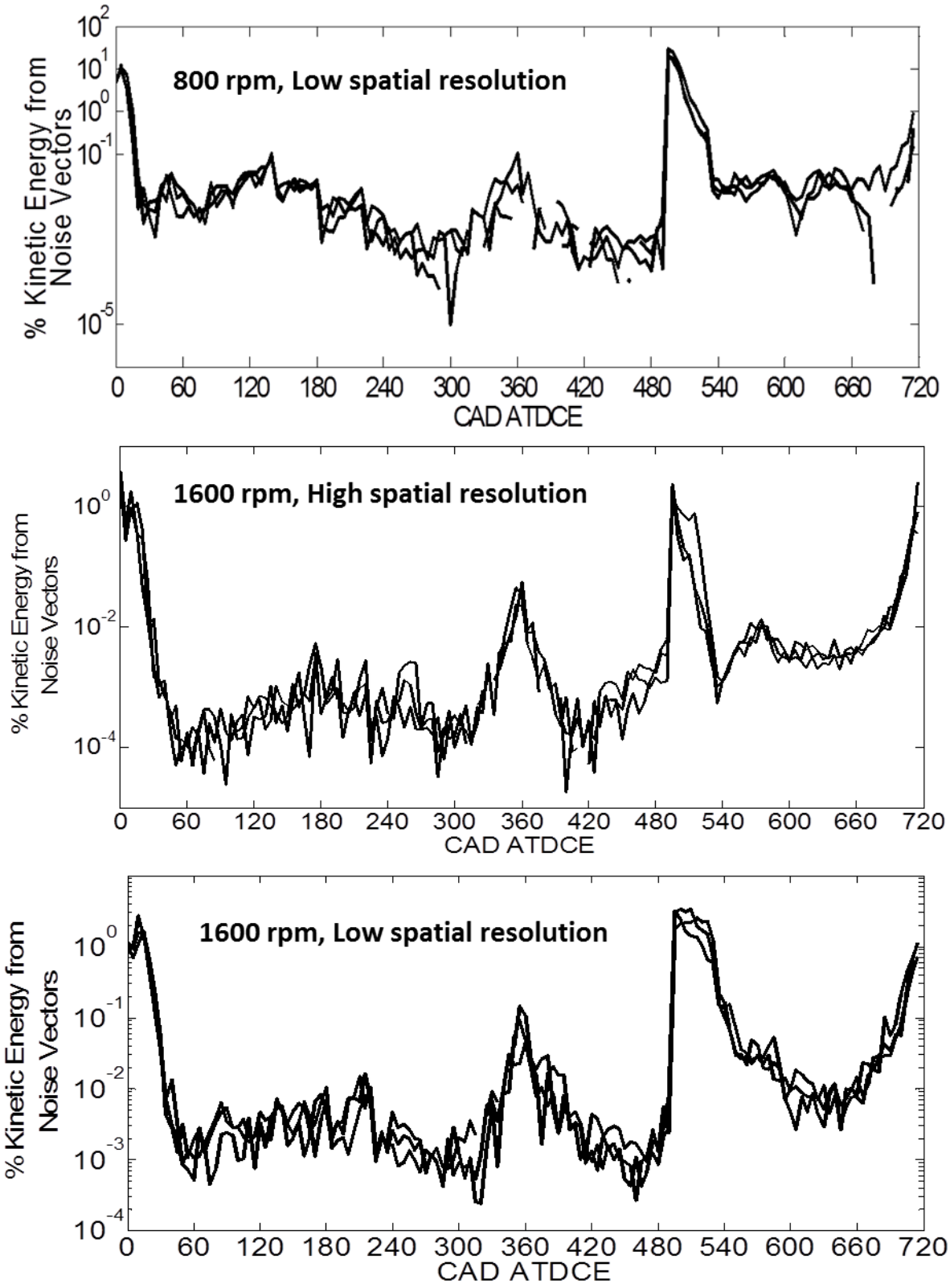

Figure 3.6: *Percent contribution of noise vectors to mass-specific kinetic energy of three randomly chosen cycles at three engine speeds (zero values not plotted)*

3.4 Comparing High and Low Spatial Resolution PIV Measurements

In order to better compare the high and low spatial resolution measurements, data was extracted from the portion of the low spatial resolution field-of-view that corresponds to the high spatial resolution field-of-view. This is illustrated graphically in Figure 3.7 and the velocities are compared in Figure 3.8.

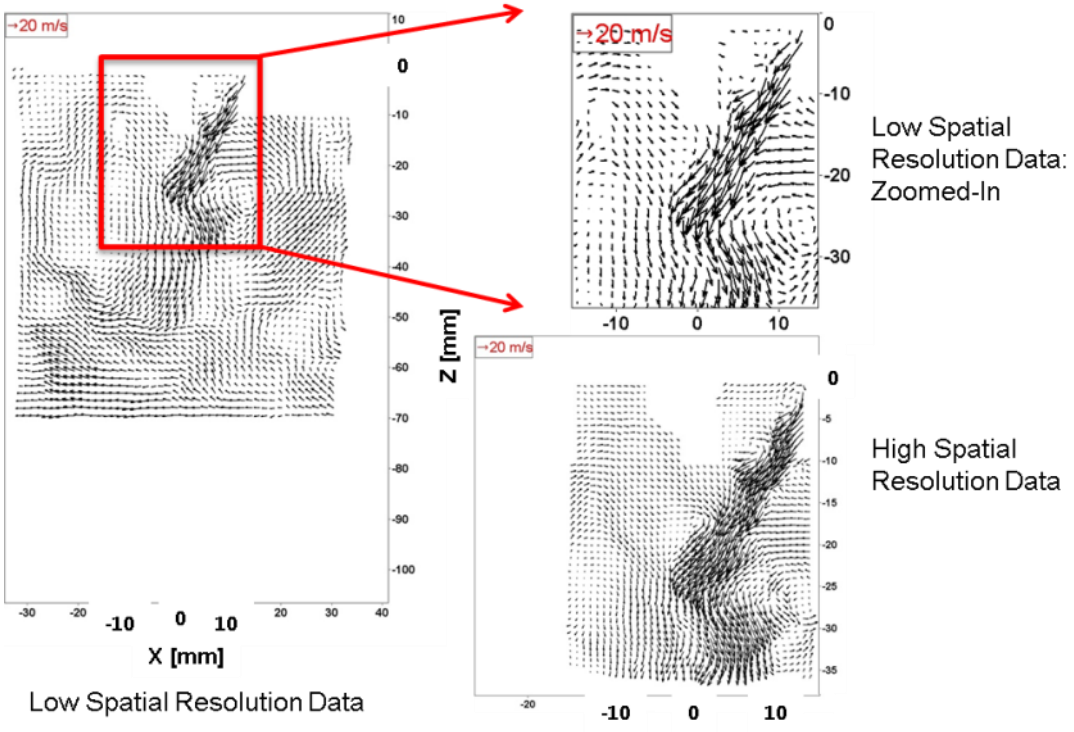

Figure 3.7: *Zoomed-in view of low spatial resolution PIV data for better comparison with high spatial resolution data*

Figure 3.8 shows spatial average and RMS velocities from instantaneous velocity fields throughout the cycle from three randomly selected cycles at 400, 800, and 1600 rpm.

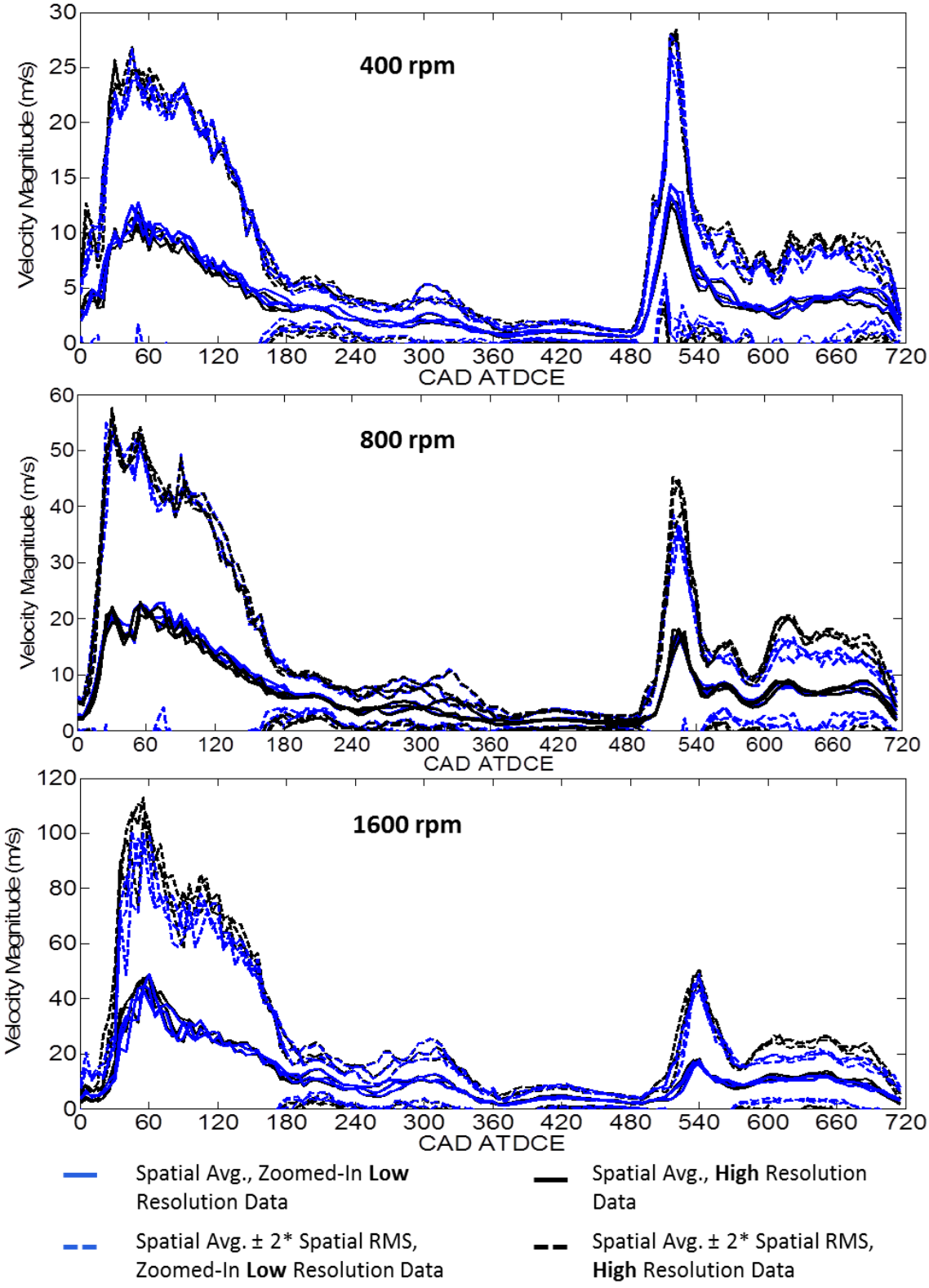

Figure 3.8: *Comparison of velocity ranges captured using high and low spatial resolution PIV measurements*

At 400 rpm, the velocity ranges observed in the high and low spatial resolution data are the same. At 800 rpm, the velocity ranges observed in the high spatial resolution data become larger than those of the low spatial resolution data after exhaust valve opening (485°-715° ATDCE) as larger flow velocities are measured in the exhaust jet region for the high spatial resolution data. We speculate that this bias is due to large spatial gradients in the flow that are not sufficiently resolved by the low spatial resolution measurements. First, the multi-pass PIV processing routine uses smoothing and a bad vector removal process between passes that identifies spurious vectors by comparing them to the median velocity of their neighbors [64]. These steps can result in the removal or reduction in magnitude of real, large predictor vectors if their neighboring vectors are small; such is the case in the low spatial resolution data in the jet shear region. Second, the dts used in the 485°-715° ATDCE range were not optimized for the large exhaust jet velocities. This was a trade-off to allow for better resolution of the low velocities outside of the exhaust jet region, which could bias the velocities due to larger displacements and larger displacement gradients in the jet region. This may explain why a similar discrepancy between the high and low spatial resolution velocity ranges is not seen during intake jet actuation (0°-230° ATDCE), where dts were optimized for the large jet flow velocities. At 1600 rpm, the minimum dt available of 6 μs was not small enough to be optimal for either the large intake or exhaust jet velocities. Thus, the velocity ranges of the high spatial resolution data is larger than that of the low spatial resolution data during both intake and exhaust jet actuation (30°-160° ATDCE and 570°-715° ATDCE).

3.5 Comparing PIV Data Acquired Using Constant and Variable Time Separations

The improvement in the quality of the PIV data acquired using variable dts is, despite any necessary compromises, significant when compared to PIV data acquired using a constant dt. In

the data set S_2011_11_21_02, PIV data was acquired using a constant dt of 10 µs every 2° from 0° to 360° ATDCE at a low spatial resolution under experimental and engine operation conditions very similar to S_2012_06_21_01. The optical setup for both experiments was the same, except the constant dt experiment employed just one camera (Phantom 7.3) looking at the central tumble plane in the engine from the engine head to the piston at BDC with the magnification set to 0.163. The constant dt of 10 µs was chosen such that the large velocity vectors in the intake jet could be measured and PIV correlations in the intake jet region would not be negatively affected by out-of-plane seeding losses. The comparison between the fixed PIV dynamic range and the velocity ranges measured is presented in Figure 3.9.

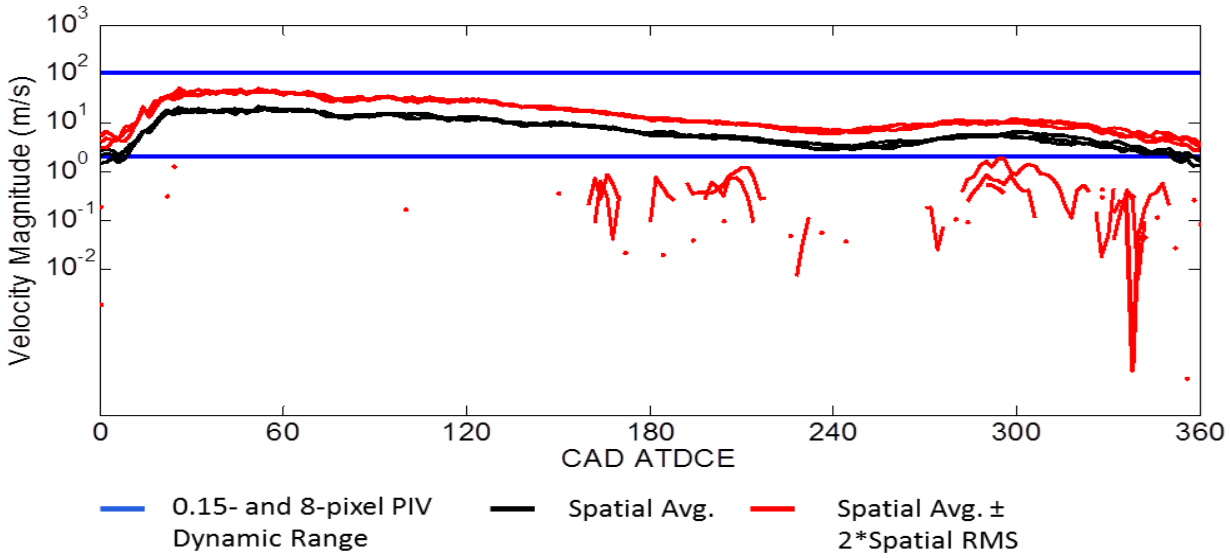

Figure 3.9: *Velocity ranges of cycles 41, 46 and 63 compared to PIV dynamic range of constant dt PIV measurements (zero and negative values not plotted)*

Figure 3.9 confirms that using a constant dt optimized for high intake jet velocities leads to under-resolved velocities in the compression stroke. As a result, larger numbers of vectors in the compression stroke fall below the 0.15 pixel displacement threshold and no vectors are found above the 8 pixel maximum displacement. Both the percentage of noise vectors and the kinetic

energy contribution of the noise vectors in the constant dt data compare unfavorably with the corresponding values from the variable dt data, as shown in Figures 3.10 and 3.11. Taken together, Figures 3.9 - 3.11 clearly show that the selected fixed value of dt is adequate for the intake stroke, where the velocities are large, but inadequate in the compression stroke, where the velocities are low. Optimizing the fixed dt for the compression stroke would not capture the high velocities in the intake stroke, and thus flow statistics would be biased to low values. In contrast, optimization of PIV dynamic ranges using variable dts allows for the accommodation of the wide range of velocity magnitudes seen during different parts of an engine cycle.

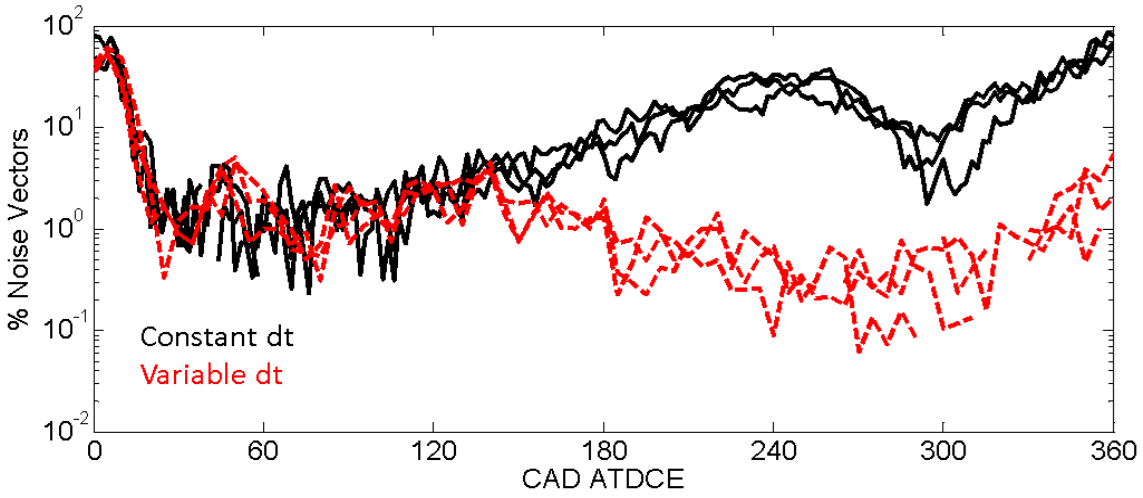

Figure 3.10: *Comparison of noise vector percentages in randomly chosen cycles of the constant dt and the variable dt data sets (zero values not plotted)*

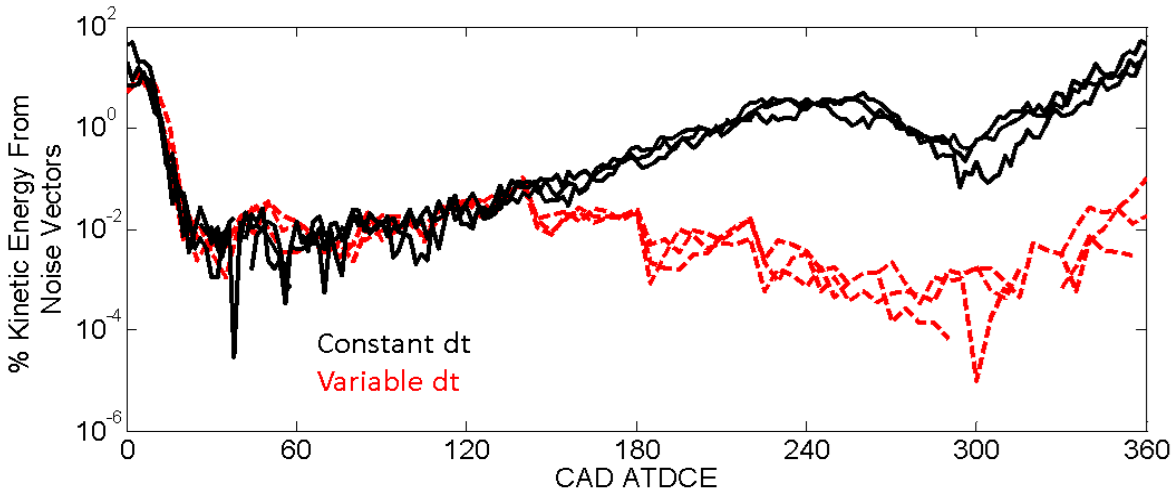

Figure 3.11: *Comparison of the contribution of noise vectors to mass-specific kinetic energies from randomly chosen cycles from the constant dt and the variable dt data sets (zero values not plotted)*

The effect on the Reynolds decomposed turbulence is quantified in Figure 3.12, which shows the noise in the mass-specific turbulent kinetic energy. The percent noise in the mass-specific turbulent kinetic energy (tke) at each crank angle is calculated as shown in Equation (3.5).

$$\%\, Noise\ in\ tke = \frac{0.5*(Velocity\ of\ 0.15\ pixel\ displacement)^2}{\overline{tke}}, \tag{3.5}$$

where the velocity magnitude associated with 0.15 pixels displacement is calculated using Equation (3.4) and $\overline{tke}$ refers to the spatially-averaged mass-specific turbulent kinetic energy at a crank angle.

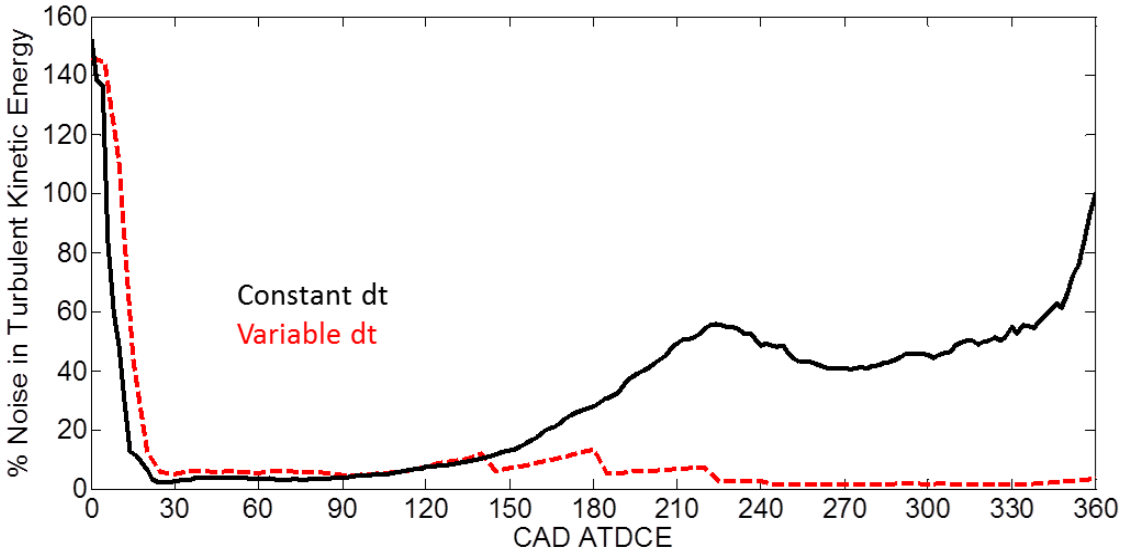

Figure 3.12: *Noise levels in spatially-averaged turbulent kinetic energy for the constant dt and the variable dt data sets*

The percent noise in the spatially-averaged turbulent kinetic energy is high for both the constant dt and variable dt data sets during early intake valve opening due to low turbulent kinetic energies in the flow in the relatively large regions away from the intake jet. During the compression stroke, noise levels in the turbulent kinetic energy of the constant dt data set are much larger than those of the variable dt data set. For most of the compression stroke, the percent noise in the turbulent kinetic energy was reduced from about 50% when using a constant dt optimized for intake jet velocities to below 5% when using variable dts.

3.6 Summary

This chapter assesses the quality of the in-cylinder PIV data acquired using varying spatial resolution and variable time separations (dts) between PIV images. The number of first-choice vectors was used as metric of correlation-peak detectability. Both the dynamic range of the velocity (minimum to maximum resolved velocity) and the velocity magnitudes captured by the high and low resolution measurements are quantified. The largest velocities captured by the high spatial resolution measurements become larger than those captured by the low spatial

resolution measurements during exhaust valve actuation. The percent kinetic energy contributed by noise vectors in the low spatial resolution data was almost an order of magnitude greater than with the high spatial resolution data. Differences between measurements made with fixed and variable dts were quantified. This revealed that the velocity during the compression stroke was highly under-resolved with a constant dt optimized for intake valve jets. The percent noise in the Reynolds decomposed turbulent kinetic energy was about 50% for the constant dt data, while remaining below 5% for the variable dt data, for most of the compression stroke. Thus, it is demonstrated that variable dt settings are necessary for intra-cycle PIV data acquisition in engines.

CHAPTER 4

IN-CYLINDER FLOW SCALING WITH ENGINE SPEED

Engine data acquired at 400, 800, and 1600 rpm (data sets S_2012_06_25_01, S_2012_06_21_01, and S_2012_06_27_02, respectively) with equivalent pressure boundary conditions were compared to establish trends with engine speed in in-cylinder flow evolution, mean flow and cycle-to-cycle flow variations. The scaling with engine speed of in-cylinder and intake and exhaust system pressure magnitudes and dynamics was also investigated. Differences in valve operation between these data sets were also studied as a potential source of in-cylinder flow variations.

4.1 Comparing In-Cylinder, Intake, and Exhaust System Pressures

The crank angle resolved pressure data obtained during optical data acquisition at 400, 800 and 1600 rpm were compared to quantify differences in engine operation at these different engine speeds. Figure 4.1 shows the in-cylinder pressure as a function of volume for all cycles at the three engine speeds.

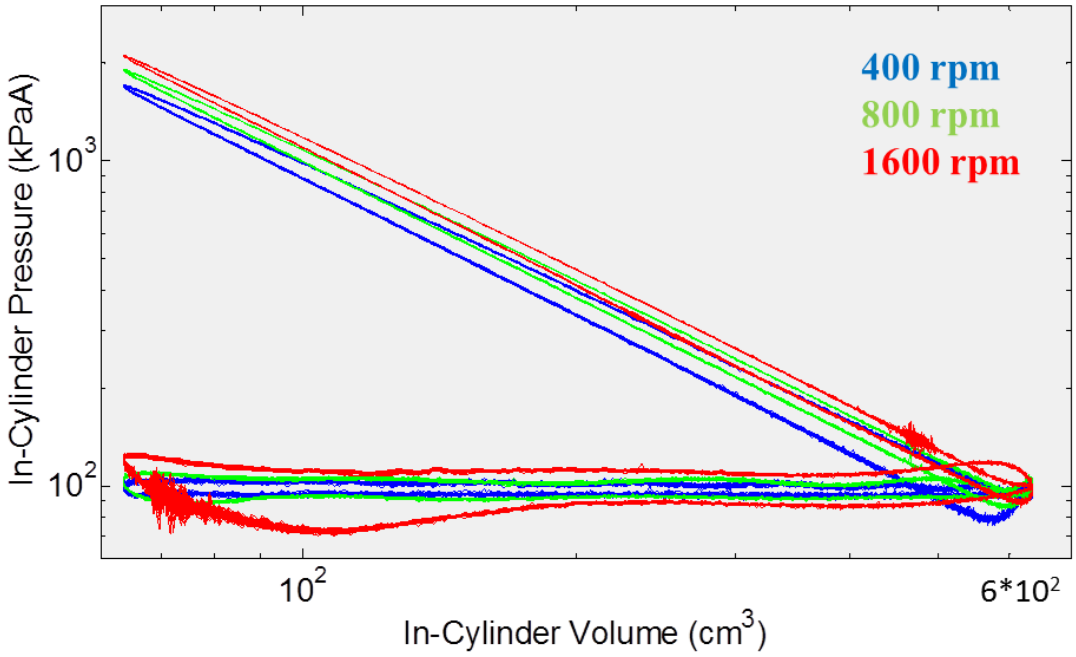

Figure 4.1: *In-cylinder log P – log V graph for 70 cycles each at 400, 800, and 1600 rpm*

Figure 4.1 shows that the peak in-cylinder pressures scale directly with engine speed. In fact, the in-cylinder pressure during all parts of the cycle, except bottom dead center and the intake stroke, scales directly with engine speed. As the engine speed increases, the time taken to complete an engine cycle decreases, decreasing the time available for heat transfer and increasing in-cylinder temperature and, consequently, peak cylinder pressure. The average cylinder surface temperatures, a guide to in-cylinder temperature trends, were 32.4 °C, 37.8 °C, and 76.3 °C at 400, 800, and 1600 rpm, respectively. Also, the higher piston speeds leads to more friction between the piston and the cylinder walls. This may result in a decrease in blow-by due to hotter rings that seal better, further contributing to higher peak cylinder pressures at higher engine speeds. The in-cylinder pressure during the intake stroke decreases with increasing engine speed. During the compression stroke, the in-cylinder pressure increases with engine speed. This is due to restricted flow through the valves at higher engine speeds. Thus, at higher engine speeds, larger pressure differences are seen across the valves, as illustrated by Figure 4.2. The

intake port, exhaust port, and in-cylinder pressures used to calculate the pressure differences shown in Figure 4.2 were first smoothed by calculating running averages over a 5° interval.

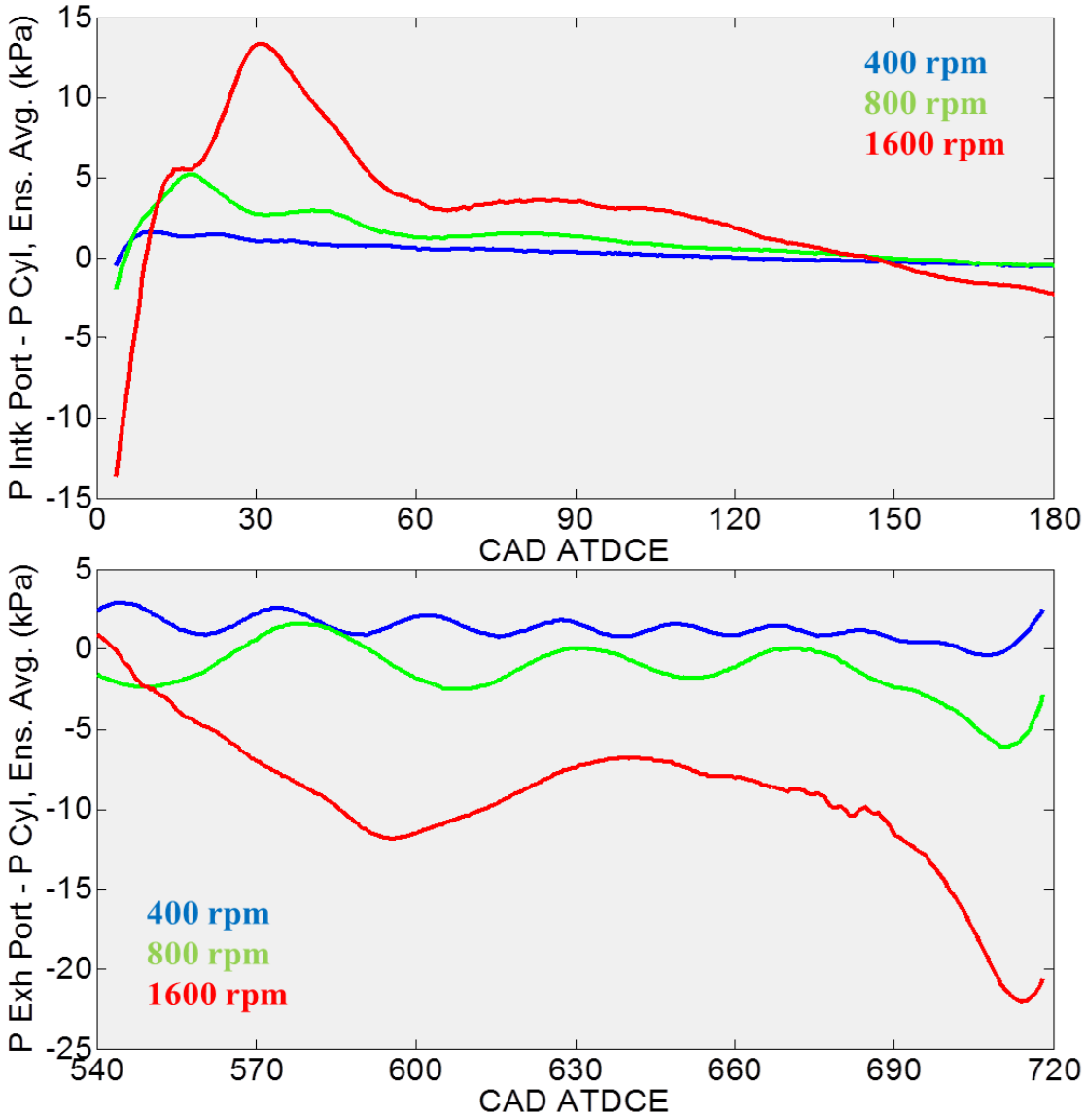

Figure 4.2: *Ensemble average pressure difference across the valves at 400, 800, and 1600 rpm*

Figure 4.3 shows the standard deviation of the in-cylinder pressure as a function of crank angle at all three engine speeds.

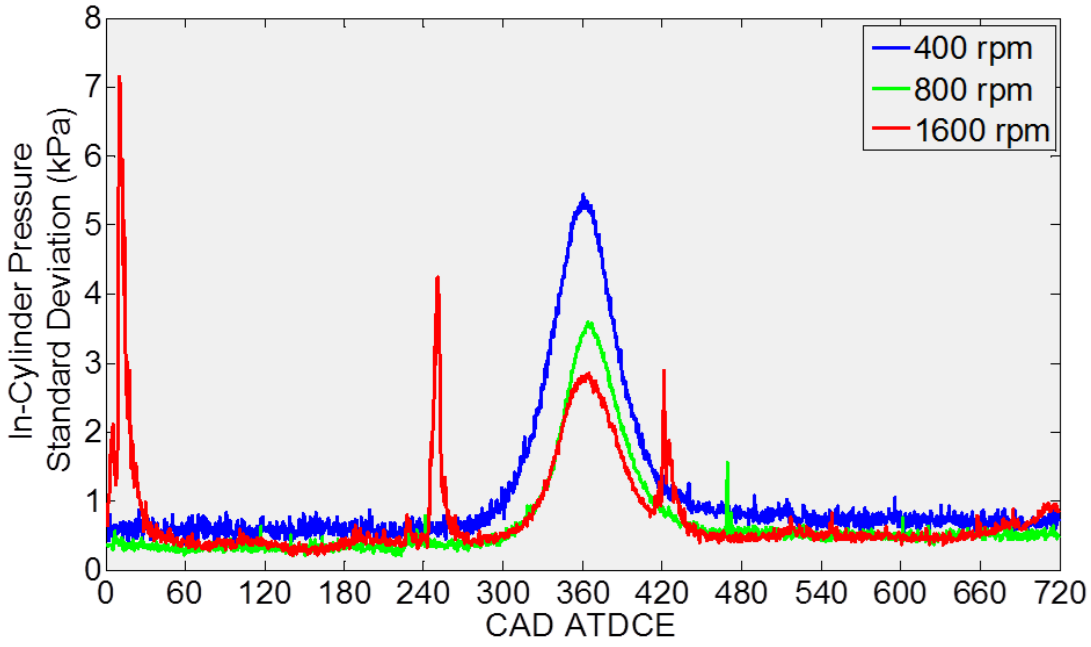

Figure 4.3: *Standard deviation of in-cylinder pressure at 400, 800, and 1600 rpm*

The standard deviation of in-cylinder pressure for the 400 rpm data is higher than that for the other two engine speeds studied throughout the cycle. Towards top dead center compression, the standard deviation decreases with increasing engine speed. This indicates that the cycle-to-cycle variation in in-cylinder pressure, particularly peak pressure, decreases at higher engine speeds. The spikes in standard deviation values near 0° and 240° ATDCE in the 1600 rpm data are noise due to exhaust and intake valve closing, respectively. The spike in standard deviation values near 420° ATDCE in the 1600 rpm data is not correlated with valve events and may be noise due to electrical interference.

Figure 4.4 shows the pressure at the inlet to the intake plenum (P Intk Plen In) as a function of crank angle for all cycles at the three engine speeds.

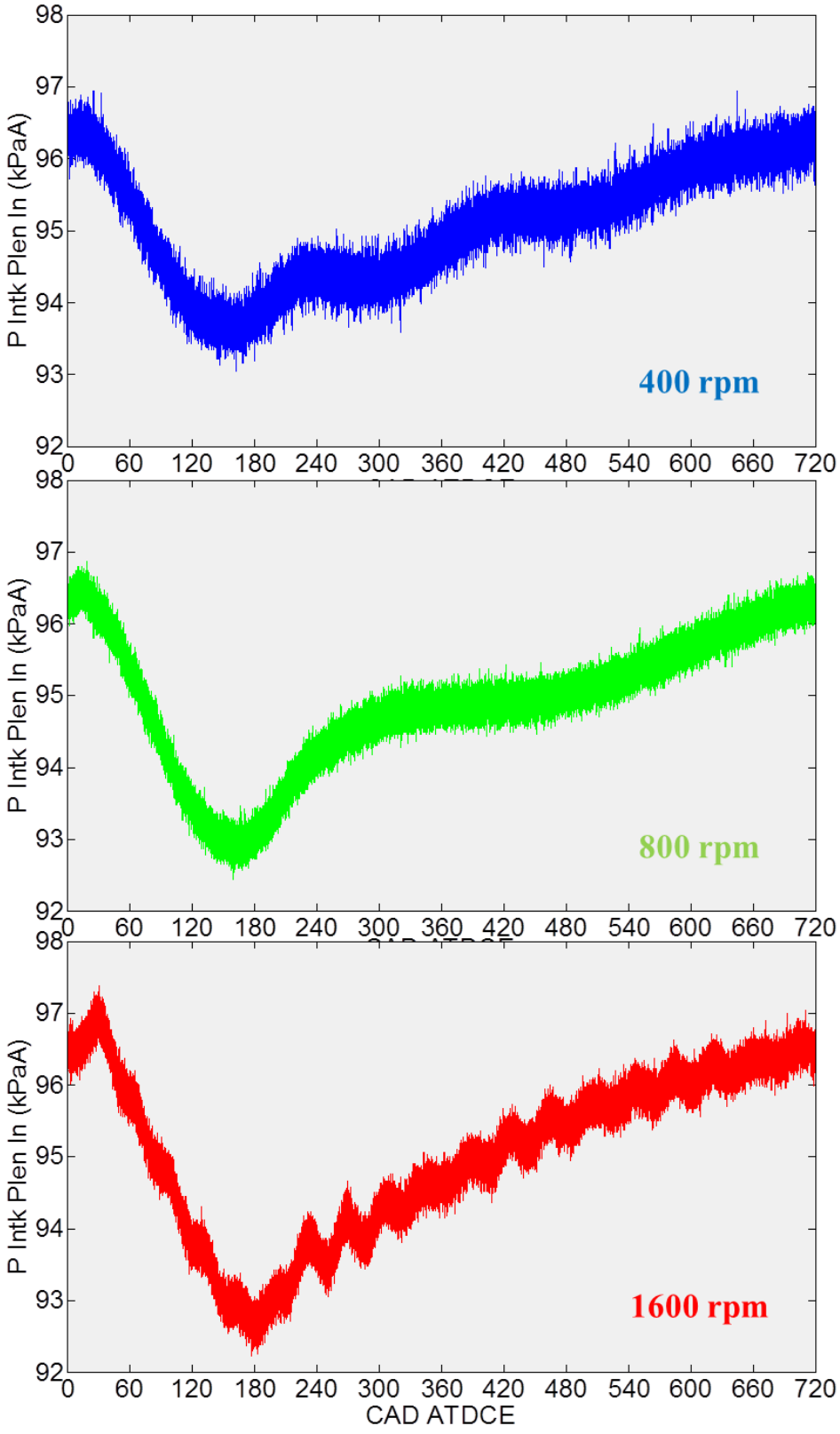

Figure 4.4: *Intake plenum inlet pressure for 70 cycles each at 400, 800, and 1600 rpm*

The initial drop in intake plenum inlet pressure between 0° and 180° ATDCE is due to the intake valve opening and the downward motion of the piston. The pressure then rises as the valve closes and the piston moves back up. The amplitude of this pressure drop increases and the trough occurs closer to bottom dead center as engine speed increases and intake processes increasingly occur in non-equilibrium conditions. The high-frequency pressure waves overlaid over the low-frequency pressure changes through the cycle are of largest frequency for 1600 rpm, followed by 400 rpm and 800 rpm. These are a function of the intake system design. The spread in intake plenum inlet pressures at a particular crank angle, a measure of cycle-to-cycle variability, is comparable at different engine speeds and is on the order of 1%.

Figure 4.5 shows the pressures in the runner blocks between the intake and exhaust runners and ports in the engine head (P Intk Port and P Exh Port) for all cycles at the three engine speeds. The amplitudes of the initial pressure drop in the intake port pressure between 0° and 60° ATDCE as the intake valve opens and the secondary wave caused by upward piston motion and intake valve closing between 180° and 240° ATDCE scale with engine speed. The exhaust port pressures show a similar scaling of pressure wave amplitudes with engine speed. Here, the initial impetus that creates these waves is the opening of the exhaust valve at 484° ATDCE. The spread in runner pressures at a particular crank angle is comparable at different engine speeds and is approximately 1% or less.

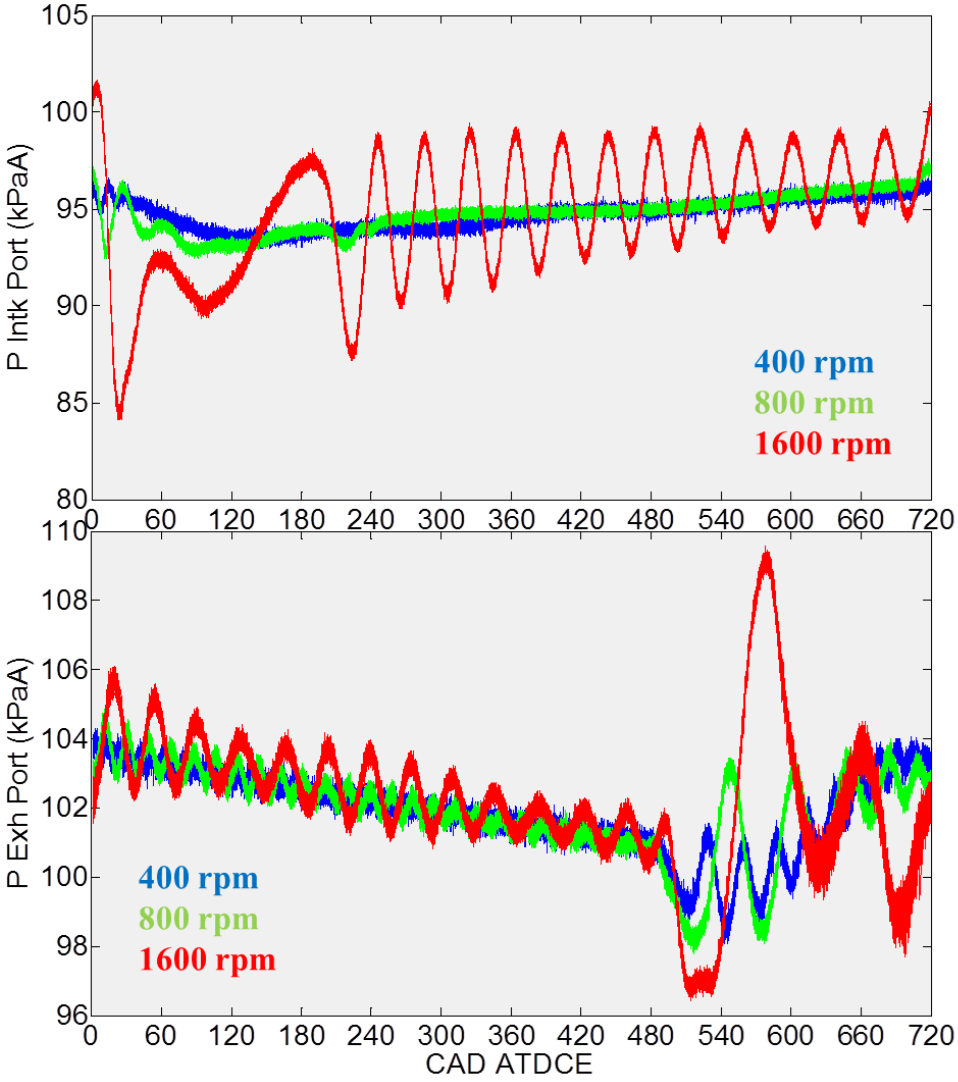

Figure 4.5: *Intake and exhaust port pressure for 70 cycles each at 400, 800, and 1600 rpm*

Figure 4.6 shows the difference between the frequencies associated with the intake port pressure waves during intake valve actuation at different engine speeds by plotting the ensemble average intake port pressures at the three different engine speed as functions of time. The intake port pressures were first smoothed by calculating running averages over a 5° interval. For all engine speeds, 0° ATDCE was set to be 0 s.

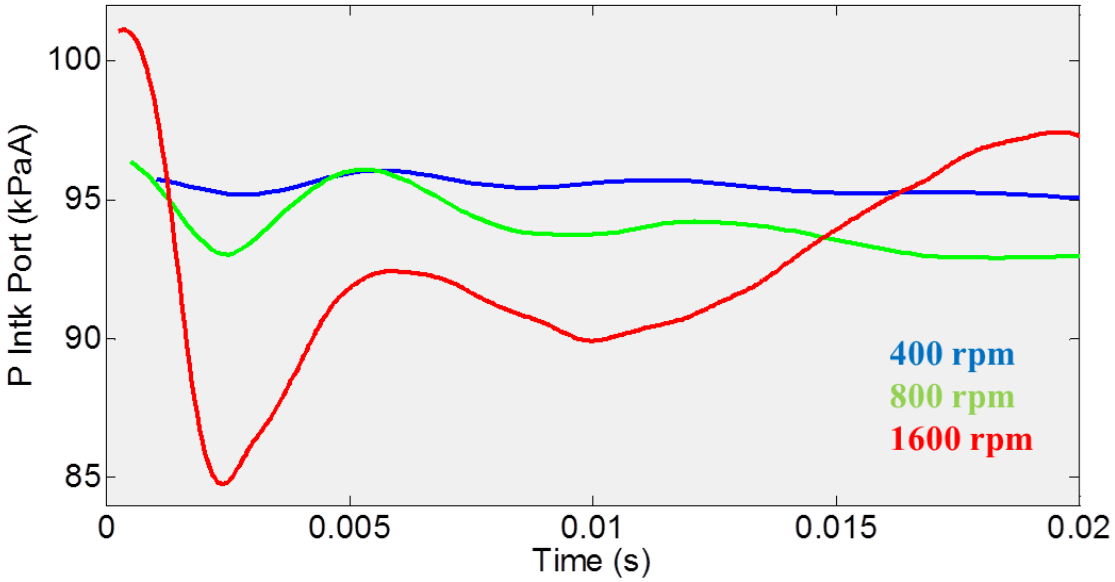

Figure 4.6: *Ensemble average intake port pressure during intake valve actuation as a function of time for 400, 800, and 1600 rpm*

Figure 4.6 shows that the frequencies associated with the intake valve opening pressure waves for the three different engine speeds are similar and independent of engine speed up to about 0.01 s. Thus, the intake process takes place on a time scale and not a crank angle scale.

Figure 4.7 shows the ensemble average intake port pressures as a function of time after intake valve closing. Again, the intake port pressures were first smoothed by calculating running averages over a 5° interval. For all engine speeds, 250° ATDCE was set to be 0 s.

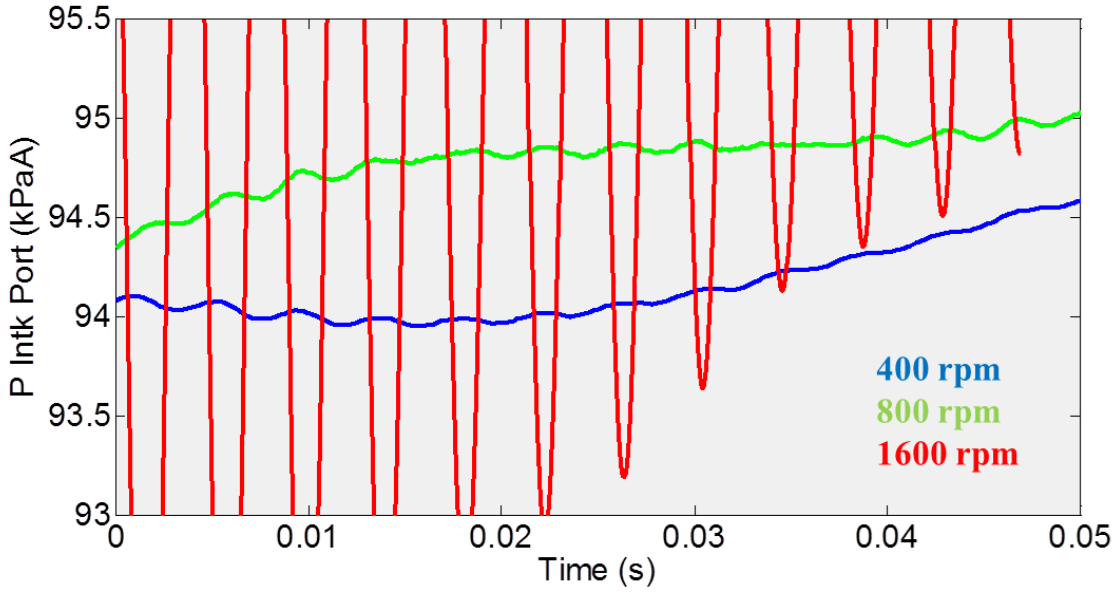

Figure 4.7: *Ensemble average intake port pressure after intake valve closing as a function of time for 400, 800, and 1600 rpm*

Figure 4.7 shows that the frequencies of the ensemble average intake port pressure waves after intake valve closing are also similar and independent of engine speed. The length of the intake port runner from the intake plenum to the intake valve, l, with a value of 0.382 m, can be used to calculate the expected open-pipe fundamental frequency, f_{op}, for each of the three data sets according to Equation (4.1)[66].

$$f_{op} = \frac{c}{4l} \tag{4.1}$$

In Equation (4.1), c is the speed of sound. For an ideal gas, a reasonable approximation of air close to room temperature and pressure, it can be calculated as shown in Equation (4.2).

$$c = \sqrt{kRT} \tag{4.2}$$

In Equation (4.2), k is the specific heat ratio, R is the ideal gas constant, and T is the gas temperature. To calculate the speed of sound in the intake port, k and R for air at room temperature and pressure were used in Equation (4.2), along with the measured test average

intake port temperatures. Table 4.1 compares the expected open-pipe fundamental frequency with the empirically obtained ensemble average frequency, f_{emp}, calculated from Figure 4.7.

	c (m/s)	f_{op} (Hz)	f_{emp} (Hz)
S_2012_06_25_01, 400 rpm	356	233	239
S_2012_06_21_01, 800 rpm	357	234	256
S_2012_06_27_02, 1600 rpm	359	235	243

Table 4.1: *Ensemble average intake port pressure wave frequencies at 400, 800, and 1600 rpm*

Table 4.1 shows that the difference between f_{op} and f_{emp} is less than 4% of f_{op} for the 400 and 1600 rpm data sets, while the 800 rpm data set shows a larger discrepancy of 9%. Figure 4.8 shows that cycle-to-cycle variation in the phase of the intake port pressure waves decreases with increasing engine speed. For all engine speeds, 250° ATDCE was set to be 0 s in Figure 4.8.

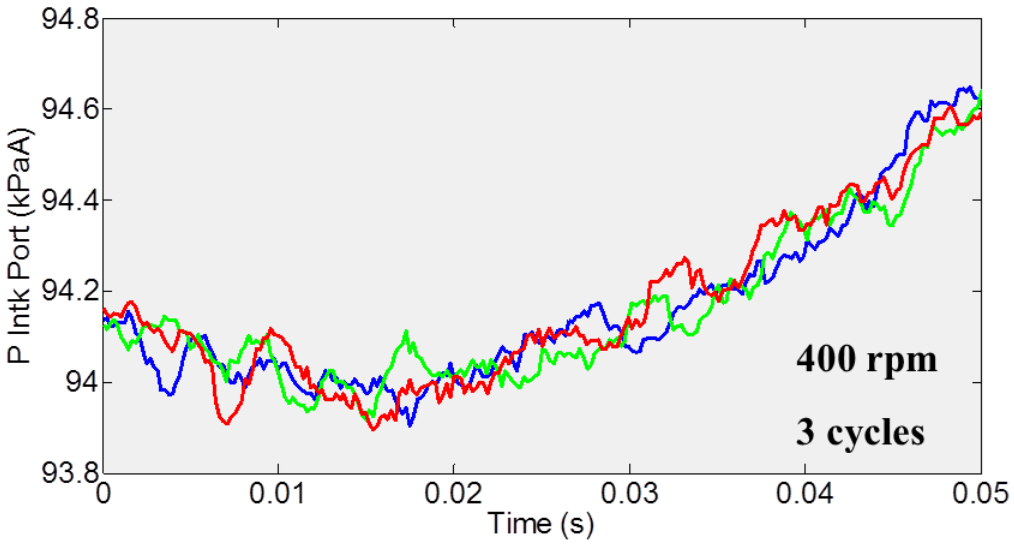

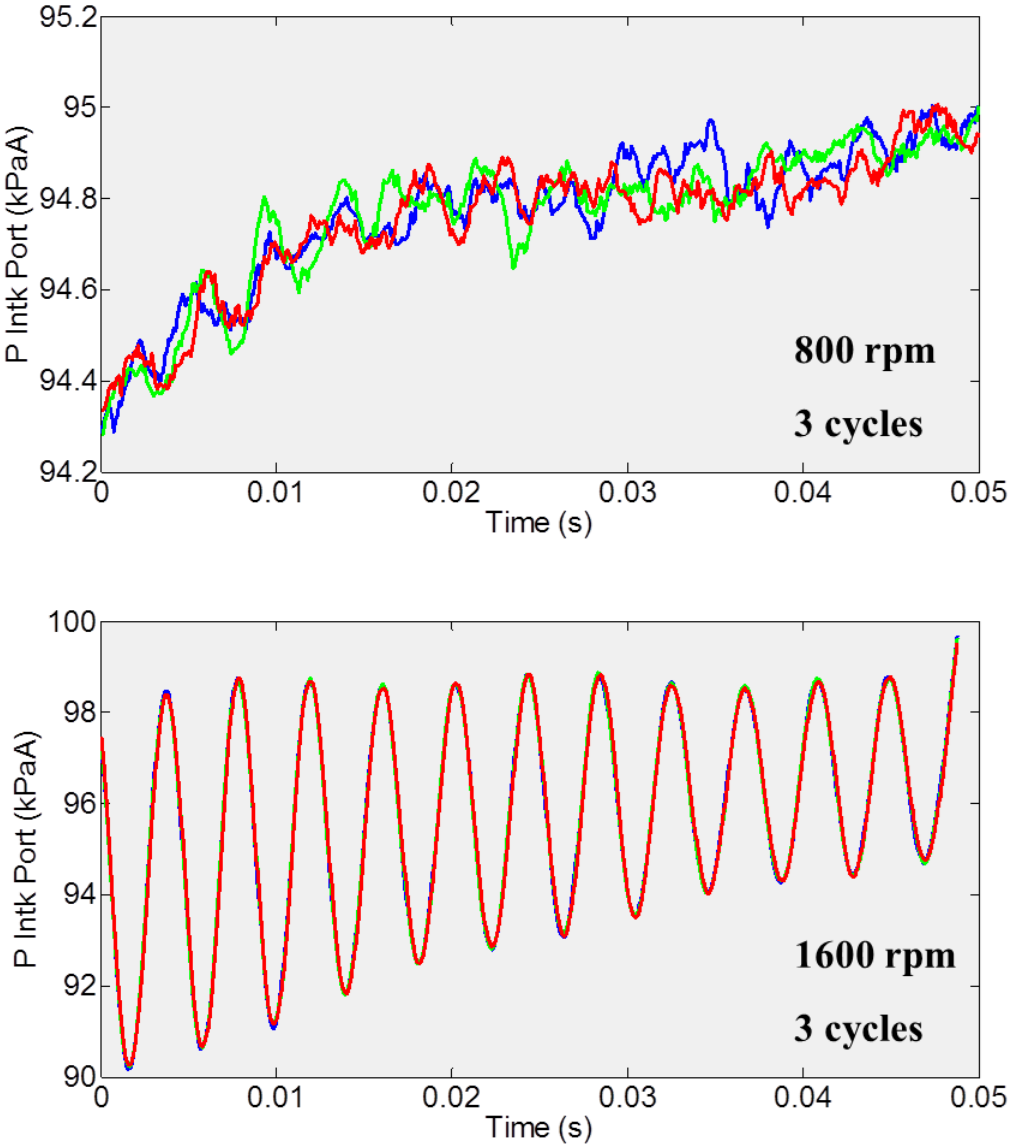

Figure 4.8: *Instantaneous intake port pressure after intake valve closing for 400, 800, and 1600 rpm*

Figure 4.9 shows the pressure at the outlet to the exhaust plenum (P Exh Plen Out) as a function of crank angle for all cycles at the three engine speeds. The pressure wave caused by the opening of the exhaust valve at 484° ATDCE dies down more rapidly at 400 and 800 rpm than at 1600 rpm. Again, the spread in exhaust plenum outlet pressures is comparable at different engine speeds and is on the order of 1%.

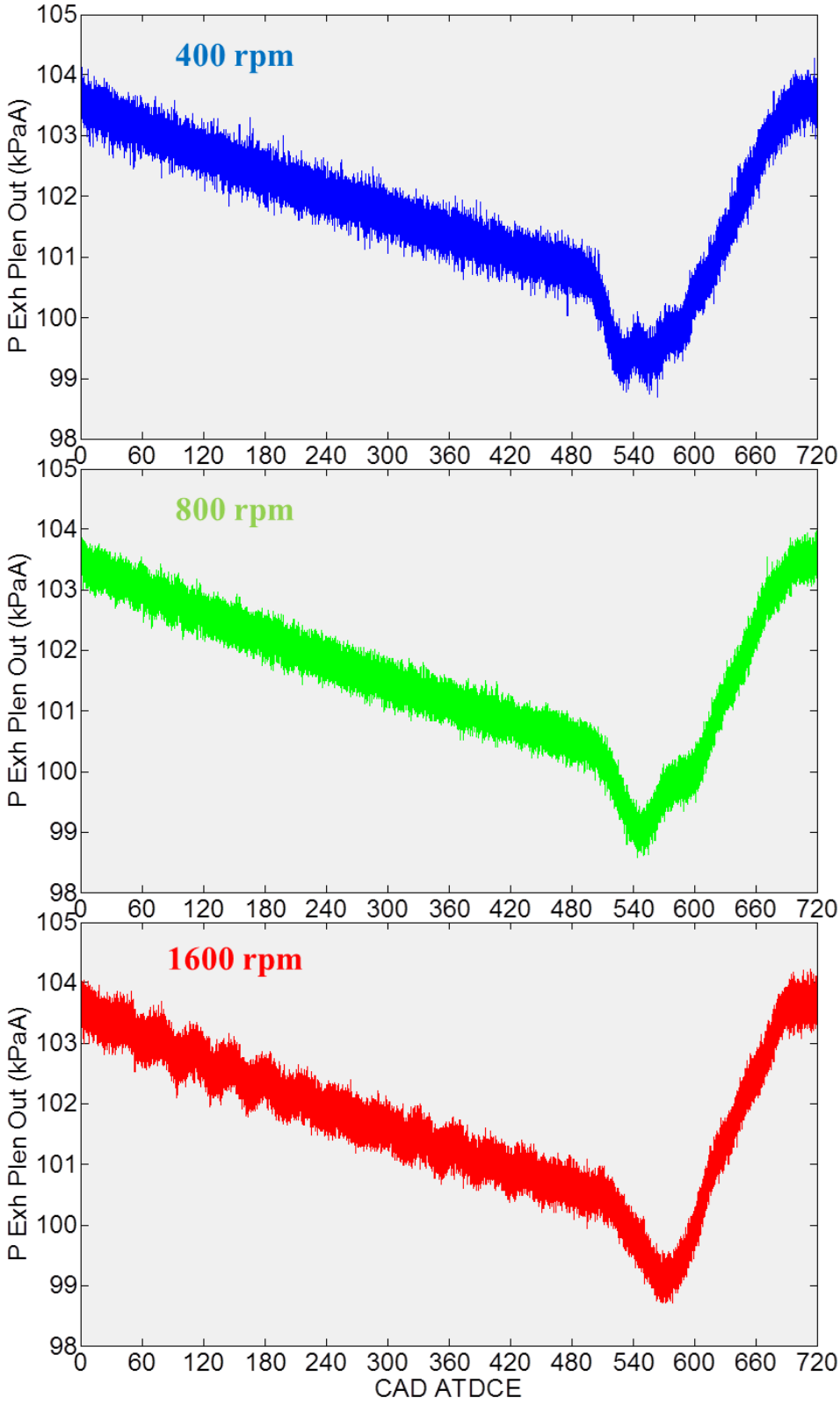

Figure 4.9: *Exhaust plenum outlet pressure for 70 cycles each at 400, 800, and 1600 rpm*

4.2 Cycle-to-Cycle and Intra-Cycle Variability of Valve Actuation

Intake and exhaust valve 'ringing', or oscillation during valve actuation, in the data sets presented in this chapter is quantified in order to assess its effect on cycle-to-cycle flow variations. Cycle-to-cycle variation in valve actuation manifests as differences in valve location at a certain crank angle through the data set. The calibrated high spatial resolution PIV images from the data sets discussed in this chapter were examined at three different crank angles, 5° ATDCE (early intake valve opening), 100° ATDCE (intake valve approaching peak lift), and 550° ATDCE (exhaust valve opening). At a particular crank angle, the locations of the valve edges are tracked from cycle to cycle by calculating and comparing the maximum and minimum intensities at each pixel in the PIV images. The laser light reflections from the valve create high intensity regions in the PIV images. The maximum intensity count of a particular pixel in the region of the valve image will be high if some part of the valve is ever imaged at that pixel. Conversely, the minimum intensity count of a particular pixel in the region of the valve image will be high only if some part of the valve is imaged at that pixel in every cycle. This process of determining the cycle-to-cycle valve oscillation is illustrated in Figure 4.10.

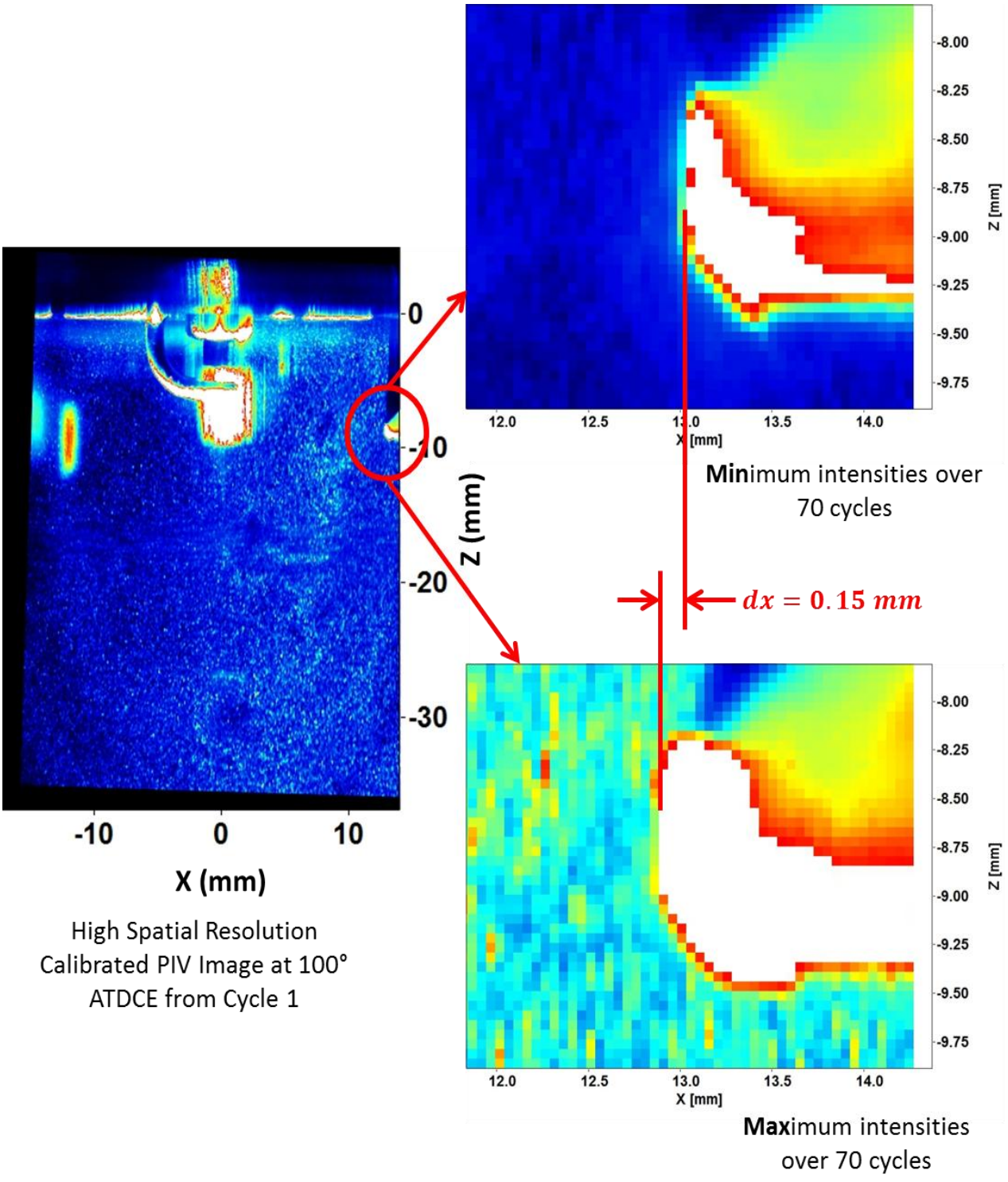

Figure 4.10: *Cycle-to-cycle variations in intake valve position at 100° ATDCE in S_2012_06_21_01*

The displacements along the X and Z axes between extreme valve positions at three crank angles are presented in Table 4.2.

	CAD ATDCE	dx (mm)	dz (mm)
S_2012_06_25_01	5	0.05	0.20
	100	0.05	0.10
	550	0.10	0.10
S_2012_06_21_01	5	0.20	0.05
	100	0.15	0.10
	550	0.05	0.05
S_2012_06_27_02	5	0.05	0.10
	100	0.05	0.05
	550	0.10	0.10

Table 4.2: *Variability in intake (at 5° and 100° ATDCE) and exhaust (at 550° ATDCE) valve position along X and Z axes*

The cells in Table 4.2 that are not highlighted show displacements of 1 pixel, which is 0.05 mm long for high spatial resolution measurements in these data sets. Due to cycle-to-cycle variations in laser light reflection from the valves, it is not possible to resolve such small displacements with any certainty. However, the highlighted cells in Table 4.2 show clearly that the position of the intake valve along the X axis varies from cycle to cycle in S_2012_06_21_01 (acquired at 800 rpm). The width of the annular intake valve opening at 100° ATDCE was estimated to be 10 mm with a centered valve. Thus, the variation of the position of the intake valve along the X axis at 100° ATDCE in S_2012_06_21_01 results in a change of around 1% in the width of the annular intake valve opening. A study examining the creation of mixing layers due to shear between two flows found that even small sinusoidal disturbances with amplitudes that, at their largest, are 1% of the height of each of the initial separated flows can result in measurable changes in the rate of increase of the mixing layer [67]. Thus, the level of cycle-to-cycle variations in the position of the intake valve observed in S_2012_06_21_01 may be expected to

have an effect on in-cylinder flow. The position of the exhaust valve in S_2012_06_25_01 (acquired at 400 rpm) and S_2012_06_27_02 also vary from cycle to cycle.

Within a cycle, valve oscillations were assessed by calculating the maximum pixel intensities through valve opening and closing. As the valve image is high intensity, this captures valve position at different crank angles in one image and enables the tracing of the position of the valve edge during valve opening or closing. This process is illustrated in Figure 4.11, which shows the maximum pixel intensities through intake valve opening from S_2012_06_21_01.

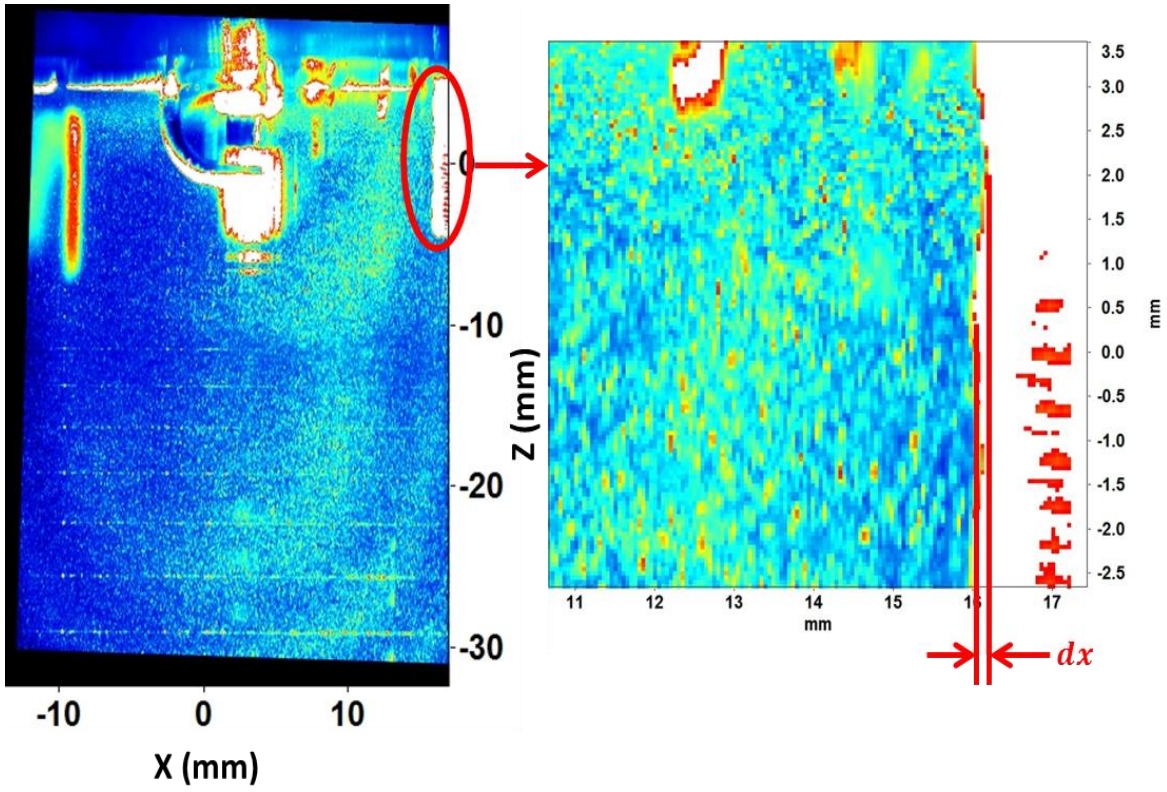

Figure 4.11: *Variations in valve position during intake valve opening during Cycle 15 of S_2012_06_21_01 (composite image from 0° to 115° ATDCE)*

The displacement along the X axis between extreme valve positions during intake and exhaust valve opening and closing for the three data sets analyzed in this chapter are presented in Table 4.3.

		CA Range (° ATDCE)			
	Cycle Number	0-115	120-230	495-605	610-715
S_2012_06_25_01	1	0.30 mm	0.25 mm	0.10 mm	0.15 mm
	39	0.25 mm	0.25 mm	0.15 mm	0.15 mm
	49	0.25 mm	0.25 mm	0.10 mm	0.15 mm
S_2012_06_21_01	15	0.20 mm	0.20 mm	0.15 mm	0.15 mm
	50	0.25 mm	0.15 mm	0.15 mm	0.20 mm
	65	0.20 mm	0.15 mm	0.15 mm	0.20 mm
S_2012_06_27_02	2	0.40 mm	0.25 mm	0.15 mm	0.20 mm
	35	0.40 mm	0.25 mm	0.15 mm	0.20 mm
	52	0.40 mm	0.25 mm	0.15 mm	0.20 mm

Table 4.3: *Intake (in blue) and exhaust (in red) valve motion during a cycle along the X axis*

Table 4.3 shows that, during intake valve actuation, the smallest displacements of the valve edge during intake valve opening and closing are observed in S_2012_06_21_01 (acquired at 800 rpm). The larger intake valve displacements seen in S_2012_06_25_01may be a result of resonance effects. Displacements of the exhaust valve during valve opening increase from S_2012_06_25_01 to the data sets acquired at higher engine speeds. Exhaust valve displacements during valve closing increase with increasing engine speed.

4.3 Comparing In-Cylinder Flow Evolution

An initial assessment of differences in in-cylinder flow at the three different engine speeds studied was made by comparing mass-specific kinetic energies of the ensemble average and RMS low spatial resolution velocity fields, normalized by mean piston speed. Due to variations in laser light reflections and intensities across the light sheet, the in-cylinder locations at which velocity vectors are obtained differ somewhat from run to run. Thus, velocity data acquired at the three different engine speeds first underwent interpolation onto a common grid such that the same grid points were populated at a particular crank angle imaged. A point on the common grid was populated only if there were at least three surrounding vectors available on the

grids at each engine speed for the interpolation at that point. This velocity interpolation is demonstrated in Figure 4.12.

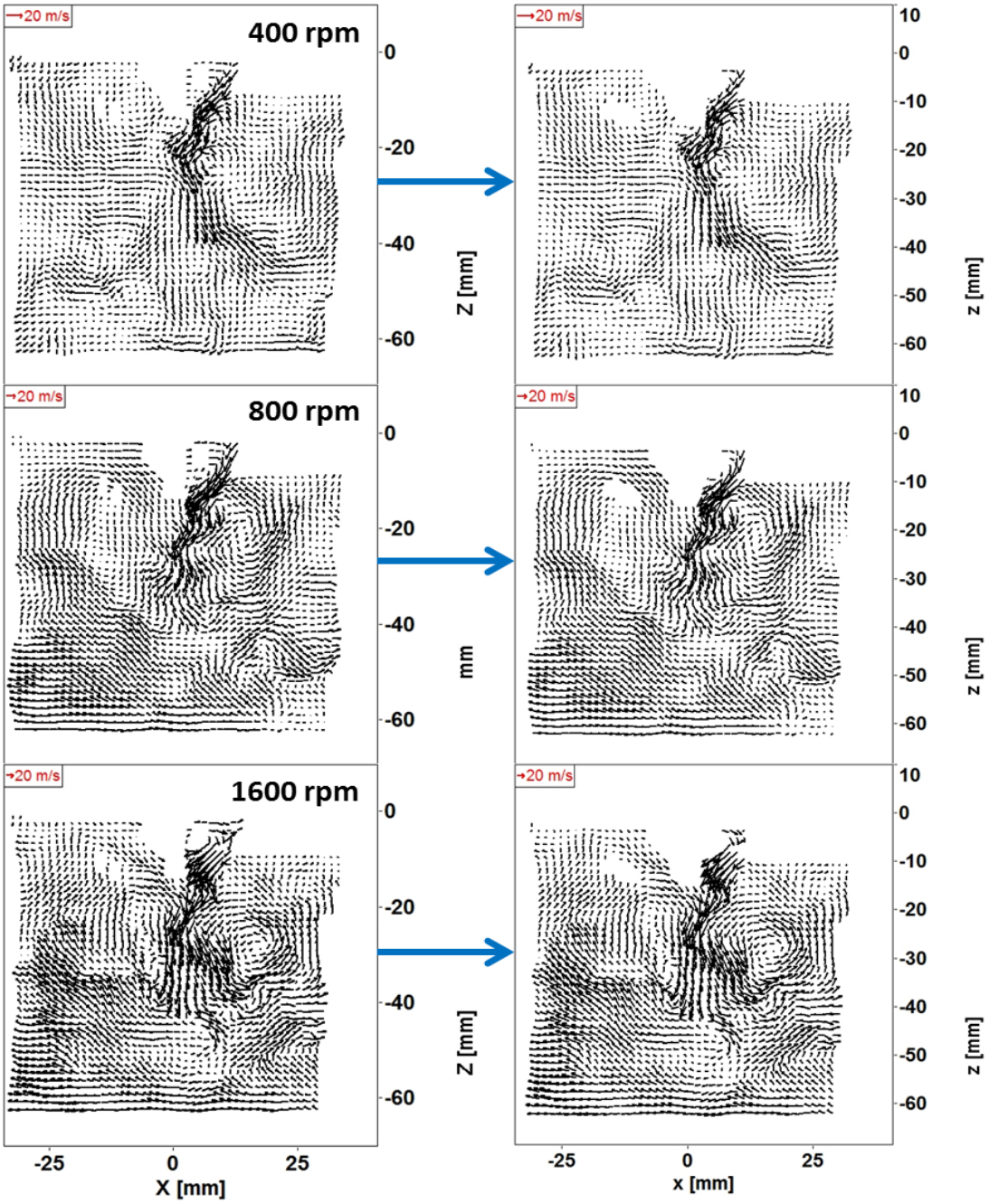

Figure 4.12: *Vector interpolation for a common grid for 400, 800, and 1600 rpm data for phase-invariant POD. Instantaneous low spatial resolution velocity fields at 100° ATDCE from cycle 15 of each data set are shown here.*

The spatial sum of the mass-specific kinetic energies associated with normalized ensemble average and RMS low spatial resolution velocity fields are shown in Figure 4.13.

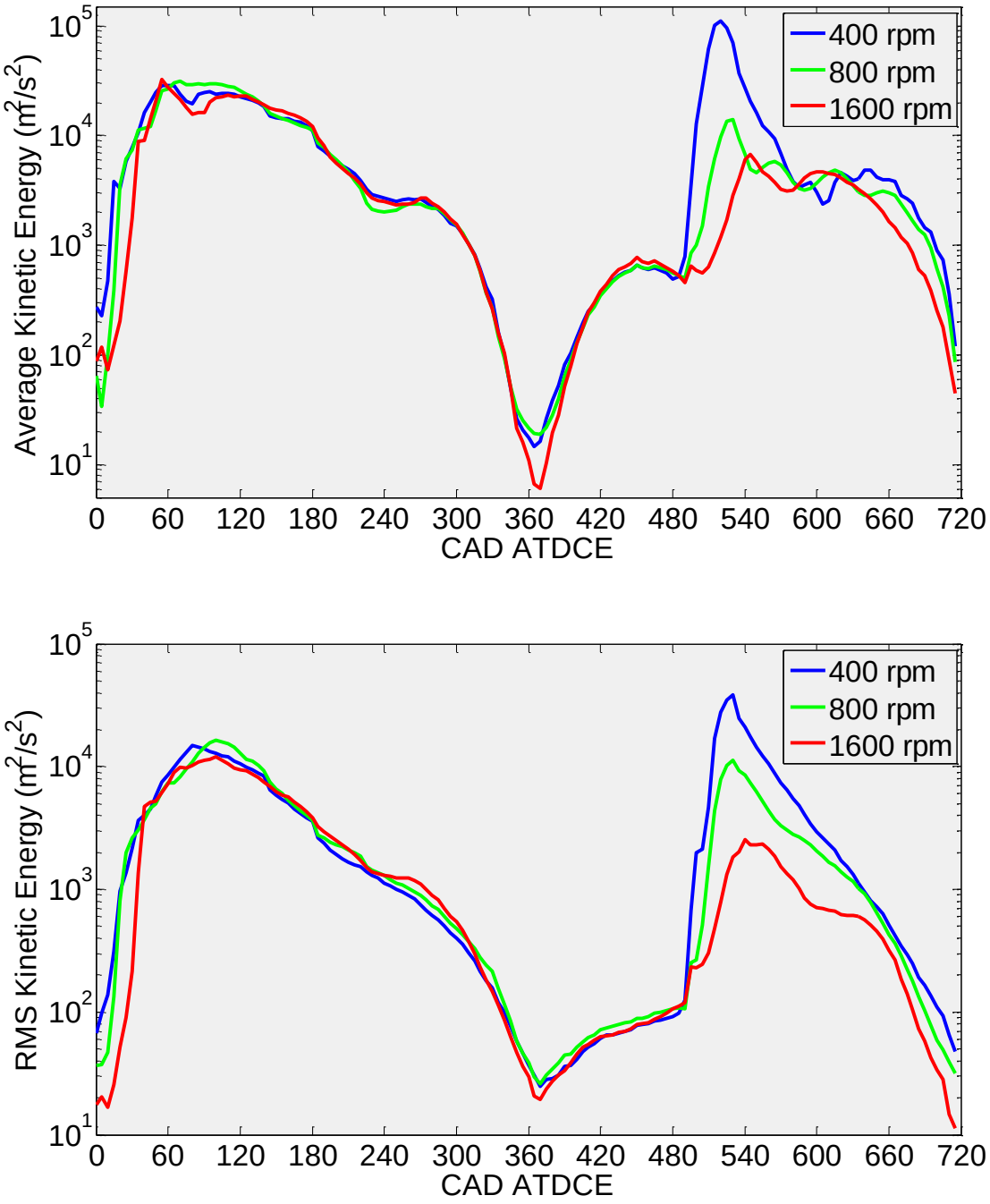

Figure 4.13: *Spatially summed mass-specific kinetic energies of normalized and remapped low spatial resolution ensemble average and RMS velocity fields at 400, 800, and 1600 rpm*

In Figure 4.13, the kinetic energies of both the average and RMS velocity fields during early intake valve opening (15°-60° ATDCE) and exhaust valve actuation (485°-720° ATDCE) scale inversely with engine speed. The scaling of the kinetic energy values from early exhaust valve opening may be a result of the large exhaust jet flow velocities being better captured in the 400 rpm low spatial resolution measurements, as described in Section 3.5. The lower kinetic energy values of the 1600 rpm data during early intake valve opening may also be a result of this data set similarly failing to capture the large intake valve flow velocities in the low spatial resolution measurements.

Phase-invariant POD was used to compare in-cylinder flow evolution at 400, 800, and 1600 rpm and to assess differences in flow structures at the different engine speeds. As phase-invariant POD requires that all vector fields from all crank angles be on the same grid, the interpolated velocity fields were spatially transformed as their grid was stretched or compressed to match that at engine midstroke. To account for the scaling of in-cylinder velocities and kinetic energies with engine speed, phase-invariant POD of the combined 400, 800, and 1600 rpm velocity fields at all crank angles and cycles was performed with unity kinetic energy normalization. This prevented the 1600 rpm data from dominating the results. Figure 4.14 shows the first three modes from the analysis.

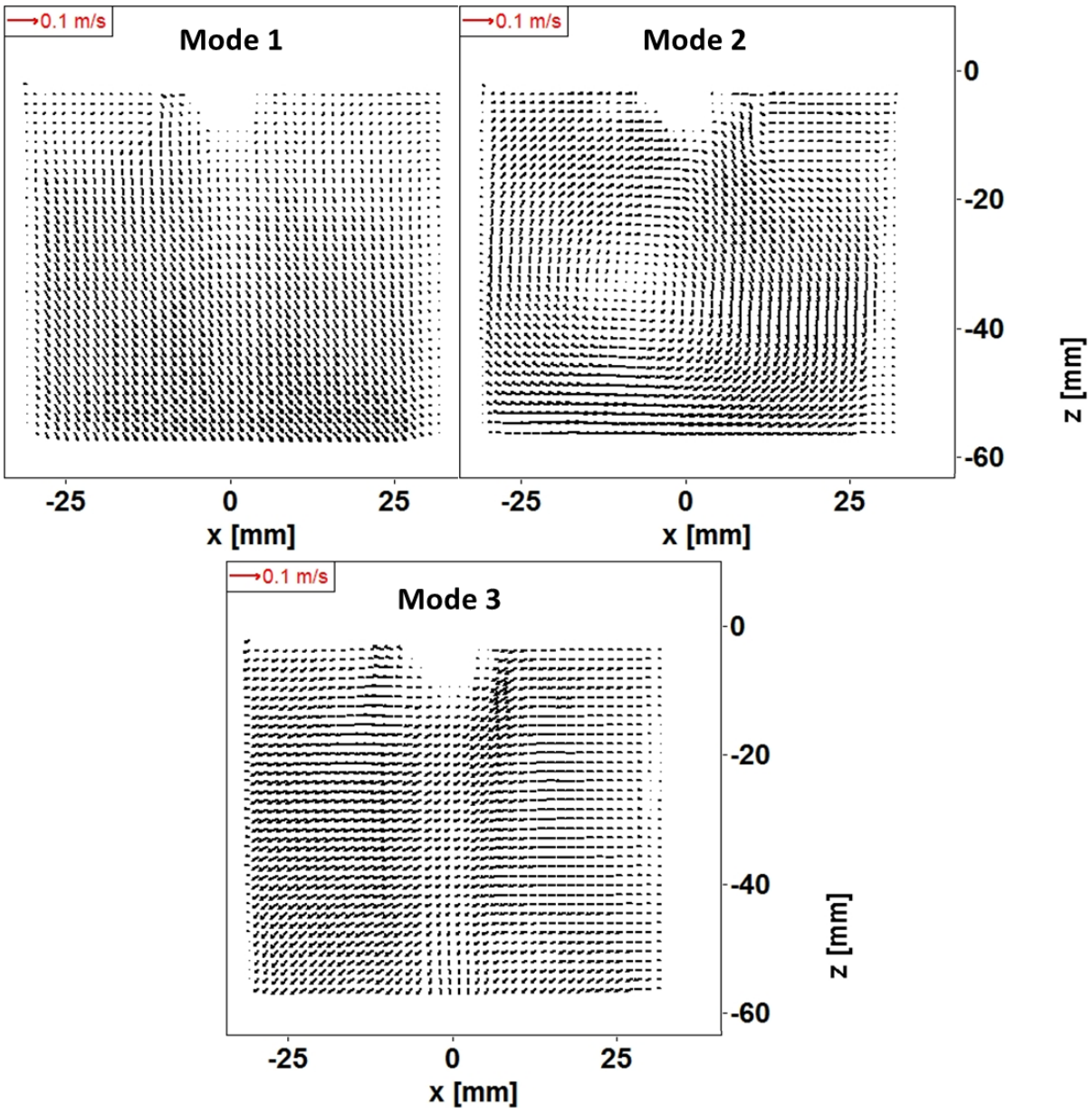

Figure 4.14: *First three modes from phase-invariant POD of low spatial resolution 400, 800, and 1600 rpm data*

Mode 1, with an overall energy fraction of 28%, shows a piston-induced in-cylinder flow pattern. Mode 2, with an overall energy fraction of 14%, shows a large-scale tumble vortex. Mode 3, with an overall energy fraction of 10%, shows flow towards the bottom-left of the cylinder.

Figure 4.15 presents the coefficients associated with these three modes as a function of crank angle for all the cycles analyzed.

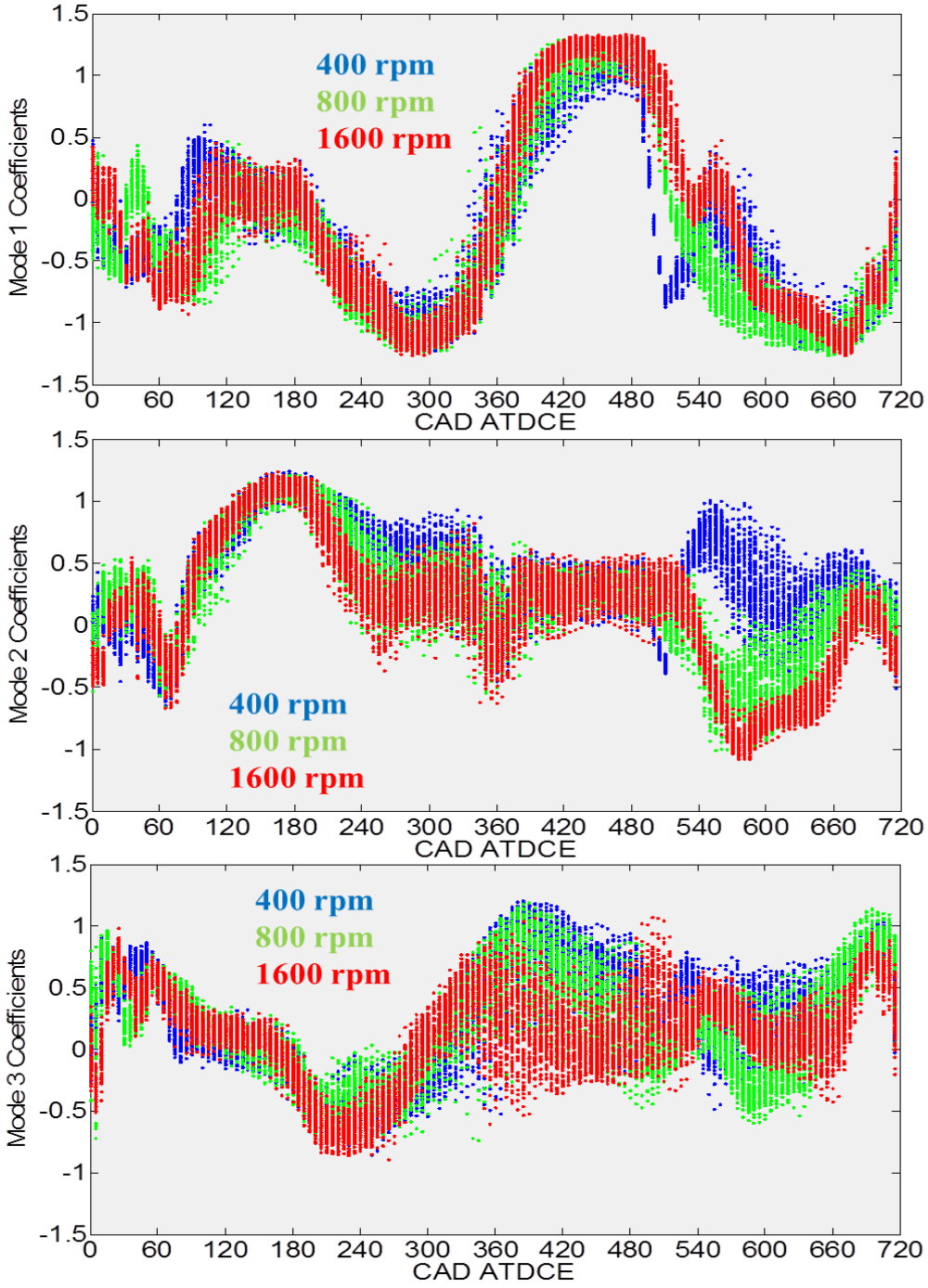

Figure 4.15: *Coefficients of the first three modes from phase-invariant POD of low spatial resolution 400, 800, and 1600 rpm data*

Figure 4.15 shows that in certain crank angle ranges, the coefficients scale directly with engine speed, suggesting that the in-cylinder flow evolution changes in a predictable fashion with engine speed. This can be seen in the Mode 1 coefficients in the crank angle range 380°-485° ATDCE where the dominance of certain aspects of the piston-induced downward flow scales with engine speed, in the Mode 2 coefficients between 180° and 350° ATDCE where the tumble vortex breaks down more quickly at higher engine speeds, and in the Mode 3 coefficients from 330° to 480° ATDCE where other aspects of a piston-driven downward flow scale inversely with engine speed. Mode 1 shows flow towards the bottom-right of the field-of-view and Mode 3 shows flow towards the bottom-left of the field-of-view. Thus, the coefficients associated with these modes in the range 380°-480° ATDCE determine the exact direction of the downward flow in this crank angle range for individual cycles. Figure 4.11 suggests that the flow tends more towards the bottom-right in the early part of the expansion stroke at higher engine speeds. The discrepancy between the coefficients associated with the different engine speeds during exhaust valve actuation, particularly the crank angle range 485°-660° ATDCE, may again be explained by the large exhaust jet flow velocities being better captured in the 400 rpm low spatial resolution measurements.

The Mode 1 ensemble average coefficients during intake valve opening, shown in Figure 4.16, also reflect any differences between the normalized ensemble average flow fields at the different engine speeds during the intake stroke.

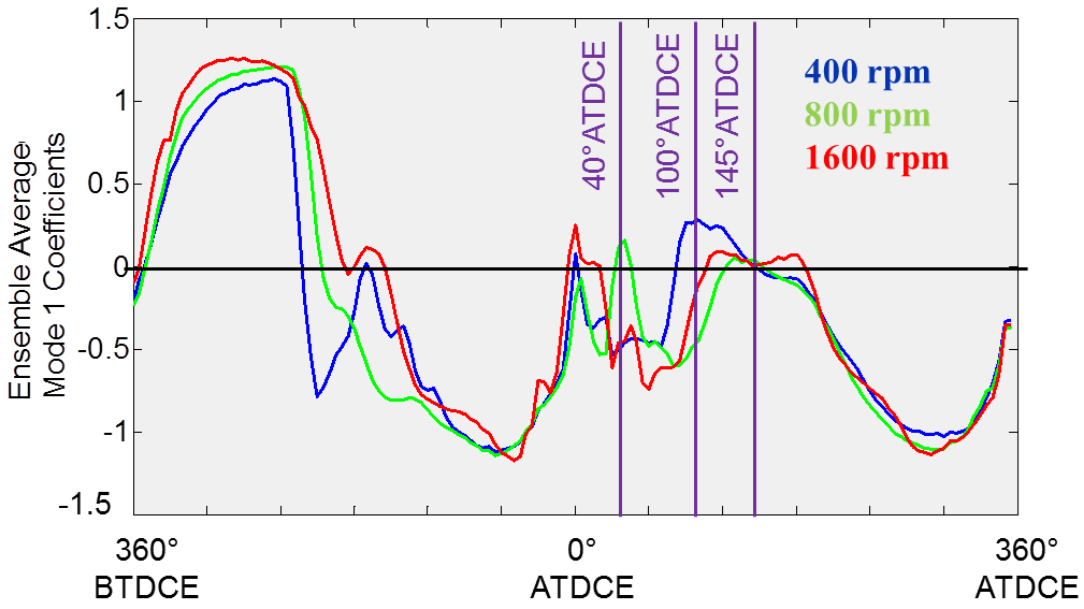

Figure 4.16: *Mode 1 ensemble average coefficients from phase-invariant POD of low spatial resolution 400, 800, and 1600 rpm data (X axis from at TDC compression)*

Three different crank angles in the intake stroke are highlighted in Figure 4.16. At 40° ATDCE, the ensemble average Mode 1 coefficient for the 800 rpm data is positive, unlike the ensemble average coefficients for the 400 and 1600 rpm data sets. The normalized ensemble average flow fields at 40° ATDCE for the three different engine speeds, shown in Figure 4.17, have flow patterns that agree with this POD analysis. At 400 and 1600 rpm, the normalized ensemble average flow fields at 40° ATDCE show a strong upward flow on the right towards the spark plug, while at 800 rpm, the flow on the right is relatively weaker and aimed towards the cylinder wall.

At 100° ATDCE, the ensemble average Mode 1 coefficient for the 400 rpm data is positive and the coefficient for the 800 and 1600 rpm data are negative. As suggested by these coefficients, the normalized ensemble average flow field for the 400 rpm data at 100° ATDCE shows a strong intake jet flow towards the bottom-right of the flow field, while the penetration of

the intake jet into the cylinder is, on average, reduced proportionate to the ensemble average Mode 1 coefficients in the central tumble plane for the 800 and 1600 rpm data. Instead, the normalized ensemble average flow field for both the 800 and 1600 rpm data at 100° ATDCE show an upward flow in the bottom-left corner consistent with the negative ensemble average Mode 1 coefficients. This similarity between the ensemble average 800 and 1600 rpm velocity data at 100° ATDCE reflects the larger cycle-to-cycle differences in valve actuation in these data sets shown in Table 4.2.

At 145° ATDCE, the Mode1 ensemble average coefficients at all three engine speeds are close to zero. Thus, the ensemble average flow fields at 145° ATDCE show a flow pattern unlike that in Mode 1. In fact, these flow fields show the developing large-scale tumble vortex seen in Mode 2. Figure 4.15 shows that the Mode 2 coefficients at 145° ATDCE are similar. This reflects the similarity of the flow structures seen in the ensemble average flow fields.

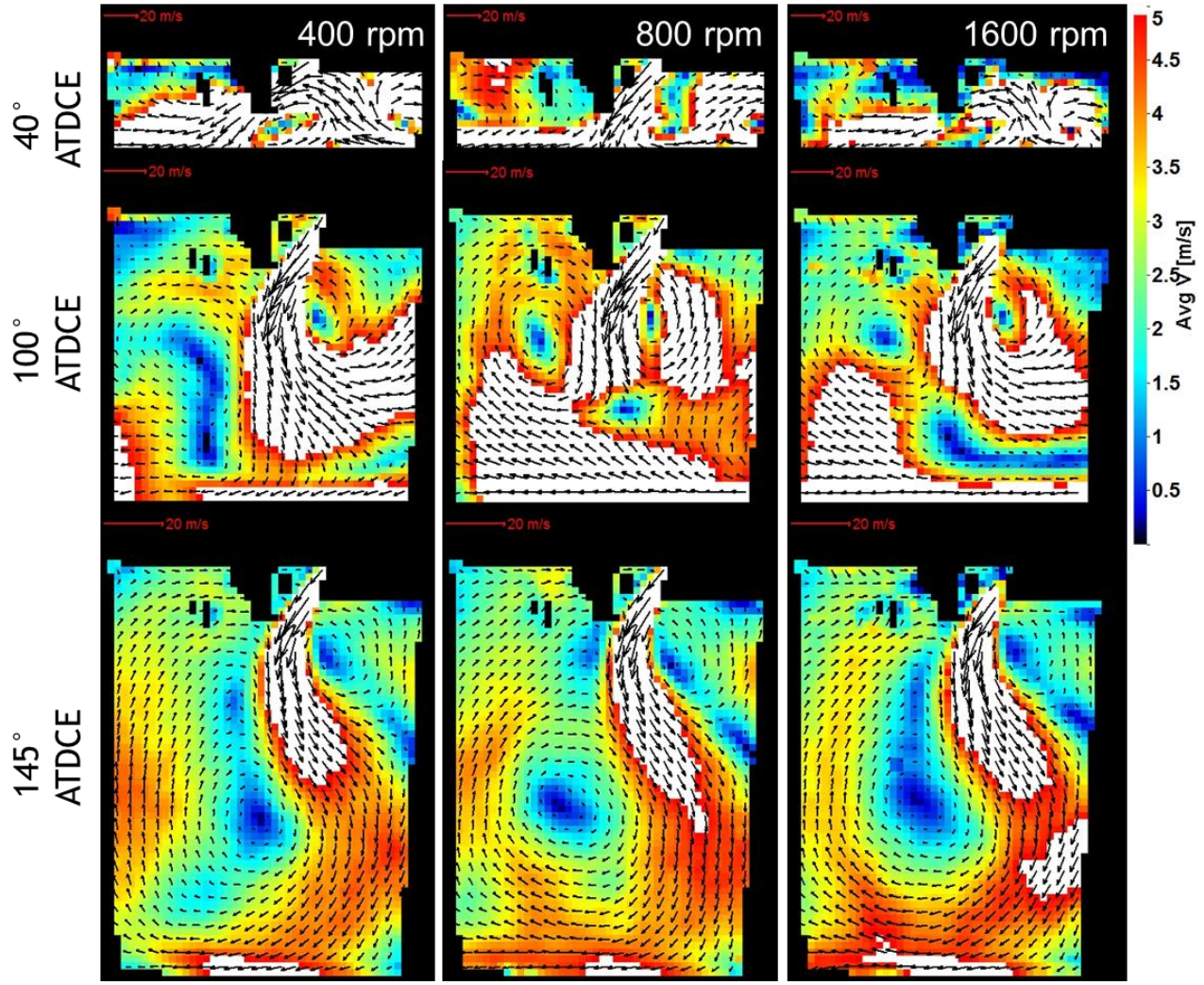

Figure 4.17: *Normalized ensemble average flow fields during the intake stroke at 400, 800, and 1600 rpm. Velocities normalized by mean piston speed.*

4.4 Comparing In-Cylinder Flow Evolution near the Spark Plug

In-cylinder flow near the spark plug may be studied using the high spatial resolution velocity data, whose field-of-view zooms in to view the flow around the spark plug and the valve flow with higher resolution. The relationship between the between the field-of-view of the data analyzed in Section 4.3 and this section is shown in Figure 3.7. An initial assessment of differences in in-cylinder flow near the spark plug at the three different engine speeds studied was made by comparing the spatially summed mass-specific kinetic energies associated with

normalized ensemble average and RMS high spatial resolution velocity fields, as shown in Figure 4.18. The velocities underwent interpolation to ensure a common velocity grid for all three engine runs, as described in Section 4.3, and were normalized by the mean piston speed.

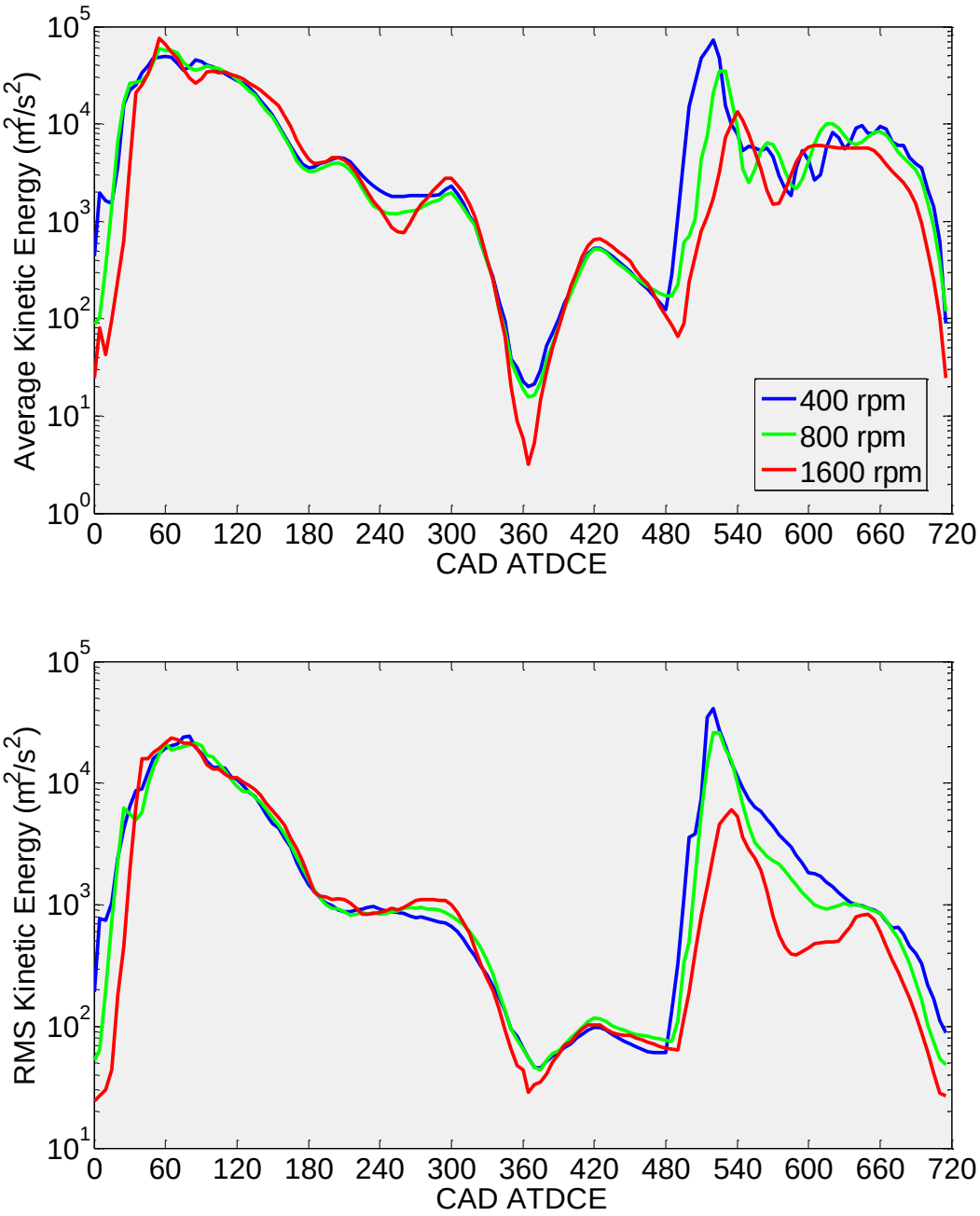

Figure 4.18: *Spatially summed mass-specific kinetic energies of normalized and remapped high spatial resolution ensemble average and RMS velocity fields at 400, 800, and 1600 rpm*

Figure 4.18 agrees with Figure 4.13 in that both the spatial average and RMS kinetic energies during early intake valve opening (15°-60° ATDCE) and exhaust valve actuation (485°-720° ATDCE) scale inversely with engine speed. The scaling of the kinetic energy values from early exhaust valve opening may be a result of the large exhaust jet flow velocities being better captured in the 400 rpm measurements, as described in Section 3.5. The lower kinetic energy values of the 1600 rpm data during early intake valve opening may also be a result of this data set similarly failing to capture the large intake valve flow velocities in the low spatial resolution measurements.

Phase-invariant POD with unity kinetic energy normalization was used to compare in-cylinder flow evolution at 400, 800, and 1600 rpm and to assess differences in flow structures near the spark plug at the different engine speeds. The first three modes from the analysis are presented in Figure 4.19.

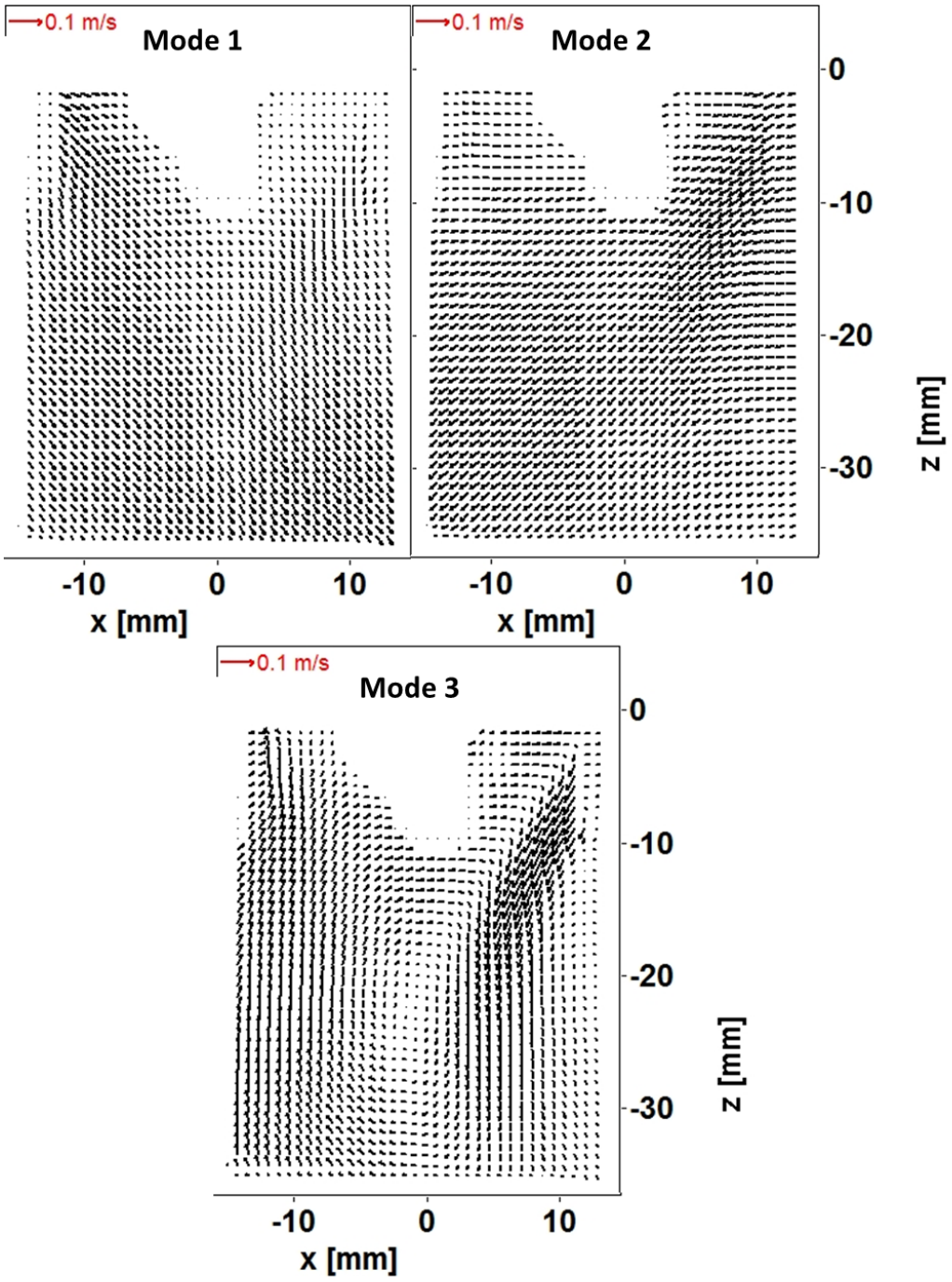

Figure 4.19: *First three modes from phase-invariant POD of high spatial resolution 400, 800, and 1600 rpm data*

Mode 1, with an overall energy fraction of 28%, shows a piston-induced in-cylinder flow pattern. Mode 2, with an overall energy fraction of 20%, shows flow towards the bottom-left of the

cylinder. Mode 3, with an overall energy fraction of 7%, shows a large-scale tumble vortex and aspects of an intake jet. These modes are similar to the first three modes from the phase-invariant POD analysis of the low spatial resolution, full field-of-view data. Figure 4.20 presents the coefficients associated with these three modes as a function of crank angle for all the cycles analyzed.

The Mode 1 coefficients shown in Figure 4.20 are similar and show trends similar to those seen in the Mode 1 coefficients in Figure 4.15, further emphasizing the similarity between the first modes from the phase invariant POD analysis of the low and high spatial resolution data despite the difference in fields-of-view. Mode 2 from the high spatial resolution analysis is also similar to Mode 3 from the low spatial resolution analysis. The restricted field-of-view of the high spatial resolution data results in the first two modes showing flow from the region of the valves towards the bottom of the field-of-view. The large-scale tumble vortex seen in Mode 2 of the low spatial resolution analysis is seen only in Mode 3 of the high spatial resolution analysis, along with aspects of the intake jet flow. This is because the tumble vortex, which develops towards BDC of the intake stroke and scales with piston position relative to the cylinder head during the intake stroke, is not fully captured in the field-of-view of the high spatial resolution measurements, making it a less prominent part of the high spatial resolution PIV data. The Mode 3 coefficients reflect this, with the values increasing from approximately 90°-160° ATDCE and then decreasing.

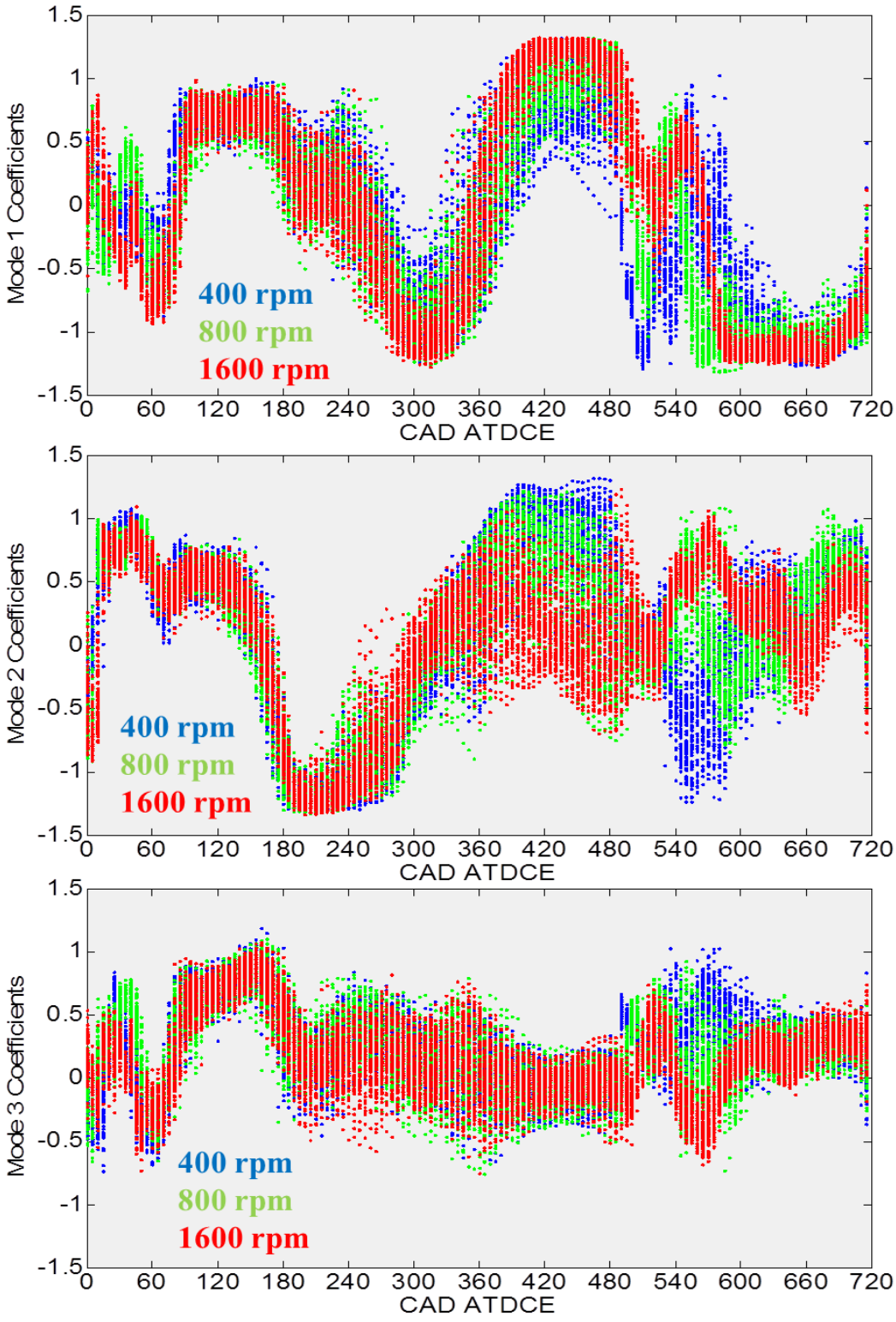

Figure 4.20: *Coefficients of the first three modes from phase-invariant POD of high spatial resolution 400, 800, and 1600 rpm data*

4.5 In-Cylinder Flow at 100° ATDCE

To better understand differences in in-cylinder flow caused by changing engine speeds and intake valve oscillations, low spatial resolution flow fields at 100° ATDCE from S_2012_06_25_01, S_2012_06_21_01, and S_2012_06_27_02 were analyzed using phase-dependent POD. The flow fields were interpolated onto a common grid and normalized by mean piston speed before the analysis. The first two modes from the decomposition are presented in Figure 4.21.

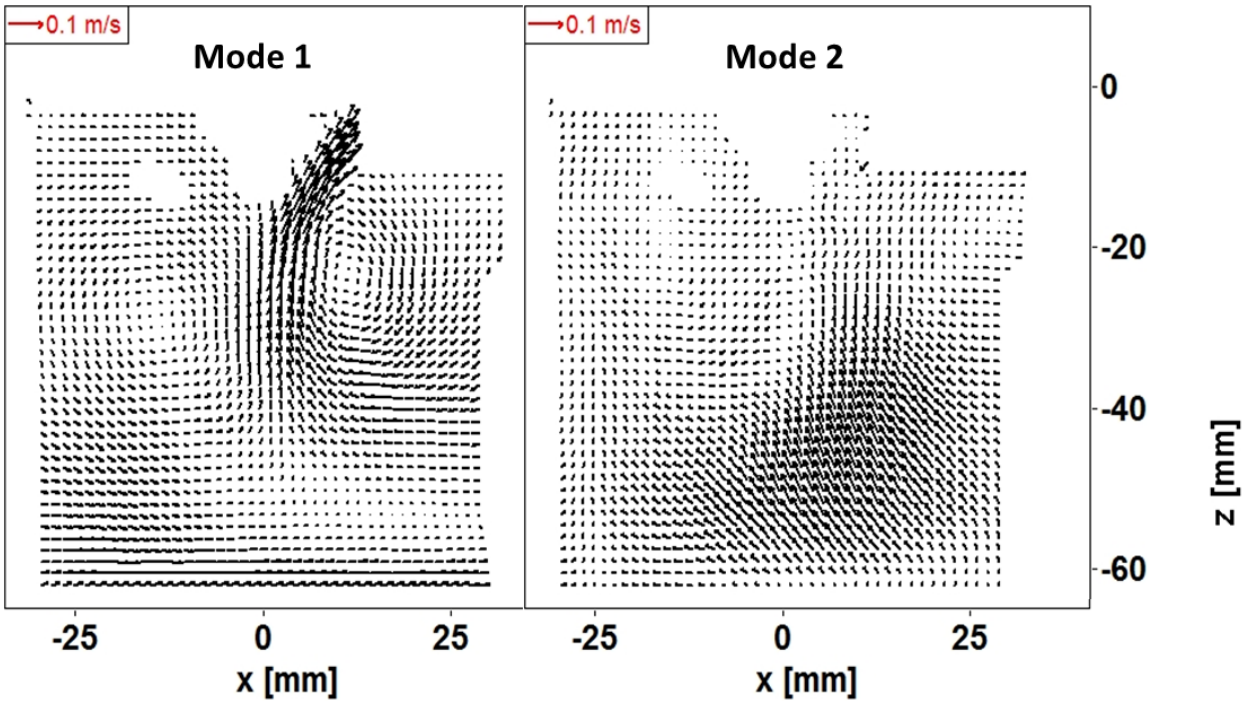

Figure 4.21: *First two modes from phase-dependent POD analysis of low spatial resolution 400, 800, and 1600 rpm data at 100° ATDCE*

Mode 1, with an energy fraction of 56%, contains aspects of the intake jet and the associated counter-rotating vortices. Mode 2, with an energy fraction of 11%, shows an upward flow from the bottom-right corner of the field-of-view. The energy fractions of higher order modes were less than 3% each. Figure 4.22 presents the coefficients associated with Modes 1 and 2.

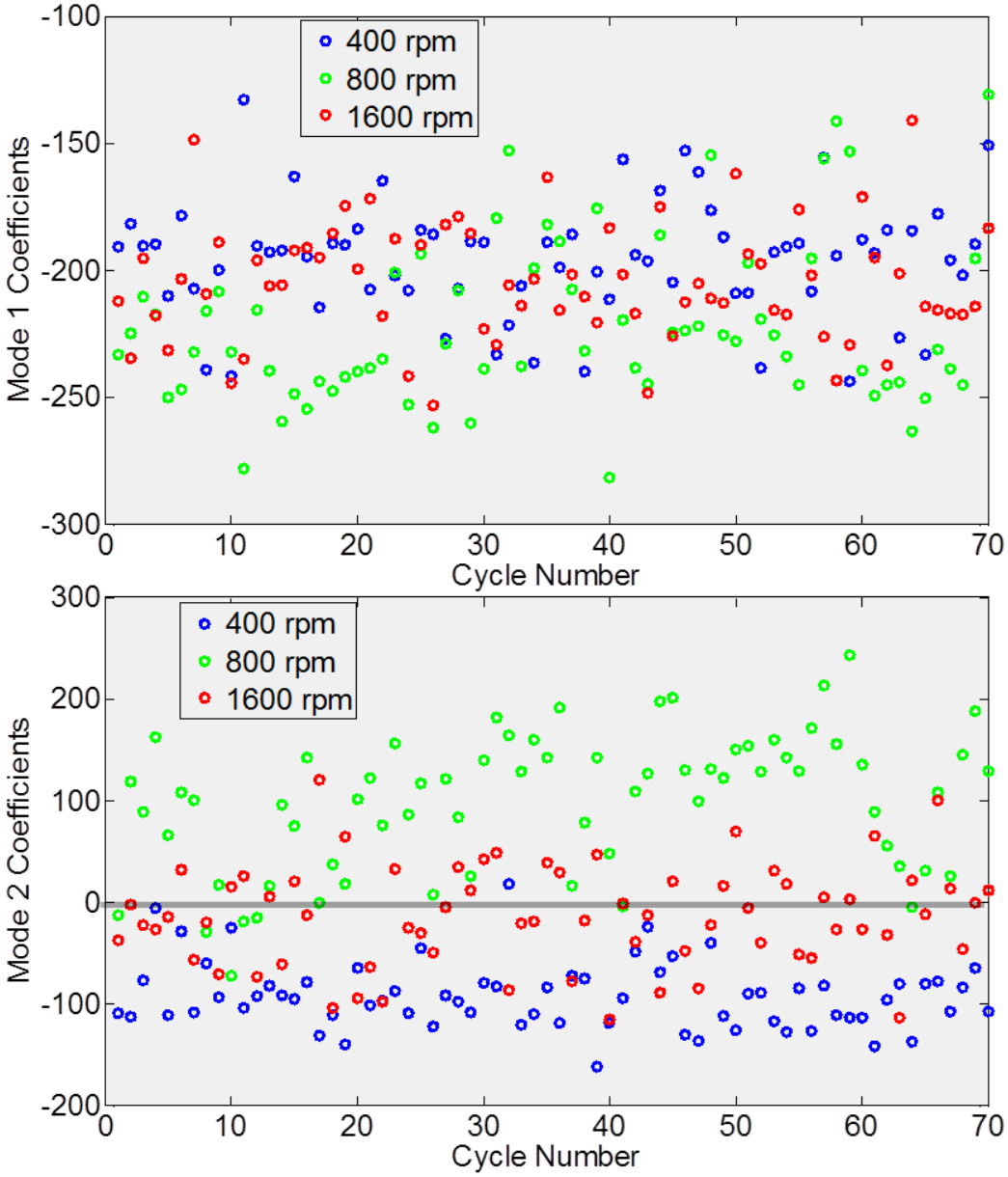

Figure 4.22: *Coefficients of the first two modes from phase-dependent POD analysis of low spatial resolution 400, 800, and 1600 rpm data at 100° ATDCE*

The Mode 1 coefficients for all three engine speeds are similar, but the Mode 2 coefficients show a directional divide between engine speeds. The 800 rpm Mode 2 coefficients are predominantly positive, indicating that most cycles from this data set have upward flow from the bottom-right corner of the field-of-view. On the hand, the 400 rpm Mode 2 coefficients are predominantly

negative, indicating that most cycles from this data set have downward flow towards the bottom-right corner. The 1600 rpm Mode 2 coefficients have values distributed about zero, which reflects the small vectors in the bottom-right corner in the 100° ATDCE ensemble average for 1600 rpm (see Figure 4.17).

Phase-dependent POD coefficients can also be used to quantify cycle-to-cycle variability in the kinetic energy contributions of the mean flow and the turbulent flow to individual velocity fields by establishing Mode 1, or a combination of lower order modes, as an estimate of the mean flow, and higher order modes as an estimate of turbulence [17, 18]. Mode 1 was compared to the mean flow at 100° ATDCE by calculating relevance indices. The absolute value of the relevance index between the 400 rpm data set and Mode 1 was less than 0.90, indicating that Mode 2 should be added to Mode 1 to estimate the mean flow adequately. The relevance indices between the mean flows and the summation of Modes 1 and 2, weighted by their average coefficients for a particular data set, were all above 0.90. These relevance indices are documented in Table 4.4.

	Mode 1	Modes 1 and 2
S_2012_06_25_01, 400 rpm	-0.895	0.989
S_2012_06_21_01, 800 rpm	-0.910	0.995
S_2012_06_27_02, 1600 rpm	-0.973	0.975

Table 4.4: *Relevance indices between Modes 1 and 2 and ensemble average velocities from low spatial resolution 400, 800, and 1600 rpm data at 100° ATDCE*

Figure 4.23 estimates the cycle-to-cycle variability in the contribution of the mean flow and the RANS turbulence to each cycle in the data sets S_2012_06_25_01, S_2012_06_21_01, and S_2012_06_27_02.

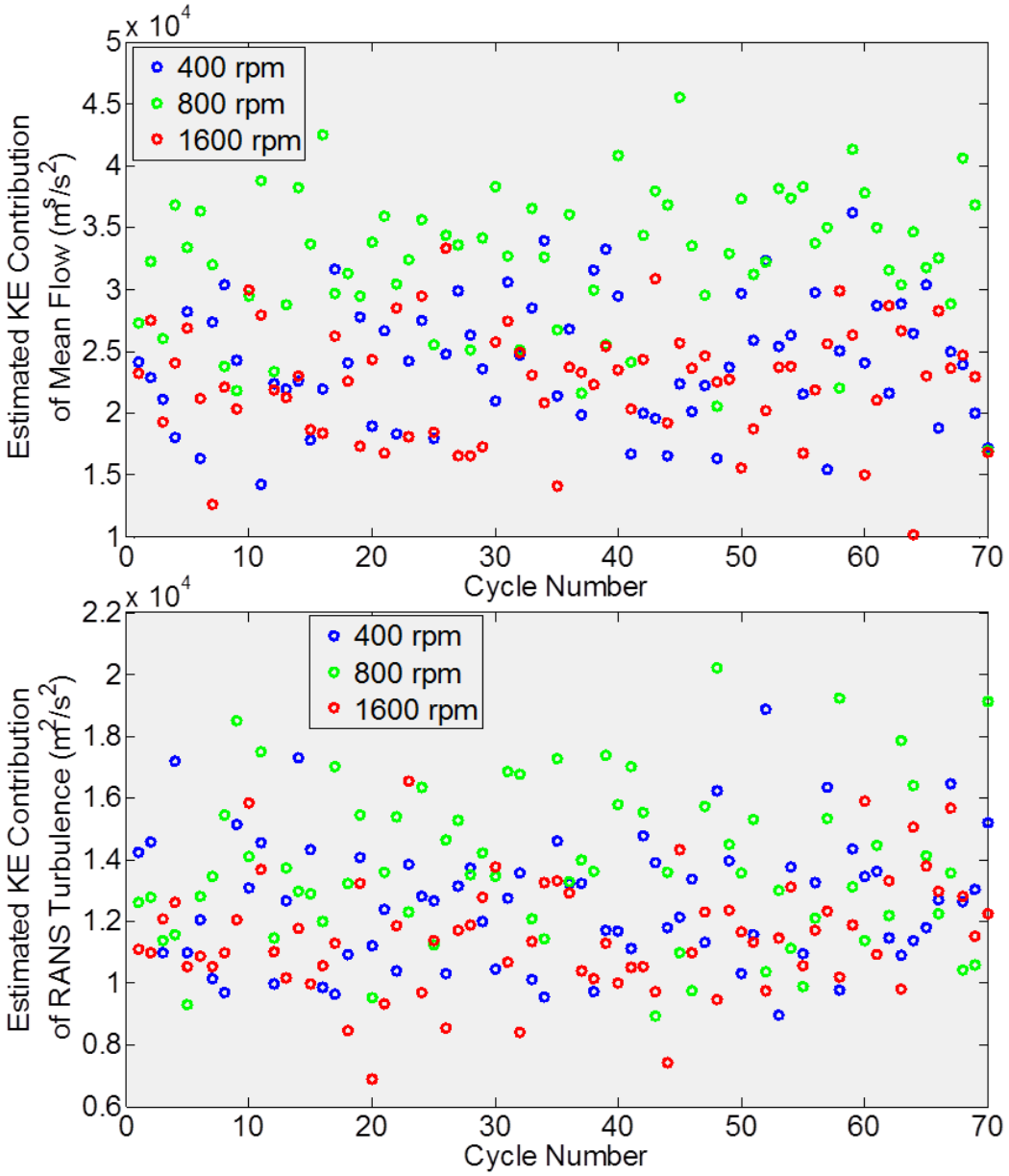

Figure 4.23: *Estimated mass-specific kinetic energy contributions of the ensemble average and fluctuating flow to low spatial resolution 400, 800, and 1600 rpm data at 100° ATDCE*

Figure 4.23 shows that the 800 rpm data set, with cycle-to-cycle variations in the intake valve position along the X axis at 100° ATDCE, has larger estimated kinetic energy contributions from the mean flow than the other two data sets presented here. The distribution of the estimated turbulent kinetic energy is similar for all three data sets.

4.6 In-Cylinder Flow at 300° ATDCE

Low spatial resolution PIV data acquired at 300° ATDCE and engine speeds of 400, 800, and 1600 rpm were analyzed using phase-dependent POD to better understand differences in in-cylinder flow during the compression stroke due to changing engine speed and differences in intake valve actuation. The flow fields were interpolated onto a common grid and normalized by mean piston speed before the analysis. The first three modes from the decomposition are presented in Figure 4.24.

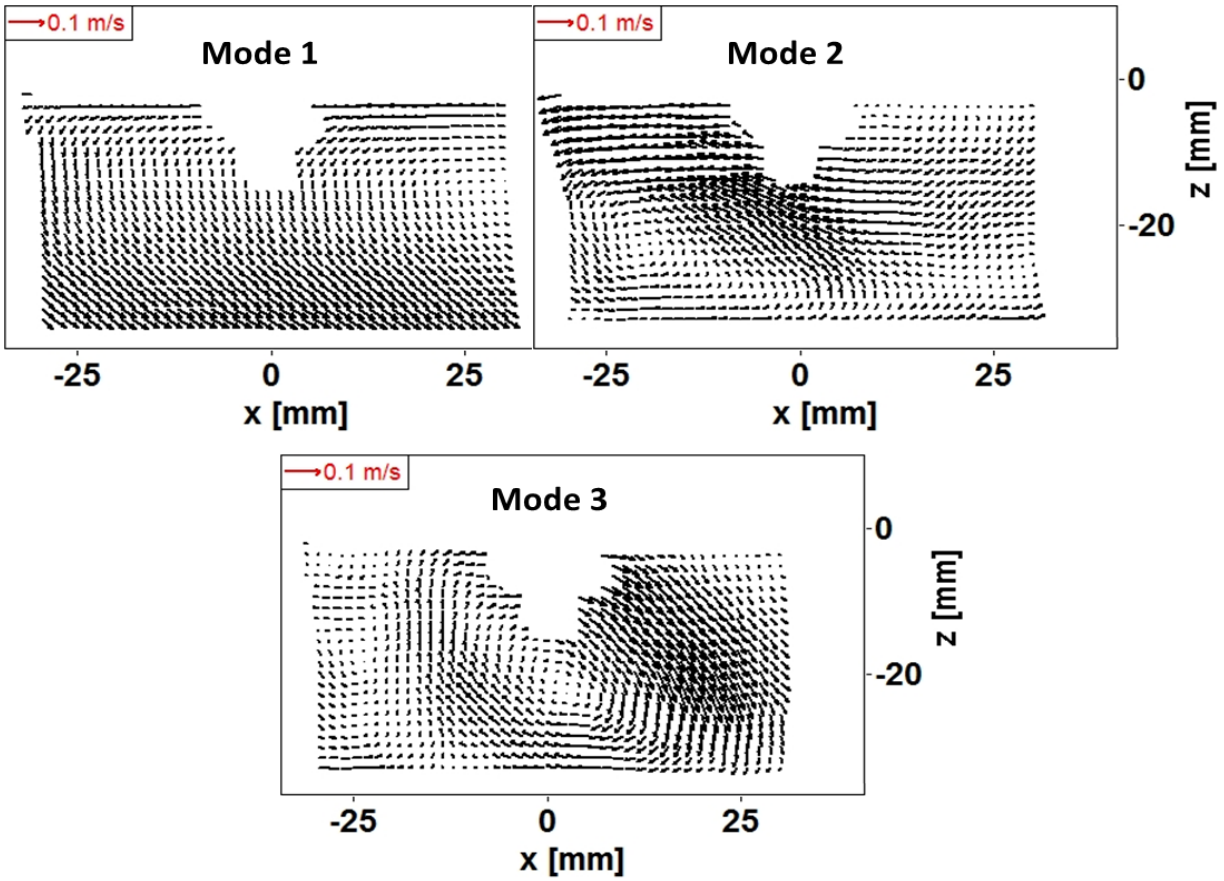

Figure 4.24: *First three modes from phase-dependent POD analysis of low spatial resolution 400, 800, and 1600 rpm data at 300° ATDCE*

Mode 1, with an energy fraction of 74%, shows piston-driven flow. Mode 2, with an energy fraction of 4%, shows a vortex towards the lower left of the field-of-view. Mode 3, with an

energy fraction of 3%, contains a vortex immediately below the spark plug. Figure 4.21 show the coefficients associated with these modes.

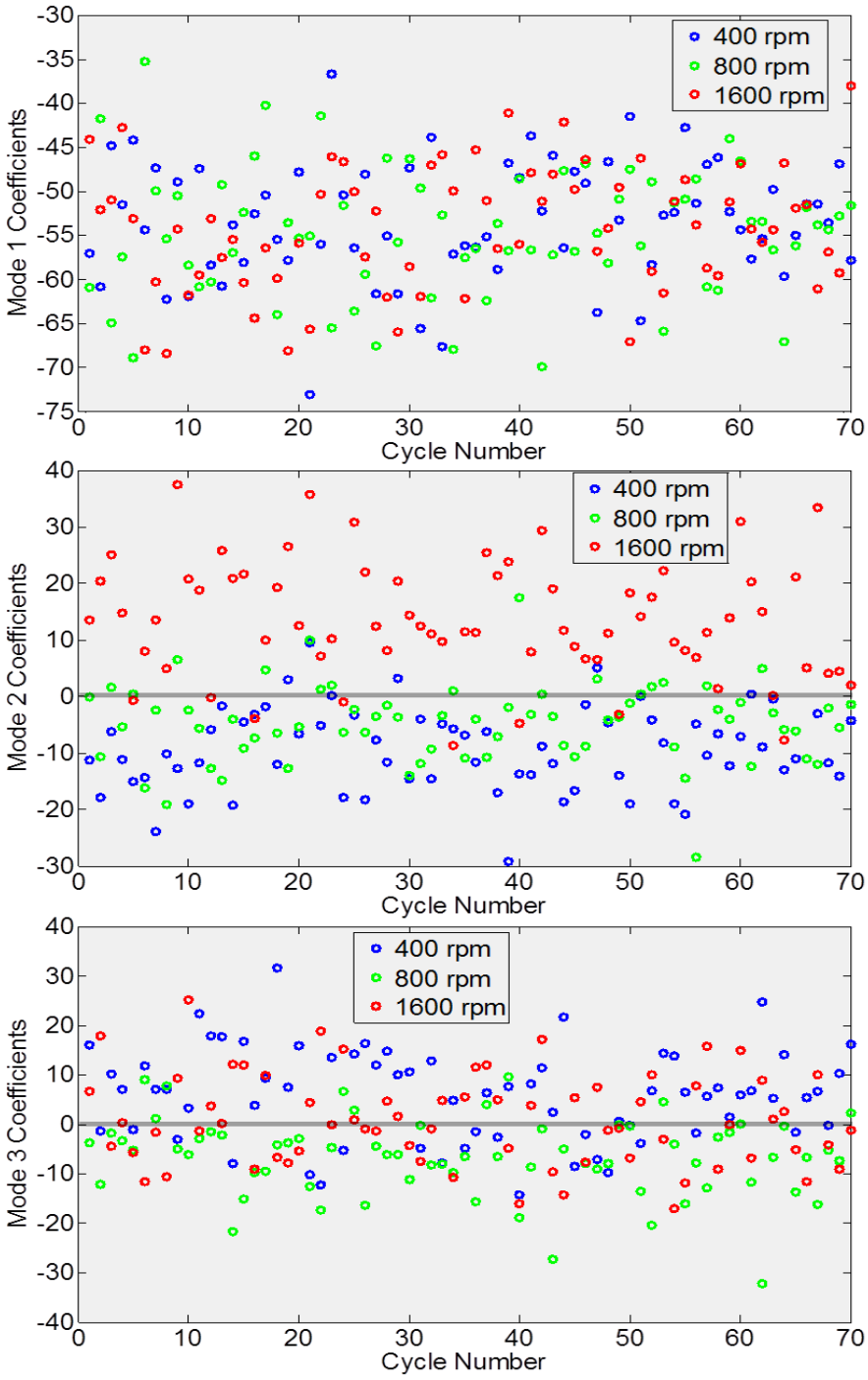

Figure 4.25: *Coefficients of the first three modes from phase-dependent POD analysis of low spatial resolution 400, 800, and 1600 rpm data at 300° ATDCE*

Figure 4.25 shows that the Mode 1 coefficient distribution is similar for all three data sets analyzed. There is a clear demarcation between the 1600 rpm Mode 2 coefficients and the rest of the Mode 2 coefficients, with the 1600 rpm coefficients being predominantly positive. This may indicate a difference in the flow pattern at 300° ATDCE at higher engine speeds. The Mode 3 coefficients of the 800 rpm data are predominantly negative, which indicates a difference in flow pattern that may be due to the cycle-to-cycle variation in intake valve position along the X axis seen in this data set. The contribution of Modes 2 and 3 to the flow pattern in a flow field is on average small, given the low energy fractions associated with them.

Mode 1 was compared to the mean flow of all three data sets using relevance indices to assess its value as an estimate of the mean flow. The relevance indices calculated were all found to have an absolute value above 0.96, indicating that Mode 1 is a good estimate of the mean flow at all three engine speeds. The higher order modes provide an estimate of the RANS turbulence. Figure 4.26 shows the estimated mass-specific kinetic energy contribution of the mean and turbulent flows to individual flow fields at 300° ATDCE.

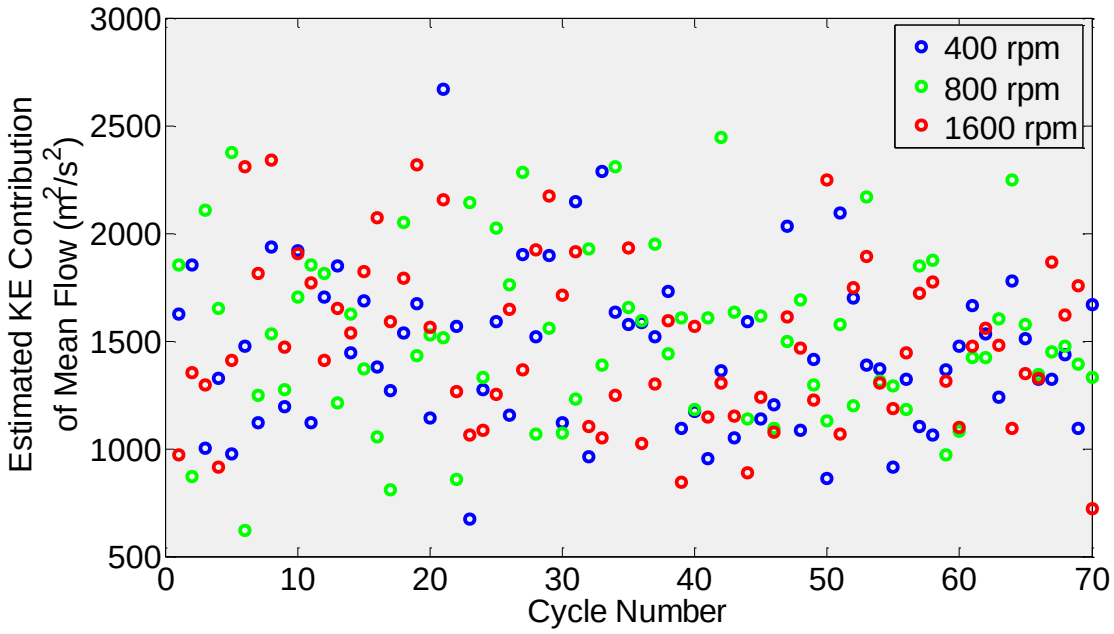

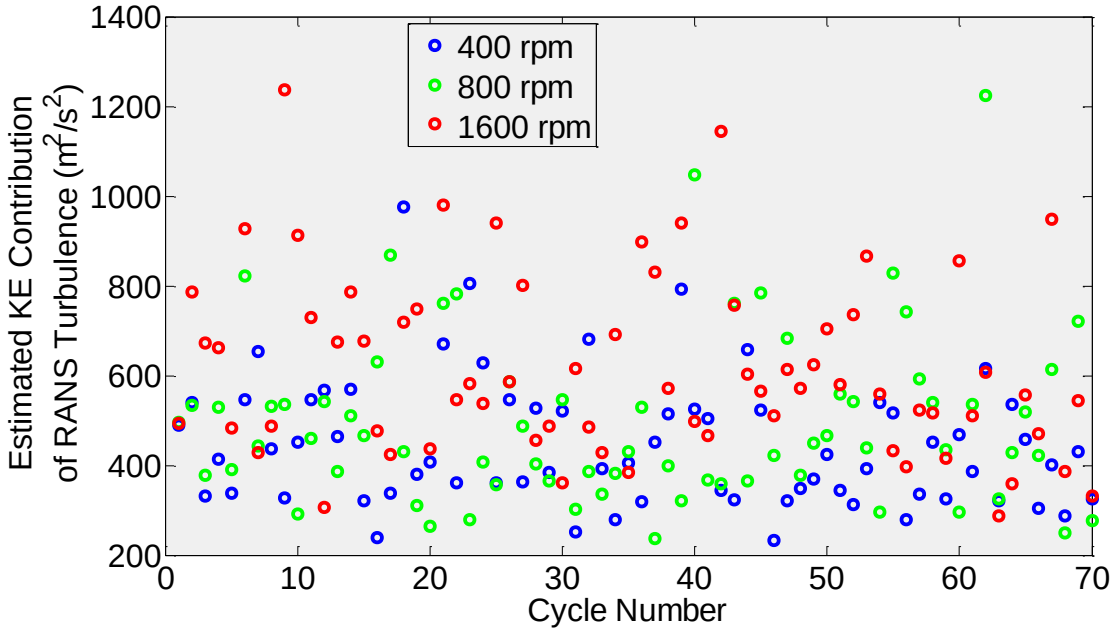

Figure 4.26: *Estimated mass-specific kinetic energy contributions of the ensemble average and fluctuating flow to low spatial resolution 400, 800, and 1600 rpm data at 300° ATDCE*

Figure 4.26 shows that the estimated mass-specific kinetic energy contribution of the mean and turbulent flow are similar magnitude and distribution for the data sets from all three engine speeds.

4.7 Summary

This chapter compares engine data acquired at 400, 800, and 1600 rpm with equivalent pressure boundary conditions to verify the scaling of in-cylinder flow evolution, mean flow and cycle-to-cycle flow variations with engine speed. The scaling with engine speed of in-cylinder and intake and exhaust system pressures was also investigated. A phase-invariant POD analysis of all three data sets revealed that in-cylinder flow evolution changes predictably with engine speed. Phase-invariant POD coefficients from the intake stroke and a phase-dependent POD analysis at 100° ATDCE showed that the in-cylinder flow during intake valve opening in the 800 rpm data set was different from that seen in the other two data sets. This difference can be

attributed to an increased cycle-to-cycle variability in intake valve operation during the intake stroke in the 800 rpm data. However, the phase-dependent POD analysis at 300° ATDCE showed no conclusive differences between the 800 rpm data and the other two data sets.

CHAPTER 5

EFFECT ON INTAKE VALVE MOTION ON IN-CYLINDER FLOW AT 800 RPM

Three PIV data sets acquired at 800 rpm were compared in this chapter to better understand the differences in dominant intake flow patterns and evolution between data sets seen in the previous chapter. Differences in valve operation between these data sets were studied as a potential source of the in-cylinder flow variations.

5.1 Comparing Engine Operation and In-Cylinder, Intake, and Exhaust System Pressures

In order to compare in-cylinder flow from different engine runs at 800 rpm, it is necessary to first quantify the differences in engine operation for the different data sets. Figure 5.1 shows the variations in engine speed and the cycle average pressure at the intake plenum inlet with cycle number for the three data sets discussed in this chapter.

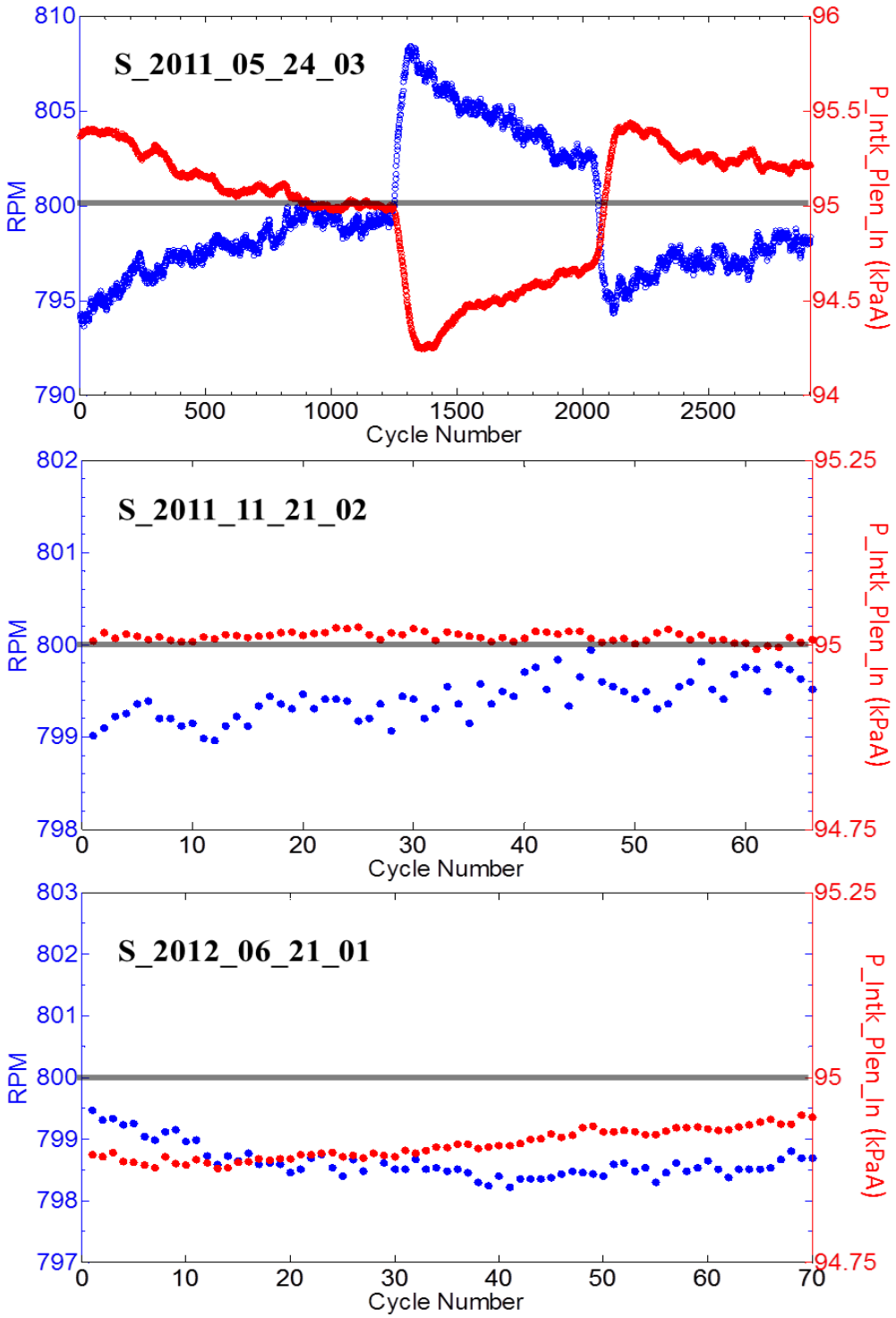

Figure 5.1: *Engine speed and intake plenum inlet pressure for S_2011_05_24_03, S_2011_11_21_02, and S_2012_06_21_01. (Engine operation setpoints are marked by grey lines.)*

Figure 5.1 shows that S_2011_05_24_03 experienced engine speed and, subsequently, intake pressure transients due to dynamometer operation errors. This data set, despite unstable engine operation, is included in this chapter to provide additional data for flow structure comparisons at 100° ATDCE. RPM and intake plenum inlet average pressure data from S_2011_11_21_02 and S_2012_06_21_01 are evidence of stable engine operation, with no more than 0.25% difference between the desired and actual values.

Figure 5.2 shows the in-cylinder pressure as a function of volume for all cycles as well as the standard deviation of the in-cylinder pressure throughout the cycle for all three data sets.

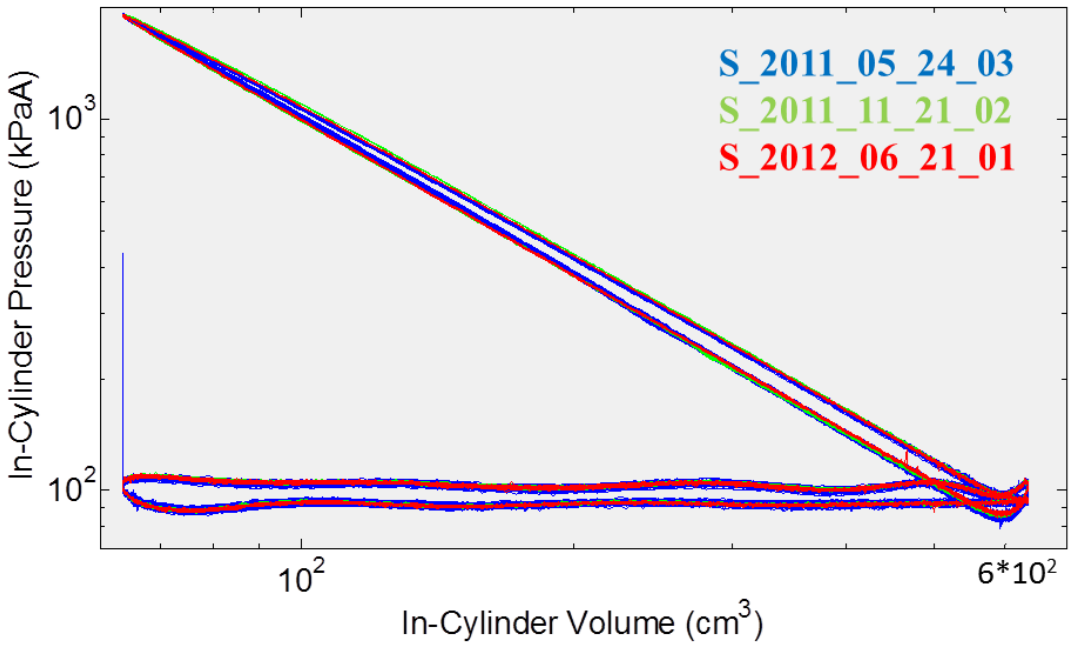

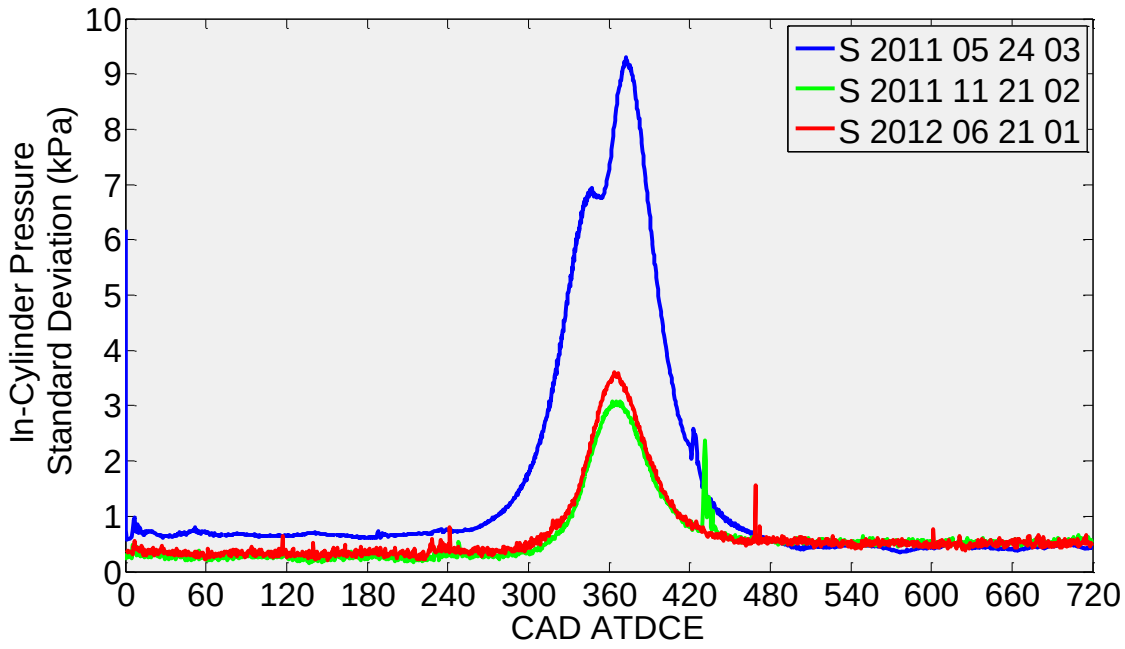

Figure 5.2: *In-cylinder log P – log V graph for all cycles and standard deviation for in-cylinder pressure in S_2011_05_24_03, S_2011_11_21_02, and S_2012_06_21_01*

Figure 5.2 shows that the log P – log V graphs for all three data sets overlap despite the dissimilarity in engine operating conditions for both data sets. However, the standard deviation in in-cylinder pressure is much higher for S_2011_05_24_03 due to the engine speed and intake pressure transients in that data set.

Figure 5.3 shows the crank angle resolved intake plenum inlet (P Intk Plen In), intake runner (P Intk Port), exhaust runner (P Exh Port), and exhaust plenum outlet (P Exh Plen Out) pressures for all cycles in all three data sets.

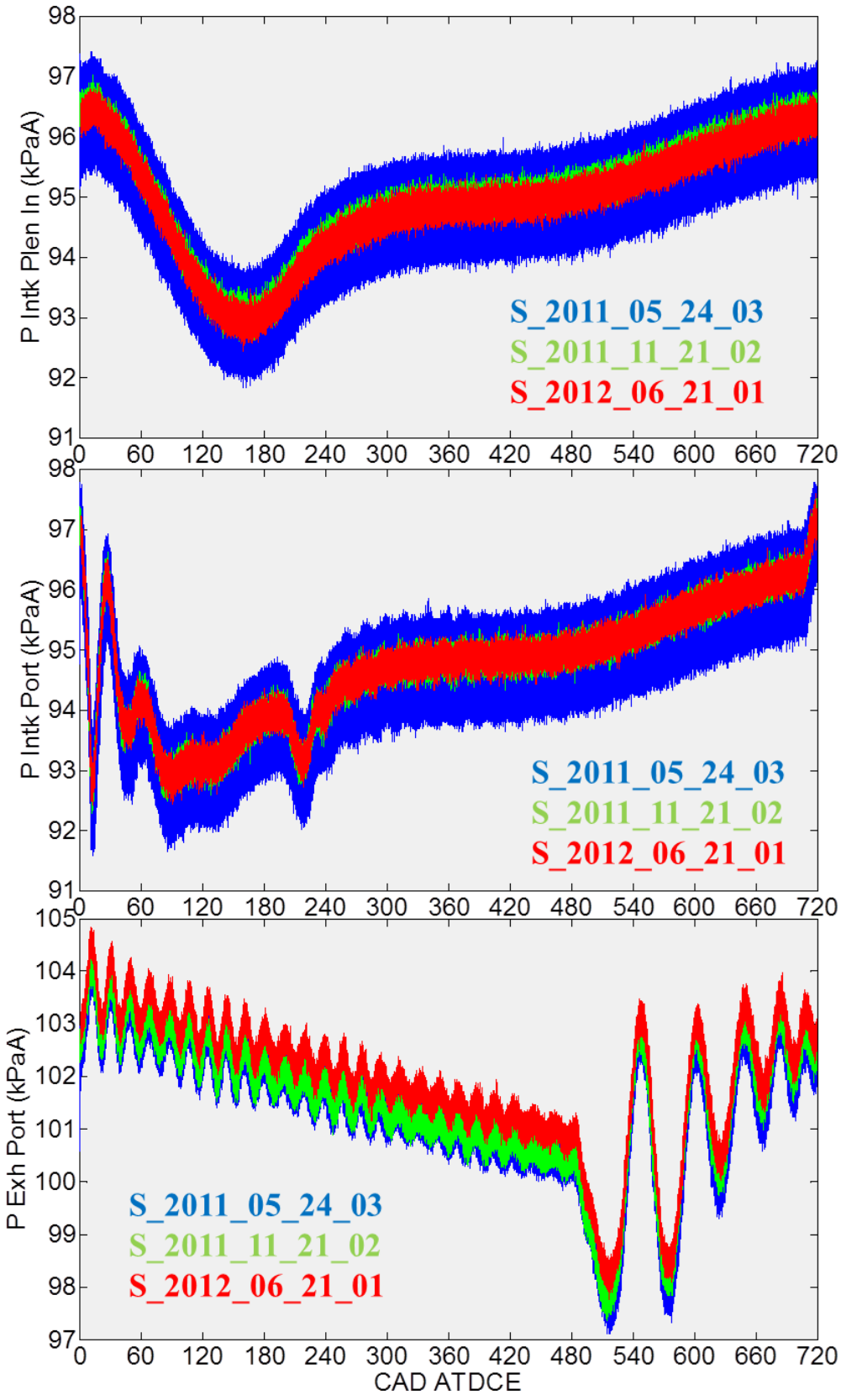
P Intk Plen In (kPaA)
P Intk Port (kPaA)
P Exh Port (kPaA)
CAD ATDCE
S_2011_05_24_03
S_2011_11_21_02
S_2012_06_21_01

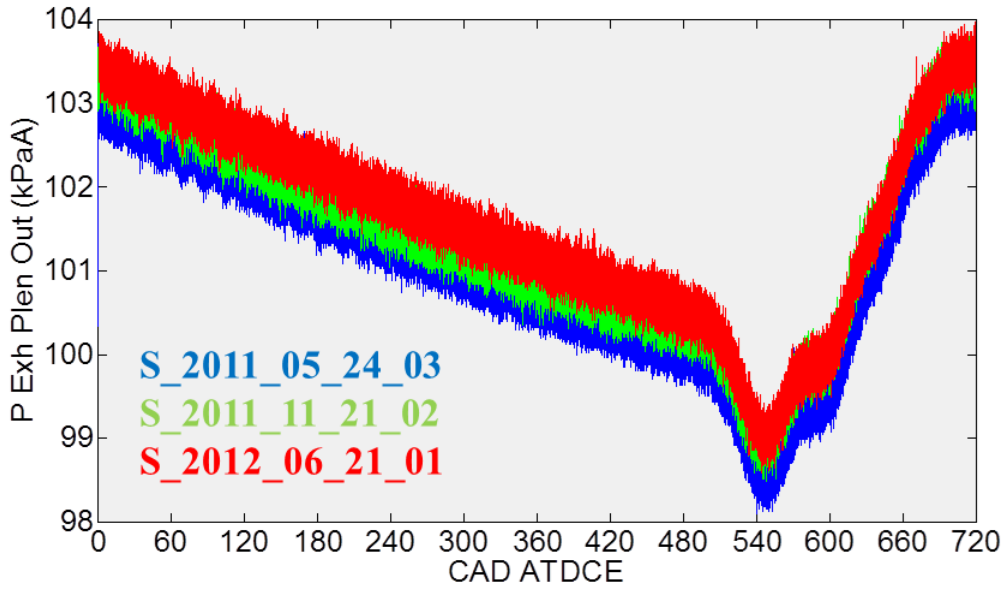

Figure 5.3: *Crank angle resolved intake and exhaust system pressure data for all cycles from S_2011_05_24_03, S_2011_11_21_02, and S_2012_06_21_01*

Figure 5.3 shows that S_2011_05_24_03, S_2011_11_21_02, and S_2012_06_21_01have similar pressure wave patterns at all four measurement points. In fact, pressure data from the intake system from S_2011_11_21_02 and S_2012_06_21_01 overlap almost completely. However, the pressure in the exhaust system is higher for S_2012_06_21_01. The pressure data from S_2011_05_24_03 has greater spread due to the unstable engine operating conditions.

5.2 Cycle-to-Cycle Variability in Intake Valve Actuation

Cycle-to-cycle variation in valve actuation in the data sets presented in this chapter is quantified in order to assess its effect on cycle-to-cycle flow variations. The calibrated high spatial resolution PIV images from the data sets discussed in this chapter were examined at different crank angles to determine differences in valve location at certain crank angles through a data set. At a particular crank angle, the locations of the valve edges are tracked from cycle to cycle by calculating and comparing the maximum and minimum intensities at each pixel in the PIV images. This process is described in greater detail in Section 4.2. The displacements along

the X and Z axes between extreme valve positions during early intake valve opening and at 100° ATDCE are presented in Table 5.1.

	CAD ATDCE	dx (mm)	dz (mm)
S_2011_05_24_03, Cycles 201-266	100	0.00	0.00
S_2011_05_24_03, Cycles 2501-2566	100	0.24	0.00
S_2011_11_21_02	6	0.00	0.14
	100	0.00	0.14
S_2012_06_21_01, Cycles 1-66	5	0.20	0.05
	100	0.15	0.10

Table 5.1: *Variability in intake valve position along X and Z axes*

The cells in Table 5.1 that are not highlighted show displacements of 1 pixel or less. Due to cycle-to-cycle variations in laser light reflection from the valves, it is not possible to resolve such small displacements with any certainty. However, the highlighted cells in Table 5.1 show clearly that the intake valve position in the later subset of S_2011_05_24_03 and in a subset of S_2012_06_21_01 vary from cycle to cycle.

Within a cycle, valve oscillations were assessed by calculating the maximum pixel intensities through valve opening and closing. As the valve image is of high intensity, this captures valve position at different crank angles in one image and enables the tracing of the position of the valve edge during valve opening or closing. This process is described in greater detail in Section 4.2. The displacement along the X axis between extreme intake valve positions during valve opening and closing for S_2011_11_21_02 and S_2012_06_21_01are presented in Table 5.2.

	Cycle Number	Intk. Valve Opening	Intk. Valve Closing
S_2011_11_21_02	12	0.14 mm	0.14 mm
	40	0.14 mm	0.14 mm
	53	0.14 mm	0.14 mm
S_2012_06_21_01	15	0.20 mm	0.20 mm
	50	0.25 mm	0.15 mm
	65	0.20 mm	0.15 mm

Table 5.2: *Intake valve motion during a cycle along the X axis*

In Table 5.2, there is a difference in spatial resolution between S_2011_11_21_02 (0.14 mm/pixel) and S_2012_06_21_01 (0.05 mm/pixel). It is not possible to distinguish between cycle-to-cycle variations in laser light reflections and actual valve oscillation in S_2011_11_21_02 with the lower spatial resolution images. However, the higher spatial resolution data from S_2012_06_21_01 clearly demonstrates valve oscillation with displacements ranging from 3 to 5 pixels.

5.3 Comparing In-Cylinder Flow Evolution

In this section, velocity data from the intake and exhaust strokes (0°-360° ATDCE) from S_2011_11_21_02 and S_2012_06_21_01 are compared. As S_2011_11_21_02 had a lower spatial resolution than the low spatial resolution data from S_2012_06_21_01, the velocity data from both data sets were interpolated onto a common grid with the same spatial resolution as S_2011_11_21_02. A point on the common grid at a particular crank angle was populated only if there were at least three surrounding non-zero vectors available on the grids at that crank angle from each data set for the interpolation at that point. As an initial assessment, the spatially summed kinetic energy associated with the ensemble average and RMS velocity fields of these interpolated data sets are compared in Figure 5.4.

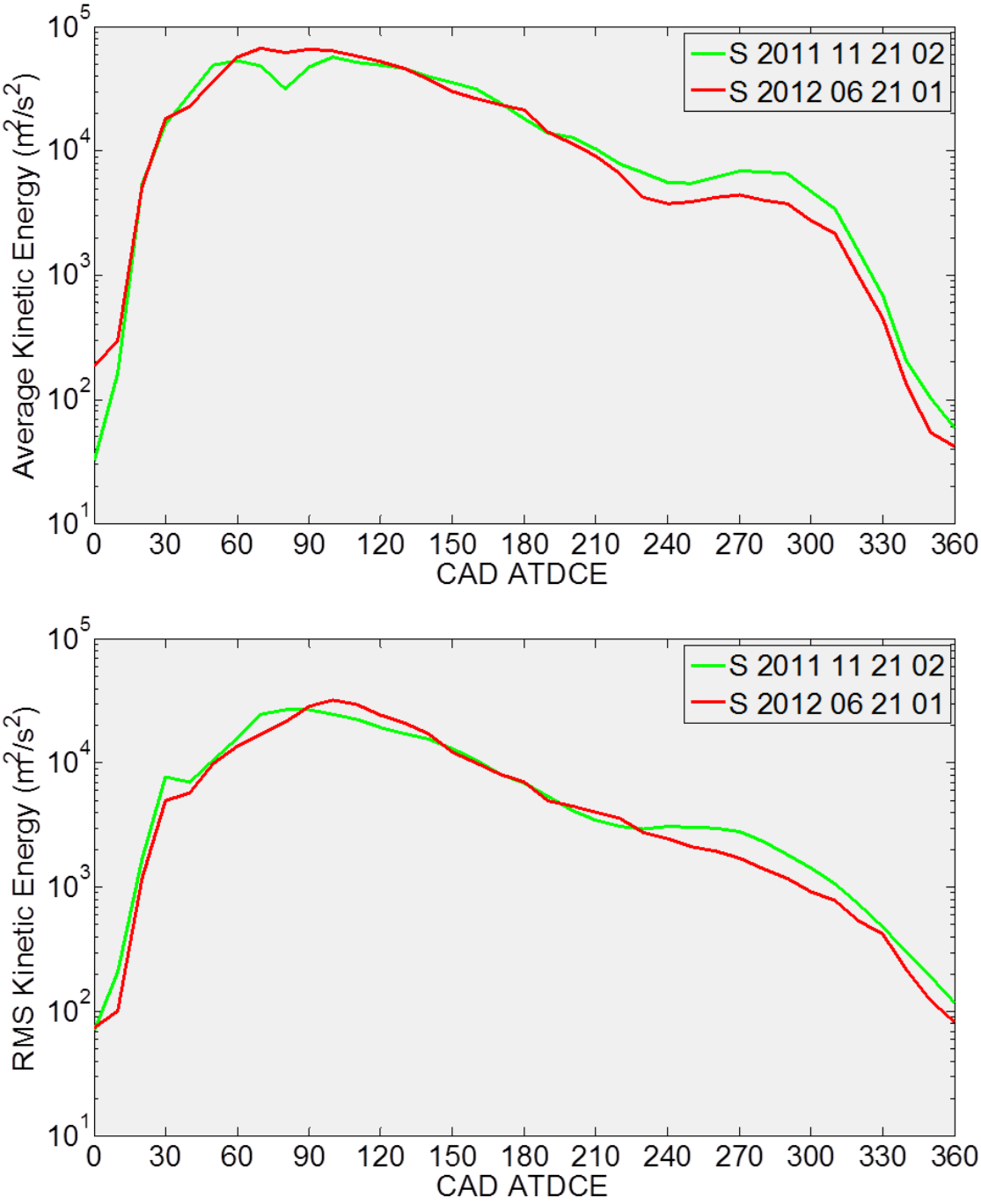

Figure 5.4: *Spatially summed mass-specific kinetic energies of ensemble average and RMS remapped velocity fields from S_2011_11_21_02 and S_2012_06_21_01*

Figure 5.4 shows that the kinetic energy values from both data sets match well during the intake stroke, but, in the compression stroke, S_2011_11_21_02 shows higher kinetic energy in both

ensemble average and RMS velocity fields than S_2012_06_21_01. This is because the PIV data in S_2011_11_21_02 were acquired with a constant time separation (dt) that was optimized for the high intake jet velocities, while S_2012_06_21_01 used variable dts to better accommodate the smaller range of velocity magnitudes seen in the compression stroke. More details were presented in Section 3.5.

Phase-invariant POD with unity kinetic energy normalization was used to compare in-cylinder flow evolution and assess differences in flow structure during the intake and compression strokes in S_2011_11_21_02 and S_2012_06_21_01. The unity kinetic energy normalization used accounts for the bias introduced by the constant dt used in S_2011_11_21_02. Velocity data obtained every 10° from 0° to 360° ATDCE was analyzed. All 66 cycles from S_2011_11_21_02 and the first 66 cycles from S_2012_06_21_01 were analyzed. The first three modes from the analysis are presented in Figure 5.5.

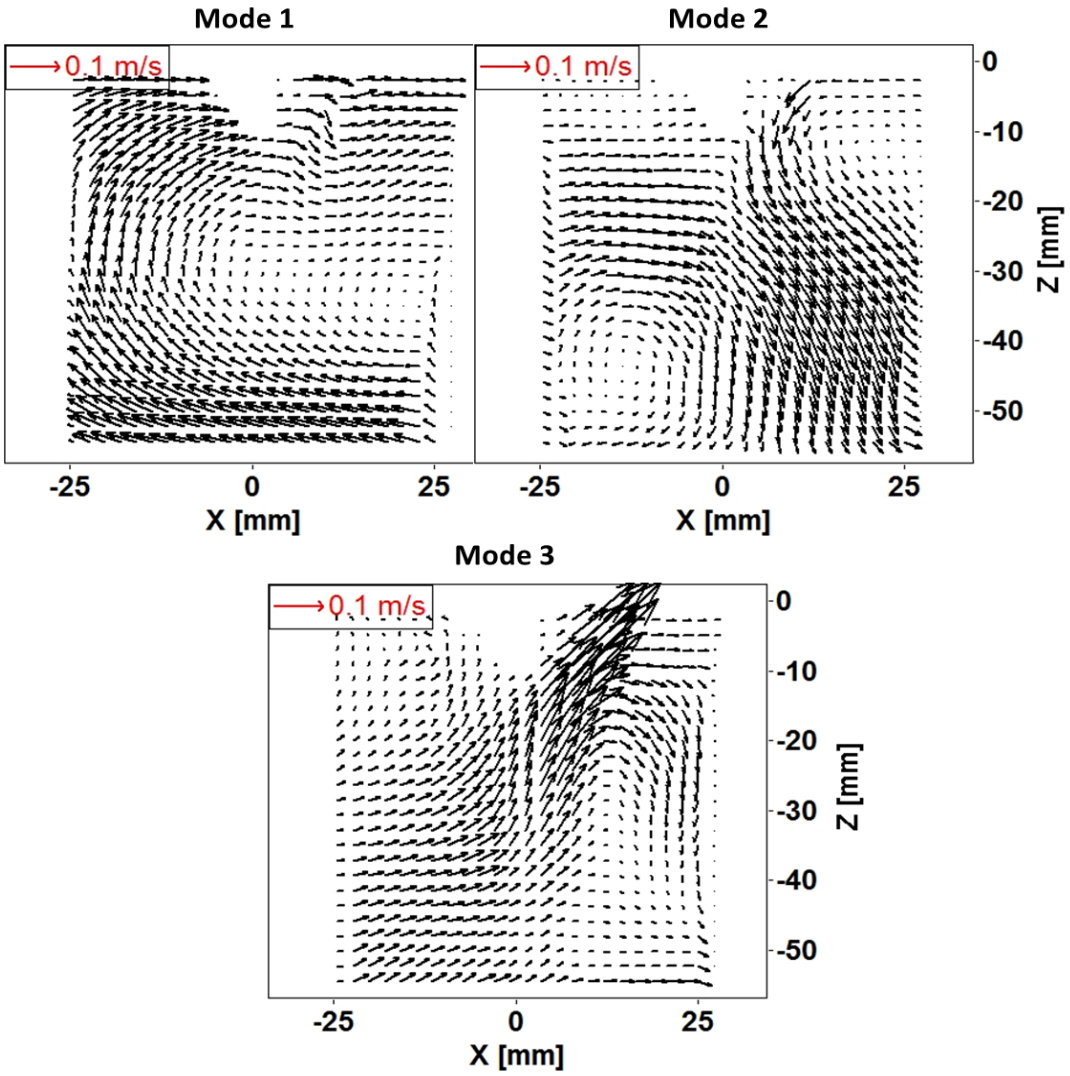

Figure 5.5: *First three modes from phase-invariant POD of intake and compression stroke data from S_2011_11_21_02 and S_2012_06_21_01*

Mode 1, with an energy fraction of 25%, shows the large-scale tumble vortex that develops during the intake stroke and breaks down during the compression stroke. Modes 2 and 3, with energy fractions of 16% and 13%, respectively, represent aspects of the intake jet and the counter-rotating vortices formed by the jet.

Figure 5.6 shows the coefficients associated with the first three modes of the phase-invariant POD analysis.

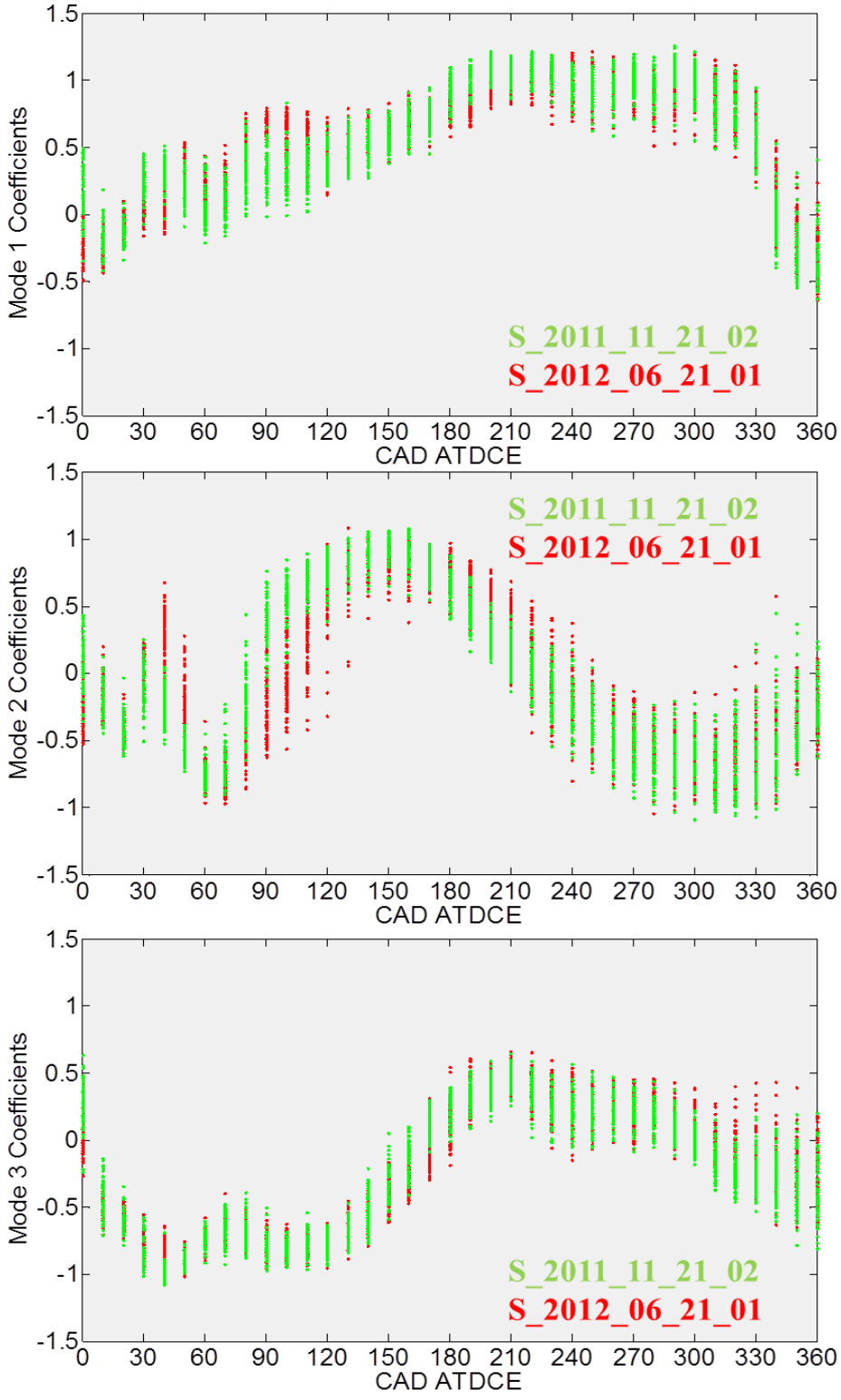

Figure 5.6: *Coefficients associated with the first three modes of phase-invariant POD of S_2011_11_21_02 and S_2012_06_21_01*

The Mode 1 coefficients in Figure 5.6 increase during the intake stroke and then decrease towards TDC compression, reflecting the development and breakdown of the large-scale tumble vortex seen in Mode 1. The Mode 2 coefficients of the two data sets differ significantly in the crank angle range of 40°-220° ATDCE. This indicates that the intake jet flow patterns in S_2011_11_21_02 and S_2012_06_21_01 are different from each other. In the compression stroke, the Mode 2 coefficients change sign, indicating that Mode 2 now contributes an upward piston-driven flow. Similarly, the Mode 3 coefficients show that Mode 3 represents intake jet flow patterns during the intake stroke and aspects of the piston-driven flow during the compression stroke.

The differences between the Mode 2 coefficients from S_2011_11_21_02 and S_2012_06_21_01 suggest differences between the ensemble average flow structures seen in these two data sets during the crank angle range of 40°-220° ATDCE. Figure 5.7 presents ensemble average flow fields from S_2011_11_21_02 and S_2012_06_21_01 at 100° ATDCE as an example of these differences.

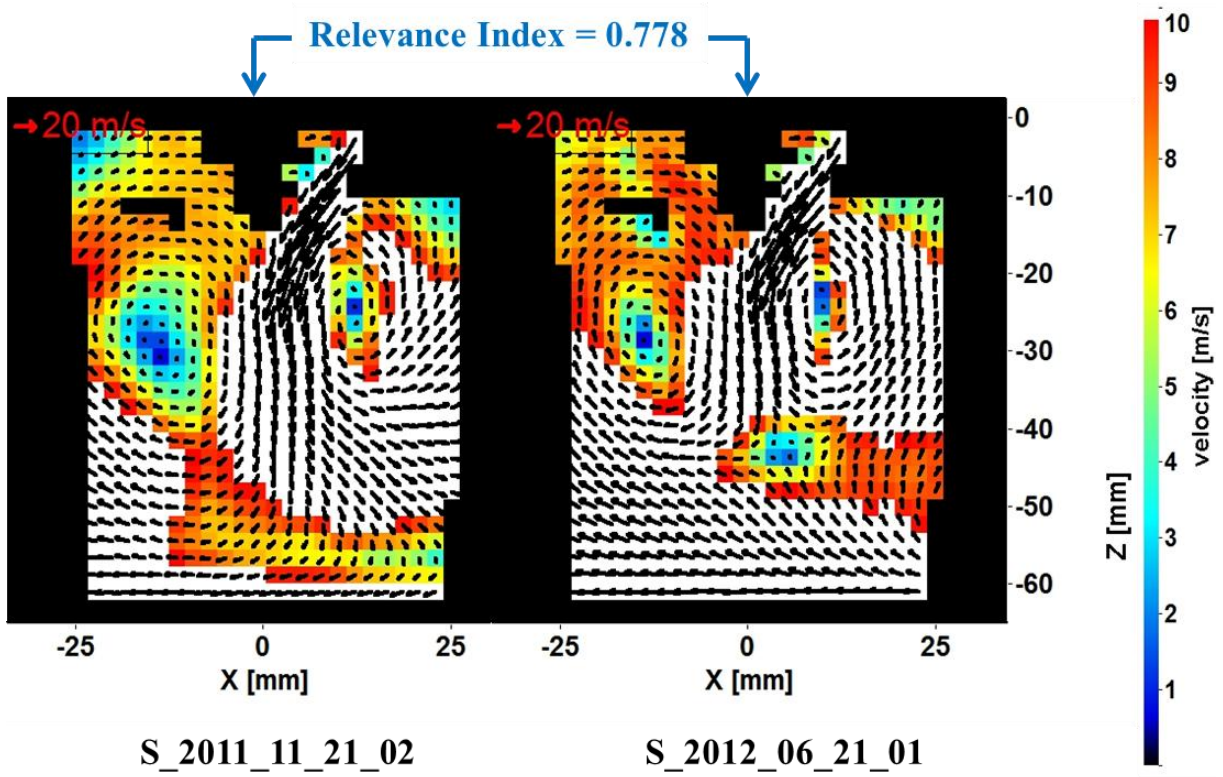

Figure 5.7: *Comparison of ensemble average flow velocities at 100° ATDCE from S_2011_11_21_02 and S_2012_06_21_01*

In Figure 5.7, the ensemble average flow field for S_2011_11_21_02 at 100° ATDCE shows a strong jet flow towards the bottom-right corner of the cylinder, as seen in Mode 2. For S_2012_06_21_01, an upward flow from the bottom-right corner is seen in the ensemble average at 100° ATDCE, which is the opposite of the flow pattern in Mode 2 and is also the flow pattern seen in Mode 3. This confirms that the differences in the Mode 2 coefficients associated with each of these data sets are related to real differences in observed ensemble average flow patterns.

A closer examination of the Mode 2 coefficients at 100° ATDCE is presented in Figure 5.8.

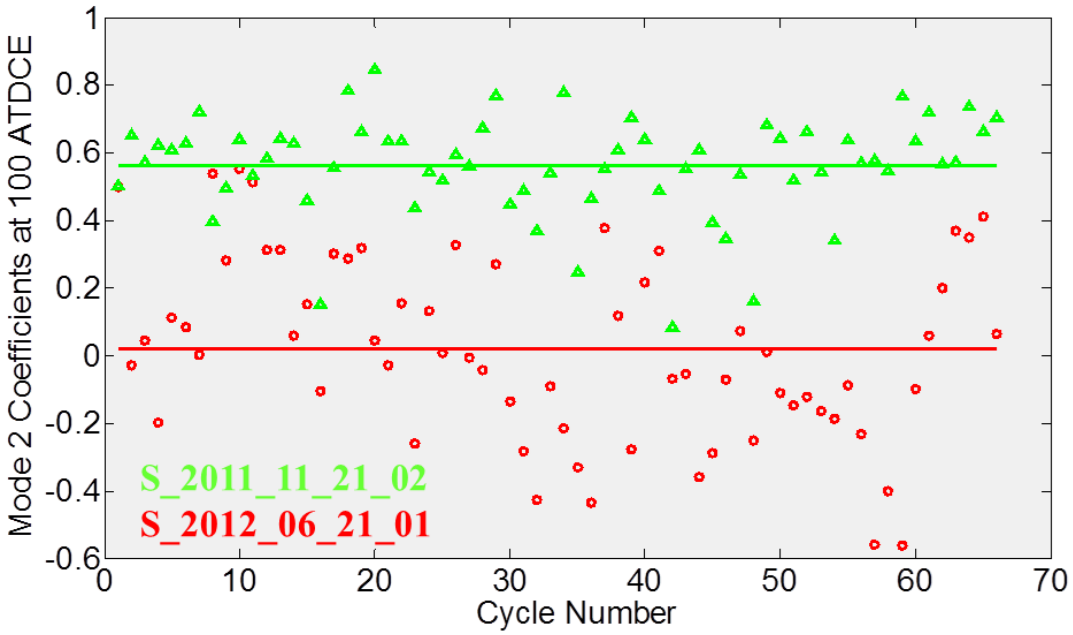

Figure 5.8: *Coefficients of Mode 2 at 100° ATDCE from phase-invariant POD analysis of S_2011_11_21_02 and S_2012_06_21_01. The solid lines indicate the ensemble average coefficient for each data set.*

Figure 5.8 shows that the ensemble average Mode 2 coefficient at 100° ATDCE for S_2011_11_21_02 is positive, agreeing with the ensemble average velocity shown in Figure 5.7. However, the ensemble average Mode 2 coefficient for S_2012_06_21_01 is close to zero, indicating that Mode 2 does not contribute significantly to the ensemble average at 100° ATDCE for this data set. From Figure 5.6, it can be seen that the Mode 3 coefficients for both data sets are large and negative at 100° ATDCE. Thus, Mode 3 contributes to the ensemble average at 100° ATDCE for S_2012_06_21_01 to create the upward flow in the bottom-right of the cylinder.

Figure 5.8 also shows that some cycles in each data set have a Mode 2 coefficient at 100° ATDCE that is very different from the ensemble average coefficient for that data set. This suggests that the flow pattern in these cycles at 100° ATDCE is also very different from the

ensemble average flow in the data set they belong to. For S_2011_11_21_02, the following cycles have Mode 2 coefficients below 0.2 at 100° ATDCE: Cycles 16, 42, and 48. For S_2012_06_21_02, the following cycles have Mode 2 coefficients above 0.4 at 100° ATDCE: Cycles 1, 8, 10, 11, and 65. The corresponding velocity fields, prior to interpolation onto a common grid, are shown in Figure 5.9. It may be seen that these outlying velocity fields from S_2011_11_21_02 show intake jet flows that do not extend into the bottom-right corner of the cylinder, unlike the ensemble average flow seen in Figure 5.7. Instead, they resemble the ensemble average flow from S_2012_06_21_01. Similarly, the outlying velocity fields from S_2012_06_21_01 from Figure 5.9 show strong intake jet flows extending into the bottom-right corner of the cylinder, unlike the ensemble average flow from that data set. Thus, at 100° ATDCE, the Mode 2 coefficients from this phase-invariant POD analysis correlate directly with the instantaneous flow patterns observed.

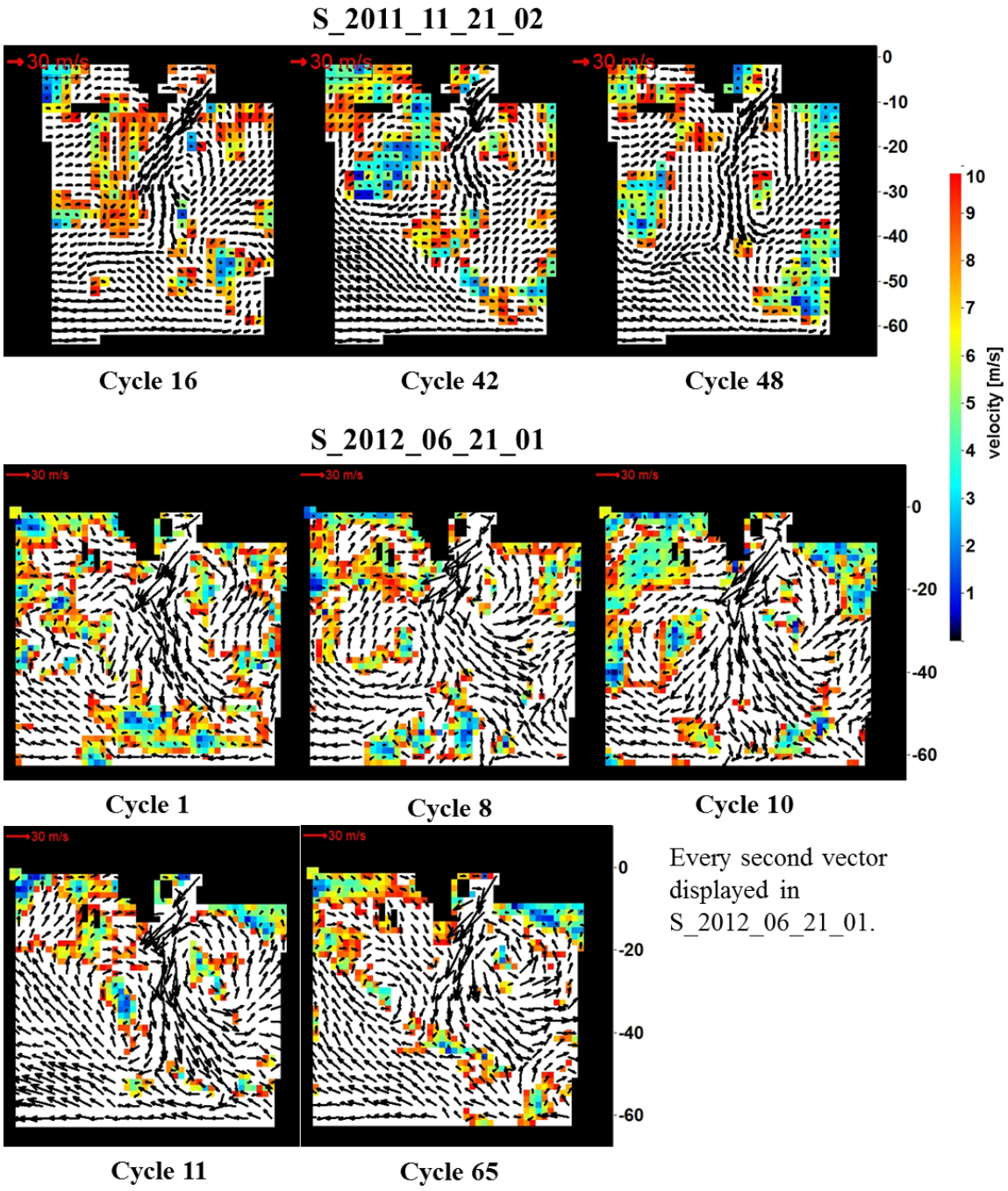

Figure 5.9: *Velocity at 100° ATDCE from S_2011_11_21_02 and S_2012_06_21_01 with outlying phase-invariant POD Mode 2 coefficients*

The larger spread in the values of the Mode 2 coefficients associated with S_2012_06_21_01 at 100° ATDCE and the difference between the Mode 2 ensemble average

coefficients of the two data sets, as seen in Figure 5.8, appears to be related to the larger intake valve oscillation in the direction of the X axis, noted in Section 5.3. The calibrated PIV images of the first 66 cycles of S_2012_06_21_01 were further examined visually to note the X coordinates of the intake valve edge at 100° ATDCE for each cycle. In order to determine the relationship between the flow pattern and the valve position at 100° ATDCE, the Mode 2 coefficients of S_2012_06_21_01 were plotted against the intake valve edge position, as shown in Figure 5.10.

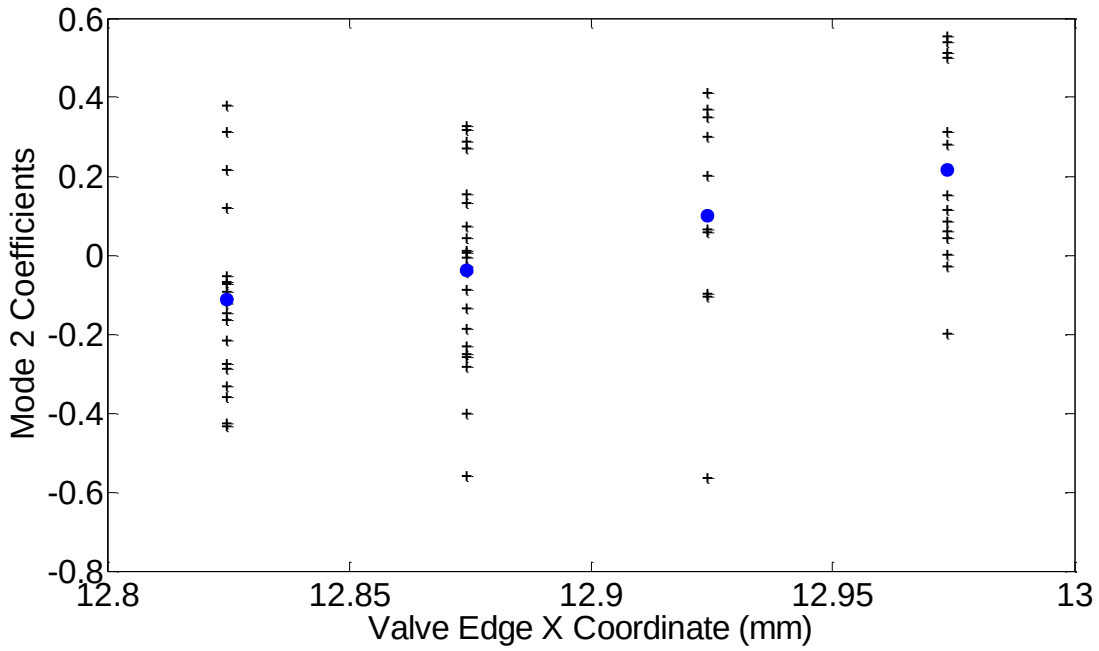

Figure 5.10: *S_2012_06_21_01 Mode 2 coefficients (black crosses) versus intake valve X coordinate. Average Mode 2 coefficient at each valve position is shown as a blue dot.*

Figure 5.10 shows that the S_2012_06_21_01 cycles with the intake valve closer to the centerline of the cylinder (X = 0 mm) have, on average, velocity vectors in the bottom-right corner of the field-of-view that point upwards and are of greater magnitude.

5.4 In-Cylinder Flow at 100° ATDCE

In order to obtain a better understanding of the variability of in-cylinder flow structures at 100° ATDCE, a phase-dependent POD analysis of two sets of 66 cycles from S_2011_05_24_03, S_2011_11_21_02 and the first 66 cycles of S_2012_06_21_01 was performed. Again, the velocity data from all data sets were interpolated onto a common grid with the same spatial resolution as S_2011_11_21_02. The two sets of 66 cycles from S_2011_05_24_03 were chosen such that their ensemble average flow patterns at 100° ATDCE would reflect the differences between the ensemble average flow patterns in S_2011_11_21_02 and S_2012_06_21_01, as shown in Figure 5.7. These similarities and differences are quantified in Figure 5.11.

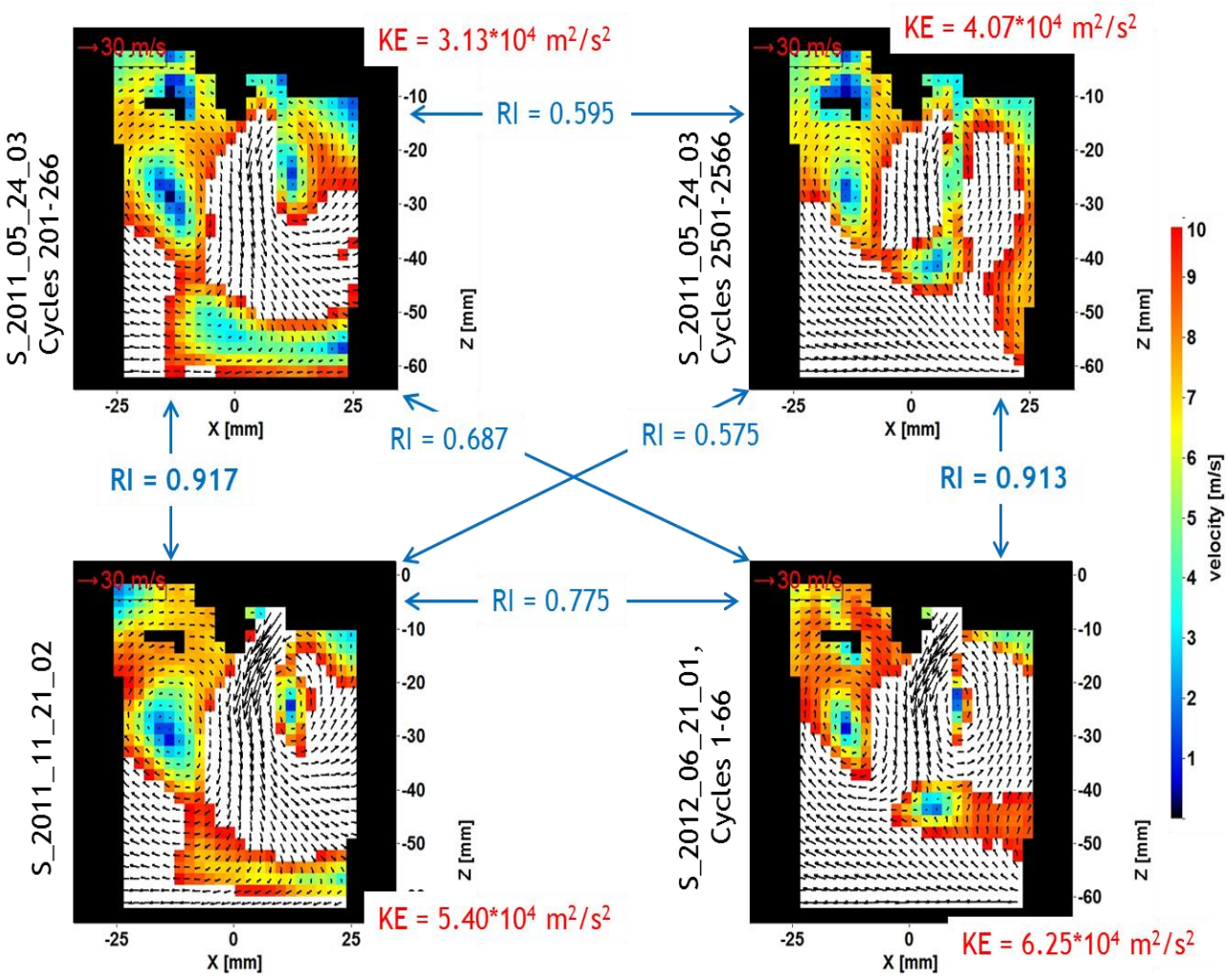

Figure 5.11: *Ensemble average velocity fields at 100° ATDCE from S_2011_05_24_03, S_2011_11_21_02, and S_2012_06_21_01 (RI – Relevance Index; KE – spatially-summed mass-specific kinetic energy of the ensemble average velocities)*

Figure 5.11 shows that the ensemble average velocity fields from S_2011_05_24_03, Cycles 201-266 and S_2011_11_21_02 are similar (as indicated by the relevance index above 0.9), with strong intake jets that extend into the bottom-right corner of the field-of-view. The ensemble average velocity fields from S_2011_05_24_03, Cycles 2501-2566 and S_2012_06_21_01 are also similar to each other, with upward flow from the bottom-right corner. The kinetic energies

of the two ensemble average velocity fields from S_2011_05_24_03 are smaller because the intake jet flow was not adequately captured by the non-optimal dt of 20 μs used in this data set.

Figure 5.12 presents the first two modes from the phase-dependent POD analysis.

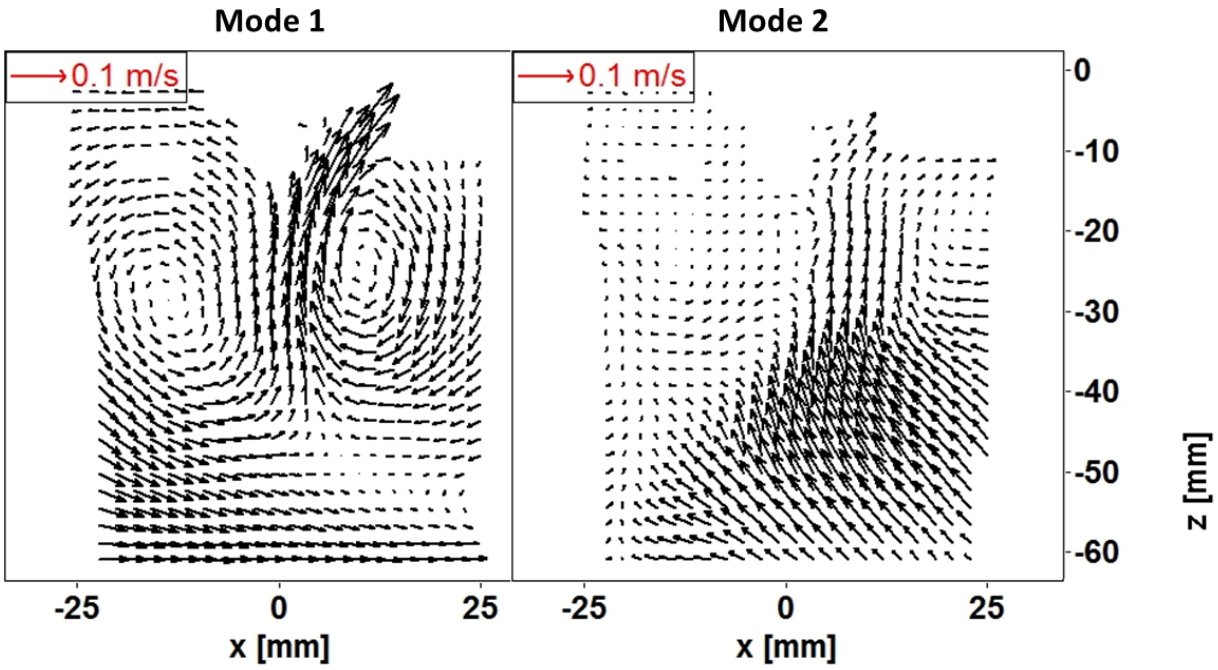

Figure 5.12: *First two modes from phase-dependent POD analysis of velocity data acquired at 100° ATDCE from S_2011_05_24_03, S_2011_11_21_02, and S_2012_06_21_01*

Mode 1, with an energy fraction of 55%, shows the intake jet flow and the counter-rotating vortices seen in the ensemble average velocity fields in Figure 5.11. Mode 2, with an energy fraction of 14%, shows large vectors pointing upwards from the bottom-right corner of the field-of-view. Higher order modes have energy fractions of 2% or less. The coefficients associated with Modes 1 and 2 are presented in Figure 5.13.

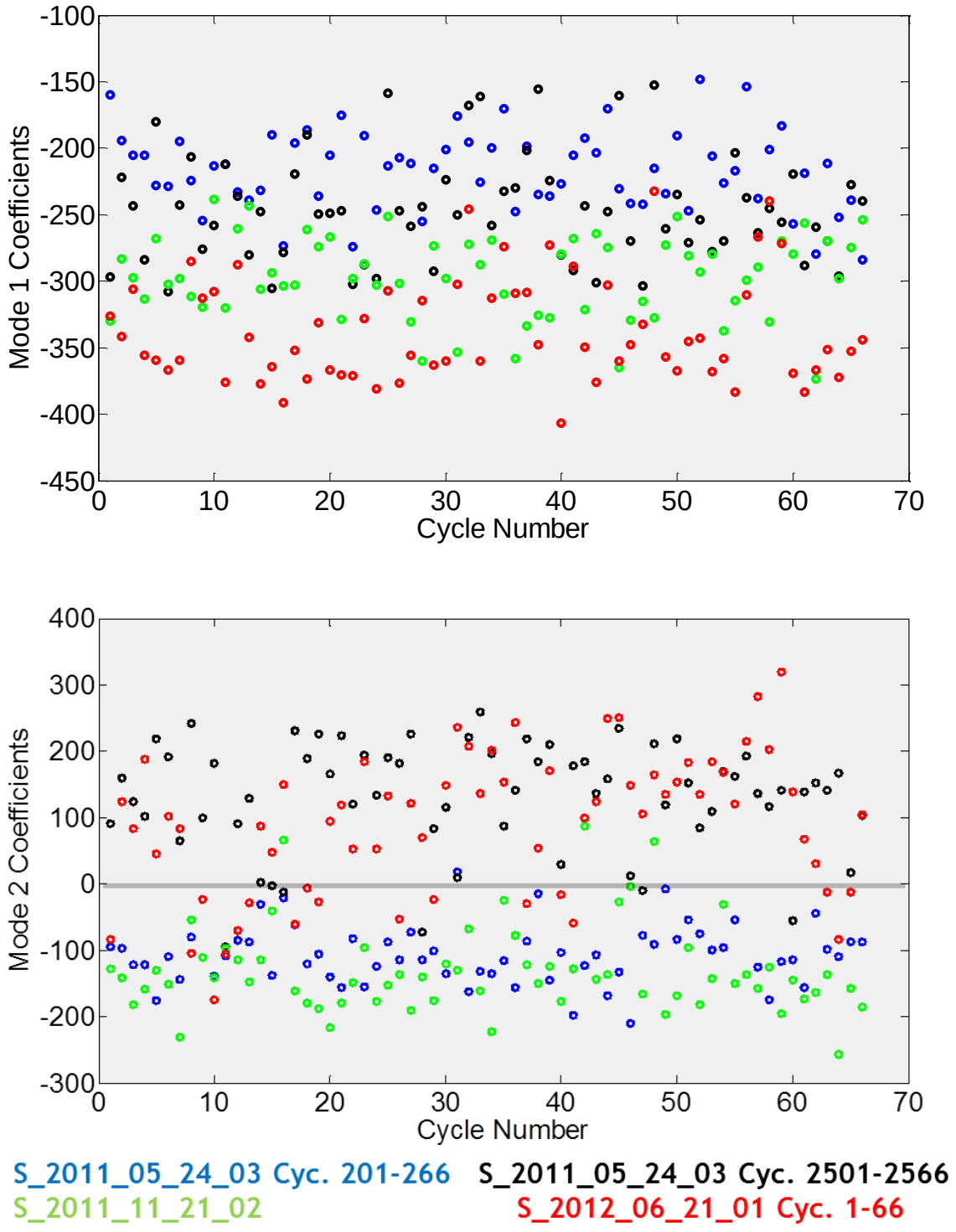

Figure 5.13: *Coefficients associated with the first two modes of the phase-dependent POD analysis of S_2011_05_24_03, S_2011_11_21_02, and S_2012_06_21_01*

The stratification of the Mode 1 coefficients seen in Figure 5.13 reflects the difference in the kinetic energies associated with the data sets analyzed. The differences between the Mode 2 coefficients indicates the differences in flow patterns, with positive coefficients for cycles in which the flow in the bottom-right corner of the field-of-view is upwards and negative coefficients for cycles with downward flow in the bottom-right corner. Most of the Mode 2 coefficients for S_2011_05_24_03, Cycles 201-266 and S_2011_11_21_01 are negative, indicating that most cycles in these data sets have downward flow in the bottom-right corner. Most of the Mode 2 coefficients for S_2011_05_24_03, Cycles 2501-2566 and S_2012_06_21_01 are positive, indicating that most cycles in these data sets have upward flow in the bottom-right corner.

Possible correlations between the intake port pressures, the pressure drop across the intake valve and the flow variations seen at 100° ATDCE were investigated. Figure 5.14 plots the intake port pressure and the difference between the intake port pressure and cylinder pressure against the Mode 2 coefficients at 100° ATDCE. Both the intake port and cylinder pressures were smoothed using running averages over 5° intervals.

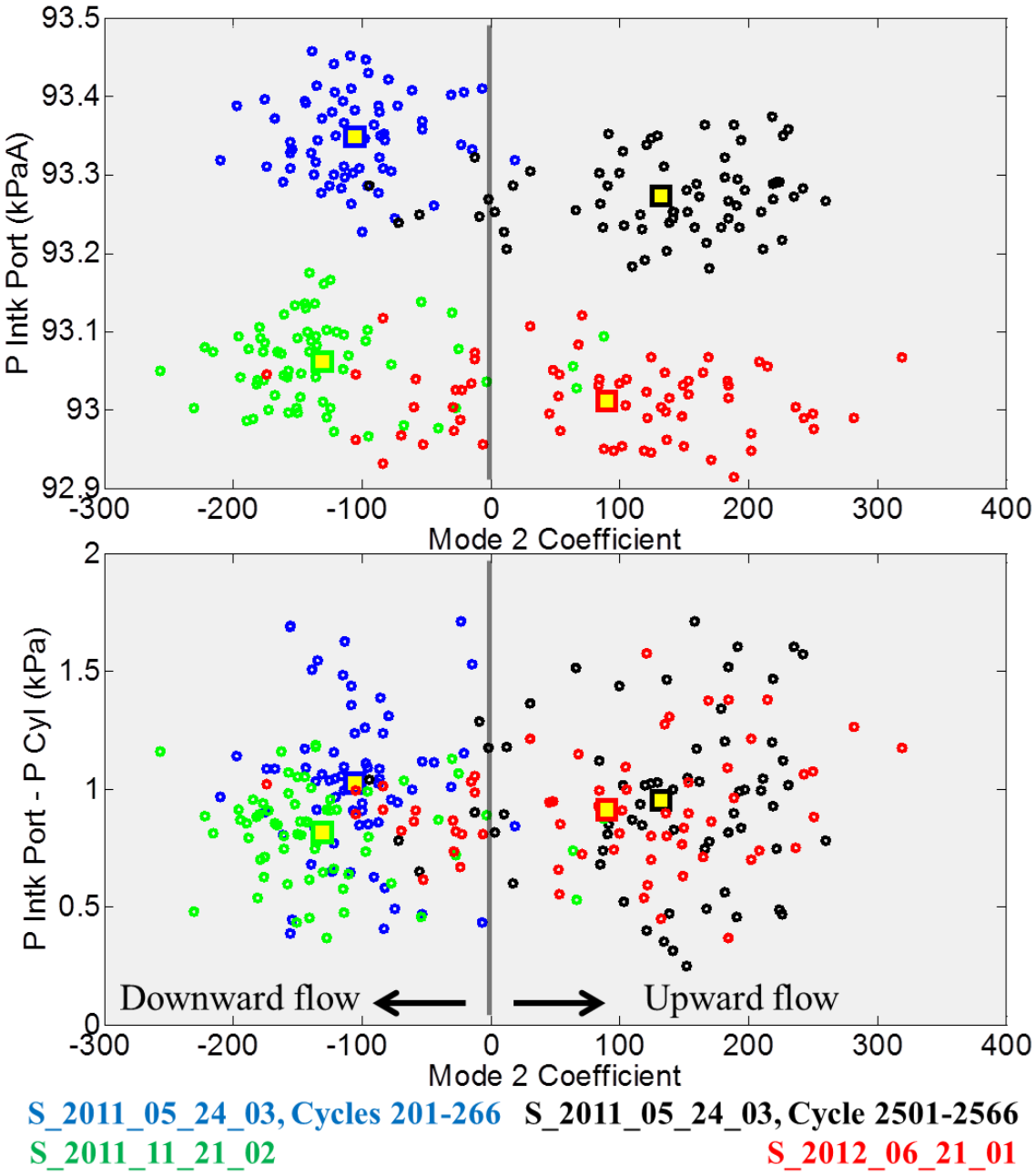

Figure 5.14: *Effect of intake port pressure and pressure drop across the intake valve on in-cylinder flow pattern at 100° ATDCE. The circles indicate values for individual cycles and the squares indicate ensemble average values.*

Figure 5.14 shows that both data sets with predominantly upward flow in the bottom-right corner of the field-of-view and those with predominantly downward jet flow towards the bottom-right

corner have similar intake port pressure values and similar pressure differences across the intake valve. Thus, there is no correlation between intake port pressure or the pressure difference across the intake valve and in-cylinder flow patterns at 100° ATDCE.

Another potential cause of the change in dominant flow pattern between data sets is the oscillatory intake valve motion detailed in Section 5.3. A comparison of Table 5.1 and Figure 5.13 reveals that only the data sets with a cycle-to-cycle variation in intake valve position along the horizontal (X) axis are dominated by the flow pattern with upward flow from the bottom-right corner of the field-of-view. Further, Table 5.2 shows that S_2012_06_21_01, one of the data sets with upward flow from the bottom-right, had larger oscillation amplitudes during both intake valve opening and closing for three randomly selected cycles than S_2011_11_21_01. In order to better understand the relationship between intake valve position and in-cylinder flow pattern at 100° ATDCE, the Mode 2 coefficients of S_2011_05_24_03, Cycles 2501-2566 and S_2012_06_21_01 were plotted against intake valve edge position, as shown in Figure 5.15.

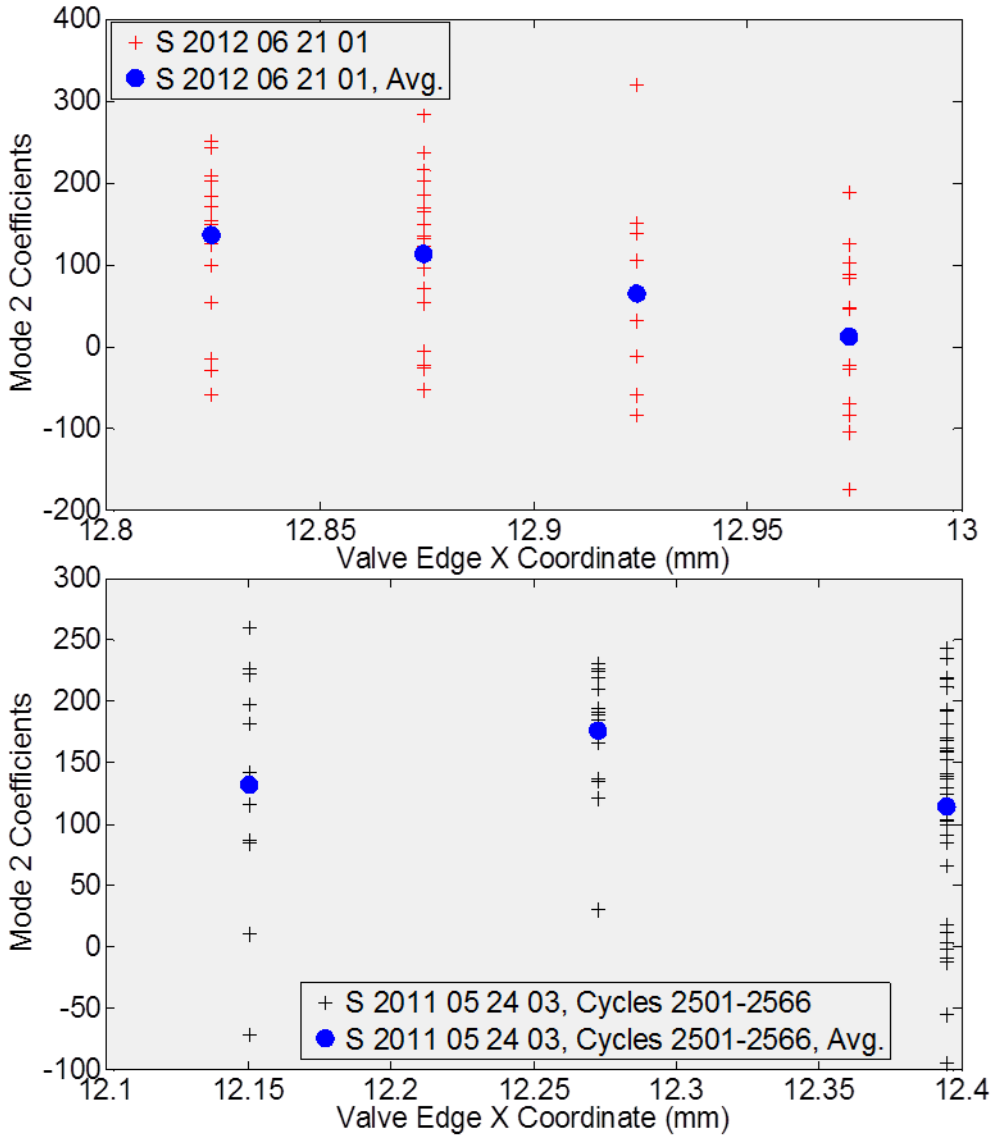

Figure 5.15: *Mode 2 coefficients (crosses) versus intake valve X coordinate. Average Mode 2 coefficient at each valve position is shown as a blue dot.*

Figure 5.15 shows that in S_2012_06_21_01, larger upward velocity vectors from the bottom-right corner are, on average, observed in cycles where the intake valve is closer to the centerline of the cylinder (X = 0). This was also seen in Figure 5.10. However, the Mode 2 coefficients for S_2011_05_24_03, Cycles 2501-2566 show no similar trend. This may partly be due to the lower spatial resolution of S_2011_05_24_03.

In order to determine if the position of the intake valve affects the velocity profile in the intake jet closer to the valve, the instantaneous velocity magnitudes along two lines, Y = -8.95 mm and Y = -15.3 mm, were extracted at 100° ATDCE for all cycles in S_2012_06_21_01. These velocity profiles were then sorted by the associated intake valve edge X coordinates, and averaged. Figure 5.16 shows the average velocity profiles for different positions of the intake valve.

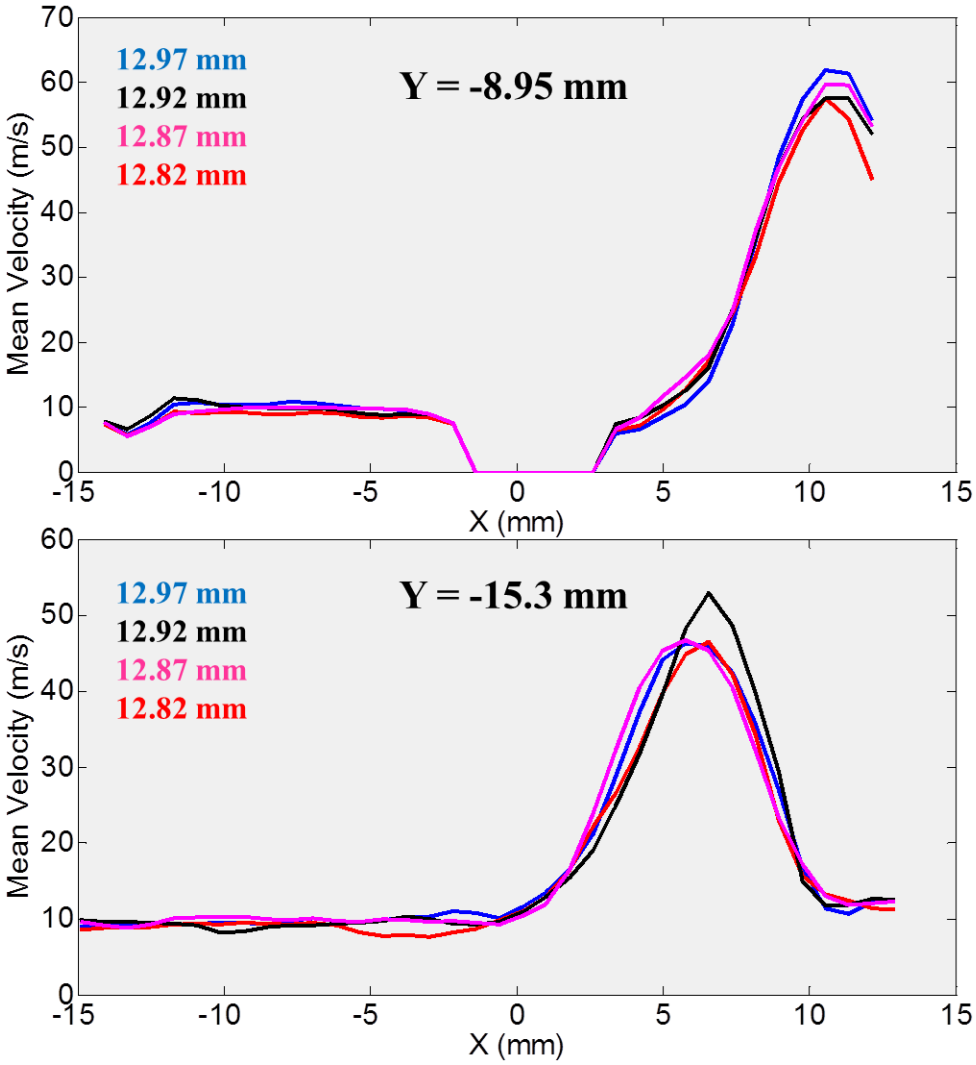

Figure 5.16: *Average velocity profiles from S_2012_06_21_01 at Y = -8.95 mm and Y = -15.3 mm at different intake valve edge X coordinates*

In Figure 5.16, velocities near the origin are zero for the Y = -8.95 graph because the spark plug is located there. Velocities rise towards X = 10 mm for the Y = -8.95 graph and towards X = 5 mm for the Y = -15.3 mm graph, showing the changing location of the intake jet as it moves towards the piston. Figure 5.16 shows no clear correlation between intake valve edge horizontal position and average intake jet velocities.

A potential cause for the shift in dominant flow pattern between S_2011_05_24_03, Cycles 201-266 and S_2011_05_24_03, Cycles 2501-2566 was the presence of engine speed transients in this data set, as shown in Figure 5.1. In order to further illustrate this shift, a spatial average of the velocity components was taken in a small area in the bottom-right corner of the velocity fields, shown in Figure 5.17. In cycles with a downward flow towards the bottom-right corner, the spatial average of U, the velocity component along the X axis, will be positive, and the spatial average of W, the velocity component along the Z axis, will be negative. However, in cycles with an upward flow from the bottom-right corner, the average of U will be negative, and the average of W will be positive.

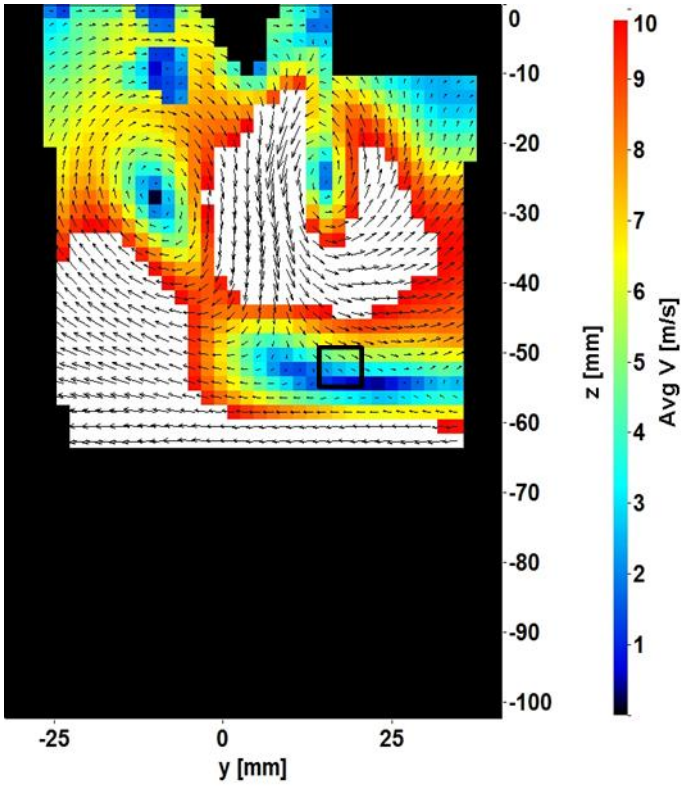

Figure 5.17: *Spatial region (outlined in black) where spatial average velocity components are used differentiate between flow patterns at 100° ATDCE in S_2011_05_24_03*

Figure 5.18 shows the spatial average velocity components from the region illustrated in Figure 5.17 and the engine speed transients for S_2011_05_24_03. It can be seen that an engine speed transient around Cycle 2000, highlighted in pink in Figure 5.18, correlates with a shift in dominant in-cylinder flow pattern as quantified by the change in sign of the spatial average velocity components from the bottom-right corner of the velocity fields. However, an earlier speed transient around Cycle 1250, shown in grey in Figure 5.18, does not correlate with a similar shift in dominant flow pattern.

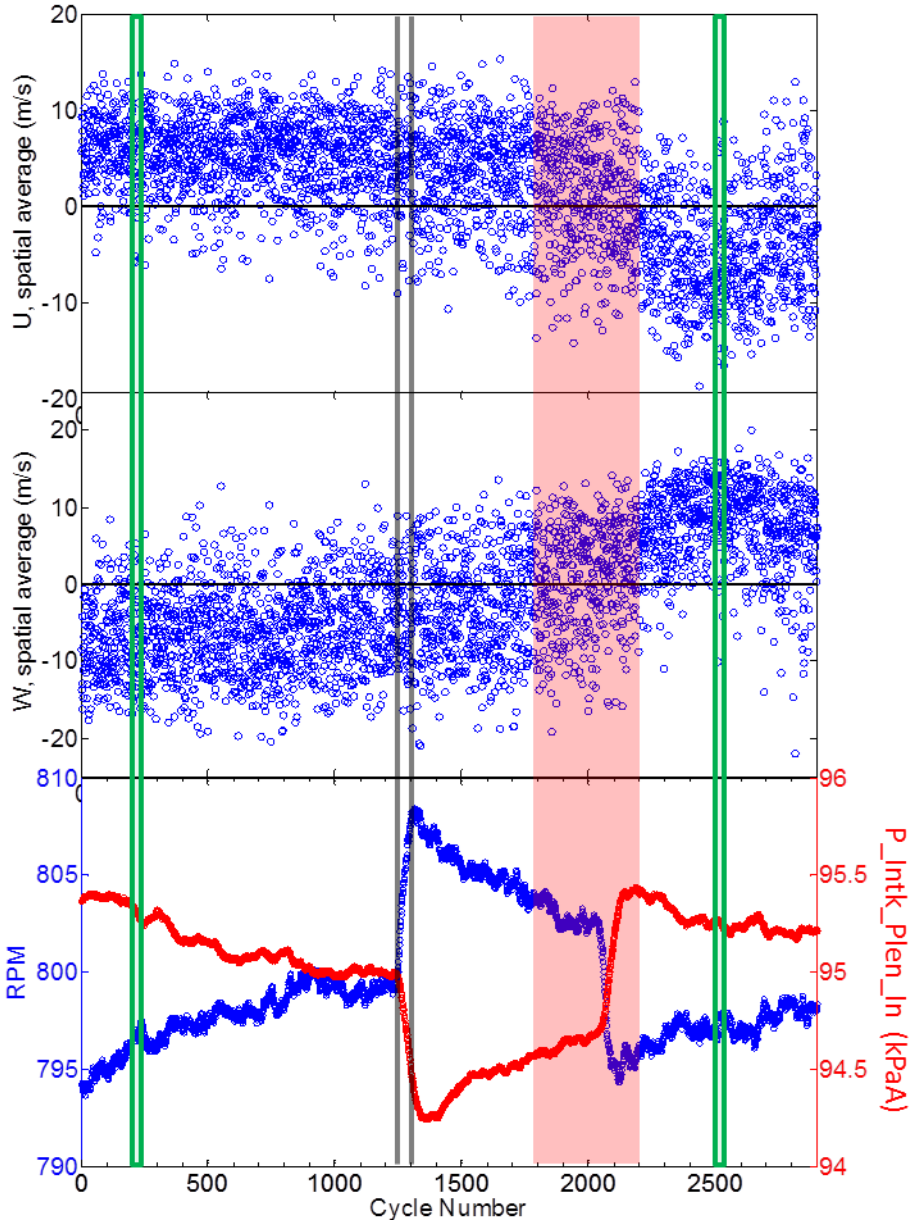

Figure 5.18: *Correlation between in-cylinder flow patterns at 100° ATDCE and engine speed transients in S_2011_05_24_03. Subsets with cycle numbers 201-266 and 2501-2566 shown in green, engine speed transients shown in grey and pink.*

Chen, et al. [17, 18] proposed that, if the first mode from a phase-dependent POD analysis is a good estimate of the mean flow, Mode 1 coefficients may be used to estimate the mass-specific kinetic energy contribution of the mean flow to any instantaneous velocity field

used in the decomposition, thus estimating how closely a particular velocity field compares to the mean flow. Similarly, the mass-specific kinetic energy contribution of the rest of the higher order modes estimates the RANS turbulence in a specific velocity field. Thus, the cyclic variability of the mean flow and the turbulence may be quantified. In order to ascertain if Mode 1 is a good estimate of the mean flow, relevance indices between the mean flow of each data set and Mode 1 were computed. It was found that the absolute value of the relevance indices for the two sets of cycles from S_2011_05_24_03 were below 0.9, which indicates Mode 1 is a poor estimate of the mean flow for these data sets. Thus, both Modes 1 and 2 were used to estimate the mean flow. Relevance indices were calculated between the mean flow of each data set and Modes 1 and 2, weighted by their mean coefficients for that data set and then summed. These relevance indices, compiled in Table 5.3, were all found to be larger than 0.9.

	Mode 1	Modes 1 and 2
S_2011_05_24_03, Cycles 201-266	-0.866	0.963
S_2011_05_24_03, Cycles 2501-2566	-0.863	0.980
S_2011_11_21_02	-0.905	0.988
S_2012_06_21_01, Cycles 1-66	-0.955	0.988

Table 5.3: *Relevance indices between Modes 1 and 2 and ensemble average velocities from S_2011_05_24_03, S_2011_11_21_02, and S_2012_06_21_01*

Figure 5.19 estimates the cycle-to-cycle variability in the contribution of the mean flow and the RANS turbulence to each cycle in the data sets S_2011_05_24_03, Cycles 201-266 and 2501-2566, S_2011_11_21_01, and S_2012_06_21_01, Cycles 1-66.

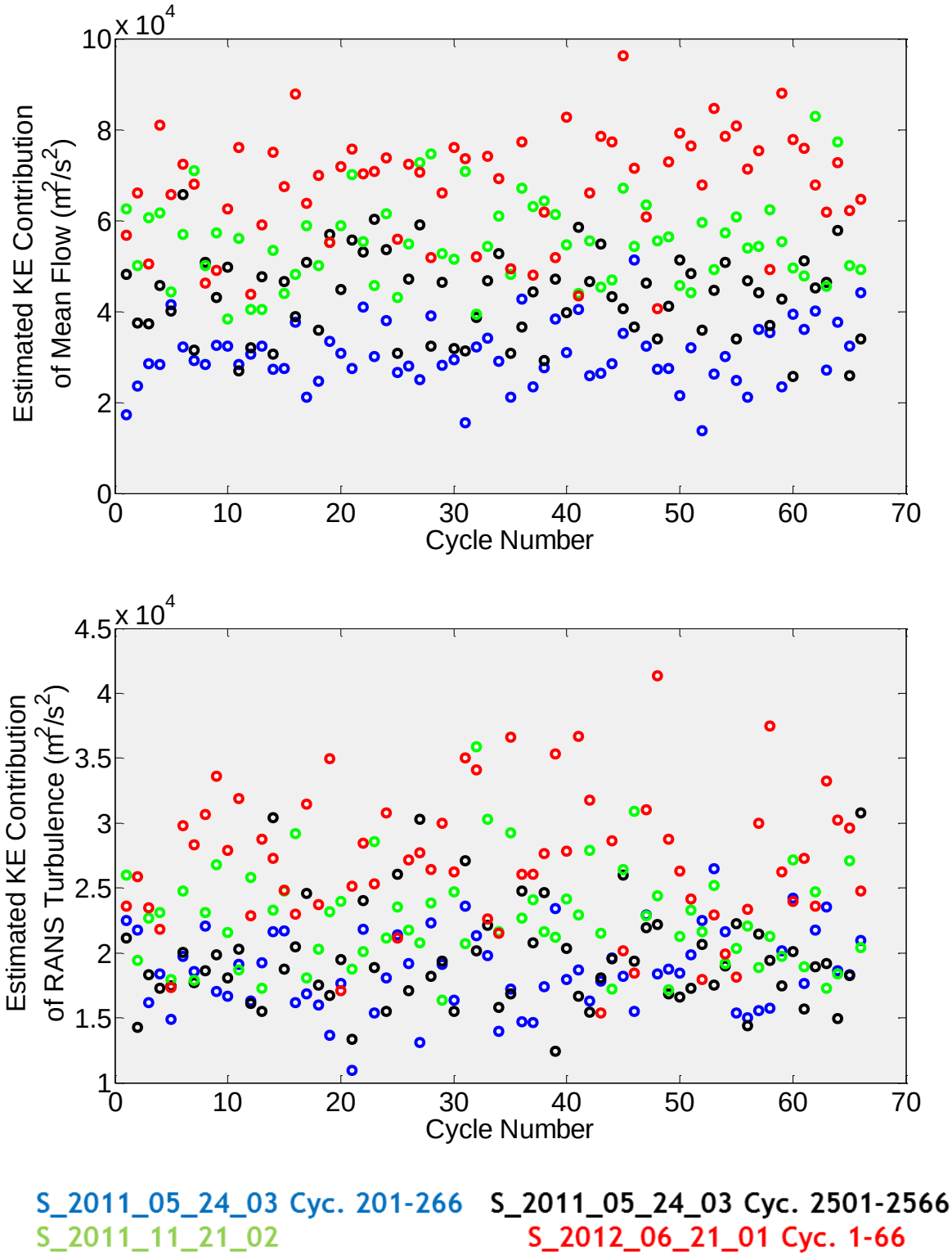

Figure 5.19: *Estimated mass-specific kinetic energy contributions of the ensemble average and fluctuating flow to S_2011_05_24_03, S_2011_11_21_02, and S_2012_06_21_01*

Figure 5.19 shows that S_2011_11_21_02 and S_2012_06_21_01 have larger mass-specific kinetic energy contributions from both the mean and turbulent flow. This is because the intake jet flow is better captured in these data sets. The spread in the estimated contributions of the mean flow to S_2012_06_21_01 is larger than that observed in the other data sets. The spread in the estimated contributions of the RANS turbulence to S_2012_06_21_01 and S_2011_05_24_03, Cycles 2501-2566 is larger than that observed in the other data sets. Thus, larger cycle-to-cycle variations in the position of the intake valve along the X axis appear to be associated with larger cycle-to-cycle variations in turbulence.

5.5 In-Cylinder Flow at 300° ATDCE

A phase-dependent POD analysis of S_2011_11_21_02 and the first 66 cycles of S_2012_06_21_01 was performed to obtain a better understanding of the variability of in-cylinder flow structures at 300° ATDCE, and to see if the different dominating flow patterns at 100° ATDCE in the two data sets result in similar differences between them during the compression stroke. The velocity data from S_2012_06_21_01 were interpolated onto a common grid with the same spatial resolution as S_2011_11_21_02. The first three modes from the phase-dependent POD analysis are shown in Figure 5.20.

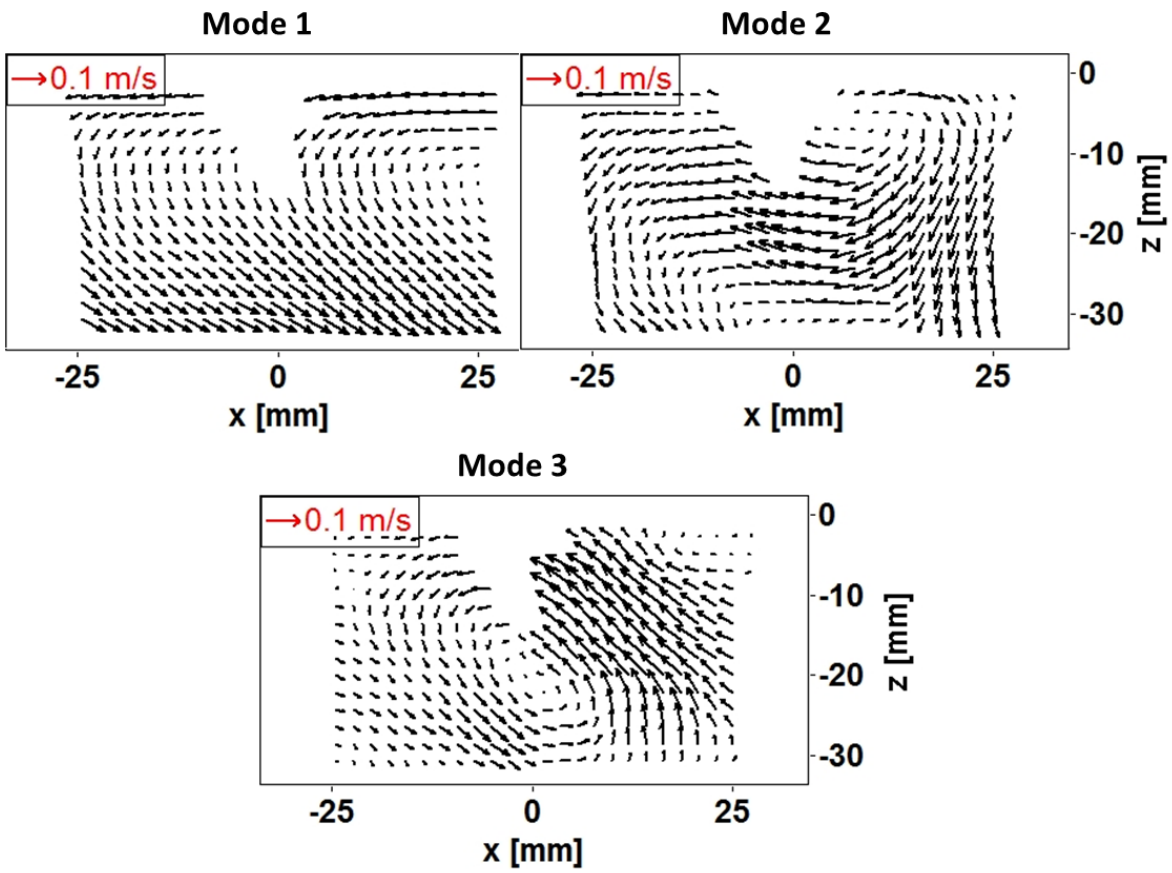

Figure 5.20: *First three modes from phase-dependent POD analysis of S_2011_11_21_02 and S_2012_06_21_01*

Mode 1, with an energy fraction of 75%, shows a piston-driven flow that dominates the flow pattern observed at 300° ATDCE. Mode 2, with an energy fraction of 4%, shows flow across the field-of-view from right to left. Mode 3, with an energy fraction of 3%, shows a vortex structure below the spark plug. Figure 5.21 shows the coefficients associated with these modes.

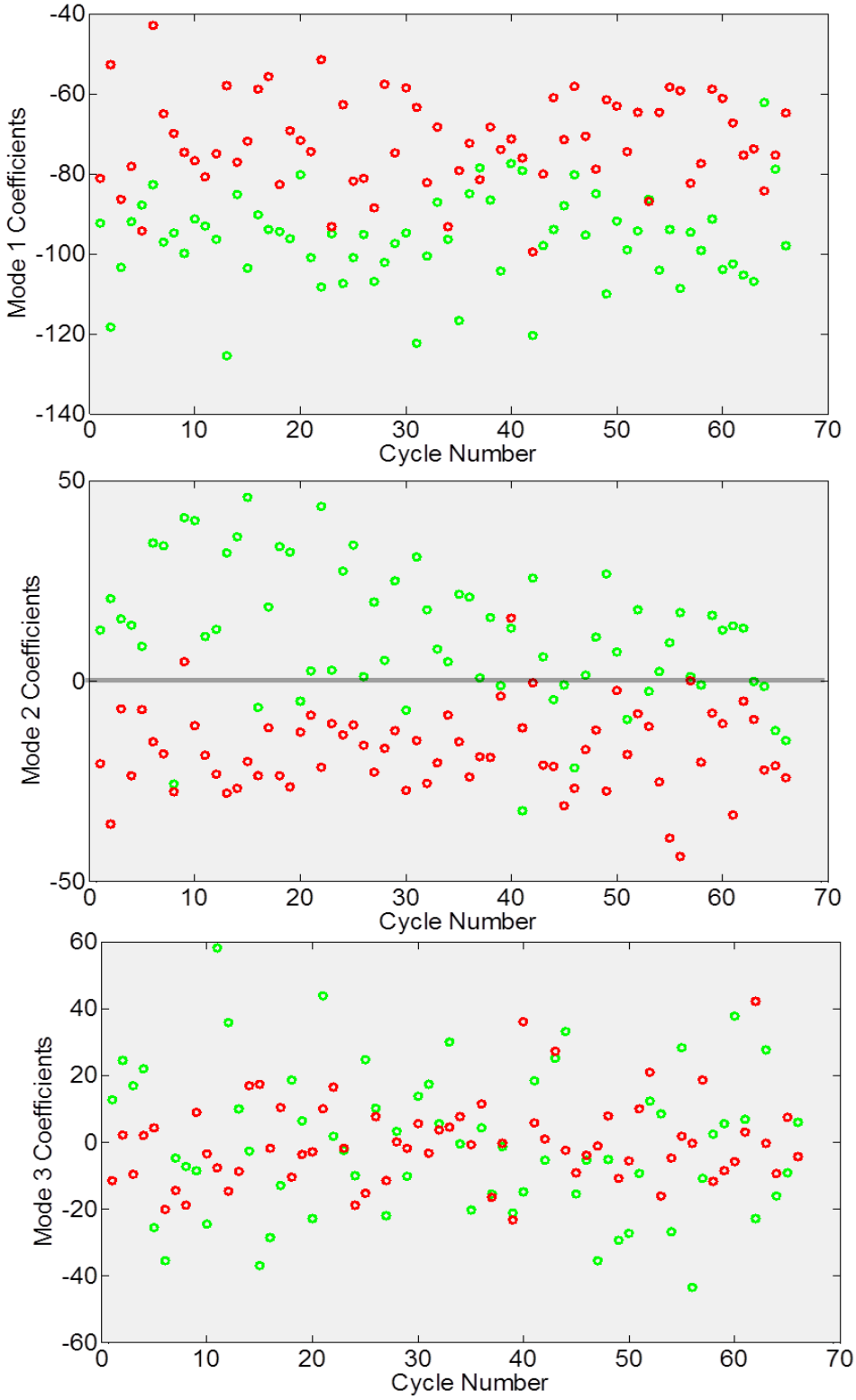

Figure 5.21: *Coefficients associated with the first three modes of the phase-dependent POD analysis of S_2011_11_21_02 (in green) and S_2012_06_21_01 (in red)*

The stratification in the Mode 1 coefficients is due to differences in mass-specific kinetic energy between the data sets. PIV data acquisition in S_2011_11_21_02 was performed with a constant dt that was optimized for the intake jet flow, while the variable dts used in S_2012_06_21_01 yielded less noisy PIV data at 300° ATDCE. More details are provided in Section 3.5. Thus, this difference in mass-specific kinetic energy between the data sets may not be related to the difference in dominant flow patterns observed at 100° ATDCE. The relevance indices between Mode 1 and the ensemble average velocity fields from S_2011_11_21_02 and S_2012_06_21_01, Cycles 1-66 are -0.991 and -0.968, showing that Mode 1 is a good approximation of the mean flow for each of these data sets. The Mode 1 coefficients are, therefore, an estimate of the cycle-to-cycle variability in the contribution of the mean flow to individual flow fields.

The Mode 2 coefficients are largely divided into positive and negative by data set. This seems to indicate that the difference in dominant flow pattern at 100° ATDCE has a small effect on the flow patterns seen at 300° ATDCE. Mode 3 coefficients show no distinctions between the two data sets.

5.6 Summary

Three PIV data sets acquired at 800 rpm were compared in this chapter to further study the relationship between intake valve oscillations and in-cylinder flow. Both phase-invariant POD with velocity data from multiple crank angles and phase-dependent POD at 100° ATDCE showed a difference in the intake flow similar to that seen in the previous chapter when comparing the data sets acquired at different engine speeds, and a similar relationship between cycle-to-cycle variations in intake valve oscillations and intake flow. Phase-dependent POD at 300° ATDCE for two of the data sets showed small differences between them.

CHAPTER 6

POD ANALYSIS OF COMBINED EXPERIMENTAL AND COMPUTATIONAL DATA

In this chapter, experimental data acquired at 800 rpm (S_2012_06_21_01) is compared to large-eddy simulation data computed by collaborators at General Motors and Pennsylvania State University [13]. In-cylinder, intake and exhaust system pressures are compared, as well as in-cylinder velocity fields using tools such as proper orthogonal decomposition and ensemble averaging.

6.1 Comparing In-Cylinder, Intake, and Exhaust System Pressure Data

In order to compare experimentally obtained and computed in-cylinder flow velocities, it necessary to first quantify the differences in engine operation and pressure boundary conditions between the data sets. Figure 6.1 compares the in-cylinder pressure data from the experimental and computational data sets. Data from the first 60 cycles of S_2012_06_21_01, 48 cycles of the General Motors (GM) LES computations, and 60 cycles of the Pennsylvania State University (PSU) LES computations were used to compile Figure 6.1.

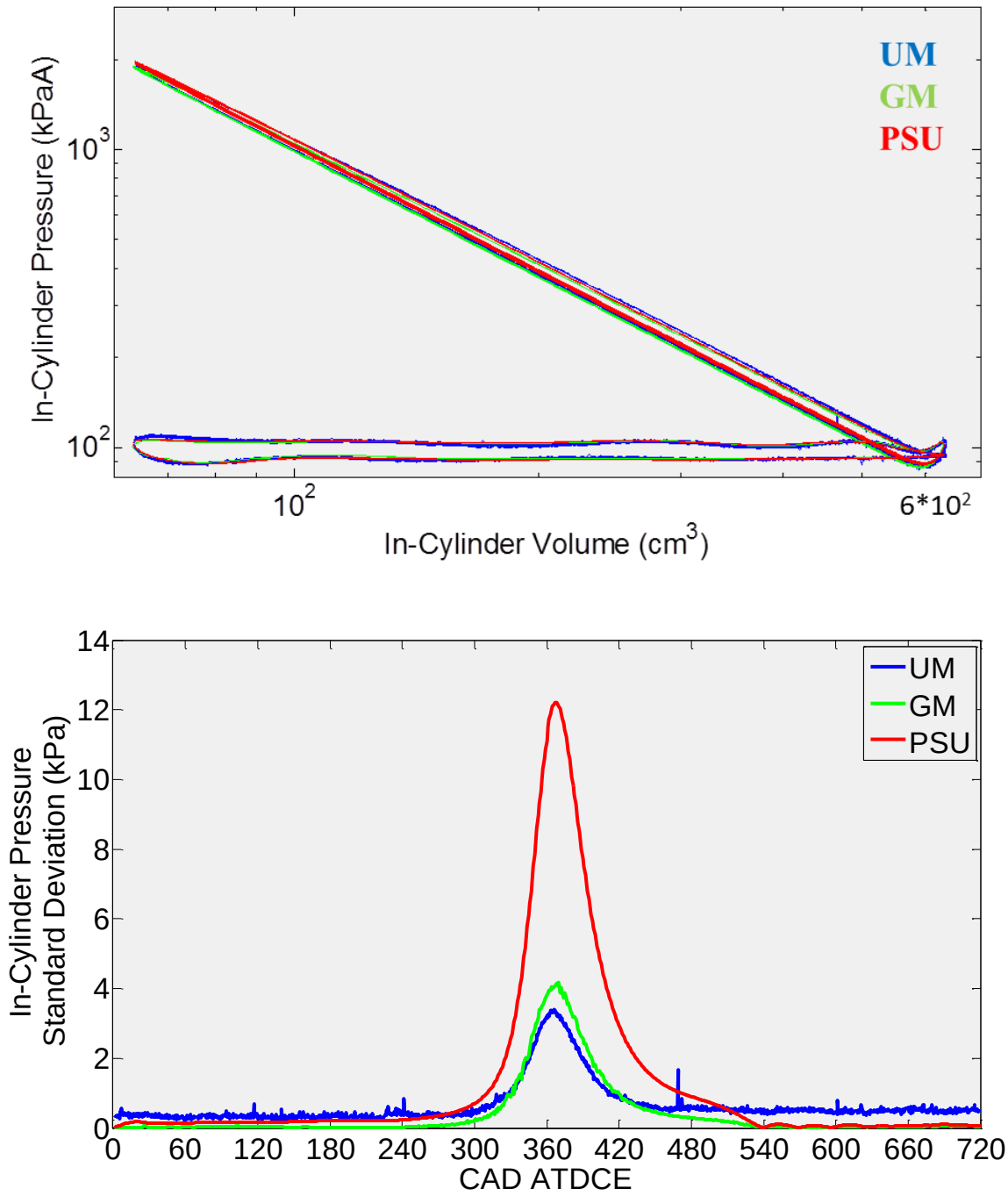

Figure 6.1: *In-cylinder log P – log V graph for multiple cycles and standard deviation for in-cylinder pressure in S_2012_06_21_01 (labeled 'UM') and computational data from GM and PSU*

Figure 6.1 shows that the log P – log V graphs for all cycles from the PSU data show higher pressure through the compression stroke and higher peak in-cylinder pressures. During the expansion stroke, the in-cylinder pressure values from S_2012_06_21_01 are highest. The standard deviation of the in-cylinder pressure in the later part of the compression stroke and the early part of the intake stroke is highest for the PSU data. For the rest of the cycle, the standard deviation of the experimentally measured in-cylinder pressure is highest. This may be interpreted partly as higher cycle-to-cycle variations in the measured in-cylinder pressure when the valves are open, and partly as noise in the measured pressure data.

Figure 6.2 compares the measured (UM) and computed (GM) pressures at the inlet to the intake plenum (P_Intk_Plen_In). Data from the first 60 cycles of S_2012_06_21_01 and 48 cycles of the GM LES computations were used to compile Figure 6.2.

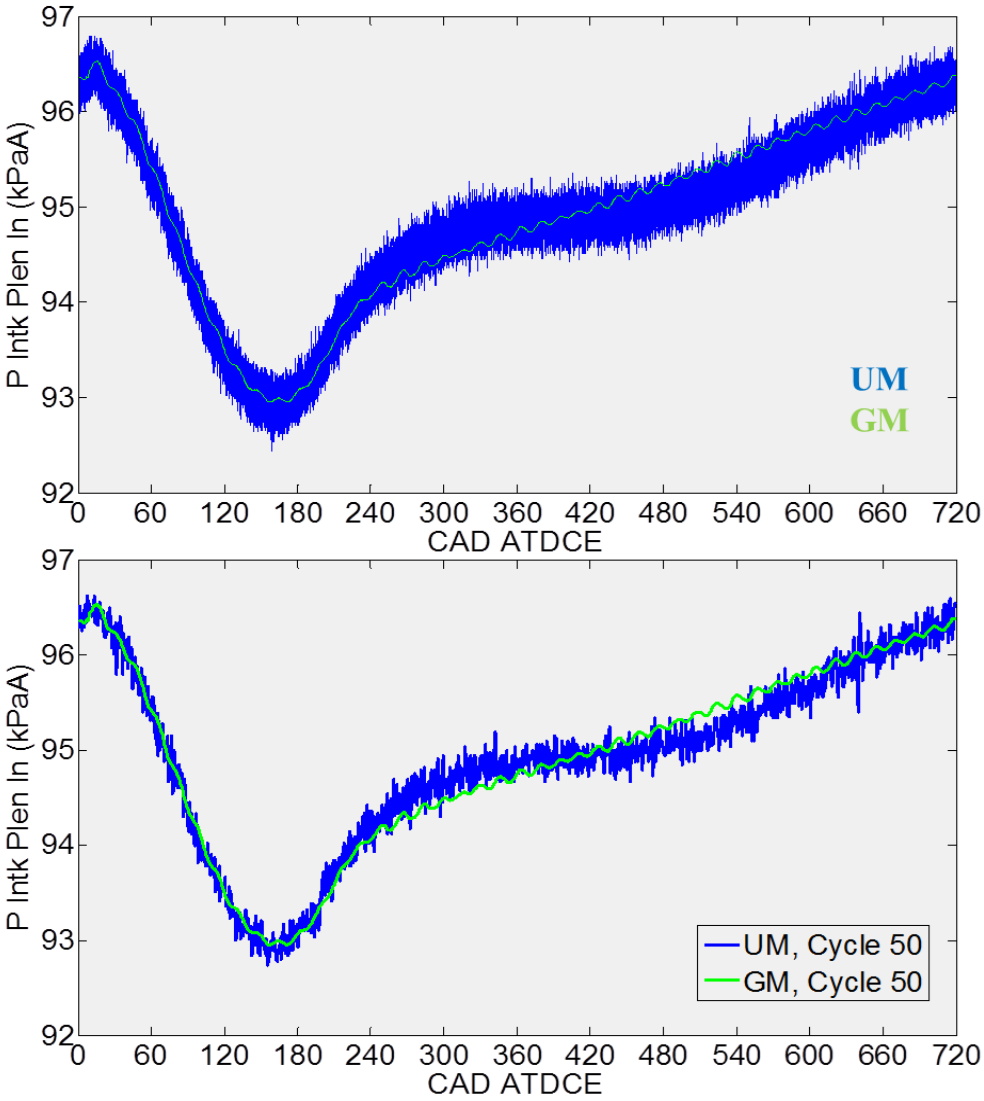

Figure 6.2: *Intake plenum inlet pressures for multiple cycles (upper graph) and for Cycle 50 (lower graph) from S_2012_06_21_01 (labeled 'UM') and computational data from GM*

Figure 6.2 demonstrates the difference in cycle-to-cycle variations and noise between the experimental and computational data. A visual examination of Figure 6.2 reveals a spread of approximately 1 kPa in the graphed experimental intake plenum inlet pressure from all cycles and a spread of approximately 0.5 kPa in Cycle 50. Thus, the intake plenum inlet pressure data from S_2012_06_21_01 has noise levels of approximately 0.5 kPa and cycle-to-cycle variations

of approximately 0.5 kPa. On the other hand, the computational intake plenum inlet pressure data from GM shows no noise and negligible cycle-to-cycle variations.

Figure 6.3 compares the measured (UM) and computed (GM and PSU) pressures at the inlet to the intake plenum (P_Intk_Port). Data from the first 60 cycles of S_2012_06_21_01, 48 cycles of the GM LES computations, and Cycles 12-60 of the PSU LES computations were used to compile Figure 6.3.

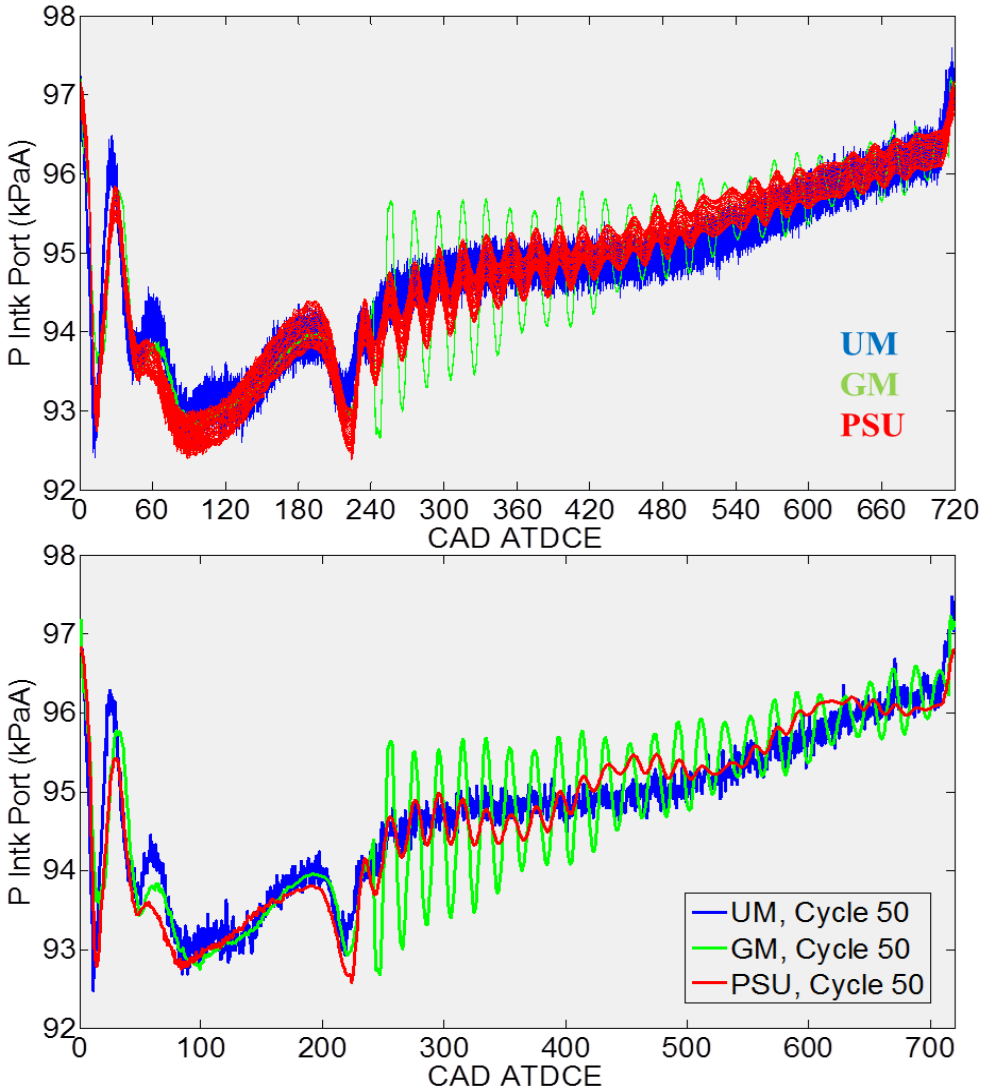

Figure 6.3: *Intake port pressures for multiple cycles (upper graph) and for Cycle 50 (lower graph) from S_2012_06_21_01 (labeled 'UM') and computational data from GM and PSU*

A comparison of the two graphs in Figure 6.3 indicates that the experimental intake port pressures were affected by both measurement noise and cycle-to-cycle variability. The computed pressures are not affected by noise, but the data from PSU shows large cycle-to-cycle variations in the intake port pressures. Cycle-to-cycle variations in the intake port pressures from the GM computations are negligible. A closer examination of the waveforms in Figure 6.3 also shows some difference in phasing between the three data sets. Both computed data sets contain high frequency pressure waves in the intake port pressures after intake valve closing at 240° ATDCE. The data from GM show higher amplitudes. The data from PSU shows a low frequency wave overlaid. No high frequency pressure oscillations are seen amidst the noise in the experimental intake port pressures after intake valve closing, but a low frequency wave is present.

In order to reduce the noise in the experimental intake port pressures, a running average over 5° intervals was used to smooth the pressure data. The smoothed experimental intake port pressures reveal high frequency pressure oscillations after intake valve closing, as shown in Figure 6.4. Figure 6.4 compares the cycle-to-cycle variation in intake port pressures for the experimental and computational data sets by plotting the pressure data associated with three cycles from each data set.

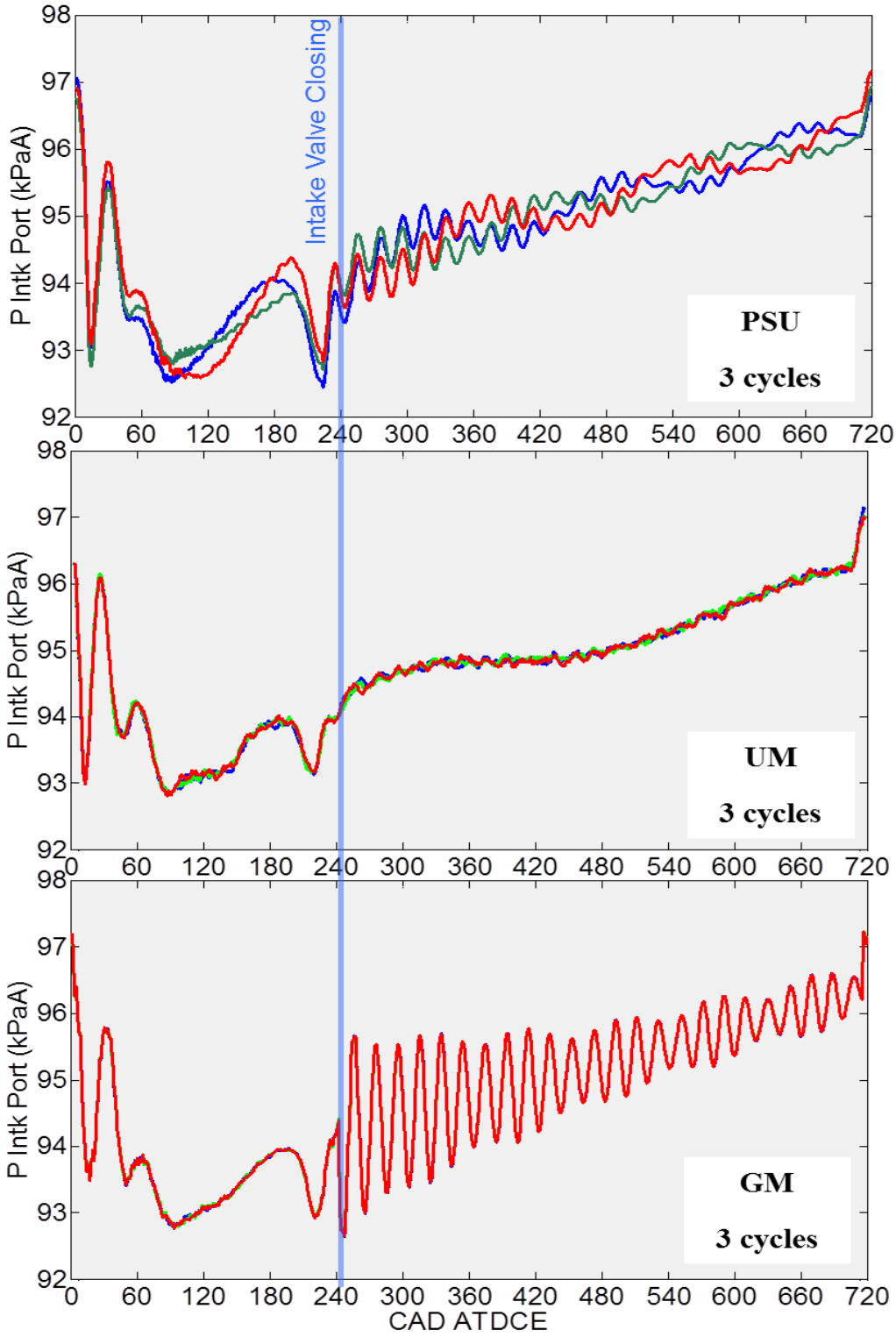

Figure 6.4: *Intake port pressure traces of three cycles each from S_2012_06_21_01 (labeled 'UM') and computational data from GM and PSU*

In Figure 6.4, the PSU intake port pressures show cycle-to-cycle variations both before and after intake valve closing. After intake valve closing, the PSU data shows cycle-to-cycle variations in phase of the low frequency wave, but both the phase and amplitude of the high frequency wave remains unchanged from cycle to cycle. The UM intake port pressure data shows some cycle-to-cycle variation in the phase of the high frequency wave after intake valve closing, but the low frequency wave shows no cyclic variability . The GM intake port pressure data shows negligible cycle-to-cycle variations.

Figure 6.5 shows the pressure drop across the intake valve for three cycles for the experimental (UM) and computational (GM and PSU) data sets. For the experimental data, a running average over 5° was used to smooth both the intake port and cylinder pressures.

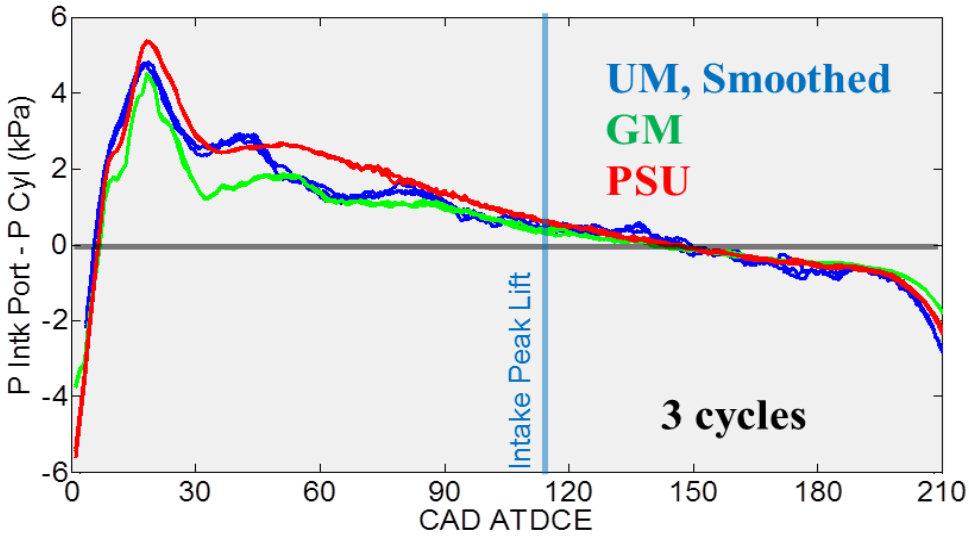

Figure 6.5: *Pressure drop across the intake valve for S_2012_06_21_01 (labeled 'UM') and computational data from GM and PSU*

The pressure drop across the intake valve provides a measure of the mass flow rate into the cylinder. The cycle-to-cycle variation in the pressure drop over three randomly chosen cycles is largest for the experimental data set.

Figure 6.6 compares the measured (UM) and computed (GM and PSU) pressures at the exhaust port (P_Exh_Port) and outlet to the exhaust plenum (P_Exh_Plen_Out). Data from the first 60 cycles of S_2012_06_21_01 and 48 cycles of the GM LES computations were used to compile Figure 6.6.

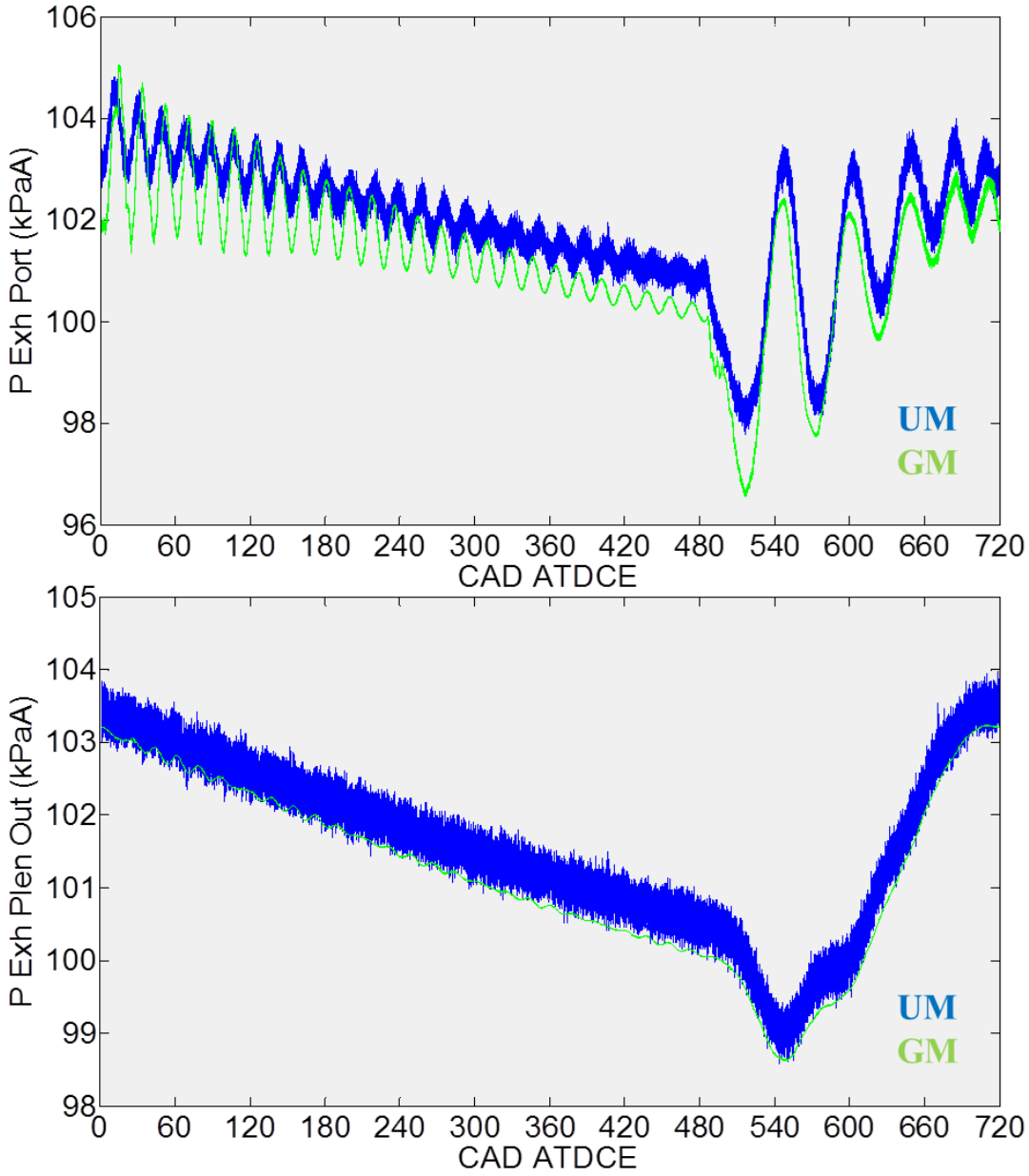

Figure 6.6: *Exhaust system pressures for multiple cycles from S_2012_06_21_01 (labeled 'UM') and computational data from GM*

Figure 6.6 shows that the average pressures measured in the exhaust system are lower for the computational data from GM. The average pressure at the exhaust plenum outlet was 101.59 kPaA for the first 60 cycles of S_2012_06_21_01 and 101.22 kPaA for 48 cycles of the computational data from GM. The nominal pressure boundary condition at the exhaust plenum

outlet was specified as 101.5 kPaA. The amplitude of the high frequency pressure waves in the GM pressure data at the exhaust port before exhaust valve opening at 484° ATDCE are larger in amplitude initially and decay more rapidly than the pressure waves from S_2012_06_21_01. The frequency of these pressure waves is higher for the GM exhaust port pressures. Again, cycle-to-cycle variations in the exhaust system pressures from the GM computations are negligible.

6.2 Comparing In-Cylinder Flow Evolution

In this section, velocity data from throughout the engine cycle (10°-710° ATDCE) from S_2012_06_21_01 and LES computations from GM and PSU are compared. 60 consecutive cycles of velocity data from each data set are studied. As the experimental data set had a lower spatial resolution that the computational data sets, all of the velocity data were interpolated onto a common grid with the same spatial resolution as S_2012_06_21_01. A point on the common grid at a particular crank angle was populated only if there were at least three surrounding non-zero vectors available on the grids at that crank angle from each data set for the interpolation at that point. As an initial assessment, the spatially summed kinetic energy associated with the ensemble average and RMS velocity fields of these interpolated data sets are compared in Figure 6.7.

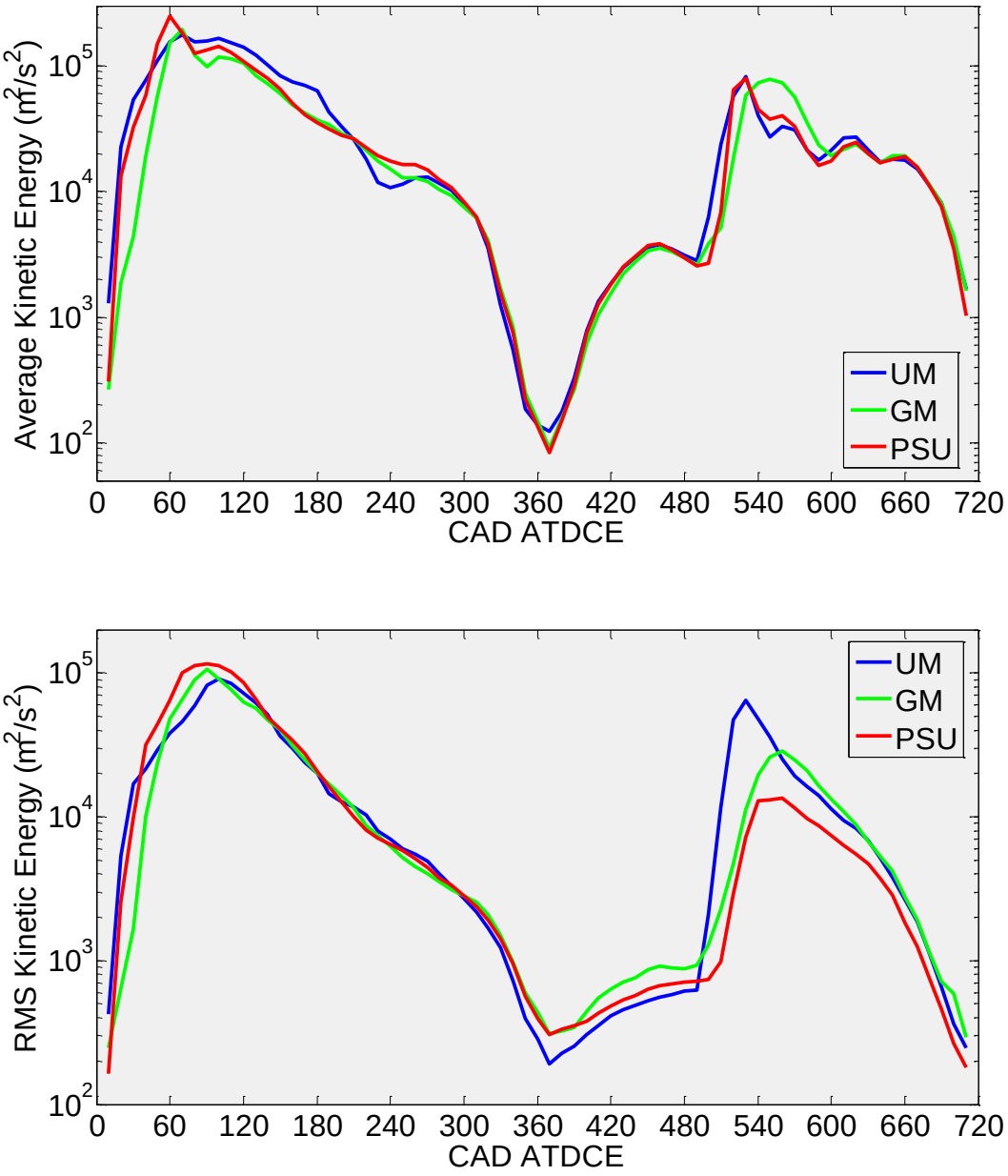

Figure 6.7: *Spatially summed mass-specific kinetic energies of ensemble average and RMS remapped velocity fields from S_2012_06_21_01 (labeled 'UM') and computational data from GM and PSU*

Figure 6.7 shows that during the early part of the intake stroke (approximately 0°-60° ATDCE), the spatially-summed mass-specific kinetic energies of the ensemble average velocity fields from S_2012_06_21_01 and the PSU computations match closely. In the later part of the intake stroke

and during part of the compression stroke (approximately 120°-300° ATDCE), the kinetic energies of the ensemble average fields from the two computational data sets match more closely. Despite the limitations of the low spatial resolution PIV measurements in fully capturing the large exhaust valve backflow velocities (from 484°-540° ATDCE), the kinetic energies of the ensemble average velocity fields from both the experiments and the computations are comparable in magnitude. However, the rise in kinetic energy due to the exhaust backflow occurs later in the cycle for the GM data. The kinetic energies associated with RMS velocity fields scale approximately with the kinetic energies of the ensemble average velocity fields. The largest discrepancy in the kinetic energies of the RMS velocity fields between the three data sets occurs during exhaust valve opening (484°-606° ATDCE).

To further investigate differences in exhaust valve backflow, the ensemble average and RMS remapped velocity fields from all three data sets at 530° ATDCE are shown in Figure 6.8. The experimental ensemble average velocity field shows a greater penetration of the exhaust backflow into the cylinder than either of the computations. The experimental data also has larger areas with high RMS velocities.

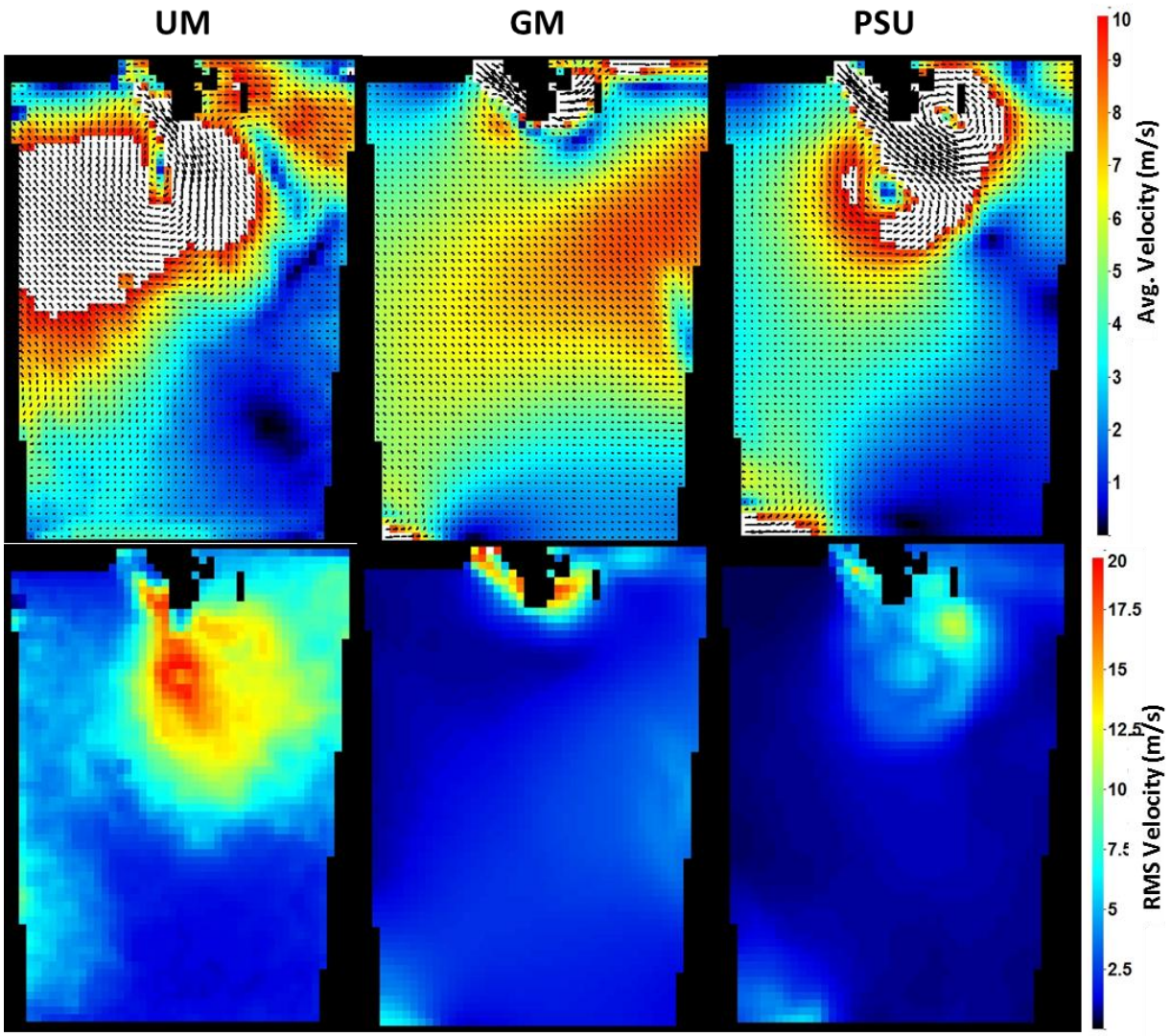

Figure 6.8: *Ensemble average and RMS remapped velocities at 530° ATDCE from S_2012_06_21_01 (labeled 'UM') and the GM and PSU LES computations*

Phase-invariant proper orthogonal decomposition with unity kinetic energy normalization was used to further assess differences in flow structures between the experimental and computational data sets. As phase-invariant POD requires that all vector fields from all crank angles be on the same grid, the interpolated velocity fields were spatially transformed as their grid was stretched or compressed to match that at engine midstroke. Unity kinetic energy

normalization was also used to ensure that velocity fields from crank angle ranges with higher kinetic energy did not dominate the decomposition. Figure 6.9 shows the first three modes from the analysis.

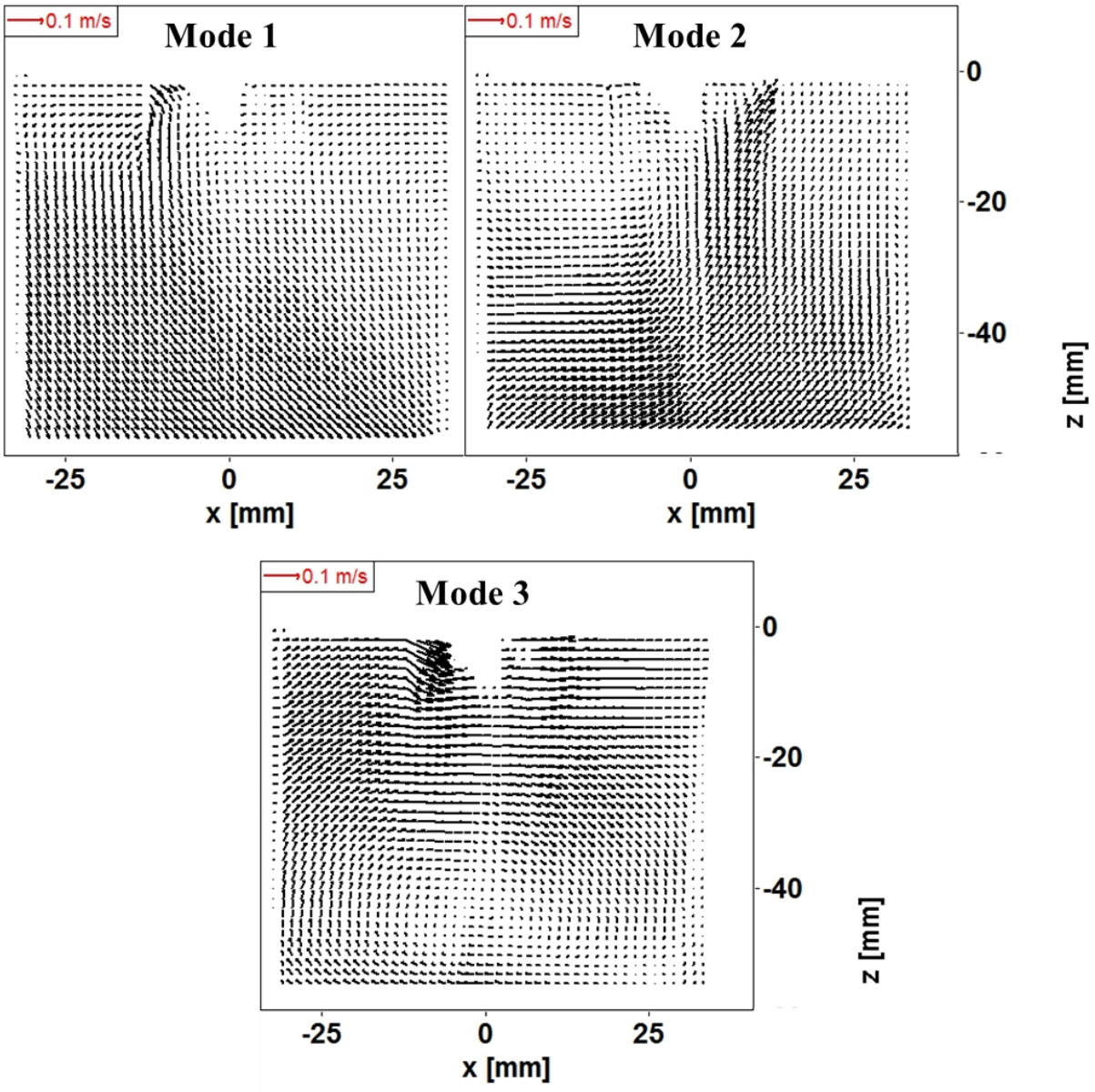

Figure 6.9: *First three modes from phase-invariant POD analysis of S_2012_06_21_01 and the GM and PSU LES computations*

Mode 1, with an energy fraction of 29%, shows some aspects of the exhaust jet and flow towards the bottom-right corner of the field-of-view. Mode 2, with an energy fraction of 13%, shows some aspects of the intake jet and upward flow from the piston. Mode 3, with an energy fraction of 11%, shows more of the exhaust jet, as well as a large-scale tumble vortex.

Figure 6.10 shows the coefficients associated with the first three phase-invariant POD modes. The Mode 1 coefficients between 180° ATDCE and exhaust valve opening at 484° ATDCE indicate that the flow pattern in Mode 1 represents the piston-induced upward or downward flow, as well as the exhaust jet flow after 540° ATDCE. From 390°-490° ATDCE, the Mode 1 coefficients of the experimental data show higher average values and less spread than those associated with the computational data sets. This suggests that in the expansion stroke the piston-induced downward flow is more dominant in the experiments. The Mode 2 coefficients from the computational data sets show larger spread throughout the cycle, suggesting more cycle-to-cycle flow variability in the computational data sets. From 540°-660° ATDCE, the Mode 2 coefficients from the experimental data set and the GM computations have opposite signs, indicating opposite contributions of Mode 2 to the flow patterns of these data sets. The Mode 3 coefficients show the formation and breakdown of the large-scale tumble vortex during the intake and compression strokes. The Mode 3 coefficients for the GM computations indicate a difference in the breakdown of the tumble vortex for this data set.

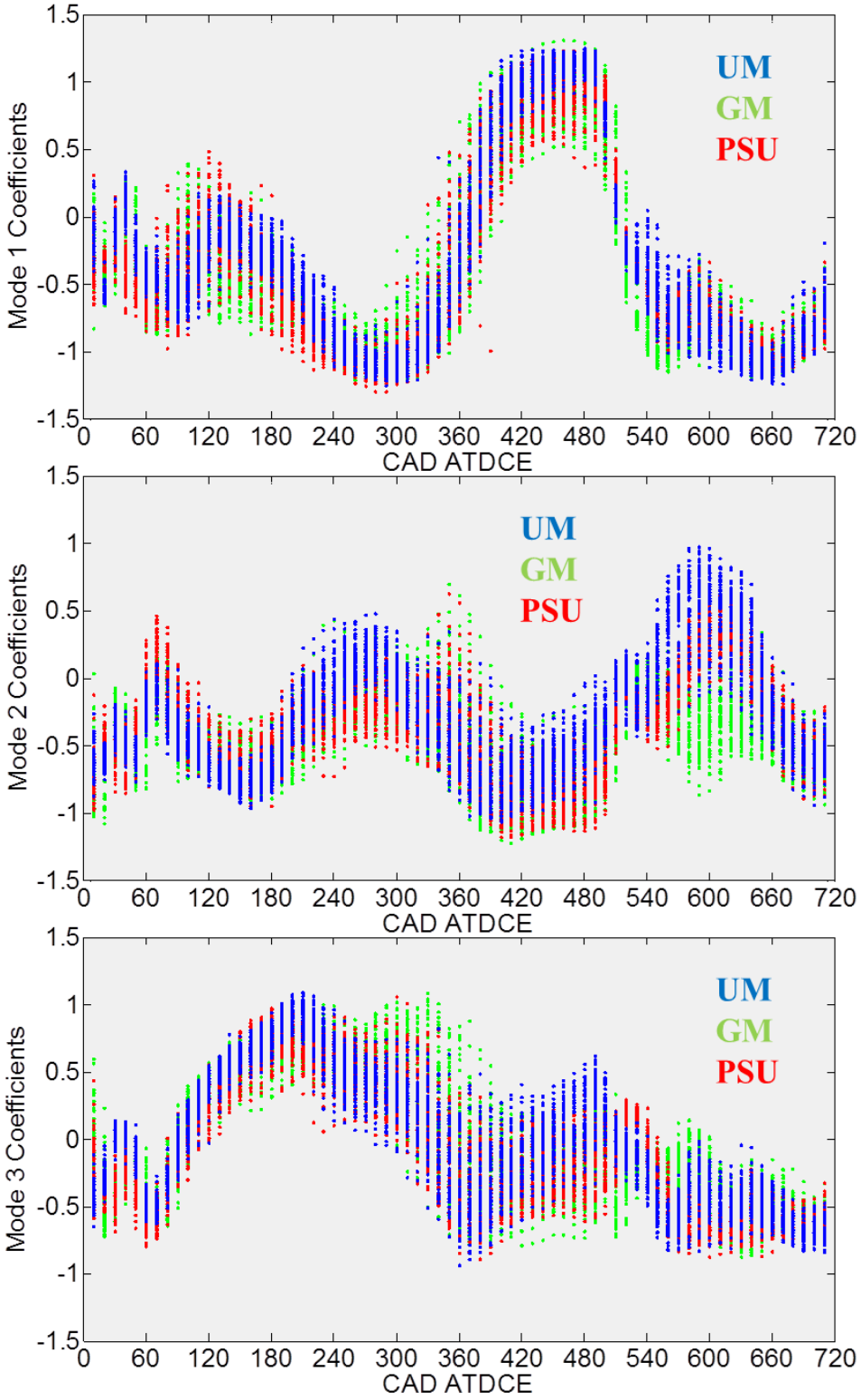

Figure 6.10: *Coefficients of the first three modes from phase-invariant POD analysis of S_2012_06_21_01 and the GM and PSU LES computations*

6.3 In-Cylinder Flow at 100° ATDCE

Discrepancies between the phase-invariant coefficients associated with the experimental and computational data sets during intake valve actuation (12°-240° ATDCE) suggest differences in the intake flow that should be further examined using phase-dependent POD. Thus, a phase-dependent POD analysis of velocity data at 100° ATDCE from the first 60 cycles of S_2012_06_21_01 and 60 cycles each of the GM and PSU LES computations was performed. Again, all velocity fields were interpolated onto a common grid with the same spatial resolution as the low spatial resolution data from S_2012_06_21_01.

Figure 6.11 presents the first three modes from the phase-dependent POD analysis of 100° ATDCE data. Mode 1, with an energy fraction of 56%, shows aspects of the intake jet and the counter-rotating vortices seen in ensemble average velocity fields at 100° ATDCE. Mode 2, with an energy fraction of 8%, shows an upward flow from the bottom-right of the field-of-view. Mode 3, with an energy fraction of 3%, shows aspects of the intake jet, upward flow in the bottom-left corner of the field-of-view, and a vortex below the spark plug.

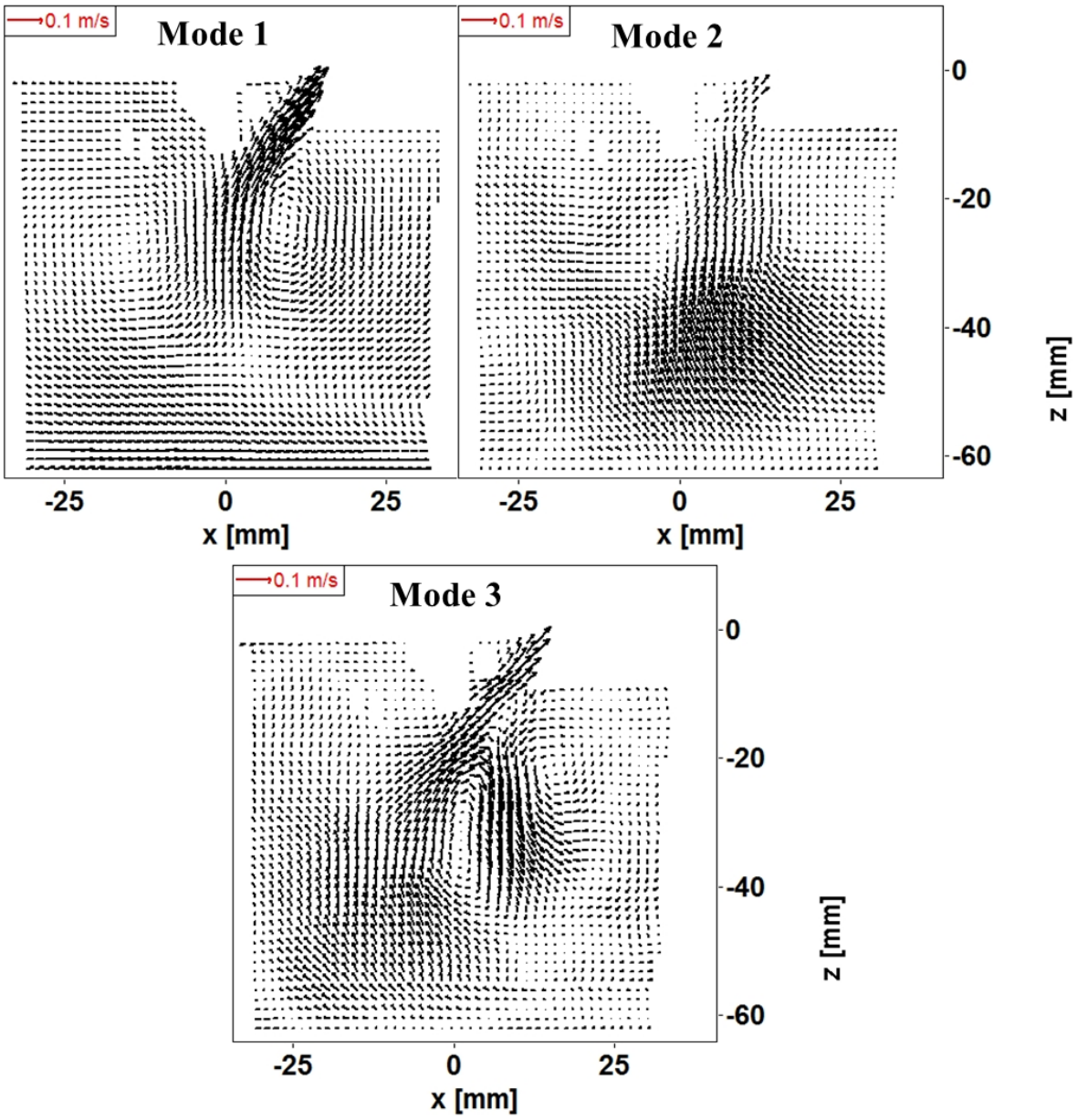

Figure 6.11: *First three modes from phase-dependent POD analysis of velocity data at 100° ATDCE from S_2012_06_21_01 and the GM and PSU LES computations*

The coefficients of the first three modes of the POD analysis are shown in Figure 6.12.

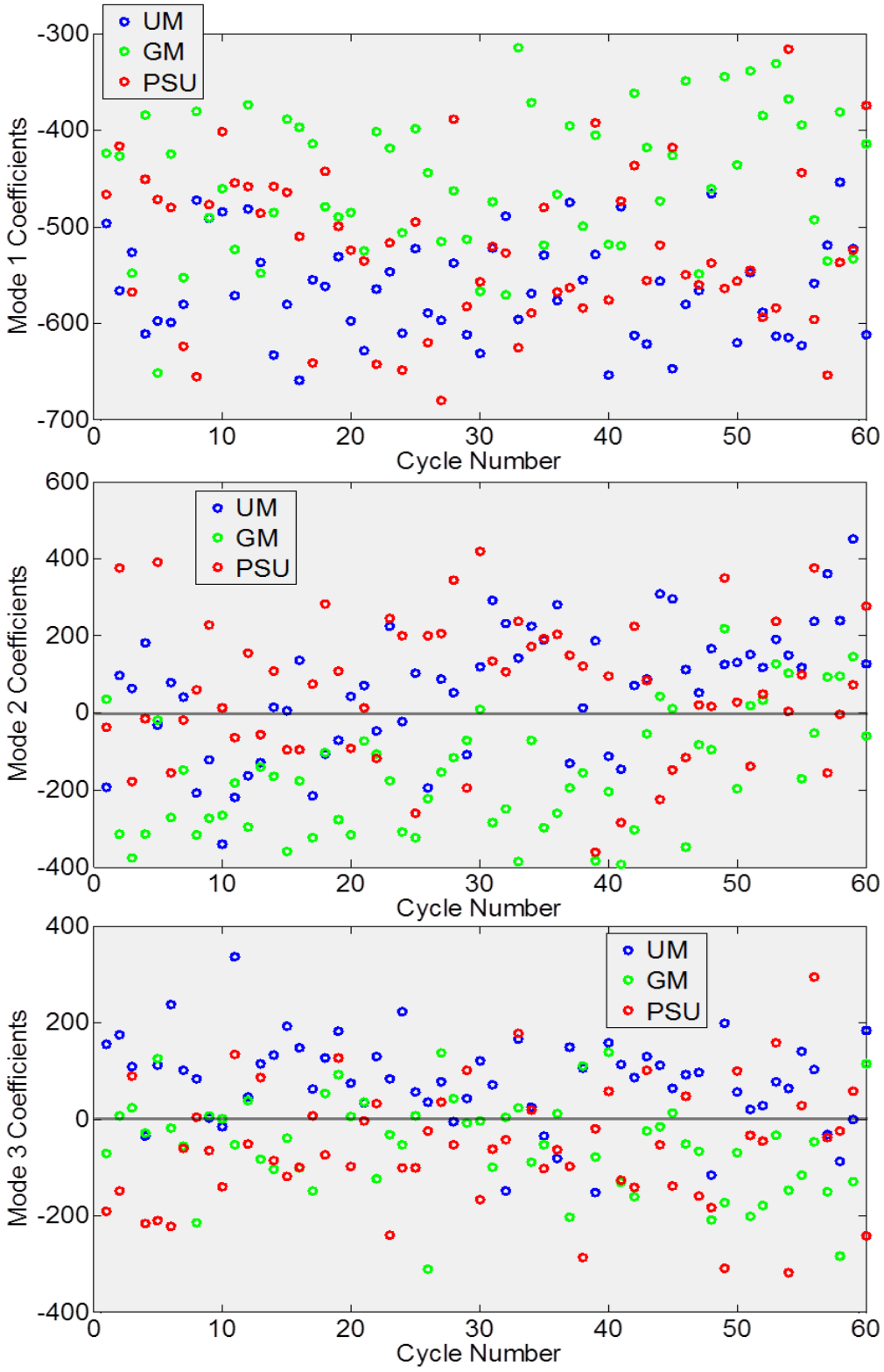

Figure 6.12: *Coefficients associated with the first three modes from the phase-dependent POD analysis of100° ATDCE data from S_2012_06_21_01 and the GM and PSU LES computations*

The coefficients associated with the PSU data in Figure 6.12 show more spread than those associated with the other two data sets. This indicates greater cycle-to-cycle variations in the velocity fields from the PSU computations. The separation between the coefficients associated with the UM and GM data suggest that the ensemble average velocity fields from these data sets at 100° ATDCE would be significantly different from each other. In fact, most of the coefficients associated with the UM and GM data from Modes 2 and 3 have opposite signs, which shows that these modes, on average, contribute oppositely to individual velocity fields at 100° ATDCE from the UM and GM data sets. Despite the larger spread in the PSU coefficients, Figure 6.12 shows that for Modes 1 and 2, the UM and PSU coefficients share a similar range of values, suggesting that the ensemble average velocity fields from these data sets at 100° ATDCE would be similar.

Figure 6.13 shows the ensemble average velocity fields at 100° ATDCE from all three data sets, along with relevance indices that quantify the differences between them. Figure 6.13 confirms the dissimilarity between the UM and GM data sets at 100° ATDCE with a relevance index between the ensemble averages that is less than 0.9, and the similarity between the UM and PSU data sets at 100° ATDCE with a relevance index above 0.9. Both the UM and PSU ensemble averages at 100° ATDCE show an upward flow from the bottom-right corner of the field-of-view. However, the GM ensemble average shows a downward flow toward the bottom-right corner. In Chapter 5 it was shown that these two different flow patterns occur in any experimental data set with the dominating flow pattern for a particular data set determined by the extent of cycle-to-cycle variations in intake valve position. The GM and PSU LES computations discussed in this chapter did not replicate the experimentally observed cycle-to-cycle variations in intake valve position. Thus, the different dominant flow patterns seen in the GM and PSU computations may be a result of the difference in the extent of cycle-to-cycle variations in intake

port pressure between the PSU and GM data sets, or due to some difference in the computational algorithms or software. More LES data sets are required to determine if the dominant flow pattern changes from data set to data set.

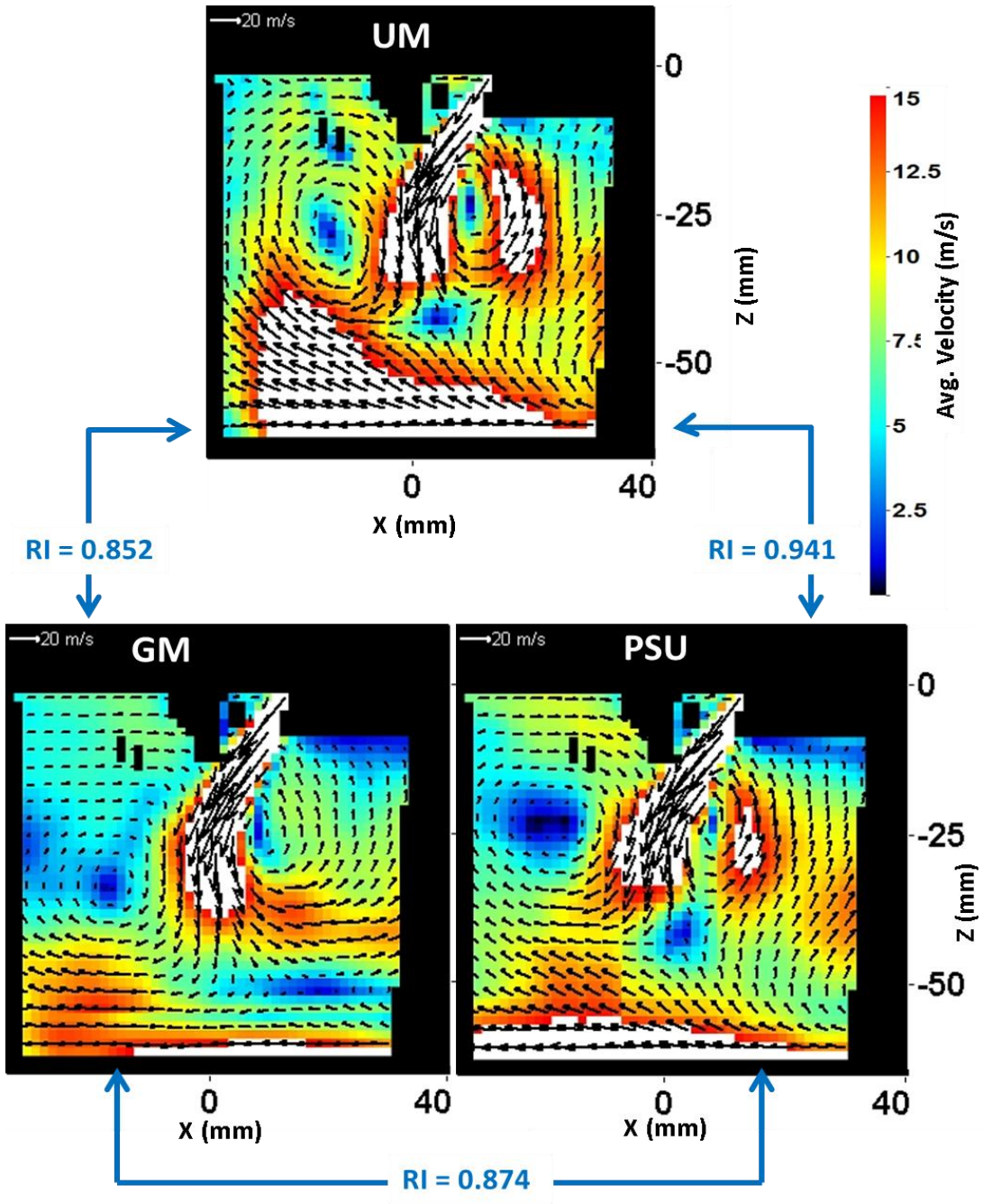

Figure 6.13: *Ensemble average velocity fields at 100° ATDCE from S_2012_06_21_01 (labeled 'UM') and the GM and PSU computations (RI – Relevance Index; every second vector shown)*

Figures 6.14 and 6.15 present the results of a more in-depth unpublished examination of the three-dimensional GM data at 100° ATDCE conducted at General Motors Research and Development [68]. Figure 6.14 shows that in a two-dimensional vertical plane + 5° away from the Y = 0 plane, the flow in the bottom-right corner is upward, and in a plane - 5° away from the Y = 0 plane, the flow in the bottom-right corner is downward. An examination of the out-of-plane velocity component (V) in the Y = 0 plane, shown in Figure 6.15, reveals a large positive out-of-plane velocity in the bottom-right corner of the cylinder. It is possible that cycle-to-cycle variations in this velocity may have resulted in the cycle-to-cycle variations in the flow pattern seen in the Y = 0 plane. A similar examination of the three-dimensional PSU data has not yet been performed.

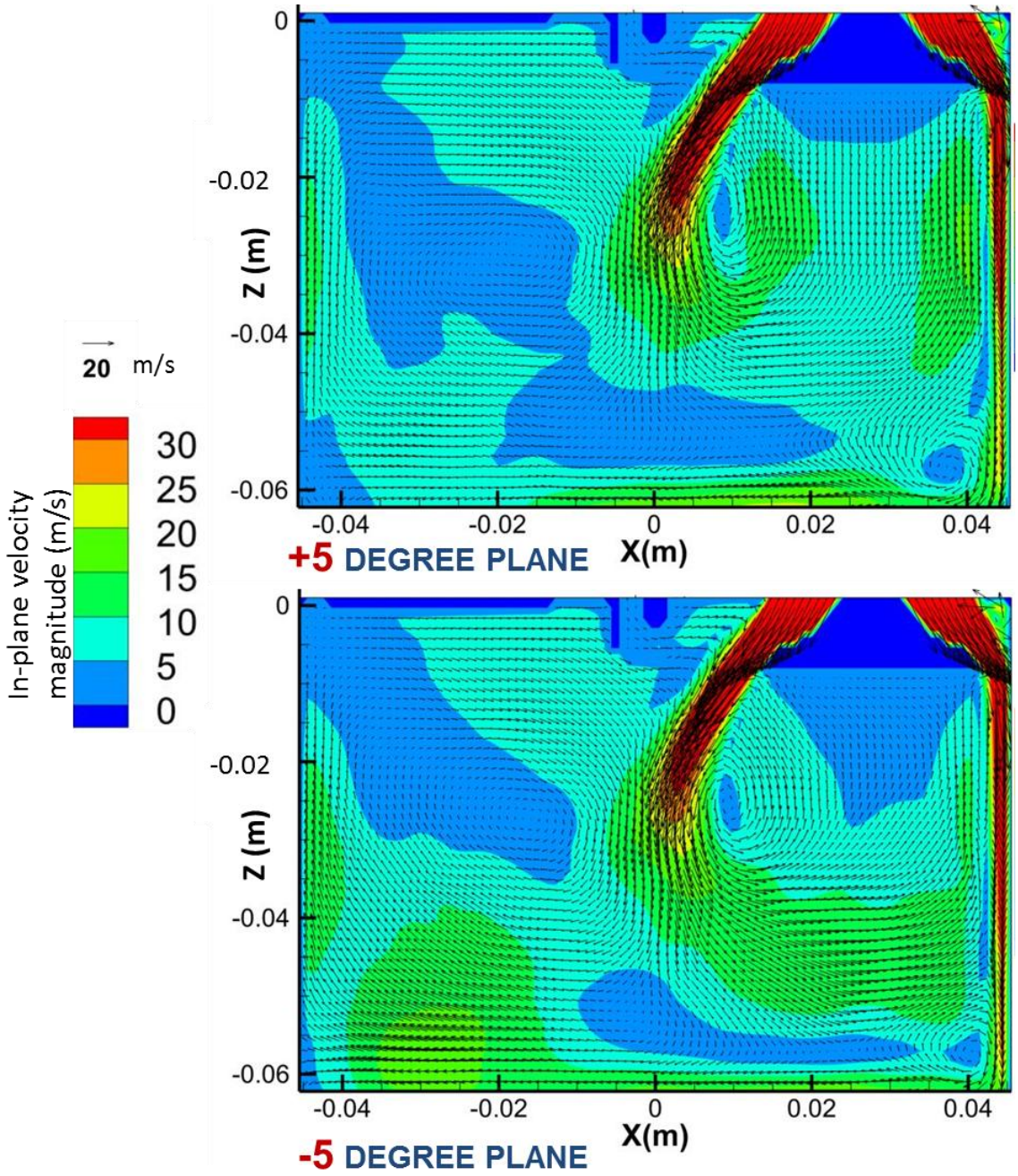

Figure 6.14: In-plane velocity in vertical planes ± 5° with respect to the Y axis at 100° ATDCE from GM LES computations [68]

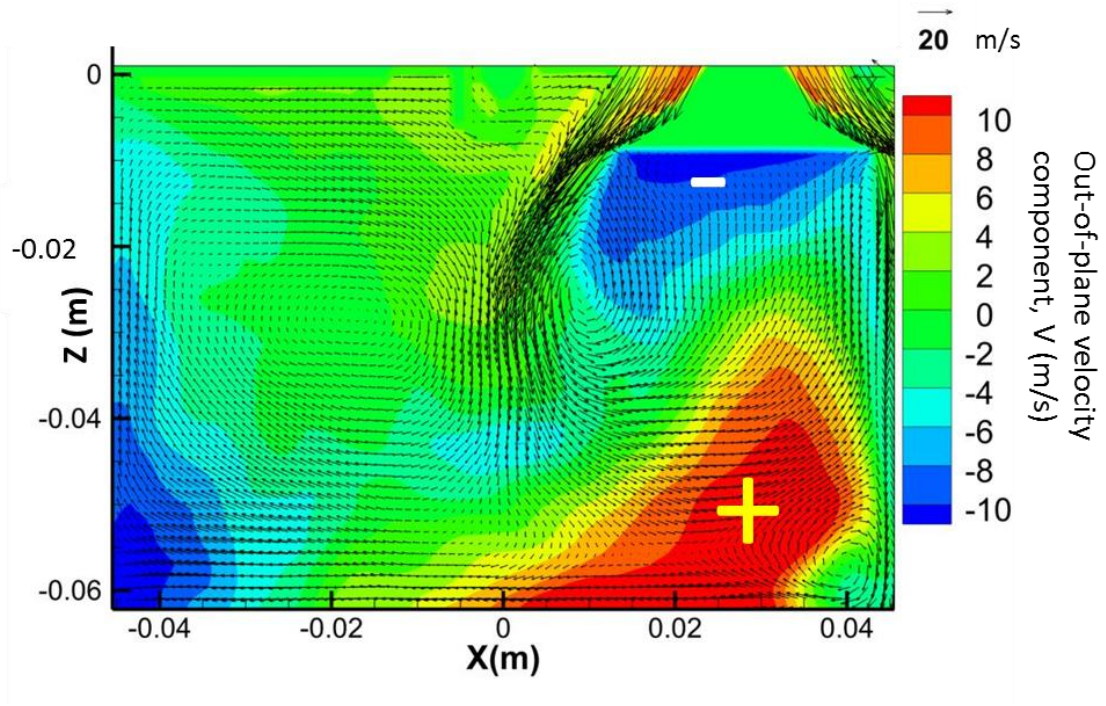

Figure 6.15: Three-component velocity in Y = 0 plane at 100° ATDCE from GM LES computations [68]

Figure 6.16 shows the RMS velocity fields at 100° ATDCE from all three data sets, confirming that the PSU data shows greater cycle-to-cycle variations at this crank angle.

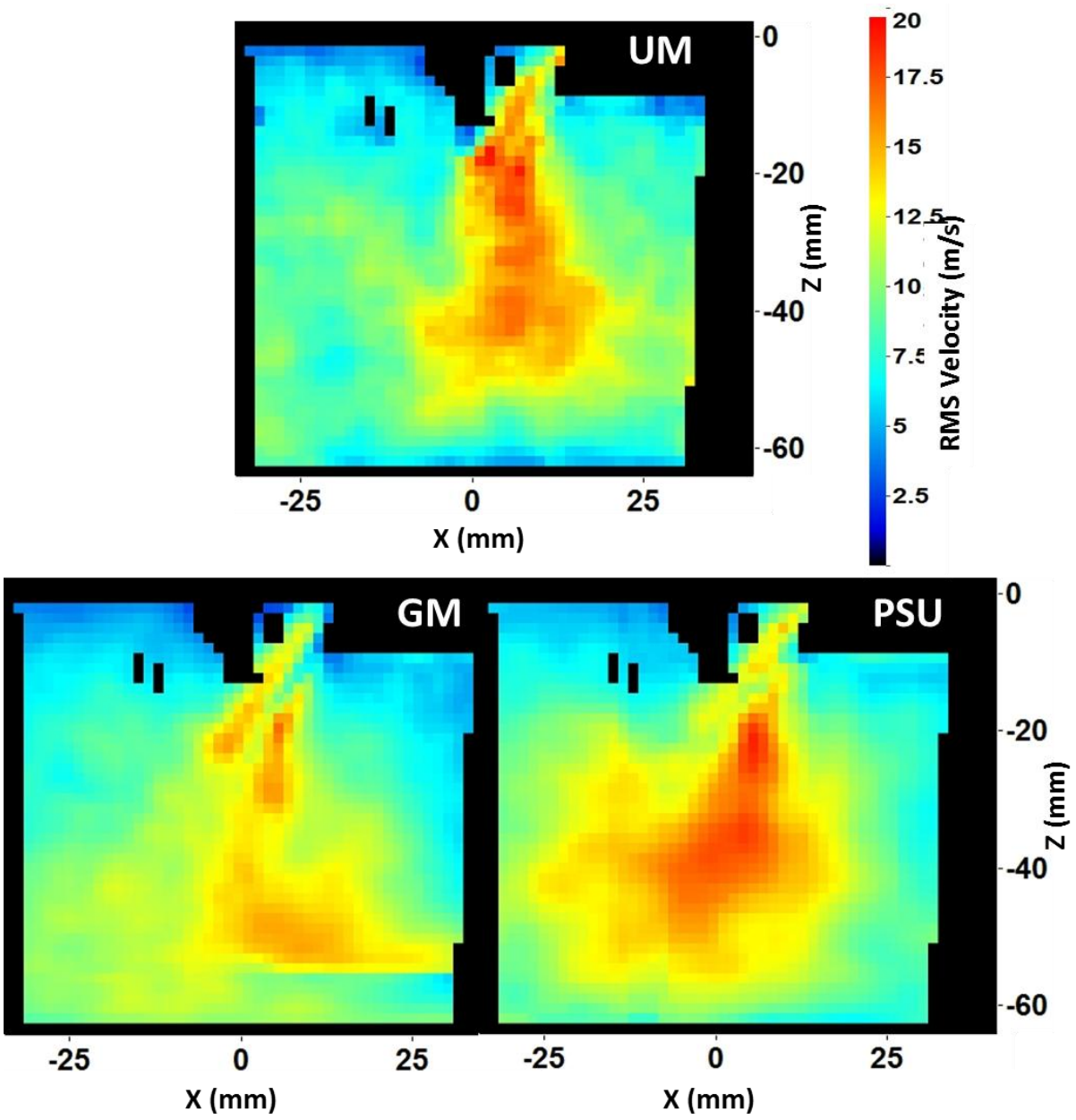

Figure 6.16: *RMS velocity fields at 100° ATDCE from S_2012_06_21_01 (labeled 'UM') and the GM and PSU computations*

Coefficients from a phase-dependent POD analysis can also be used to quantify cycle-to-cycle variability in the kinetic energy contributions of the mean flow and the turbulent flow to individual velocity fields by establishing Mode 1, or a combination of lower order modes, as an estimate of the mean flow, and higher order modes as an estimate of RANS turbulence [17, 18].

Mode 1 was compared to the mean flow at 100° ATDCE by calculating relevance indices. These values are presented in Table 6.1.

	Mode 1
S_2012_06_21_01 (UM)	-0.977
GM	-0.930
PSU	-0.977

Table 6.1: *Relevance indices between Mode 1 of the phase-dependent POD analysis and ensemble average velocity fields at 100° ATDCE*

As the relevance indices between the mean flow of each data set and Mode 1 at 100° ATDCE are greater than 0.9, Mode 1 is a good estimate of the mean flow.

Figure 6.17 estimates the cycle-to-cycle variability in the kinetic energy contributions of the mean flow and the RANS turbulence to individual cycles in S_2012_06_21_01 and the GM and PSU LES computations.

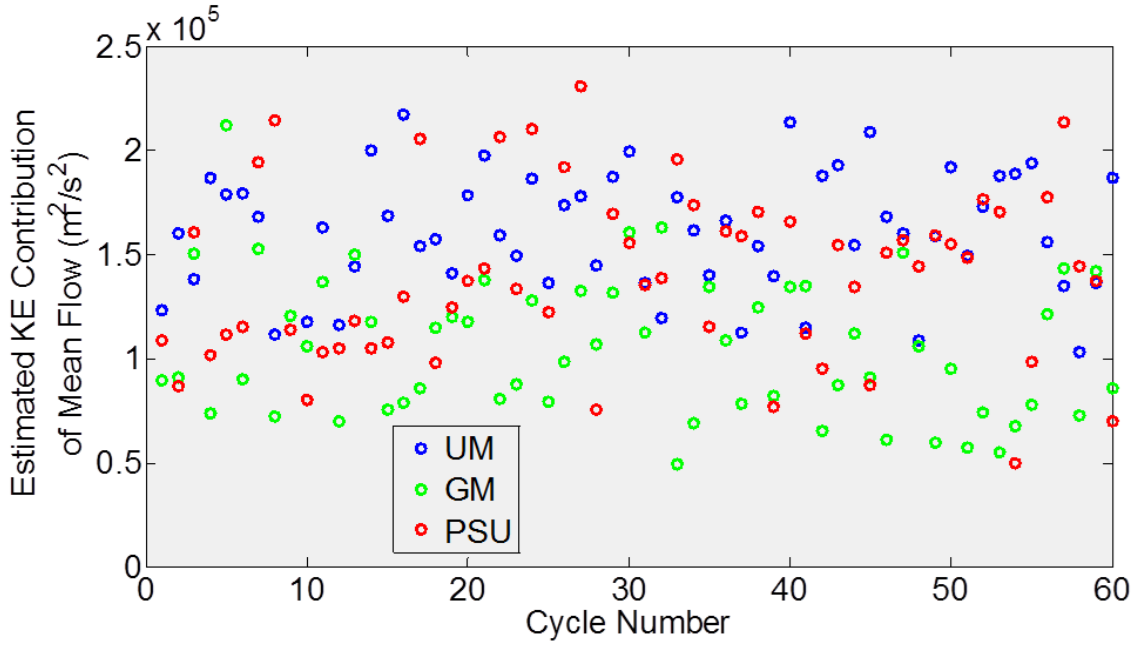

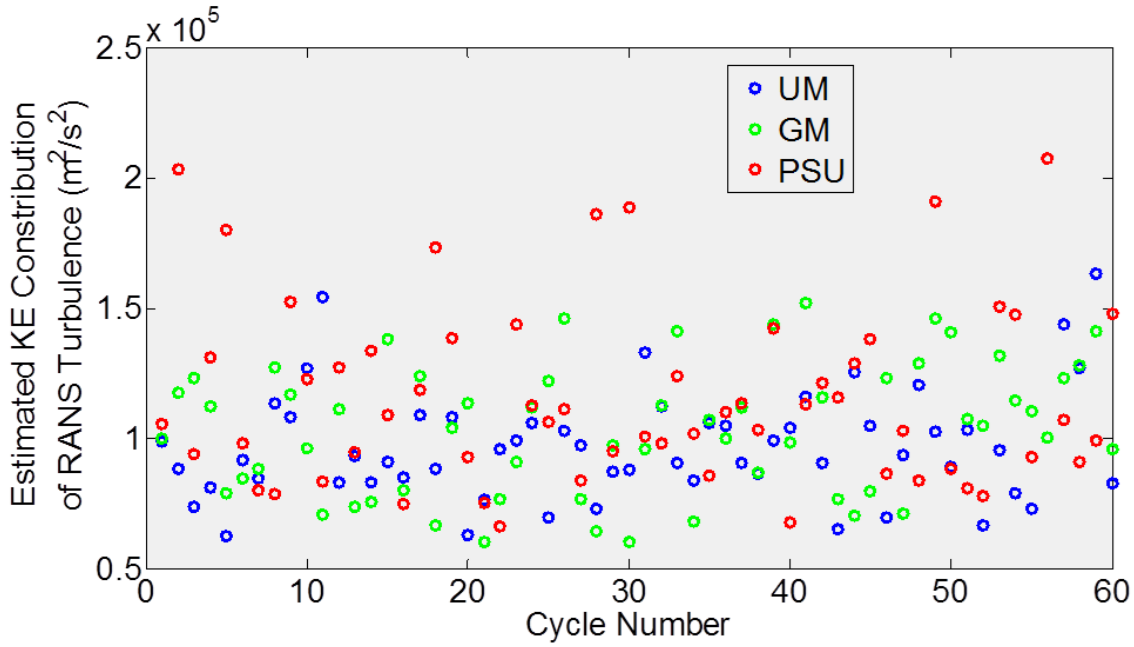

Figure 6.17: *Estimated mass-specific kinetic energy contributions of the ensemble average and fluctuating flow to S_2012_06_21_01 (labeled 'UM') and the GM and PSU LES computations at 100° ATDCE*

As suggested by Figure 6.12, the estimated kinetic energy contributions of the mean flow to the PSU data set show the most cycle-to-cycle variations. The GM data set has, on average, lower kinetic energy contributions from the mean flow. The PSU data set also shows the most cycle-to-cycle variations in the estimated kinetic energy contributions of the turbulent flow. Turbulent kinetic energy contributions to the UM and GM data sets have similar ranges.

6.4 In-Cylinder Flow at 300° ATDCE

A phase-dependent POD analysis of the first 60 cycles of S_2012_06_21_01 and 60 consecutive cycles each of the GM and PSU LES computations was performed to obtain a better understanding of the variability of in-cylinder flow structures at 300° ATDCE, and to see if the different dominating flow patterns at 100° ATDCE these data sets result in similar differences between them during the compression stroke. The computational velocity data were interpolated

onto a common grid with the same spatial resolution as the low spatial resolution data from S_2012_06_21_01. The first three modes from the phase-dependent POD analysis are shown in Figure 6.18.

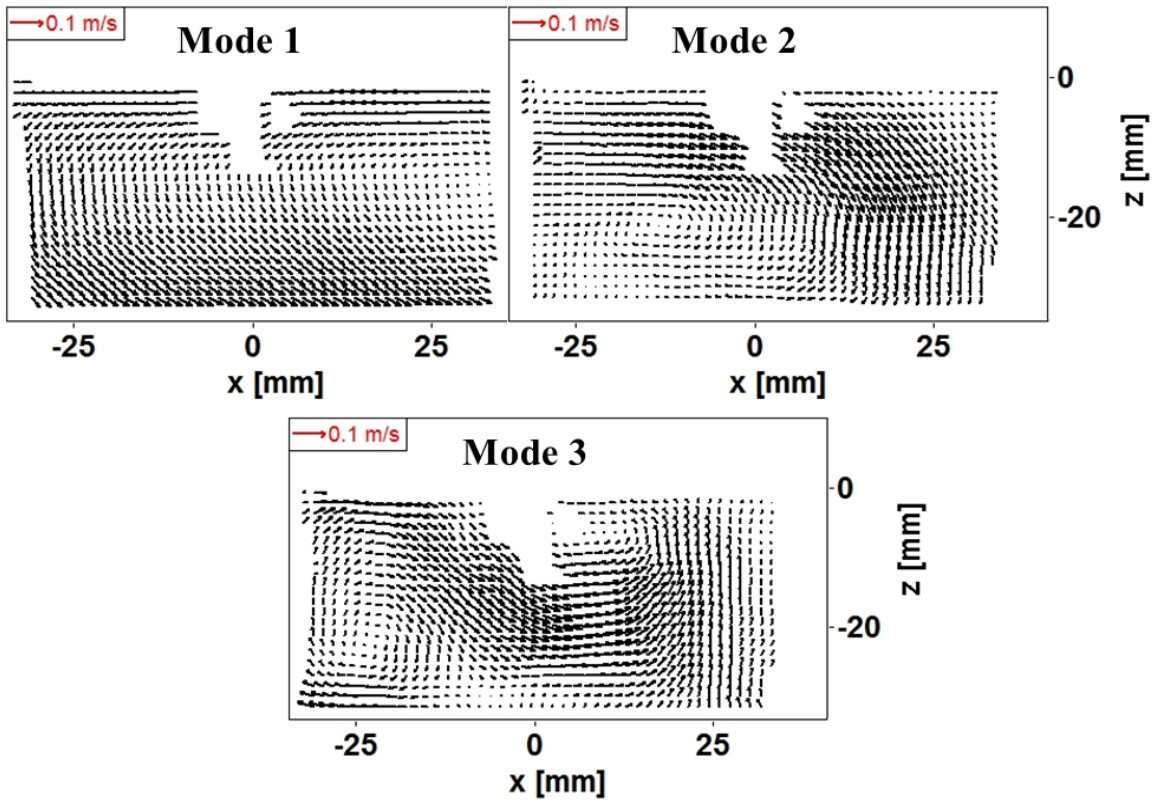

Figure 6.18: *First three modes from phase-dependent POD analysis of 300° ATDCE velocity fields from S_2012_06_21_01 and the GM and PSU LES computations*

Mode 1, with an energy fraction of 73%, shows aspects of a piston-driven flow and part of a vortex in the right-hand side of the field-of-view. Mode 2, with an energy fraction of 4%, shows a vortex to the left of and below the spark plug. Mode 3, with an energy fraction of 3%, shows flow from the left to the right of the field-of-view about the spark plug and a vortex in the bottom-left corner.

Figure 6.19 shows the coefficients associated with the first three modes of the phase-dependent POD analysis.

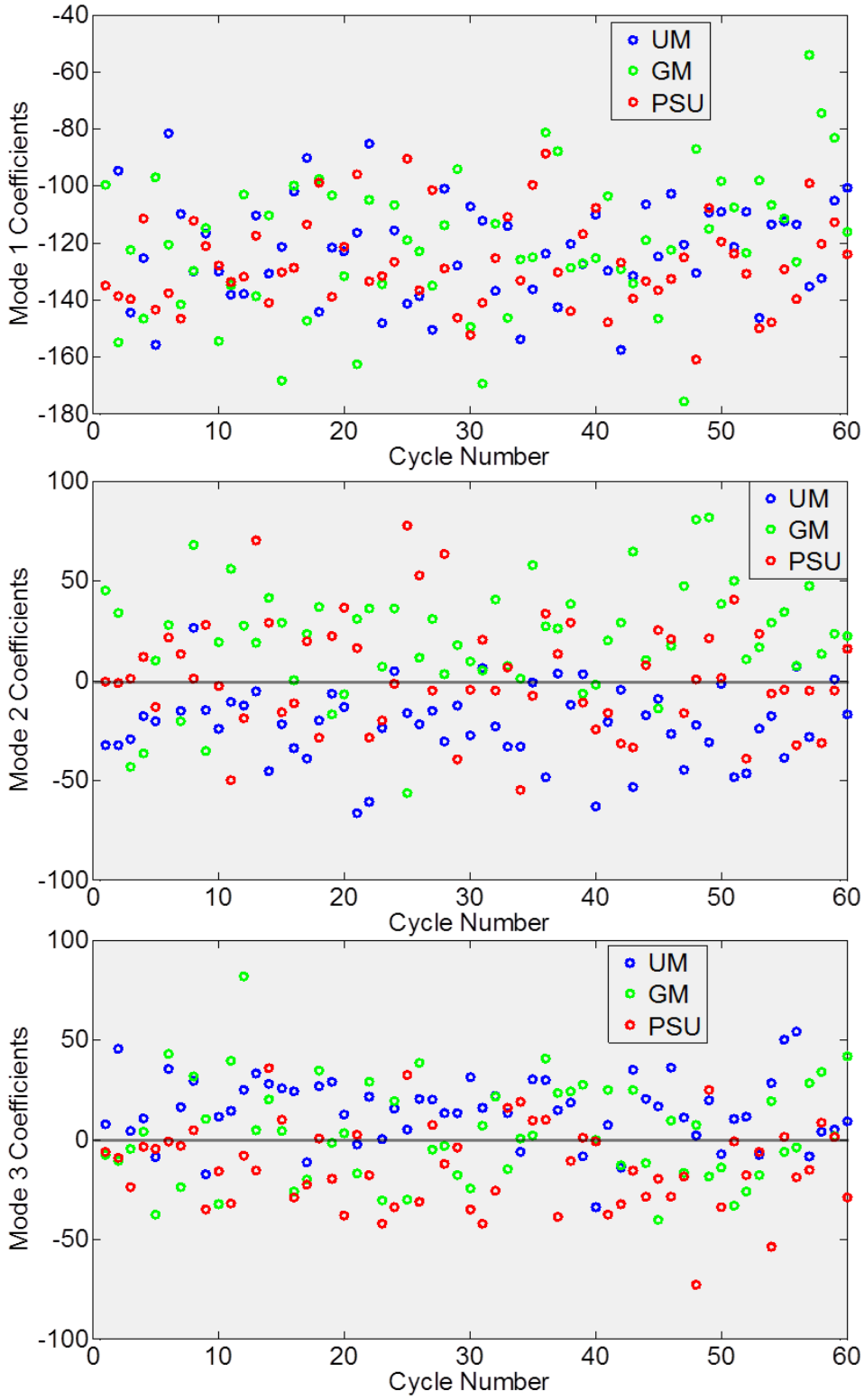

Figure 6.19: *Coefficients of the first three modes from the phase-dependent POD analysis of S_2012_06_21_01 (labeled 'UM') and the GM and PSU LES computations at 300° ATDCE*

The Mode 1 coefficients from the UM and PSU data sets occupy a similar range. The GM Mode 1 coefficients have a larger spread, indicating greater cycle-to-cycle variability in this data set at 300° ATDCE. This may be related to the dominant flow pattern at 100° ATDCE in the GM data set being different from that seen in the UM and PSU data sets. However, such a difference in the cycle-to-cycle variability of Mode 1 coefficients was not seen in the comparisons performed in Chapters 5 and 6. The Mode 2 coefficients of the GM data set have, on average, signs opposite that of the UM Mode 2 coefficients. However, the Mode 3 coefficients of the UM and PSU data sets have, on average, opposing signs. Thus, there are no conclusive difference between the GM data set and the UM and PSU data sets at 300° ATDCE.

Mode 1 was compared to the mean flow of all three data sets using relevance indices to assess its value as an estimate of the mean flow. The relevance indices calculated were all found to have an absolute value above 0.97, indicating that Mode 1 is a good estimate of the mean flow for all three data sets. The higher order modes provide an estimate of the RANS turbulence. Figure 6.20 shows the estimated mass-specific kinetic energy contribution of the mean and turbulent flows to individual flow fields at 300° ATDCE. These kinetic energy contributions are of similar magnitude and distribution for all three the data sets.

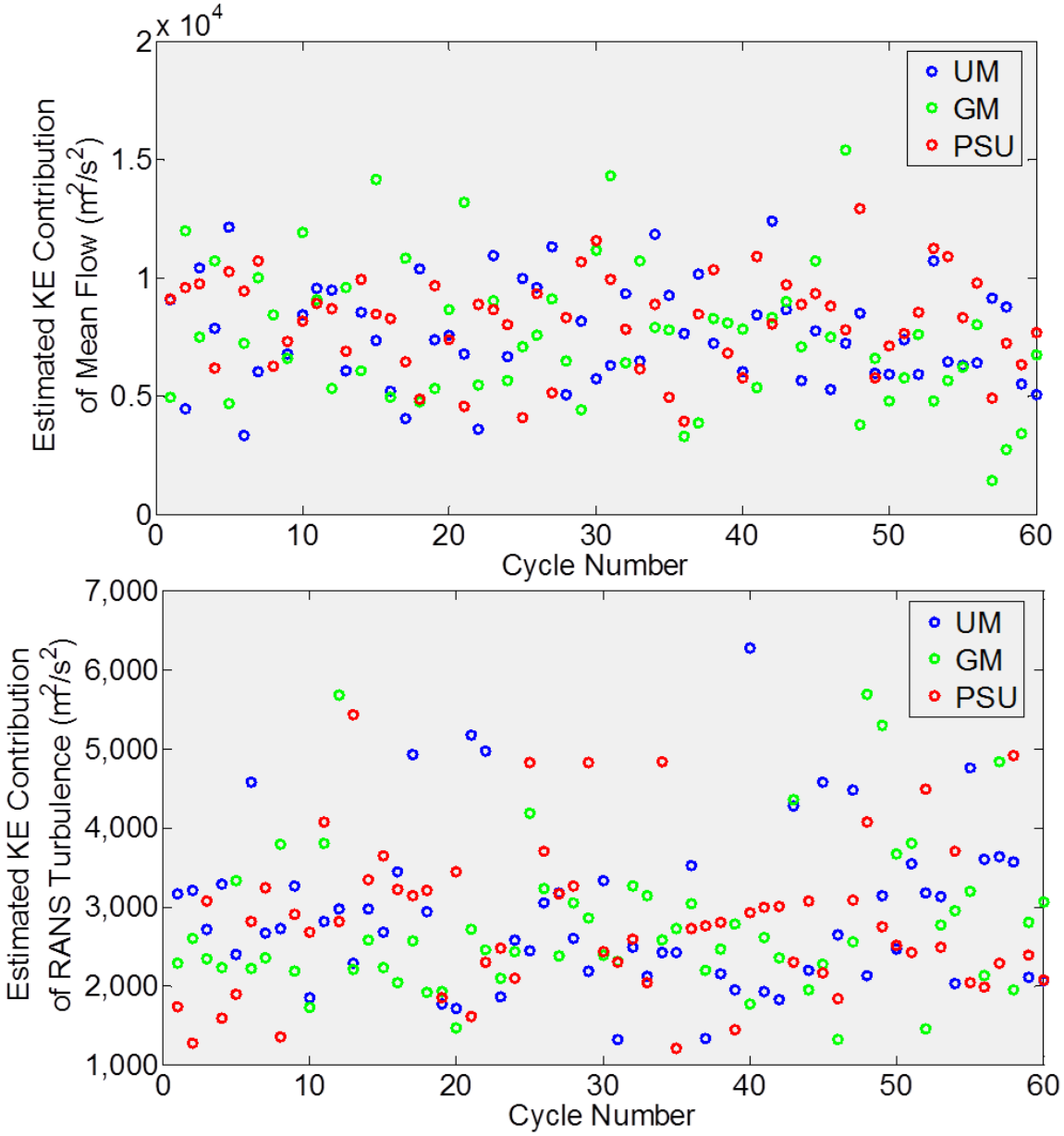

Figure 6.20: *Estimated mass-specific kinetic energy contributions of the ensemble average and fluctuating flow to S_2012_06_21_01 (labeled 'UM') and the GM and PSU LES computations at 300° ATDCE*

6.5 Summary

In this chapter, experimental data acquired at 800 rpm is quantitatively compared to two sets of large-eddy simulation data using POD. Phase-invariant POD of the combined

experimental and computational data set showed that POD coefficients can accurately trace in-cylinder flow evolution and variations. Phase-dependent POD of the combined flow fields at 100° ATDCE showed that the difference in flow patterns between different PIV sets seen in the earlier chapters also exists between the two LES data sets presented here. However, phase-dependent POD at 300° ATDCE showed no conclusive difference between the data sets.

CHAPTER 7

CONCLUSION

Cycle-to-cycle combustion variations, including misfires and partial burns, inhibit the development of cleaner and more efficient internal combustion engine technologies, such as direct injection spark ignition, exhaust gas recirculation, and the use of lower idle speeds. One of the leading causes of cycle-to-cycle combustion variations is thought to be cycle-to-cycle in-cylinder flow variations. This dissertation attempts to characterize the effect of cycle-to-cycle flow variations in the intake flow on cycle-to-cycle in-cylinder flow variations later in the cycle in an optical research engine. The potential causes of intake flow variations, such as intake system pressure fluctuations, intake valve oscillations, and engine speed variations, were also investigated. The scaling of in-cylinder flow with engine speed was studied by measuring in-cylinder velocities at three different engine speeds. Further, experimentally acquired data was compared to two different large-eddy simulation data sets. Proper orthogonal decomposition was used to quantitatively compare flow patterns in different data sets. Both phase-dependent POD, where velocity fields at the same crank angle from different cycles are analyzed together, and phase-invariant POD, where velocity fields from a range of crank angles from different cycles are analyzed together, were utilized.

To study the relationship between intake valve oscillations and in-cylinder flow, three particle image velocimetry data sets acquired at 800 rpm were examined. Four subsets with an

equal number of cycles were extracted from these data sets and ensemble average velocity fields were calculated at 100° ATDCE. Two different flow patterns were seen in the ensemble average velocity fields, one with an upward flow from the bottom-right corner of the field-of-view and the other with a downward intake jet flow towards the bottom-right corner. A phase-dependent POD analysis of velocity fields at 100° ATDCE revealed that mode coefficients may be used to identify these two different flow patterns in individual cycles from all four data subsets. While investigating the effect of pressure variations on in-cylinder flow, the coefficient of variation in in-cylinder pressure for the three data sets was found to be approximately 0.5% or less, and the spread in intake system pressure traces was found to be 1-2%. However, no correlation was found between intake port pressure or the pressure drop across the intake valve and the in-cylinder flow pattern of individual cycles in the PIV measurement plane during the intake stroke. It is possible that flow in other areas of the cylinder was affected by these pressure variations, but, in the experiments presented in this dissertation, PIV data was only acquired in the central tumble plane.

In the optical engine used in the experiments presented in this dissertation, both the intake and exhaust valves experienced horizontal oscillations during valve opening and closing. A comparison of ensemble average flow patterns and variations in intake valve position at 100° ATDCE showed that data subsets with a dominant flow pattern of upward flow from the bottom-right corner also had variations in intake valve horizontal position. Further, a comparison of POD coefficients and intake valve horizontal position at 100° ATDCE showed that cycles in which the intake valve was closer to the centerline of the cylinder had, on average, upward flow of greater magnitude from the bottom-right corner of the field-of-view at 100° ATDCE. However, it was

not possible to establish a one-on-one connection between intake valve motion and intake flow in the PIV measurement plane for individual cycles.

In order to study the relationship between engine speed and in-cylinder flow patterns during the intake stroke, one of the three data sets acquired at 800 rpm with engine speed transients was examined further. This data set had variations in engine speed of approximately ± 1% of the desired engine speed. A correlation was found between one of the engine speed transients, during which the engine speed rapidly decreased, and a shift in dominant flow pattern during the intake stroke. Thus, the engine speed transient may have triggered a change in intake valve oscillations that then resulted in a shift in dominant flow pattern. However, the other engine speed transient that occurred in this data set, during which the engine speed rapidly increased, did not correspond with a shift in dominant flow pattern.

Phase-dependent POD was performed at 300° ATDCE for two of the four data subsets to investigate the effect of differences in dominant flow patterns during the intake stroke on flow patterns observed during the compression stroke. Some small differences (on the order of an average of 4% of the kinetic energy in each velocity field) were seen between the two subsets.

POD was also used to quantitatively compare experimental and computational data sets at 800 rpm. Phase-invariant POD of experimental data and large-eddy simulation data from collaborators at General Motors Research and Development and Pennsylvania State University showed that POD coefficients can accurately reflect differences in in-cylinder flow evolution and variation. Phase-dependent POD at 100° ATDCE showed that the experimental data and the data from the PSU computations had similar flow patterns at 100° ATDCE, with upward flow from the bottom-right corner of the field-of-view, while the GM data set had velocity vectors in the opposite direction in that part of the field-of-view. The spread in POD coefficients also indicated

that the PSU data set had more cycle-to-cycle variability. These conclusions based on the POD coefficients were also confirmed by ensemble average and RMS velocity fields at 100° ATDCE. However, phase-dependent POD at 300° ATDCE showed no conclusive differences between experimental and computational data sets.

High-speed PIV and pressure data was acquired at three different engine speeds (400, 800 and 1600 rpm) and compared to understand the scaling of in-cylinder flow structures and pressure waves with engine speed. Velocity data was acquired with variable time separations between PIV image frames to improve velocity dynamic range throughout the engine cycle, and with two cameras using different magnifications to improve spatial resolution. A phase-invariant POD analysis of all three data sets revealed that the POD coefficients, representing the contribution of flow structures seen in the associated modes to individual flow fields, scale with engine speed. This indicates that in-cylinder flow evolution changes predictably with engine speed. POD analysis from the intake stroke also showed that the in-cylinder flow during intake valve opening in the 800 rpm data set was different from that seen in the other two data sets. In the 800 rpm data set, there was an upward flow from the bottom-right corner of the field-of-view in the ensemble average velocity field at 100° ATDCE. In the 400 and 1600 rpm data sets, the ensemble average velocity field at 100° ATDCE shows a downward flow toward the bottom-right corner instead. This difference can be attributed to cycle-to-cycle variability in intake valve position in the horizontal direction during the intake stroke in the 800 rpm data. The phase-dependent POD analysis at 300° ATDCE showed no conclusive differences between the 800 rpm data and the other two data sets.

This dissertation has presented evidence of engine speed transients influencing valve oscillations, which, in turn, influence in-cylinder flow patterns during the intake stroke.

However, it was not possible to establish a clear link between variations in intake flow pattern and flow close to top dead center compression using two-component velocity data from the central tumble plane. Stereoscopic PIV data and further analysis of the three-dimensional LES data sets can lead to a more complete understanding of the in-cylinder flow. Velocity and combustion data from a fired engine can also be analyzed using POD to determine the relationship between in-cylinder flow variations and cycle-to-cycle combustion variations.

BIBLIOGRAPHY

1. Dahm, W.J.A., *Introduction to Turbulent Flows*, 2008.
2. Reuss, D.L., *Cyclic Variability of Large-Scale Turbulent Structures in Directed and Undirected IC Engine Flows*. SAE Technical Paper Series, 2000. *2000-01-0246*.
3. St. Hill, N., Asadamongkon, P., and Lee, K.C., *A study of turbulence and cyclic variation levels in internal combustion engine cylinder*, in *10th International Symposium on Application of Laser Techniques to Fluid Mechanics*2000: Lisbon, Portugal.
4. Li, Y., et al., *Characterization of an in-cylinder flow structure in a high-tumble spark ignition engine.* International Journal of Engine Research, 2004. **5**(5): p. 375-400.
5. Amelio, M., Bova, S., and De Bartolo, C., *The Separation Between Turbulence and Mean Flow in ICE LDV Data: The Complementary Point-of-view of Different Investigation Tools.* Journal of Engineering for Gas Turbines and Power, 2000. **122**: p. 579-587.
6. Liu, D., et al., *Cycle-to-cycle variation analysis of in-cylinder flow in a gasoline engine with variable valve lift.* Experiments in Fluids, 2012. **53**(3): p. 585-602.
7. Enotiadis, A.C., Vafidis, C., and Whitelaw, J.H., *Interpretation of cyclic flow variations in motored internal combustion engines.* Experiments in Fluids, 1990. **10**: p. 77-86.
8. Jarvis, S., et al., *Motored SI IC Engine In-Cylinder Flow Field Measurement Using Time Resolved Digital PIV for Characterisation of Cyclic Variation*. SAE Technical Paper Series, 2006. *2006-01-1044*.

9. Li, Y., et al., *Analysis of Tumble and Swirl Motions in a Four-Valve SI Engine*. SAE Technical Paper Series, 2001. *2001-01-3555*.

10. Elzahaby, A.M., Elshenawy, E.A., and Gadallah, A.H., *Cyclic Variability in I.C. Engines: Insights from Particle Image Velocimetry Measurements*, in *6th International Symposium on Diagnostics and Modeling of Combustion in Internal Combustion Engines (COMODIA 2004)*2004, Japan Society of Mechanical Engineers: Yokohama, Japan.

11. Chen, H., Reuss, D.L., and Sick, V., *Analysis of misfires in a direct injection engine using proper orthogonal decomposition.* Experiments in Fluids, 2011. **51**(4): p. 1139-1151.

12. Fogleman, M., et al., *Application of the proper orthogonal decomposition to datasets of internal combustion engine flows.* Journal of Turbulence, 2004. **5**.

13. Liu, K. and Haworth, D., *Development and Assessment of Proper Orthogonal Decomposition for Analysis of Turbulent Flow in Piston Engines*. SAE Technical Paper Series, 2011. *2011-01-0830*.

14. Baby, X., et al., *A New Methodology to Analyze Cycle-to-Cycle Aerodynamic Variations*. SAE Technical Paper Series, 2002. *2002-01-2837*.

15. Cosadia, I., et al., *Cyclic variations of the swirling flow in a Diesel transparent engine.* Experiments in Fluids, 2006. **41**: p. 115-134.

16. Enaux, B., et al., *LES study of cycle-to-cycle variations in a spark ignition engine.* Proceedings of the Combustion Institute, 2011. **33**(2): p. 3115-3122.

17. Chen, H., et al., *A practical guide for using proper orthogonal decomposition in engine research.* International Journal of Engine Research, 2012.

18. Chen, H., Reuss, D.L., and Sick, V., *On the use and interpretation of proper orthogonal decomposition of in-cylinder flows.* Measurement Science and Technology, 2012. **23**(8).

19. Vu, T.-T. and Guibert, P., *Proper orthogonal decomposition analysis for cycle-to-cycle variations of engine flow. Effect of a control device in an inlet pipe.* Experiments in Fluids, 2012. **52**(6): p. 1519-1532.

20. Cosadia, I., Boree, J., and Dumont, P., *Coupling time-resolved PIV flow-fields and phase-invariant proper orthogonal decomposition for the description of the parameters space in a transparent Diesel engine.* Experiments in Fluids, 2007. **43**: p. 357-370.

21. Voisine, M., et al., *Spatio-temporal structure and cycle to cycle variations of an in-cylinder tumbling flow.* Experiments in Fluids, 2011. **50**: p. 1393-1407.

22. Bizon, K., et al., *Application of Proper Orthogonal Decomposition to the Analysis of I.C.E. Space and Time Resolved Data*. SAE Technical Paper Series, 2007. *2007-24-0007*.

23. Druault, P., Guibert, P., and Alizon, F., *Use of proper orthogonal decomposition for time interpolation from PIV data.* Experiments in Fluids, 2005. **39**(6): p. 1009-1023.

24. Brandstätter, W., Johns, R.J.R., and Wigley, G., *Calculation of the flow produced by a tangential inlet port*, in *International Symposium on Flows in Internal Combustion Engines, ASME Winter Annual Meeting*1985: Miami Beach, Florida.

25. Imberdis, O., et al., *A Numerical and Experimental Investigation of a DISI-Engine Intake Port Generated Turbulent Flow*. SAE Technical Paper Series, 2007. *2007-01-4047*.

26. Kapitza, L., et al., *An experimental analysis of the turbulent structures generated by the intake port of a DISI-engine.* Experiments in Fluids, 2010. **48**: p. 265-280.

27. Dent, J.C. and Chen, A., *An Investigation of Steady Flow Through a Curved Inlet Port*. SAE Technical Paper Series, 1994. *940522*.

28. Gosman, A.D. and Ahmed, A.M.Y., *Measurement and Multidimensional Prediction of Flow in a Axisymmetric Port/Valve Assembly*. SAE Technical Paper Series, 1987. *870592*.

29. Węcłaś, M., Melling, A., and Durst, F., *Combined application of surface flow visualization and laser-Doppler anemometry to engine intake flows.* Experiments in Fluids, 1993. **15**: p. 323-331.

30. Khalighi, B., Haworth, D., and Huebler, M.S., *Multidimensional Port-and-in-Cylinder Flow Calculations and Flow Visualization Study in an Internal Combustion Engine with Different Intake Configurations*. SAE Technical Paper Series, 1994. *941871*.

31. Desantes, J.M., Benajes, J., and Urchueguia, J., *Evaluation of the non-steady flow produced by intake ports of direct injection Diesel engines.* Experiments in Fluids, 1995. **19**(1): p. 51-50.

32. Mattarelli, E., et al., *The Influence of Swirl Control Strategies on the Intake Flow in Four Valve HSDI Diesel Engines*. SAE Technical Paper Series, 2004. *2004-01-0112*.

33. Arcoumanis, C., et al., *Three-Dimensional Flow Field in Four-Stroke Model Engines*. SAE Technical Paper Series, 1984. *841360*.

34. Arcoumanis, C., Bicen, A.F., and Whitelaw, J.H., *Effect of Inlet Parameters on the Flow Characteristic in a Four-Stroke Model Engine*. SAE Technical Paper Series, 1982. *820750*.

35. Justham, T., et al., *Simultaneous Study of Intake and In-Cylinder IC Engine Flow Fields to Provide an Insight into Intake Induced Cyclic Variations.* Journal of Physics: Conference Series, 2006. **45**: p. 146-153.

36. Khalighi, B., et al., *Computation and Measurement of Flow and Combustion in a Four-Valve Engine with Intake Variations*. SAE Technical Paper Series, 1995. *950287*.

37. Kim, M. and Ohm, I., *The Effect of Intake Valve Angle on In-cylinder Flow during Intake and Compression Process*. SAE Technical Paper Series, 2007. *2007-01-4045*.

38. Johansson, B. and Soderberg, F., *The Effect of Valve Strategy on In-Cylinder Flow and Combustion*. SAE Technical Paper Series, 1996. *960582*.

39. Huang, R.F., et al., *In-cylinder tumble flows and performance of a motorcycle engine with circular and elliptic intake ports.* Experiments in Fluids, 2009. **46**: p. 165-179.

40. Wilson, T., et al., *In-cylinder Flow with Negative Valve Overlapping - Characterised by PIV Measurement*. SAE Technical Paper Series, 2005. *2005-01-2131*.

41. Melling, A., *Tracer particles and seeding for particle image velocimetry.* Measurement Science and Technology, 1997. **8**: p. 1406-1416.

42. Adrian, R.J., *Dynamic ranges of velocity and spatial resolution of particle image velocimetry', Measurement Science and Technology.* Measurement Science and Technology, 1997. **8**: p. 1393-1398.

43. Willert, C.E. and Gharib, M., *Digital particle image velocimetry.* Experiments in Fluids, 1991. **10**: p. 181 - 193.

44. Keane, R.D. and Adrian, R.J., *Optimization of particle image velocimeters. Part I: Double pulsed systems.* Measurement Science and Technology, 1990. **1**: p. 1202 - 1215.

45. Reuss, D.L., Megerle, M., and St. Hill, N., *Particle-image velocimetry measurement error when imaging through a transparent engine cylinder.* Measurement Science and Technology, 2002. **13**: p. 1029-1035.

46. Haworth, D., *Large-eddy simulation of in-cylinder flows.* Oil & Gas Science and Technology, 1999. **54**: p. 175-185.

47. Haworth, D., *A review of turbulent combustion modeling for multidimensional in-cylinder CFD.* SAE Technical Paper Series, 2005. *2005-01-0993*.

48. Celik, I.B., Yavuz, I., and Smirnov, A., *Large eddy simulations of in-cylinder turbulence for internal combustion engines: A review.* International Journal of Engine Research, 2001. **2**: p. 119-148.

49. Haworth, D. and Jansen, K., *Large-eddy simulation on unstructured deforming meshes: Towards reciprocating IC engines.* Computers and Fluids, 2000. **29**: p. 493-524.

50. Celik, I.B., et al., *Prediction of in-cylinder turbulence for IC engines.* Combustion Science and Technology, 2000. **153**: p. 339-368.

51. Celik, I.B., et al., *Towards large eddy simulation using the KIVA code*, in *11th International Multidimensional Engine Modeling User's Group Meeting*1998: Detroit, Michigan.

52. Naitoh, K., et al., *Large eddy simulation of premixed-flame in engine based on the multi-level formulation and renormalization group theory*. SAE Technical Paper Series, 1992. *920590*.

53. Smirnov, A., Yavuz, I., and Celik, I.B., *Diesel combustion and LES of in-cylinder turbulence for IC engines*, in *In-Cylinder Flows and Combustion Processes, ASME Fall Technical Conference*1999: Ann Arbor, Michigan.

54. Smith, J., et al., *Simulation of swirling flows related to an intake stroke of a diesel engine*, in *ASME ICE-Division Fall Conference*1998: Clymer, New York.

55. Vermorel, O., et al., *Multi-cycle LES simulations of flow and combustion in PFI SI 4-valve production engine*. SAE Technical Paper Series, 2007. *2007-01-0151*.

56. Richard, S., et al., *Towards large eddy simulation of combustion in spark ignition engines.* Proceedings of the Combustion Institute, 2007. **31**: p. 3059-3066.

57. Vermorel, O., et al., *Towards the understanding of cyclic variability in a spark ignited engine using multi-cycle LES.* Combustion and Flame, 2009. **156**: p. 1525-1541.

58. Laget, O., et al., *LES calculations of a four cylinder engine*. SAE Technical Paper Series, 2011. *2011-01-0832*.

59. Naitoh, K., Kaneko, Y., and Kayuza, I., *SI-Engine Design Concept for Reducing Cyclic Variations*. SAE Technical Paper Series, 2005. *2005-01-0992*.

60. Rutland, C.J., *Large-eddy simulations for internal combustion engines - a review.* International Journal of Engine Research, 2011. **12**(4): p. 421-451.

61. Reuss, D.L., et al., *Particle Image Velocimetry Measurements in a High-Swirl Engine Used for Evaluation of Computational Fluid Dynamics Calculations*. SAE Technical Paper Series, 1995. *952381*.

62. Reuss, D.L. and Rosalik, M., *PIV Measurements During Combustion in a Reciprocating Internal Combustion Engine*, in *9th International Symposium on Applications of Laser Technologies in Fluid Mechanics*1998: Lisbon, Portugal.

63. Bowditch, F.W., *A New Tool for Combustion Research - A Quartz Piston Engine*. SAE Technical Paper Series, 1961. *610002*.

64. *Product-Manual: Flow Master, Item Number(s): 1105011-4*, 2011, LaVision GmbH: Gottingen, Germany.

65. Prasad, A.K., *Stereoscopic particle image velocimetry.* Experiments in Fluids, 2000. **29**: p. 103 - 116.

66. Borgnakke, C. and Sonntag, R.E., *Fundamentals of Thermodynamics*2009: John Wiley & Sons, Inc.

67. Oster, D., et al., *On the effect of initial conditions on the two dimensional turbulent mixing layer,* in *Structure and Mechanisms of Turbulence I*, H. Fiedler, Editor 1978, Springer Berlin Heidelberg. p. 48-64.

68. Gupta, S., Yang, X., and Kuo, T.-W., *Personal Communication*, 2013.